Ferroelectric Glass-Ceramics

By

KAMONPAN PENGPAT

A thesis submitted to the University of Warwick, U.K.
For admission to the degree of
DOCTOR OF PHILOSOPHY

Department of Physics

May 2001

Contents

Page

List of Figures

List of Tables

Acknowledgement

Abstract

Chapter 1: General 1

1.1 Introduction 1

1.2 Aims of the research 2

1.3 Choice of system 2

1.4 Thesis plan 3

References 6

Chapter 2: Ferroelectric behaviour and ferroelectrics 7

2.1 Dielectrics and polarization 7

2.1.1 Dipole moment 7

2.1.2 Polarisation 8

2.1.3 Capacitor and permittivity 10

2.1.4 Complex permittivity 12

2.1.5 Frequency dependence 13

2.2 Definition and Classification of ferroelectrics 18

2.3 Ferroelectric behaviour 20

2.3.1 Curie-Weiss law 20

2.3.2 Ferroelectric prototype: Barium Titanate ($BaTiO_3$) 21

2.3.3 Ferroelectric hysteresis loop 22

2.3.4 Domain wall and grain boundary 23

2.3.5 Poling ferroelectrics 26

2.3.6 Unusual characteristic of ferroelectrics 26

2.4 Ferroelectric crystals of interest 27

2.4.1 Bismuth germanium pentaoxide (Bi_2GeO_5) 27
2.4.2 Lead germanate ($Pb_5Ge_3O_{11}$) 28
2.4.3 Lead metaniobate ($PbNb_2O_6$) 31
References 33

Chapter 3: Theoretical background of glass-ceramics 35
3.1 Introduction to glass-ceramics 35
3.1.1 History 35
3.1.2 The science of glass-ceramics 36
3.1.3 Some applications of glass-ceramics 36
3.2 Glass formation and stability (non-silicate glasses) 38
3.2.1 Glass definition 38
3.2.2 Glass former 42
3.2.3 Atomic hypothesis of glass formation 43
3.2.4 Glass formation and stability of GeO_2 44
3.3 Nucleation and crystallisation in glasses 46
3.3.1 Phase transformation in glasses 46
3.3.2 Nucleation and crystallisation of glasses 47
3.3.3 Controlled crystallisation of glass to give a glass-ceramic 51
3.4 Review of ferroelectric glass-ceramics 52
3.4.1 Ferroelectric glass-ceramics based on silicate glasses 53
3.4.2 Ferroelectric glass-ceramics based on tellurite glasses 55
3.4.3 Ferroelectric glass-ceramics based on phosphate and borate glasses 56
3.4.4 Solid solution in ferroelectric glass-ceramics 58
3.4.5 Ferroelectric crystals containing glass-former(s) 59
3.4.6 Other related materials 61
References 65

Chapter 4: Experimental materials and techniques 68
4.1 Glass-ceramics development 68
4.2 Preparation of a homogeneous glass 69

4.3 Differential thermal analysis (DTA) 69
4.4 Controlled heat treatment to produce the glass-ceramics 71
4.5 X-ray diffraction analysis (XRD) 72
4.6 Scanning Electron Microscopy (SEM) 77
4.7 Thermal expansion 80
4.8 Density and Molar volume 83
4.9 Dielectric measurement 84
4.10 Ferroelectric hysteresis loop measurement 87
References 90

Chapter 5:The bismuth germanate system 91
5.1 Introduction 91
5.2 Glass preparation 93
5.3 Bi_2O_3-GeO_2 93
5.4 Bi_2O_3-GeO_2-B_2O_3 95
5.4.1 Introduction 95
5.4.2 The stability of glasses 99
5.4.3 The simple phase diagram 99
5.4.4 Phase formation in glass-ceramics 101
5.4.5 Metastable phase formation 103
5.4.6 The calculation of volume fraction ratios 106
5.4.7 Glass density 110
5.4.8 Optimisation of composition 113
5.4.9 The calculation of crystallite size 118
5.4.10 Dielectric measurement 125
5.4.11 Hysteresis loop 130
5.5 $BiO_{1.5}$-GeO_2-TeO_2 132
5.6 Summary 138
References 139

Page

Chapter 6: The lead germanate and lead niobate systems 141

6.1 Introduction 141

6.2 $Pb_5Ge_3O_{11}$ (PG) 142

6.3 $Pb_5Ge_3O_{11}$:$PbNb_2O_6$ (PG-PN) 143

6.4 Dielectric measurement 151

6.5 Hysteresis loop 155

6.6 Further investigation of the PbO:GeO_2:Nb_2O_5 system 156

6.7 Summary 160

References 162

Chapter 7: The $Pb_5Ge_3O_{11}$: $PbNb_2O_6$: SiO_2 + Al_2O_3 system 164

7.1 Introduction 164

7.2 Glass preparation 164

7.3 The amorphous XRD patterns and immiscibility 166

7.4 DTA and XRD analysis for crystallisation information 168

7.4.1 PGS and PGSAl 168

7.4.2 PNSAl 171

7.4.3 PGNSAl1 174

7.4.4 PGNSAl2 176

7.4.5 PGNSAl3 178

7.4.6 PGNSAl4 180

7.5 Summary 183

References 184

Chapter 8: Conclusions and future work 185

List of Figures **Page**

Chapter 2

Figure 2.1 Elementary segments of polarised material. 8

Figure 2.2 Various polarisation processes. 9

Figure 2.3 The role of the dielectric in a capacitor. 10

Figure 2.4 Capacitative and 'loss' components of total current i. 13

Figure 2.5 Variation in permittivity with frequency for a dielectric showing 'Debye' relaxation. 15

Figure 2.6 Permittivity dispersion and dielectric loss for a glass ($18Na_2O{\cdot}10CaO{\cdot}72SiO_2$). 15

Figure 2.7 Variation of ε_r' and ε_r''. 16

Figure 2.8 Cole-Cole plot. 17

Figure 2.9 The unit cell of $BaTiO_3$. 21

Figure 2.10 Dielectric constant of tetragonal $BaTiO_3$. 22

Figure 2.11 Ferroelectric hysteresis loop (schematic). 23

Figure 2.12 The distinction between (a) a grain boundary and (b) a domain wall 24

Figure 2.13 Hysteresis loops for (a) a single-domain single crystal of $BaTiO_3$ and (b) $BaTiO_3$ ceramic. 25

Figure 2.14 Perspective view of the contents of one unit cell of Bi_2GeO_5 from $x = 0$ to $x = 0.33$ showing the deformed $Bi_2O_2^{2+}$ layers and the GeO_3^{2-} chains. 27

Figure 2.15 Comparison of idealised apatite, nasonite, and lead germanate structures showing section parallel to (010) $\approx$ 4 Å thick. 30

Figure 2.16 The basic octahedral framework of the tungsten bronze structure looking down the tetragonal c-axis. 32

Chapter 3

Figure 3.1 Comparison of the radial distribution function of a glass with that of the gaseous, liquid and crystalline states. 39

Figure 3.2 Effect of temperature on the enthalpy of a glass-forming melt. 40

Figure 3.3 Two-dimensional representation of an oxide M_2O_3 in (a) the crystalline form (b) the glassy form. 44

Figure 3.4 Diagram of phase transformations in glasses. 46

Figure 3.5 Rates of homogeneous nucleation and crystal growth in a viscous liquid. 50

Figure 3.6 Idealised heat-treatment schedule for a glass-ceramic. 51

Chapter 4

Figure 4.1 Diagram of glass-ceramic development. 68

Figure 4.2 Classical apparatus (S = sample; R = reference). 70

Figure 4.3 Differential thermal analysis curve for a devitrifiable glass. 71

Figure 4.4 The diagram of the heat treatment schedule used in this study. 72

Figure 4.5 (a) Simple illustration of Bragg's law (b) Ewald sphere Construction. 73

Figure 4.6 The diffractometer equatorial geometry. 74

Figure 4.7 A summary of the effects which may be detected when a primary beam of high energy electrons hits specimen. 78

Figure 4.8 Simple diagram of the excitation volume in SEM. 80

Figure 4.9 Cross section of the inside of the quartz dilatometer. 82

Figure 4.10 A simple diagram of a linear variable differential transformer (LVDT). 82

Figure 4.11 The simple diagram of a digital density balance (Precisa 125A). 83

Figure 4.12 Schering bridge. 85

Figure 4.13 The diagram for dielectric measurement. 86

Figure 4.14 Circuit for investigation of the hysteresis loop. 87

Figure 4.15 Circuit with compensation added. 88

Chapter 5

Figure 5.1 Bi_2O_3-GeO_2 phase diagrams. 92

Figure 5.2 The comparison of devitrified glasses produced from different initial substances. 94

Figure 5.3 X-ray powder diffraction pattern of the sintered ceramic containing 50 mole% Bi_2O_3 and 50 mole% GeO_2. (sintered at 710°C for 24 hours) 95

Figure 5.4 The seven samples in the phase diagram of the $BiO_{1.5}$-GeO_2-$BO_{1.5}$ system. 96

Figure 5.5 Amorphous XRD patterns of glasses of samples 1-5 from the $BiO_{1.5}$-GeO_2-$BO_{1.5}$ system. 97

Figure 5.6 DTA traces of samples $BiGeB_1$ to $BiGeB_5$. 98

Figure 5.7 A plot of the onset temperature of the first exothermic peak from DTA cooling curve of five glasses 1 – 5. (Red line is fitted by a simple polynomial) 100

Figure 5.8 SEM backscattering image of $BiGeB_3$ cross-sectional glass-ceramic heat treated at 509°C for four hours. 102

Figure 5.9 The DTA trace of $BiGeB_4$ sample shows the metastable sharp peaks (T_{X2} - T_{X4}). 104

Figure 5.10 The XRD patterns of $BiGeB_4$ sample heated at four different temperatures: T_{X1}, T_{X2}, T_{X3} and T_{X4}. 105

Figure 5.11 XRD pattern of $BiGeB_2$. (Tx = 509°C) 106

Figure 5.12 SEM backscattering image and EDS spectra of each phase in $BiGeB_2$ cross-sectional glass-ceramic heat treated at 509°C for four hours. 108

Figure 5.13 Density of $BiGeB_1$-$BiGeB_5$ samples (constant amount of 28.58 mol% $BO_{1.5}$) as a function of $BiO_{1.5}$ content. 111

Figure 5.14 Density of $BiGeB_2$, $BiGeB_6$, $BiGeB_7$ and additional glasses as a function of $BO_{1.5}$ content. 112

Figure 5.15 XRD patterns of melted glasses of sample $BiGeB_6$ and $BiGeB_7$. 113

Figure 5.16 the DTA trace of $BiGeB_6$ glass. 114

Figure 5.17 SEM backscattering image of $BiGeB_6$ cross-sectional glass-ceramic heat treated at 467°C for four hours. 117

Figure 5.18 SEM backscattering image of $BiGeB_6$ cross-sectional glass-ceramic heat treated at T_{X1} = 475°C for four hours. 117

Figure 5.19 The XRD pattern of $BiGeB_6$ glass-ceramics heat treated at 475 °C for 4 hours. (a) ground powder and (b) bulk piece. 118

Figure 5.20 The typical plots illustrating the positions of the straight lines of very large crystallite sizes ($L = \infty$), no strain ($\eta = 0$) and when crystallite size and lattice strain contribute to peak broadening (L and $\eta \neq 0$). 120

Figure 5.21 The linear regression of FWHM of silicon standard for the correction of instrumental effects. 122

Figure 5.22 The Gaussian fit of the peak from XRD pattern of $BiGEB_6$ of $T_{X1} = 475$ °C for 4 hours, the heating rate = 5 °C/min. 122

Figure 5.23 The linear regression of $B_r\cos\theta$ versus $\sin\theta$ using three reflections from the XRD pattern of $BiGeB_6$ glass-ceramic of $T_{X1} = 475$ °C, hold for 4 hours and heating rate = 5 °C/min. 123

Figure 5.24 The XRD pattern of $BiGeB_6$ glass-ceramics heat treated at 475 °C for 0 hour. 124

Figure 5.25 Dielectric constant (at 10 kHz) versus temperature for the $BiGeB_6$ glass-ceramic at different heat treatment schedules. 126

Figure 5.26 Temperature dependence of real (ε_r') and imaginary (ε_r'') parts of the complex permittivity of a $BiGB_6$ thin sample (heat-treated at 475°C for 12 hours). 127

Figure 5.27 Frequency dependence of real (ε_r') and imaginary (ε_r'') parts of the complex permittivity of a $BiGB_6$ thin sample (heat-treated at 475°C for 12 hours). 128

Figure 5.28 Cole-Cole plots from a $BiGB_6$ thin sample (heated at 480°C for 12 hours) at different temperatures. The continuous curves are fitted with the Cole-Cole model. 129

Figure 5.29 Hysteresis loop at room temperature (100 Hz) of a $BiGeB_6$ glass-ceramic of 0.024±0.002 cm thickness, heated at 480°C for 12 hours. 131

Figure 5.30 The five samples prepared from the $BiO_{1.5}$-GeO_2-TeO_2 system. 132

Figure 5.31 XRD patterns of glasses of samples 1-4 from the $BiO_{1.5}$-GeO_2-TeO_2 system. 134

Figure 5.32 The optical microscopic image of $BiGeTe_2$ quenched glass. 135

Figure 5.33 The comparison of DTA traces of $BiGeTe_2$ and $BiGeTe_3$ glasses. 136

Chapter 6

Figure 6.1 Five compositions from the PbO-GeO_2-Nb_2O_5 system. 143

Figure 6.2 The comparison of the X-ray diffraction patterns of the PG-PN quenched samples. 144

Figure 6.3 The location of five compositions: PG (1), PG:0.5PN (2), PG:PN (3), PG:2PN (4) and PG:3PN (5), with the glass formation region in PbO:GeO_2:Nb_2O_5 system. 146

Figure 6.4 The electron back-scattering image and EDS spectra of the PG-0.5PN quench-melt cross- section of 306μm in thickness. 147

Figure 6.5 The XRD pattern of ground powder and top and bottom surface of PG:0.5PN quenched sample. 149

Figure 6.6 The DTA trace of PG:0.5PN quench sample. 150

Figure 6.7 The XRD pattern of the top and bottom surface of PG-0.5PN subjected to heat treatment at 667°C for 48 hrs. 150

Figure 6.8 Temperature dependence of real (ε_r') and imaginary (ε_r'') part of complex permittivity of PG-0.5PN quenched sample of about 0.040±0.002 cm in thickness. 151

Figure 6.9 Temperature dependence real (ε_r') and imaginary (ε_r'') part of complex permittivity of PG-0.5PN subjected to heat treatment at 667°C for 48 hrsof about 0.140±0.002 cm in thickness. 152

Figure 6.10 Hysteresis loop at room temperature (50 Hz) of PG-0.5PN glass-ceramic of 0.026±0.002 cm thickness, heated at 667°C for 48 hours. 155

Figure 6.11 Additional samples in the $PbO:GeO_2:Nb_2O_5$ system. 157

Figure 6.12 The amorphous powder diffraction patterns of the 5%PN (7) and 5%PN2 (8). 158

Figure 6.13 The Differential Thermal Analysis (DTA) trace of 50%PbO: 40%GeO_2: 5%Nb_2O_5 (10%$NbO_{2.5}$) glass powder with 5°C/min heating rate. 159

Figure 6.14 The phase transitions diagram of SiO_2. 159

Chapter 7

Figure 7.1 The position of samples along the designed tieline in the ternary diagram (axis labels are presented in mole fraction). 165

Figure 7.2 XRD patterns of six glasses from the $Pb_5Ge_3O_{11}$: $PbNb_2O_6$: SiO_2+15%Al_2O_3 system and PGS glass (no addition of Al_2O_3). 167

Figure 7.3 The comparison between the DTA trace of PGS and PGSAl glass. 169

Figure 7.4 The XRD patterns of PGS glass-ceramics: (a) T_{X1} = 417 °C and (b) T_{X2} = 532 °C. 170

Figure 7.5 The DTA heating and cooling trace of PNSAl glass. 172

Figure 7.6 The XRD patterns of PNSAl glass-ceramics: (a) T_{X1} = 684 °C and (b) T_{X2} = 866 °C. 173

Figure 7.7 The DTA heating and cooling trace of PGNSAl1 glass. 174

Figure 7.8 The XRD patterns of PGNSAl1 glass-ceramics at T_X = 729 °C. 175

Figure 7.9 The DTA heating and cooling trace of PGNSAl2 glass. 176

Figure 7.10 The XRD patterns of PGNSAl2 glass-ceramics: (a) T_{X1} = 711 °C and (b) T_{X2} = 784 °C. 177

Figure 7.11 The DTA heating and cooling trace of PGNSAl3 glass. 178

Figure 7.12 The XRD patterns of PGNSAl2 glass-ceramics: (a) T_{X1} = 742 °C and (b) T_{X2} =905 °C. 179

Figure 7.13 The DTA heating and cooling trace of PGNSAl4 glass. 180

Figure 7.14 The XRD patterns of PGNSAl4 glass-ceramics: (a) T_{X1} = 691 °C, (b) T_{X2} = 919 °C and (c) T_{X3} = 935 °C. 182

Chapter 5

Table 5.1 The nominal compositions prepared from the $BiO_{1.5}$-GeO_2-$BO_{1.5}$ system. 97

Table 5.2 The To – Tg values of the five glass samples. 99

Table 5.3 The crystalline phases formed by cooling the melt from just above the liquidus temperatures of samples (1) to (5) 100

Table 5.4 Thermal parameters, crystallisation temperatures and crystalline phases formed from $BiGeB_1$, $BiGeB_2$, $BiGeB_3$, $BiGeB_4$ and $BiGeB_5$. 101

Table 5.5 Calculation of R values of $Bi_4(GeO_4)_3$ (R_I)and Bi_2GeO_5 (R_{II}). 107

Table 5.6 The volume fraction ratios of some glass ceramics. 110

Table 5.7 The density of $BiGeB_1$-$BiGeB_5$ glasses 111

Table 5.8 The density of other $BiO_{1.5}$-GeO_2-$BO_{1.5}$ glasses 112

Table 5.9 The crystal phases formed from different heat treatments of $BiGeB_6$ glass. 116

Table 5.10 The calculated and experimental values of the three unidentified peaks. 116

Table 5.11 Calculations for $BiGeB_6$ heat-treated at 475 °C for 4 hours (heating rate 5°C/min) 121

Table 5.12 The effect of heat treatment schedule on crystallite size of $BiGeB_6$ glass-ceramics.(measure the crystallite size of Bi_2GeO_5 phase) 123

Table 5.13 The comparison of T_C (Curie temperature), P_s (spontaneous polarisation) and E_r (coercive field) of Bi_2GeO_5 and some well-known ferroelectrics. 132

Table 5.14 The nominal compositions prepared from the $BiO_{1.5}$-GeO_2-TeO_2 system. 133

Table 5.15 The crystallisation information from $BiGeTe_1$-$BiGeTe_5$ samples. 135

Table 5.16 Thermal parameters, crystallisation temperatures and crystalline phases of all glass-ceramics from $BiGeTe_2$ and $BiGeTe_3$ glasses. 137

Page

Chapter 6

Table 6.1 The crystallisation information for PG, PG:0.5PN, PG:PN, PG:2PN and PG:3PN samples. 145

Table 6.2 The comparison of T_C (curie temperature), P_s (spontaneous polarisation) and E_r (coercive field) of the PG-0.5PN sample and some related ferroelectrics. 156

Table 6.3 The nominal compositions of the samples 6-7 from the $PbO:GeO_2:Nb_2O_5$ system. 157

Table 6.4 Thermal parameters, crystallisation temperatures and crystalline phases of all glass-ceramics from 5%PN and 5%PN2 glasses. 160

Chapter 7

Table 7.1 The nominal compositions prepared from the of $Pb_5Ge_3O_{11}$: $PbNb_2O_6:SiO_2$+ 15%Al_2O_3 system. 165

Table 7.2 Thermal data and crystalline phases of glass-ceramics formed from PGS and PGSAl glasses. 169

Table 7.3 Thermal parameters and crystalline phases from PNSAl glass. 172

Table 7.4 Thermal parameters and crystalline phases in the glass-ceramic from PGNSAl1 glass. 175

Table 7.5 Thermal parameters, crystallisation temperatures and crystalline phases of glass-ceramics for PGNSAl2 glass. 177

Table 7.6 Thermal parameters and crystalline phases of glass-ceramics from PGNSAl3 glass. 179

Table 7.7 Thermal parameters and crystalline phases of glass-ceramics for PGNSAl4 glass. 181

Chapter 8

Table 8.1 The glass-ceramics of interest from this study. 189

Acknowledgement

I would like to record my thanks to my supervisor, Dr. Diane Holland for her invaluable help, excellent guidance, interest and inspiration that made this study an interesting and rewarding experience. My special thanks go to Dr. David Hall, Dr. Jiang Quanzhong and Anuson Niyompan for their continuous assistance throughout the dielectric measurement and ferroelectric hysteresis loop. Also, my thanks to all my work colleagues in the glass-ceramic group for convenience of using instrument.

Last but not least, my very sincere thanks to my sponsor Ms. Duangsamorn Klongsara and her colleagues from the Institute for the Promotion of Teaching Science and Technology (IPST), Thailand who jointly provided me financial support and great understanding. Most importantly, I would not have been able to read and complete this degree at the University without their support.

I would also like to thank my family for their love and encouragement to finish this work, and for always being there for me when I need them. Finally, my thanks go to my boyfriend, Terence Cheung who helped me through all this hard work and gave me comfort and support.

Abstract

Ferroelectric glass-ceramics have been investigated from the Bi_2O_3-GeO_2, $BiO_{1.5}$-GeO_2-$BO_{1.5}$, $BiO_{1.5}$-GeO_2-TeO_2, 5PbO-3GeO_2, PbO-GeO_2-Nb_2O_5, and $Pb_5Ge_3O_{11}$-$PbNb_2O_6$-SiO_2+15%Al_2O_3 systems. DTA, XRD and SEM analysis were used to obtain crystallographic and microstructural information. The dielectric properties and ferroelectric hysteresis loop behaviour of selected samples were determined.

The stoichiometric Bi_2O_3:GeO_2 (Bi_2GeO_5) composition devitrified on cooling, giving rise to the investigation of new systems $BiO_{1.5}$-GeO_2-$BO_{1.5}$ and $BiO_{1.5}$-GeO_2-TeO_2. It was found that the glass-forming region in $BiO_{1.5}$-GeO_2-TeO_2 is narrow and good parent glasses for precipitating Bi_2GeO_5 crystals were not obtained. However, pure Bi_2GeO_5 based glass-ceramic can be successfully formed from $BiO_{1.5}$-GeO_2-$BO_{1.5}$. SEM backscatter imaging of these glass-ceramics showed surface crystallisation and XRD analysis confirmed that the preferred orientation is perpendicular to (311) planes. The dielectric behaviour and ferroelectric hysteresis loop study of the Bi_2GeO_5 based glass-ceramic heat treated at 475 °C for 12 hours, showed that this material can be ferroelectric at room temperature with P_s = 14 $\mu C/cm^2$ and has Curie temperature at about 407 °C.

Glasses of compositions PG($Pb_5Ge_3O_{11}$)-xPN($PbNb_2O_6$) (x = 0.5, 1, 2 3) were investigated from the PbO-GeO_2-Nb_2O_5 system. Most of the samples devitrified on cooling and have poor mechanical strength except the sample PG-0.5 PN sample which also contains interesting phases: ferroelectric $Pb_5Ge_3O_{11}$ and dielectric pyroniobate $Pb_2Nb_2O_7$. The surface crystallisation of $Pb_5Ge_3O_{11}$ with a-axis orientation and the bulk crystallisation of $Pb_2Nb_2O_7$ phase in this sample could be observed using SEM and XRD analysis. By applying heat treatment at 667 °C for 48 hours to this sample, surface crystallisation along the a-axis can be enhanced. The Curie temperature of this heat treated sample is about 166 °C with P_s = 1 $\mu C/cm^2$ from dielectric measurement and ferroelectric hysteresis loop behaviour. More samples were also investigated but it was difficult to form glass-ceramics containing both $Pb_5Ge_3O_{11}$ and $PbNb_2O_6$ crystals from this PbO-GeO_2-Nb_2O_5 system.

In order to obtain the multiple ferroelectric $Pb_5Ge_3O_{11}$ and $PbNb_2O_6$ based-glass ceramics, six glasses along the tie line from 62.5 mol%PbO: 25 mol%GeO_2: 12.5 mol%SiO_2 to 40 mol%$PbNb_2O_6$: 60 mol%SiO_2 were investigated from the $Pb_5Ge_3O_{11}$: $PbNb_2O_6$: SiO_2+15%Al_2O_3 system. Most of the glasses exhibited glass-in glass phase separation. From DTA analysis and subsequent crystallisation information, the most likely possible parameters, which control the glass-in glass phase separation, may be the Nb_2O_5/SiO_2 ratio for the glasses near the $Pb_5Ge_3O_{11}$ rich composition and Al_2O_3 for the glasses near the $Pb_2Nb_2O_6$ rich composition. This system offered many interesting materials such as cubic pyrochlore $Pb_2Nb_2O_7$ based glass-ceramics and the orthorhombic $PbNb_2O_6$ based glass-ceramics, and they are also mechanically robust.

Chapter 1

General

1.1 Introduction

Ferroelectric materials are used world-wide in many applications of electronic devices as a result of their specific properties, such as their high dielectric constant, large piezoelectric coefficient and large pyroelectric effects. They can also be used as good ceramic capacitors because the dielectric constant can be as high as 20,000. Their piezoelectric properties can give rise to a number of applications: underwater sonar, gas lighters, bulk wave filters, surface acoustic wave devices, piezoelectric transformers, etc. Their pyroelectric properties enable the production of useful devices such as fire alarms, thermal imaging equipment and intruder detection. Because ferroelectrics have a non-linear piezoelectric property, they can be used for direct amplification of sound and as matrix stores in computer circuits. [1] The extremely well-known ferroelectric material $BaTiO_3$ (Barium Titanate), was discovered by Wul and Goldman in 1945 [2] and the polycrystalline barium titanate, made by sintering routes, formed the first Multilayer Ceramic Capacitors (MLC), which have become the basic ceramic dielectric capacitor in various substituted forms. [3,4]

Generally, ferroelectric materials have nonlinear optical (NLO) properties and hence transparent materials are needed for their applications. However, it is difficult to make transparent ceramics with ferroelectric properties by a sintering route. As a result of this, many workers have attempted to disperse ferroelectric crystals in glass, using different types of network-forming oxides, such as SiO_2, TeO_2, B_2O_3 and GeO_2. Glass-ceramics have several advantages, particularly the fact that they are made from a pore-free precursor glass and have good thermal, mechanical and electrical properties. As a result of their high mechanical strength, good dimensional stability

and abrasion resistance, they can be applied in a number of devices in mechanical engineering, such as bearings, pumps, heat exchangers, furnace construction. Moreover, they can also be applied to many technologies, for example: applications in electrical engineering and electronics, applications in aerospace engineering, lighting and optical applications and applications in nuclear engineering. As a result of their combination of properties , glass-ceramics have the potential to replace the traditional materials used in applications where the requirements of more cost effective and improved performance are paramount. Recently, many researchers have become interested in the glass-ceramic method and have attempted to open up entirely new fields. Unfortunately, a number of applications still wait for industrial exploitation. [5,6]

1.2 Aims of the research

Since ferroelectric materials can give good electro-optic properties and a useful electro-optic material needs to be transparent, glass-ceramics usually fulfil these requirements. Bismuth and lead oxides play a most important role in this study because the glasses containing Bi^{3+} and Pb^{2+} ions have a large electro-optic coefficient. Consequently, this research is aimed at investigating the ferroelectric glass-ceramics based on these heavy metal oxides and germanium oxide as a glass former. Germanium oxide is chosen because there has not been a substantial amount of work done using this oxide. The new interesting phases, which might be possible to crystallise from the germanate-based glasses are studied.

1.3 Choice of system

The following glass systems were chosen for study:

a) Bismuth germanate system

- Bi_2O_3-GeO_2 : the stoichiometric composition of Bi_2GeO_5.
- $BiO_{1.5}$-$BO_{1.5}$-GeO_2: seven different compositions of bismuth germanate with the addition of 28.58, 18.18 and 9.52 mol% of $BO_{1.5}$.
- $BiO_{1.5}$-TeO_2-GeO_2: seven different compositions of bismuth germanate with the addition of 16.67, 20, 25 and 30 mol% of TeO_2.

b) Lead germanate system

- PbO-GeO_2: the stoichiometric composition of $Pb_5Ge_3O_{11}$.
- PbO-Nb_2O_5-GeO_2: nine samples of lead germanate with nominal Nb_2O_5 contents between 5.5 and 21.4 mol%.

c) Lead germanate plus lead niobate system

- $PbNb_2O_6$- $Pb_5Ge_3O_{11}$-SiO_2: six compositions from this system with the addition of 15 mol%Al_2O_3.

1.4 Thesis plan

The following seven chapters are included in this thesis:

Chapter 2 is the introduction to ferroelectric materials and some basic background. It will continue with reviews of the ferroelectric crystals of interest including bismuth germanium pentaoxide (Bi_2GeO_5), lead germanate ($Pb_5Ge_3O_{11}$) and lead metaniobate ($PbNb_2O_6$).

Chapter 3 presents the theoretical background of glass-ceramics containing some important basic discussion of glass formation and stability (non-silicate

glasses), nucleation and crystallisation in glasses. A review of ferroelectric glass-ceramics is also included.

Chapter 4 introduces the experimental techniques employed in the research program. The glass-ceramic process, preparation of homogeneous glass, differential thermal analysis (DTA), controlled heat treatment, X-ray diffraction analysis (XRD), scanning electron microscopy (SEM), thermal expansion, density and molar volume, dielectric measurement and ferroelectric hysteresis loop measurement will be described.

Chapter 5 is devoted to the bismuth germanate system including Bi_2O_3-GeO_2, $BiO_{1.5}$-GeO_2-$BO_{1.5}$ and $BiO_{1.5}$-GeO_2-TeO_2 systems. It presents the results and discussion of glass preparation, the stability of glasses, phase formation in glass-ceramics, metastable phase formation, the optimised composition, glass density, dielectric measurement and ferroelectric hysteresis loop.

Chapter 6 concerns the lead germanate system. The difficulty in preparing lead germanate glass of stoichiometric $Pb_5Ge_3O_{11}$ is described. The multiple glass-ceramic $Pb_5Ge_3O_{11}$:$PbNb_2O_6$ (PG:PN) is introduced. Ten glasses were prepared in the PbO:Nb_2O_5:GeO_2 system. Phase compositions and dielectric properties of some glass-ceramic are reviewed.

Chapter 7 introduces the new system $PbNb_2O_6$-$Pb_5Ge_3O_{11}$-SiO_2+Al_2O_3. Six compositions from this system were studied. The crystallisation study was conducted using XRD and DTA methods.

Chapter 8 presents the conclusions on the work done on the bismuth germanate, lead germanate and lead germanate plus lead niobate systems. Future work will also be suggested in this chapter.

References

1. Jack, C. B. *Ferroelectrics*, 1976 (D. Van Nostrand Company Ltd.).
2. Wul, B. and Goldman, I.M. 1945, *C.R. Acad. Sci. URSS.*, volume 46, p. 139; volume 49, p. 177.
3. Levinson, M. *Electronic Ceramics*, 1987 (Marcel Dekker INC, New York Basel).
4. Moulson, A.J. and Herbert, J.M. *Electroceramics*, 1990 (Chapman & Hall).
5. Komatsu, T., Tawarayama, H. and Matusita, K. *Journal of Ceramic Society Japan*, 1993, Volume 101, p.48.
6. McMillan, P.W. *Glass Ceramics*, 1979 (Academic Press)

Chapter 2

Ferroelectric behaviour and ferroelectrics

2.1 Dielectrics and polarisation

Dielectric materials are important in the world of insulators. Early experiments showed that dielectric materials, placed between electrostatic charges, could prevent the conduction of the charge. The first practical insulating materials were amber, bees-wax and glass. These materials have low *dielectric strength* [1] (the field which, when applied to the material, causes a breakdown current across it) compared to the high dielectric strength materials now available, such as ceramics and particularly ferroelectric ceramics. At this stage, it is essential to understand the basic theory of dielectrics and polarisation, in order to truly appreciate the basis of ferroelectric materials.

2.1.1 Dipole moment

Dielectrics may be defined as electrically insulating (non-metallic) materials, exhibiting an electric dipole structure, which is a separation of positive and negative electrically charged entities on a molecular or atomic level. [2] An electric dipole moment consists of a pair of opposite charges Q, separated by a small distance ($\delta\mathbf{x}$). This relationship can be shown in equation 2.1.

$$\mathbf{p} = Q\delta\mathbf{x} \text{ coulombs} \cdot \text{metres}, \qquad (2.1)$$

where $\mathbf{p}$ is the electric dipole moment vector with its positive sense directed from the negative charge to the positive charge. It can be assumed that $\mathbf{p}$ is proportional to a local electric field inside the dielectric and may be defined by:

$$\mathbf{p} = \alpha \mathbf{E}_{int}, \qquad (2.2)$$

where α is the polarisability of the dipole and $\mathbf{E}_{int}$ is a local electric field inside the dielectric.

2.1.2 Polarisation

Polarisation (**P**) may be defined as the dipole moment per unit volume

$$\mathbf{P} = N\alpha \mathbf{E}_{int}, \qquad (2.3)$$

where N is the number of elementary dipoles per unit volume. [1] Figure 2.1 shows an example of elementary dipolar segments. The magnitudes of the vectors are presented as

$$\frac{\delta p}{\delta V} = P = \sigma_p, \qquad (2.4)$$

where $\sigma_p = \mathbf{n} \cdot \mathbf{P}$ (**n** is the unit vector normal to the surface)

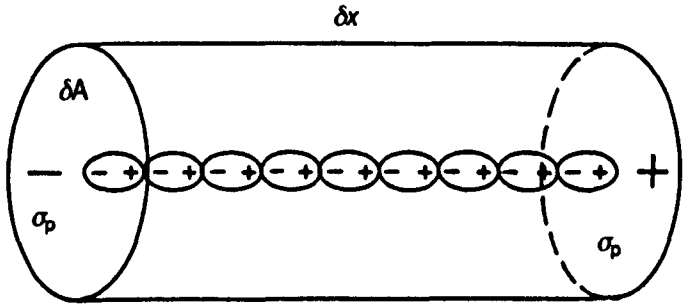

Figure 2.1 *Elementary segments of polarised material.* [3]

Furthermore, the magnitude of α (polarisability) is dependent on the configuration of the electric dipoles, which is determined by atoms and molecules. The four different polarisation processes are shown in figure 2.2. [3]

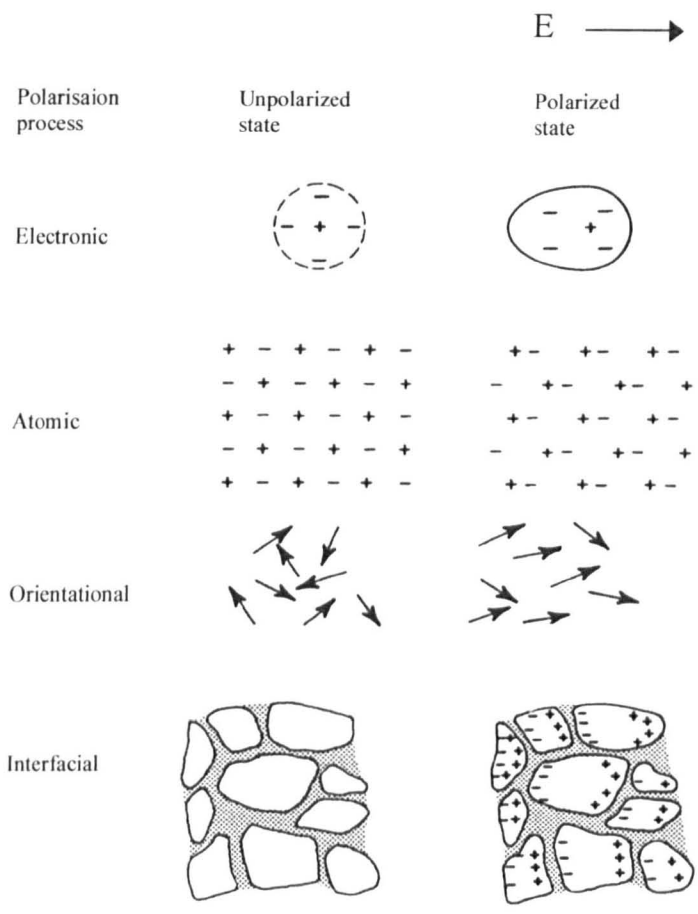

Figure 2.2 *Various polarisation processes. (After Moulson [3])*

From Fig. 2.2, electronic polarisation is the separation of the centre of gravity of the electron and nuclear charges by a small displacement when the field is applied. Because the natural frequencies of the dipoles are ≥ the frequencies of visible light, the specific description of the polarisability, in this case, is *optical polarisability* or *electronic polarisability* (α_e). Ionic polarisation and dipolar polarisation are sometimes grouped together as molecular polarisation. In ionic materials, the field may cause the separation of cation and anion, changing the dipole moment of the molecule, and this is referred to as *atomic polarisability* (α_a). Dipolar materials are polarised when an electric field is applied to orient the molecules. Then the whole molecule may rotate about its axis of symmetry, causing the alignment of the molecule with the field. This

mechanism is called *orientational polarisability* (α_d). The last type of polarisation is space charge polarisation. It is related to a limited transport of charge carriers when they are stopped at a potential barrier, such as a grain boundary, phase boundary, lattice vacancies, dislocation and so on. This might give rise to a localised accumulation of charge and create its own dipole moment. This is generally known as *interfacial polarisability* (α_i).[1,3] The magnitude of polarisability depends on the formation of electric dipoles in materials, which might result from the four mechanisms as mentioned above. Therefore, the total polarisability (α) can be the sum of individual polarisabilities, such as, $\alpha = \alpha_e+\alpha_a+\alpha_d+\alpha_i$.

2.1.3 Capacitor and permittivity

When a parallel-plate capacitor is filled by a dielectric material (Fig. 2.3), an important relationship can be developed.

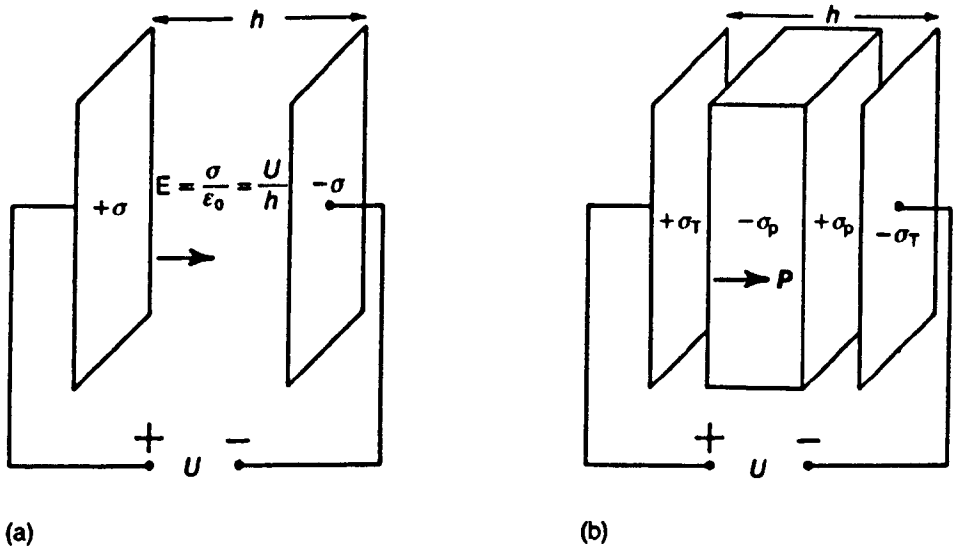

***Figure 2.3** The role of the dielectric in a capacitor.* [3]

The electric field E between two parallel plates, which have surface charge density σ in vacuum is

$$E = \frac{\sigma}{\varepsilon_0} \qquad \text{(Gauss's theorem),} \qquad (2.5)$$

where ε_0 is the *dielectric permittivity* or *dielectric constant* of free space.

From figure 2.3, both situation (a) and (b) have the same E because the applied voltage is the same. However, when the plates are separated by a dielectric material, the polarisation charge density σ_p appears on its surfaces. Therefore, the effective charge density E is reduced to

$$E = \frac{\sigma_T - \sigma_p}{\varepsilon_0}, \qquad (2.6)$$

where σ_T is the total charge density and is equal to the magnitude of the dielectric displacement vector **D**, so that

$$\mathbf{D} = \varepsilon_0 \mathbf{E} + \mathbf{P} \qquad (2.7)$$

and

$$\mathbf{P} = \chi_e \varepsilon_0 \mathbf{E}, \qquad (2.8)$$

where χ_e (chi) is the dimensionless constant, the electric susceptibility.

Using Equations (2.7), (2.8) and $D = \sigma_T$, it can be shown that

$$\frac{Q_T}{A} = (1 + \chi_e)\varepsilon_0 \frac{U}{h} \qquad (2.9)$$

in which U and h are the voltage across the capacitor plates and the distance between them respectively. Q_T is the total charge on the parallel-plate capacitor. Thus the capacitance is

$$C = \frac{Q_T}{U} = (1 + \chi_e)\varepsilon_0 \frac{A}{h}, \qquad (2.10)$$

where A is the area of the plate. In vacuum, χ_e is equivalent to zero so the capacitance C_0 of an empty parallel plate capacitor is

$$C_0 = \varepsilon_0 \frac{A}{h} \qquad (2.11)$$

When the plates are filled with a dielectric of χ_e, the capacitance is increased by a factor $1+\chi_e$.

Since the permittivity ε of the dielectric is defined as

$$\varepsilon = \varepsilon_0(1+\chi_e) \tag{2.12}$$

and

$$\frac{\varepsilon}{\varepsilon_0} = 1+\chi_e = \varepsilon_r, \tag{2.13}$$

where ε_r is the *relative permittivity* or *dielectric constant* of the dielectric, then the capacitance of plates filled with dielectric may be expressed as

$$C = \varepsilon_r\varepsilon_0\frac{A}{h} \text{ farads} \tag{2.14}$$

2.1.4 Complex permittivity

When an alternating e.m.f., v, is used to provide an alternating current, i, across the capacitor and if the dielectric is perfect (no loss of energy), the current is given by

$$i = j\omega\varepsilon_r C_0 v, \tag{2.15}$$

where $j=\sqrt{(-1)}$, ω = angular frequency and $v = v_0\sin(\omega t)$ (where a sinusoidal voltage is applied).

In practice, the in-phase or loss component of current will arise because of a resistive current between the parallel plates. This current is proportional to the permittivity of the dielectric medium, which can be introduced as a complex relative permittivity as follows:

$$\varepsilon_r^*(\omega) = \varepsilon_r'(\omega) - j\varepsilon_r''(\omega). \tag{2.16}$$

From equation 2.15 and 2.16, the current through the capacitor, filled with a lossy dielectric, then becomes

$$i = j\omega\left(\varepsilon_r' - j\varepsilon_r''\right)C_0 v$$

or $$i = \omega\varepsilon_r'' C_0 v + j\omega\varepsilon_r' C_0 v. \qquad (2.17)$$

From 2.17, there are two components, one is capacitative or 'lossless' and the other is in phase with v and 'lossy', as shown in figure 2.4.

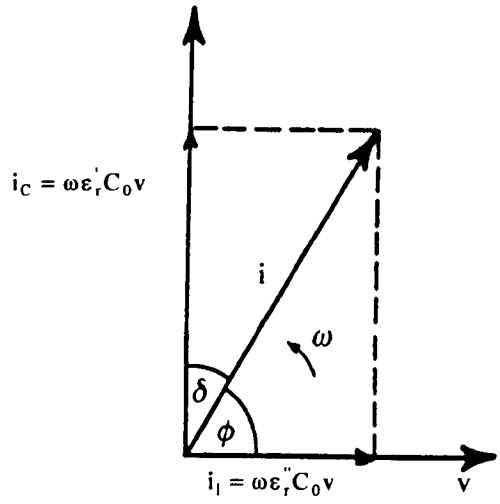

Figure 2.4 *Capacitative and 'loss' components of total current i.*

From the phasor diagram in figure 2.4, $\tan\delta = \frac{\varepsilon_r''}{\varepsilon_r'}$ and the current i_l, in phase with v, causes the power loss, while the capacitative component i_C does not.

Equation 2.18 shows the dissipated power density in the dielectrics:

$$\frac{\overline{P}}{V} = \frac{1}{2} E_0^{\,2} \omega\varepsilon_r\varepsilon_0 \tan\delta, \qquad (2.18)$$

where V is an applied voltage, $\varepsilon_r \tan\delta$ is the 'loss factor' of the dielectric and $\omega\varepsilon_0\varepsilon_r \tan\delta$ is the 'dielectric or AC conductivity':

$$\sigma_{AC} = \omega\varepsilon_r\varepsilon_0 \tan\delta.^{(3)} \qquad (2.19)$$

2.1.5 Frequency dependence

The inertia of the charges gives rise to a 'relaxation' of measured permittivity in dielectric materials. This happens when the dipoles cannot follow the field variation at

certain frequencies, depending on the type of polarisation. The real and imaginary parts of the permittivity can be explained by Debye equations, which are stated below:

$$\varepsilon_r' - 1 = \frac{\varepsilon_{rs}' - \varepsilon_{r\infty}'}{1 + \omega^2\tau^2} \tag{2.20}$$

and

$$\varepsilon_r'' = \left(\varepsilon_{rs}' - \varepsilon_{r\infty}'\right)\frac{\omega\tau}{1 + \omega^2\tau^2}, \tag{2.21}$$

where the additional subscripts: 's' and '∞' indicate the value of permitivity measured at low frequencies (or with a static field applied) and at infinite frequency respectively. The symbol τ is represented as a relaxation time, which may be a function of temperature but not time. Equation 2.22 presents the relationship between the relaxation time τ and temperature.

$$\tau = \tau_0 \exp\left(\frac{E_A}{kT}\right), \tag{2.22}$$

where E_A is an activation energy.

Equations 2.20 and 2.21 can be plotted as shown in figure 2.5 and from this figure it may be assumed that $\omega_r = \frac{1}{\tau}$, which is called a relaxation frequency. Figure 2.6 shows the various polarisation processes, leading to the dielectric dispersion and attendant energy dissipation.

Figure 2.6 shows the experimental graph of the dielectric dispersion and absorption curves of a common soda lime silica glass. It can be seen that this experimental figure is consistent with that of the Debye prediction from figure 2.5. Moreover, figure 2.7 demonstrates the dielectric dispersion and attendant energy dissipation of the various polarisation processes.

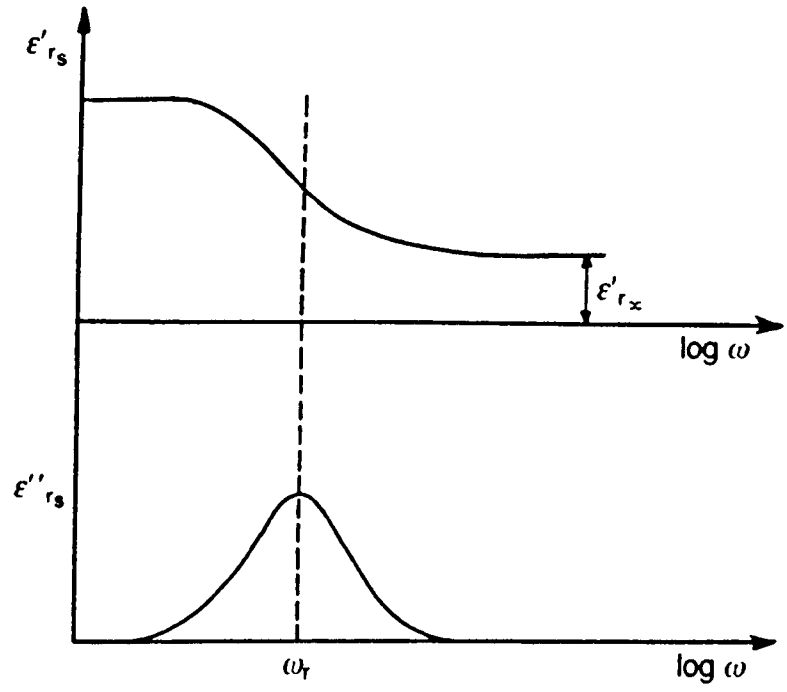

Figure 2.5 Variation in permittivity with frequency for a dielectric showing 'Debye' relaxation.[3]

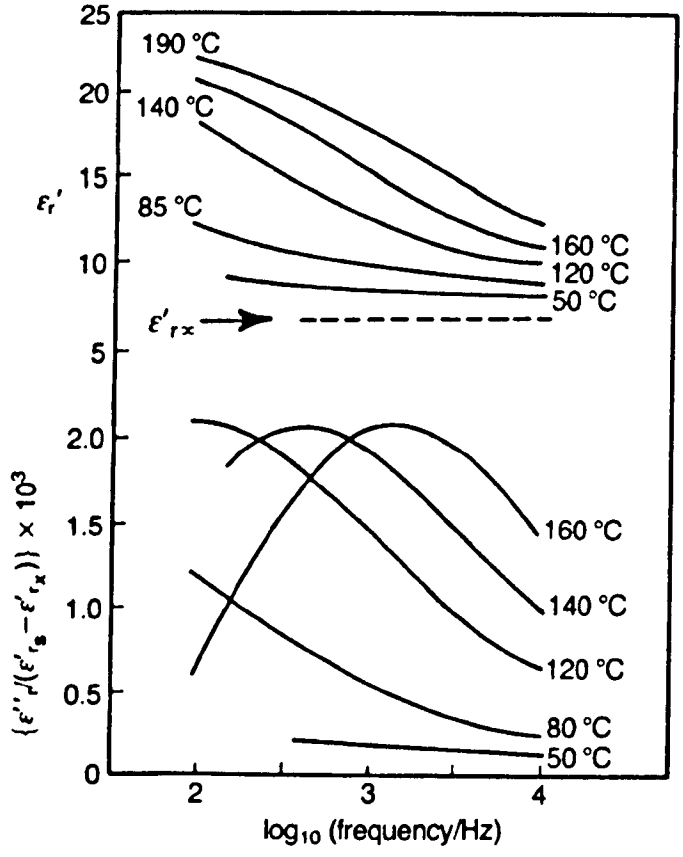

Figure 2.6 Permittivity dispersion and dielectric loss for a glass ($18Na_2O{\cdot}10CaO{\cdot}72SiO_2$).[3]

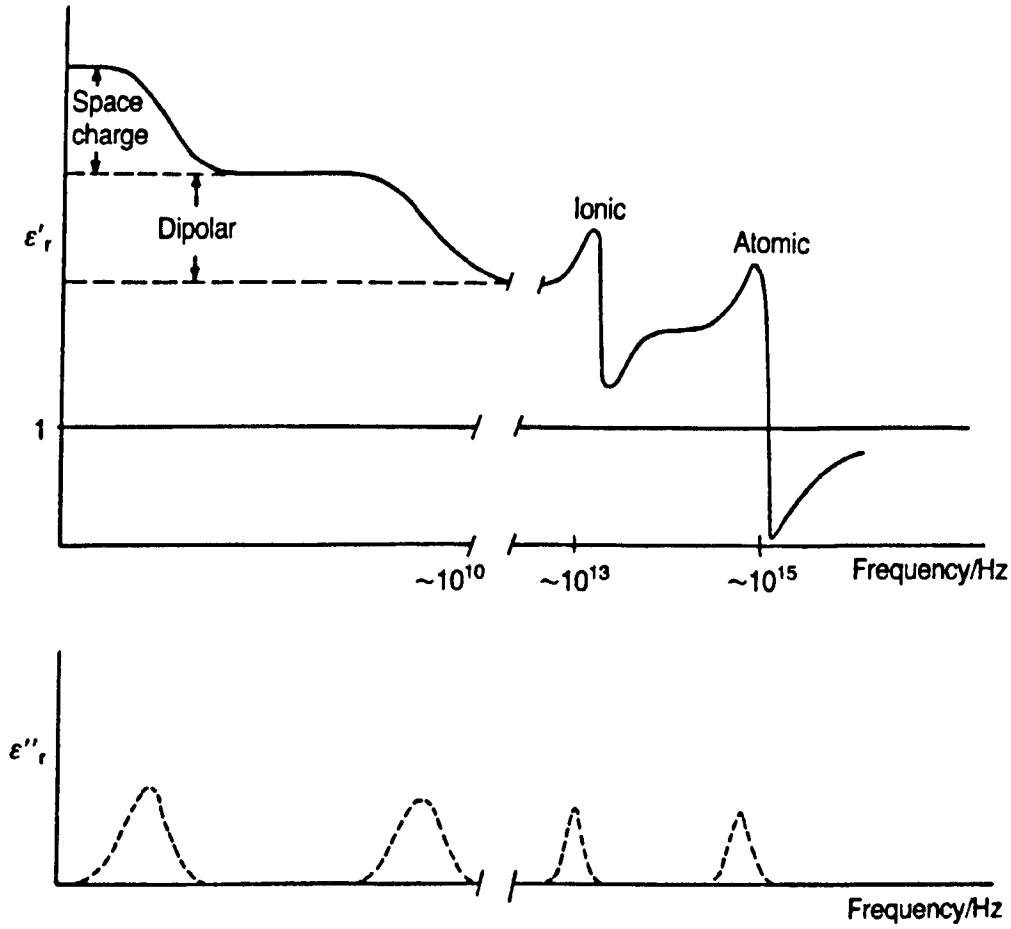

Figure 2.7 Variation of ε_r' *and* ε_r''.[3]

Consequently, it can be concluded that space charge and dipolar polarisations are relaxation processes and depend on temperature. In contrast, the ionic and electronic polarisations are resonance processes and sensibly temperature independent. The energy dissipation is a maximum at the critical frequency ranges as illustrated by peaks in $\varepsilon_r''(\omega)$.

In dipolar liquid, the dipoles have one equilibrium position while in solids, a number of equilibrium positions occur as a dipole finds itself in a regular electrostatic field causing by the other dipoles. Debye type relaxation is formulated from the simplest case of two equilibrium positions of the potential double-well model. However, in general solids, the molecular dipoles have more than two equilibrium

positions, giving rise to broader and flatter permittivity-frequency spectra than predicted by the simple Debye formulae. Thus, the relaxation time, obtained from these formulae, is an average of many different relaxation times which relate to transitions between the different equilibrium positions.[1] Therefore, the Cole-Cole function (equation 2.23) was introduced by Cole and Cole in 1942. [4]

$$\varepsilon_r^* - \varepsilon_{r\infty}' = \frac{\varepsilon_{rs}' - \varepsilon_{r\infty}'}{[1+(i\omega\tau)^{1-\alpha}]}, \qquad (2.23)$$

where the additional parameter α is the width of the distribution of relaxation times within the material. The Cole-Cole distribution is a plot of the imaginary part ε_r'' as a function of the real part ε_r'. Figure 2.8 shows the characteristic Cole-Cole plot of a RC circuit where the circuit values are

$$\tau = RC_2 \qquad (2.24)$$

$$C_2 = (\varepsilon_{rs} - \varepsilon_{r\infty})\varepsilon_0 \qquad (2.25)$$

$$C_1 = \varepsilon_{r\infty}\varepsilon_0 \qquad (2.26)$$

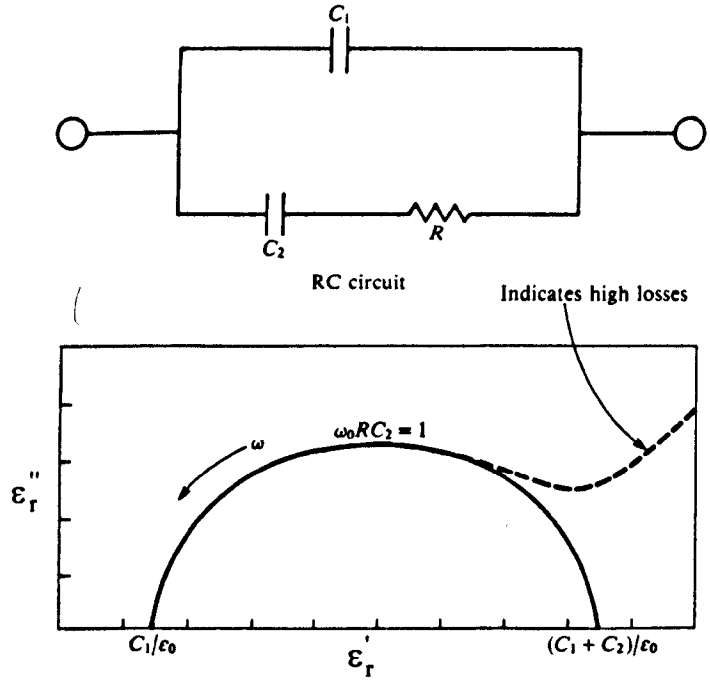

Figure 2.8 Cole-Cole plot. (After Hench and West [5])

The maximum of the semicircle occurs at

$$\omega_0 RC_2 = 1 \qquad (2.27)$$

as shown in figure 2.8. A perfect semicircle of Cole-Cole plot indicates low loss dielectric materials while a tail (increasing ε_r'' with increasing ε_r') occurs in the plot of high loss dielectrics.

2.2 Definition and Classification of ferroelectrics

Applying a stress field to piezoelectric crystals makes them polarised. Conversely they become strained when an electric field is applied. For pyroelectric crystals, a change in temperature gives a change in spontaneous polarisation. Some of them have the additional property, which is *the reversibility of spontaneous polarisation or permanent polarisation by an applied electric field*, these materials are called *ferroelectrics*. [6] This phenomenon can only be presented in a hysteresis loop, which will be explained in the next section.

Materials having ferroelectric behaviour are limited according to their crystal structures. In general, crystals are classified into seven systems: triclinic (the least symmetrical), monoclinic, orthorhombic, tetragonal, trigonal, hexagonal and cubic. Then these systems can be subdivided into 32 classes or point groups; 11 of which are centrosymmetric and non-piezoelectric, while the remaining 21 are non-centrosymmetric and 20 of these are piezoelectric. Of the 20 piezoelectric, 10 are polar classes, which are called pyroelectric. These 10 polar classes are mmm, 4mm, and their subgroups: 6, 4, 3m, 3, mm2, 2, m and 1. [7] A few polar crystals are *ferroelectric*. [3]

Ferroelectrics have finite polarisation even at zero external field E - known as spontaneous polarisation.[8] Spontaneous polarisation produces a resultant vector and can occur only in pyroelectrics, which have a low symmetry. A slight distortion of a

related non-polar crystal, which is observed above the transition temperature or Curie temperature T_C leads to the origin of a ferroelectric material. This temperature is the boundary when a ferroelectric phase (with spontaneous polarisation) changes to a paraelectric phase (without spontaneous polarisation).

The analogy between the dielectric properties of Rochelle salt ($NaKC_4H_4O_6 \cdot 4H_2O$) and the magnetic properties of ferromagnetic materials were first reported by Valasek in 1930. Later, around 1935 to 1938, some scientists reported behaviour in the ferroelectric crystals: KDP (KH_2PO_4) and ADP ($(NH_4)H_2PO_4$), which was related to the hydrogen bond hypothesis of ferroelectricity by Slater in 1941. Slater presented the first basic microscopic model, giving six possible ways in which two hydrogens could be connected with the four tetrahedral corners. However, because of this model, the pursuit of new ferroelectrics was discontinued until, 1945, $BaTiO_3$, was reported by Wul and Goldman in Russia[8]. They found that barium titanate ceramic had a high dielectric constant, at room temperature, about 1000 to 3000 and even higher when the temperature was increased. After this finding, the hydrogen bond model was abandoned. Studies of materials related to barium titanate, such as $KNbO_3$, $KTaO_3$, $LiNbO_3$, $LiTaO_3$ and $PbTiO_3$ and other new ferroelectrics have been carried out world-wide. [8,10]

Ferroelectrics may be classified into two categories in term of directions allowed to the spontaneous polarisation as follows: [8]

1. One axis of polarisation ('up' or 'down'): for example; Rochelle salt and related tartrates, KH_2PO_4-type ferroelectrics, $(NH_4)_2SO_4$ and $(NH_4)_2BeF_4$, colemanite, thiourea, glycine sulfate and glycine selenate.
2. Multiple axis polarisation, such as $BaTiO_3$-type ferroelectrics, $Cd_2Nb_2O_7$, $PbNb_2O_6$, certain alums and $(NH_4)_2Cd_2(SO_4)_3$.

This classification may be important in the study of ferroelectric domains. Another important classification is with regard to the piezoelectric properties of ferroelectrics. All polar crystals are piezoelectric and every ferroelectric, being polar, must possess piezoelectric properties. In addition, some ferroelectrics are also piezoelectric in the unpolarised phase, such as Rochelle salt and related tartrates, and KH_2PO_4-type ferroelectrics. Ferroelectrics which are not piezoelectric in the unpolarised phase include $BaTiO_3$-type ferroelectrics, $Cd_2Nb_2O_7$, $PbNb_2O_6$ and colemanite $CaB_3O_4(OH)_3 \cdot H_2O$.[8]

Some crystals, which are isomorphous or similar in structure to ferroelectrics, may contain dipoles in antiparallel arrangement, leading to zero net polarisation. These materials are called *antiferroelectrics*.[11] They still exhibit some common ferroelectric properties, such as the Curie point, and some antiferroelectrics, for example $PbZrO_3$, can be forced to be ferroelectrics by applying high electric fields. Furthermore, there is an interesting feature of some crystals, which at a given temperature can be ferroelectric in one axis and antiferroelectric in another. In this case, they are known as ferrielectrics, such as $NaNbO_3$. [10]

2.3 Ferroelectric behaviour

2.3.1 Curie-Weiss law

Ferroelectrics are important because of their very high and unusually temperature-dependent values of the dielectric constant (ε_r), the piezoelectric effect, the pyroelectric effect and electro-optical effects, including optical frequency doubling. Since they have high dielectric constants which vary with applied field strength and

temperature, the relative permittivity can be expressed by the Curie-Weiss law in (2.21).[3]

$$\varepsilon_r = \frac{A}{T - \theta_C} \qquad (2.21)$$

where A is constant for a given material and θ_C is a temperature near to but not exactly the same value as the Curie temperature (T_C).

2.3.2 Ferroelectric prototype: Barium Titanate ($BaTiO_3$)

Some materials present a whole series of ferroelectric structures at different temperatures. A good example of a ferroelectric single crystal is barium titanate ($BaTiO_3$) which has the perovskite structure, shown in figure 2.9. $BaTiO_3$ is non-ferroelectric when its temperature is above 120°C. This is because the unit cell is cubic. If the temperature is reduced below 120°C (Curie point) the unit cell is slightly distorted to the tetragonal form and then it becomes ferroelectric. When the temperature falls below 5°C, the unit cell becomes orthorhombic and below -90°C, the unit cell is rhombohedral. [7,12]

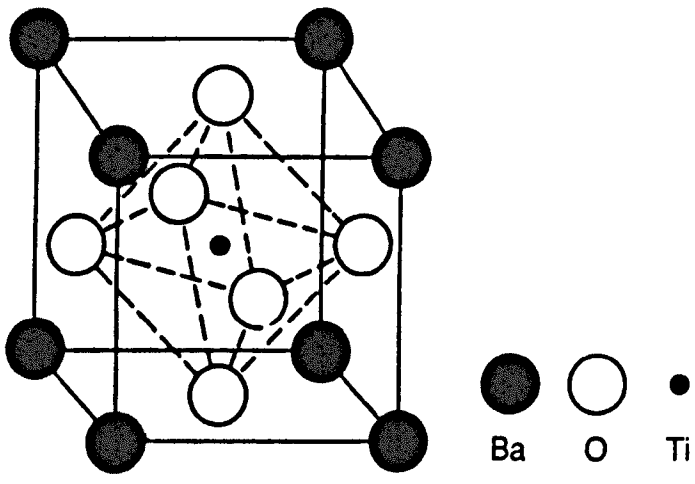

***Figure 2.9** The unit cell of $BaTiO_3$.*[3]

The temperature dependence of the dielectric constant is shown in figure 2.10.

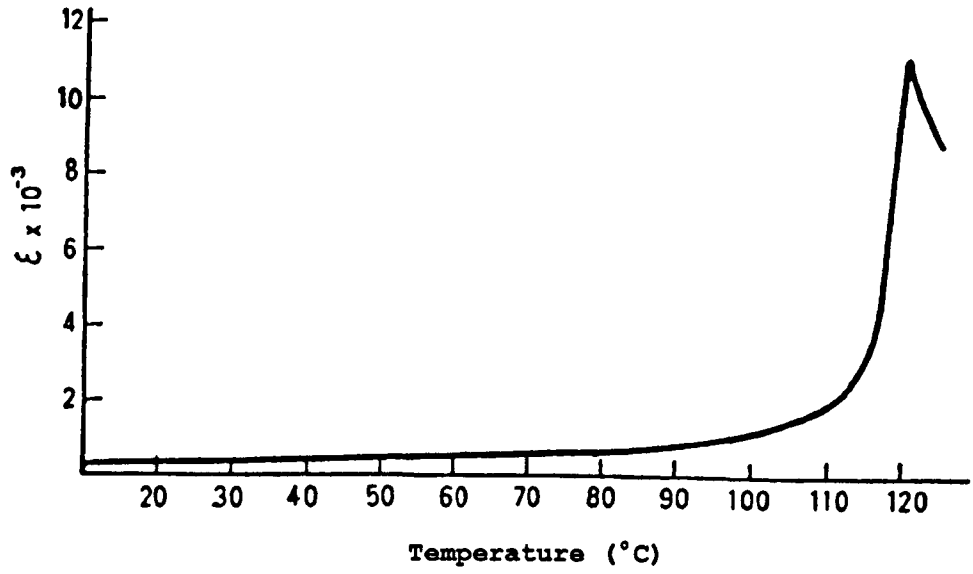

Figure 2.10 Dielectric constant of tetragonal $BaTiO_3$. [12]

From this figure, it can be seen that the dielectric constant has a sharp peak at the Curie point.

2.3.3 Ferroelectric hysteresis loop

The spontaneous electric polarisation P_s of ferroelectrics can be reversed by applying an appropriate electric field E, known as switching. This process can exhibit dielectric or ferroelectric hysteresis as shown in figure 2.11. The hypothetical crystal is assumed initially to have zero value of the overall polarisation since the crystal is composed of equal numbers of positive and negative domains. Domains may be defined as regions of uniform polarisation. When a small electric field in the positive direction, which is not large enough to switch any of the domains, is applied, the crystal behaves like a normal dielectric. Therefore, from the plot the portion OA is obtained. On increasing the electric field strength, most of the negative domains are switched over to the positive direction, giving rise to the dramatic increase in the polarisation (portion AB). This increase continues until all negative domains are

aligned in the positive direction. Then the plot reaches the saturation state (portion BC) and the crystal consists of only a single domain.

If the field strength is reduced, the polarisation will decrease but instead of going back to zero, it will follow the path CD, because of *a remanent polarisation* P_r (OD), some domains remaining aligned in the positive direction. The *spontaneous polarisation* (P_s) can be represented as portion OE.

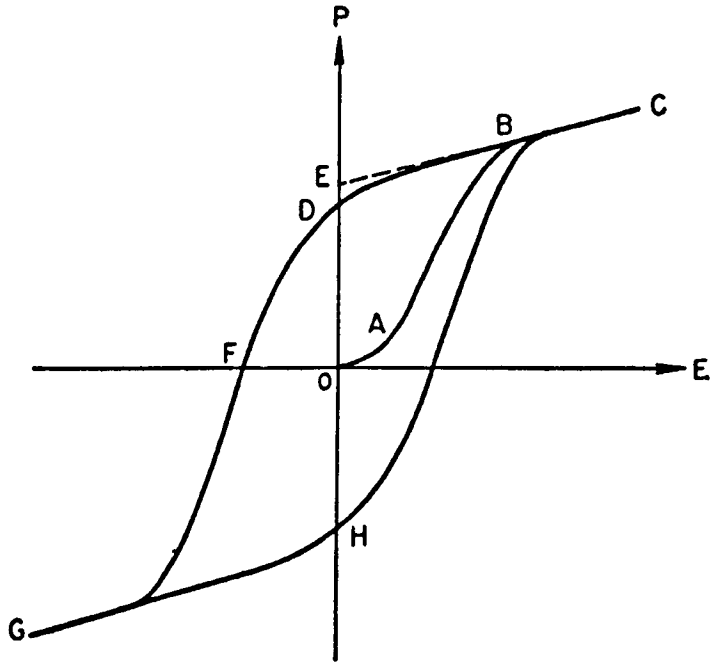

Figure 2.11 *Ferroelectric hysteresis loop (schematic).*[13]

A negative electric field is applied in order to obtain the zero value of overall polarisation. This value is called the *coercive field*: E_c (portion OF). Then increase of the electric field in the negative direction will give complete alignment of the dipoles in this direction (portion FG). Eventually, the cycle can be finished by reversing the field again (GHC).

2.3.4 Domain wall and grain boundary

Ferroelectric materials have spontaneous polarisation, which is normally arranged in the form of domains to minimise electrostatic energy. These regions

contain dipoles, which are all aligned in the same direction. The examples of 180° domains are shown in uniaxial crystals, with polarisation in opposite directions in adjacent domains. On the other hand, in multiaxial crystals, neighbouring domains are polarised in directions forming an angle θ between them. This angle equals the angle between certain crystallographic directions in the non-polar phase. A good example is the 90° domains in barium titanate ($BaTiO_3$), caused by its cubic symmetry and large mechanical stresses during cooling, which leads to domains polarised 90° apart. [1,3]

In general, most samples used to study ferroelectricity are single crystal. In polycrystalline materials, one grain may have several domains. Figure 2.12 shows the distinction between a grain boundary and domain wall.

(a) (b)

Figure 2.12 *The distinction between (a) a grain boundary and (b) a domain wall* [7]

From Fig. 2.11(b), it can be seen that the crystal lattice is not interrupted by the domain wall. As a result of this, some properties of ceramics or polycrystalline materials differ from single-crystal materials. This is because the grains are randomly oriented and porosity is always present in the polycrystalline materials. The difference in behaviour of single-crystal and polycrystalline materials is demonstrated by their hysteresis loops (figure 2.13). Therefore, it is important to understand the microstructure of ferroelectrics because it can affect not only electrical properties but also strongly effect Curie temperature, dielectric constant, piezoelectric coupling factor and piezoelectric strain constant of polycrystalline ferroelectrics.

The important characteristics of microstructures are grains, grain boundaries and pores. Grain size and porosity can produce space charge field and internal stresses in the materials, resulting in shift of the Curie temperature and variation of piezoelectric properties. Moreover, the size of individual grains and internal stresses of neighbouring grains control the domain structure, which has an important influence on dielectric and piezoelectric properties. Some processing of polycrystalline ceramics, such as heat treatment and electrical poling, can generate thermal or electric stress and give rise to microcracks, which affect the variation in ferroelectric properties. [14]

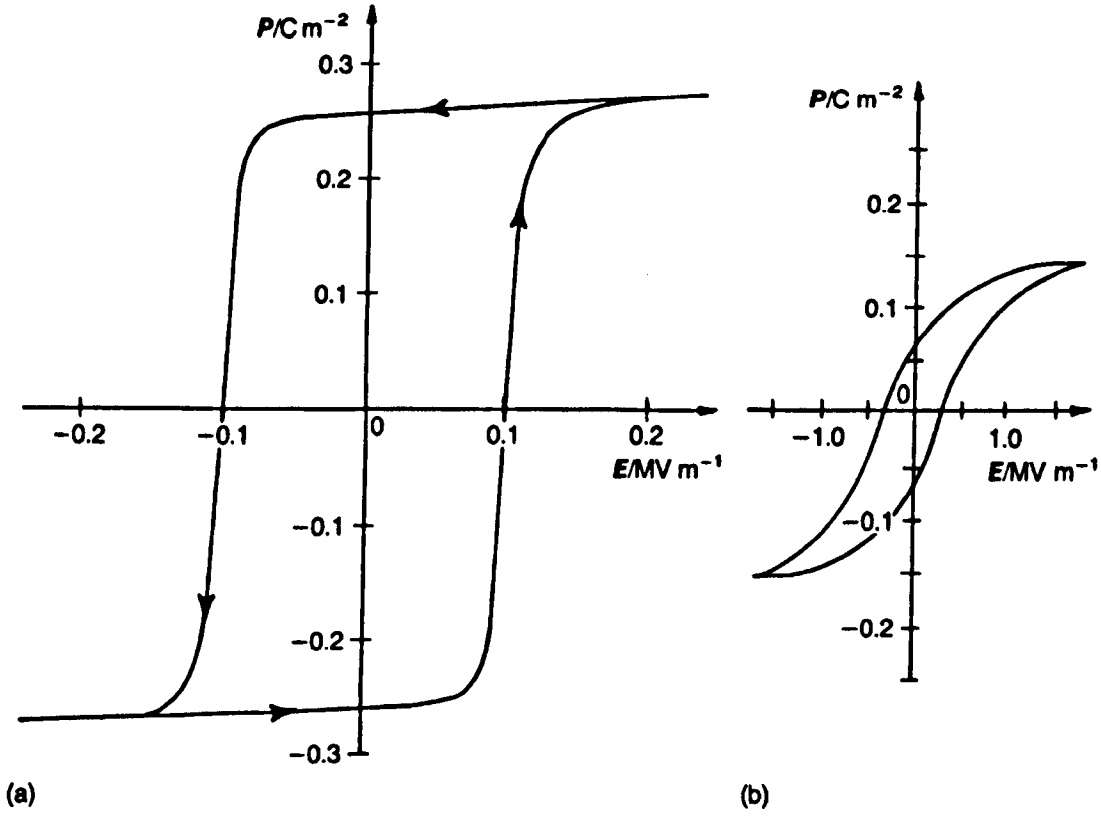

Figure 2.13 Hysteresis loops for (a) a single-domain single crystal of $BaTiO_3$ and (b) $BaTiO_3$ ceramic.[3]

It can be clearly seen from the above figure that the coercive field is higher and the remanent polarisation is lower than that of the single crystal.

2.3.5 Poling ferroelectrics

Without external static field, a polycrystalline ceramic acts as a non-polar material because the dipoles are randomly oriented, giving rise to zero net polarisation. However, by applying an external static field, polycrystalline ceramics can be transformed into polar materials. This feature is known as 'poling', which is one of the most important characteristics of ferroelectric ceramics. However, by applying a stress field or appropriate electric field, the poled ceramics can be depoled.

2.3.6 Unusual characteristic of ferroelectrics

The properties of ferroelectric materials can change with time on applying an external mechanical field, electrical field or heat. This is caused by the reduction of domain wall mobility through gradual formation of inhibiting structures. Such an inhibiting structure may result from two major problems. One is the internal field caused by the alignment of dipoles formed by lattice defects and impurity ions. Another is the redistribution of internal strains because of crystal anisotropy or the accumulation of defects in the domain walls. The relationship between the ferroelectric properties (p) and time is presented in equation 2.22:[3]

$$p = a \log_{10}\left(\frac{t}{t_0}\right), \qquad (2.22)$$

where $a = a' \log_e 10$ and t_0 is an arbitrary zero for the time. In commercial ferroelectrics, a should be less than 0.05.

Furthermore, the ferroelectric properties of materials can be changed by the substitution of alternative cations. The effects are listed below:[3]

- the change in Curie or other transition temperatures;
- the restriction of domain wall motion;

- the addition of second phases or compositional heterogeneity;
- the advantage of controlled crystallite size and oxygen content.

2.4 Ferroelectric crystals of interest

Because crystals containing Bi^{3+} and Pb^{2+} ions have large electro-optic properties, the three ferroelectric phases; Bi_2GeO_5, $Pb_5Ge_3O_{11}$, and $PbNb_2O_6$; are discussed in the following sections.

2.4.1 Bismuth germanium pentaoxide (Bi_2GeO_5)

In 1964, Aurivillius et al.,[15] first reported the crystal structure of Bi_2GeO_5 using X-ray single crystal diffraction. They identified the lattice as orthorhombic; the space group as $Cmc2_1$; crystal class as mm2; and unit-cell dimensions as a = 15.69 Å, b = 5.429 Å and c = 5.383 Å. The cell contains four formula units of Bi_2GeO_5. Figure 2.14 shows the illustratively simplified structure of Bi_2GeO_5.

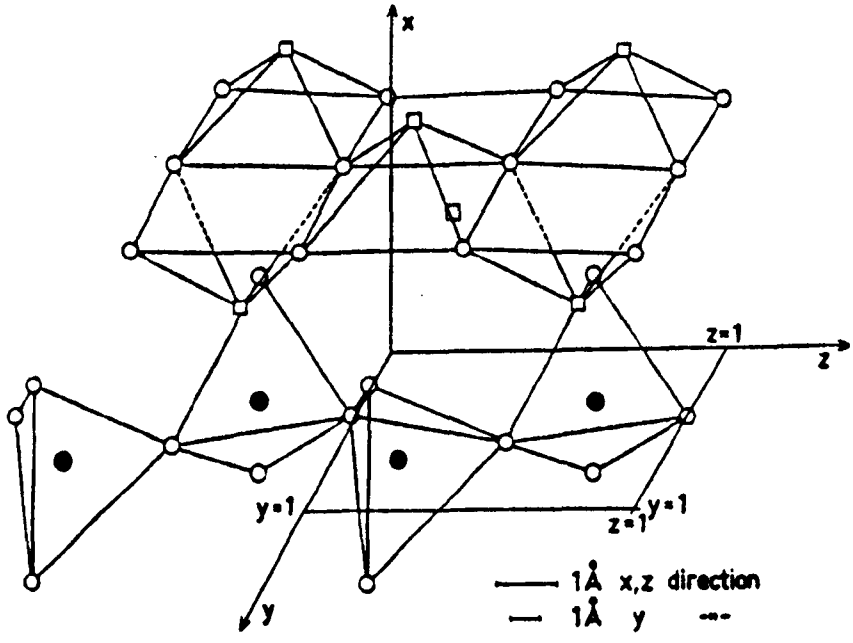

Figure 2.14 *Perspective view of the contents of one unit cell of Bi_2GeO_5 from x = 0 to x = 0.33 showing the deformed $Bi_2O_2^{2+}$ layers and the GeO_3^{2-} chains.* [15]
Bi = □; *Ge* = ●; *O* = ○

The GeO_3^{2-} chains lie along the C axis of the unit cell, with repeat distance equal to c and the bismuth atoms are connected with their closest oxygen atoms in the $Bi_2O_2^{2+}$ layer. The GeO_4 tetrahedra are linked by full lines and the Cartesian axes correspond to the crystallographic ones. In the $Bi_2O_2^{2+}$ layer, it can be seen that only three out of four possible bismuth atoms are connected with oxygen.

After the work done by Aurivillius et al., single crystal Bi_2GeO_5 was grown using the spontaneous crystallisation method in 1984 by Firsov et al.[16], Their crystallographic results are slightly different. They found unit cell dimensions a = 15.68 Å, b = 5.493 Å and c = 5.384 Å but identified the space group as C2cm, in contrast to $Cmc2_1$ identified by Aurivillius. They also concluded that crystals of Bi_2GeO_5 are polar between 100 K and 800 K. Even though they could observe no hysteresis loops in the crystals in electric fields up to 10 kV/cm, they suggested, from the data on properties of these crystals and their isomorphism with Bi_2SiO_5 crystals, that the crystals can be ferroelectric with $T_C > 800$ K.

2.4.2 Lead germanate ($Pb_5Ge_3O_{11}$)

Recently, crystals of $Pb_5Ge_3O_{11}$ and related materials have been studied extensively, because of their distinctive ferroelectric properties. Originally, this compound was reported by Speranskaya [17] in 1959. Sugii et al. (1971) [18] successfully grew single crystal $Pb_5Ge_3O_{11}$ by the Czochralski technique and found that these crystals are ferroelectric below 177°C and optically active. During the same year, Nanamatsu and his co-workers [19] also produced a single crystal of $Pb_5Ge_3O_{11}$ by the Bridgman method and observed a room temperature D-E hysteresis loop in the direction of the c-axis at 50 Hz. A spontaneous polarisation of 4 $\mu C/cm^2$ and coercive field of 14 kV/cm were observed. The Curie temperature from this work is 178°C. The

$Pb_5Ge_3O_{11}$ crystals have 180° domains unlike other common ferroelectrics because the polarisation occurs only along the c axis. This is very useful for the application of information storage and the processing of light signals.

The crystallographic information on these crystals was comprehensively described by Eysel et al. (1973)[20]. The crystals are hexagonal above the Curie point with the space group P3/m and, when the crystals are cooled below this temperature, a slight distortion obtains and they become ferroelectric with trigonal space group P3. At room temperature, the lattice parameters for the trigonal cell are a = 10.24 Å and c = 10.67 Å. Within the same year, Iwata et al. [21] also reported the crystal structure of this phase using three dimensional neutron and X-ray diffraction. The value of unit cell parameters: a = 10.251 and c = 10.685 are marginally different from the previous paper. Iwata also found that the space group is P3 and the number of formula units in the unit cell is three.

The structure of $Pb_5Ge_3O_{11}$ was correlated with those of chlorapatite and nasonite. The diagrams of the three structures are compared from the view of the layers perpendicular to the hexagonal c axis as shown in figure 2.15. From this figure, the lead germanate one should probably be expressed as $Pb_5 \cdot GeO_4 \cdot Ge_2O_7$, as a result of the chain-like structure of one germanate tetrahedron GeO_4 and double tetrahedral Ge_2O_7 forming along the c-axis. Chlorine sites in lead germanate are empty, in contrast to those of apatite and nasonite. The lack of chorine sites often occurs in certain lead apatite, forming open channels along the c-axis. This leads to the high possibility of crystal-chemical substitution into lead germanate crystals.

Generally, the areas of research concerning $Pb_5Ge_3O_{11}$ might be divided into three categories as follows:

1. Solid solution

2. Sintering aids

3. Production of textured or oriented microstructures.

In the first case, there are some advantages: $Sr^{2+}$and Nd^{3+} doping [22,23] could lower the phase transition temperature and improve the optical properties of $Pb_5Ge_3O_{11}$ respectively. Moreover, the $Pb_5(Ge,Si)_3O_{11}$ solid solution, [20] containing up to 62% Si contents, has a lower melting point, Curie point and coercive field than pure $Pb_5Ge_3O_{11}$. In the second case, the lead germanate can act as a sintering aid because of its low melting point. This phase has been mixed with other ferroelectric phases, such as $PbTiO_3$ and $PbZrO_3$, in order to lower the processing temperature, improve the density of final product and possibly produce new ferroelectric phases.[24,25] In the last case, as this phase has the tendency to grow along c-axis preferred orientation, leading to the 180° domains, it is useful in the application of thin and thick films. [24,26-27]

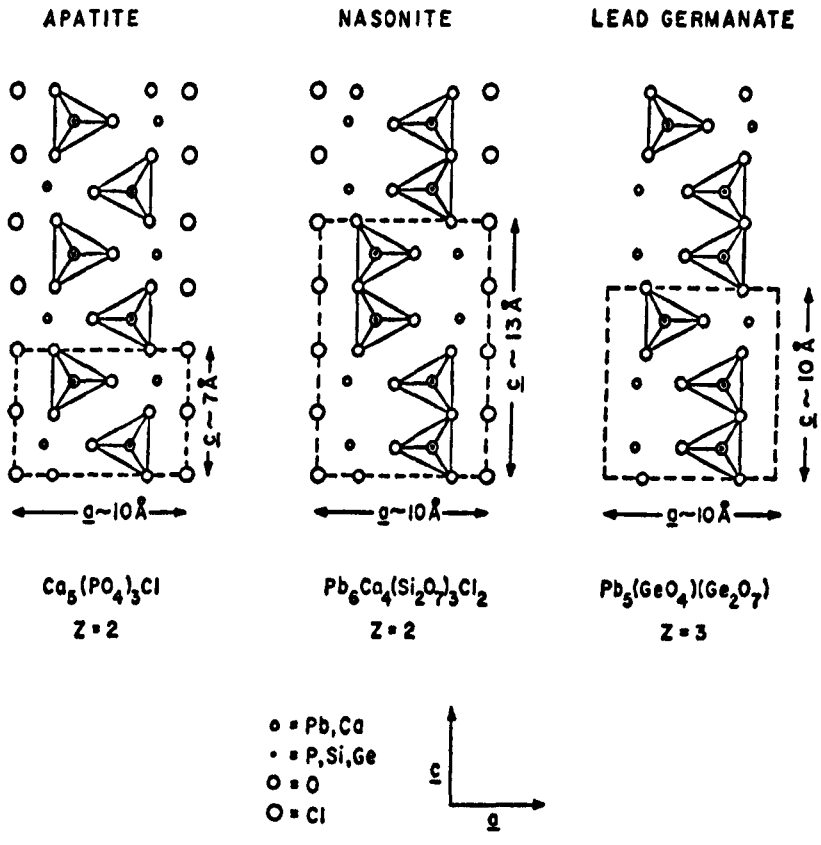

Figure 2.15 Comparison of idealised apatite, nasonite, and lead germanate structures showing section parallel to (010) ≈ 4 Å thick.[20]

2.4.3 Lead metaniobate ($PbNb_2O_6$)

Ferroelectric properties of lead metaniobate ($PbNb_2O_6$) were discovered by Goodman in 1953.[28] Because of its high Curie temperature: ~570°C, lead metaniobate can be used in high-temperature piezoelectric applications, such as hydrostatic pressure detectors. At room temperature, the lead metaniobate has two polymorphic forms. The first one is the rhombohedral form, which is stable up to 1200°C. The other one is the ferroelectric orthorhombic form, which is obtained by rapid cooling from temperature >1250°C.[14] The lattice parameters at 20°C of the ferroelectric orthorhombic are a = 17.51, b = 17.91 and c = 7.736 Å. [29] Above the Curie temperature there is one stable phase, which has a tetragonal structure with lattice dimensions: a = 12.46 and c = 3.907 Å. [13]

In 1958, Francombe and Lewis [30] showed that the structures of $PbNb_2O_6$ and $PbO{\cdot}x(Nb_2O_5)$ where $1.0 \leq x \geq 3.0$, are closely related to the tetragonal tungsten bronzes $K_{0.57}WO_3$ and $Na_{0.28}WO_3$. The structure is illustrated in figure 2.16. [10]

The tetragonal unit cell above can be also expressed as ABO_3-type oxygen octahedra. From figure 2.16, the A-type cations, such as K, Pb, and Na can be situated in any of A1, A2 or C interstitial sites. The B-type cations: W, Ta, Nb, Ti, are located at the octahedron centres (B1 or B2 sites). The spaces between BO_6 form tunnels, which can be clearly seen as the largest A2, the smaller A1 and the smallest C tunnel. C sites normally are empty unless small ions with r = 50-70 pm, such as Li^+ or $Mg^{2+}$are substituted. The general formula for the tungsten bronze structure is $[(A1)_2(A2)_4C3][(B1)_2(B2)_8]O_{30}$. [3,10]

In the case of $PbNb_2O_6$, C sites and one in six of the A1 and A2 sites are vacant, leading to the formula $A_5B_{10}O_{30}$ which eventually is simplified as AB_2O_6. The polar axis of $PbNb_2O_6$ is perpendicular to the A-site, in contrast to most of

ferroelectric tungsten bronzes' polar axes, which are parallel to the A-site tunnel. Consequently, as the $PbNb_2O_6$ is related to the large family of the tungsten bronze type, many scientists have studied the possibility of ion substitution. Goodman [31] found that the electrical properties can be dramatically increased by partial addition of Mg, Ca, Sr and Ba to the lead metaniobate and Francombe [29] also reported properties of the system (Ba, Sr)Nb_2O_6 and (Pb,Ba)Nb_2O_6.

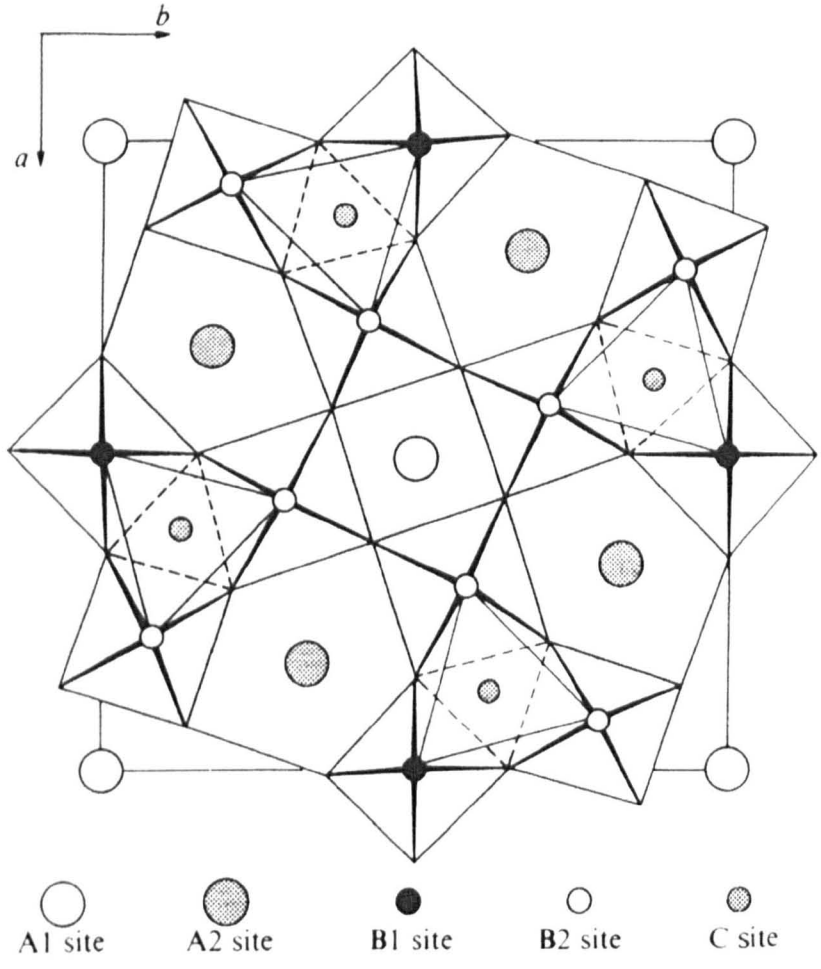

Figure 2.16 *The basic octahedral framework of the tungsten bronze structure looking down the tetragonal c-axis.* [10]

References

1. Anderson, J. C. *Dielectrics*, 1964 (Chapman and Hall Ltd and Science paperbacks).
2. Callister, W. D. JR., *Materials Science and Engineering*: An Introduction, 1985 (John Wiley & Sons, INC.).
3. Moulson, A. J. and Herbert, J. M. *Electroceramics*, 1990 (Chapman & Hall).
4. Cole, K. S. and Cole, R. H. *Chem. Phys.*, 1942, Volume 10, p. 98.
5. Hench, L. L. and West J. K. *Principles of Electronic Ceramics*, 1990 (John Wiley & Sons)
6. Burfoot, J. C. F. *Ferroelectrics*, 1976 (D. Van Nostrand Company Ltd.).
7. Hahn T. *International Tables for Crystallography, Volume A:space-group symmetry*, 1987 (D. Reidel Publishing Company).
8. Kanzig, W. *Ferroeletrics and Antiferroelectrics*, 1957 (Academic press, New York and London).
9. Wul, B. and Goldman, I.M. 1945, *C.R. Acad. Sci. URSS.*, volume 46, p. 139; Volume 49, p. 177.
10. Lines, M.E. and Glass, A.M. *Principles and Applications of Ferroelectrics and Related Materials*, 1977 (Clarendon Press, Oxford)
11. Kittel, C. 1951, *Physics Review*, Volume 82, p. 729.
12. Helen, D. M. *Ferroelectricity in Crystals*, 1957 (Methuen & Co Ltd.).
13. Jona, F. and Shirane, G. *Ferroelectric Crystals*, 1962 (Pergamon Press).
14. Lee, H.S. and Kimura, T. 1998, *Journal of American Ceramics Society*, Volume 81, Number 12, p. 3228.
15. Aurivillius, B., Lindblom C.I. and Stenson P. 1964, *Acta Chemica Scandinavica*, Volume 18, Number 6, p. 1555.
16. Firov, A.V., Skorokhodov, N.E., Astaf'ev, A.V., Stefanovich, S.Yu. and Venevtsev, Yu. N. 1984, *Soviet Physic Crystallographic*, Volume 29, Number 3, p. 304.
17. Speranskaya, E.I. 1959, *Izv. Akad. Nauk SSSR*, Otdel. Khim. Nauk 162.
18. Sugii, K., Iwasaki, H. and Miyazawa, S. 1971, *Material Research Bulletin*, Volume 6, p. 503.
19. Nanamatsu, S., Sugiyama, H., Doi, K. and Kondo, Y. 1971, *J. Phys. Soc. Japan*, Volume 31, p. 616
20. Eysel, W., Wolfe, R.W. and Newnham, R.E. 1973, *Journal of the American Ceramic Society*, Volume 56, Number 4, p. 185.
21. Iwata, U., Koizumi, H., Koyano, N., Shibuya, I. and Niizeki, N. 1973, *J. Phys. Soc. Japan*, Volume 35, p. 314.
22. Kim, J.H., Kim, J.B. and Lee, K.S. 1993, *Solid State Communications*, Volume 88, Number 9, p. 727.
23. Ying, X.L. and Chen, L.J. 1985, *Prog. Crystal Growth and Charact.*, Volume 11, p. 237.
24. Cornejo, I.A., Collier, J. and Haun, M.J. 1994, *Ferroelectrics*, Volume 154, p. 53.
25. Cornejo, I.A. and Haun, M.J. 1996, *Materials Research Society Symposium Proceeding*, Volume 400, p. 353.
26. Takahashi, K., Ueda, H., Suzuki, T. and Kakegawa, K. 1994, *Ferroelectrics*, Volume 154, p. 41.
27. Kageyama, Y., Sakata, J. and Taga, Y. 1995, *Japanese Journal of Applied Physics*, Volume 34, part 1, Number 9B, p. 5158.
28. Goodman, G. 1953, *Journal of the American Ceramic Society*, volume 36, p. 368.

29. Francombe, M.H. 1960, *Acta. Cryst.*, Volume 13, p.131.
30. Francombe, M.H. and Lewis, B. 1958, *Acta. Crys.*, Volume 11, p. 696.
31. Goodman, G. 1953, *U.S. patent*, Service Number 2,805,165.

Chapter 3

Theoretical background of glass-ceramics

3.1 Introduction to glass-ceramics

3.1.1 History

Glass-ceramics may be defined as polycrystalline solids prepared by the controlled crystallisation of glasses. Crystallisation can be achieved by putting appropriate glasses through a regulated heat-treatment schedule that causes nucleation and growth of crystal phases inside the glass. However, a small amount of residual-glass often occurs and strongly affects a number of important properties of glass-ceramics. [1]

It has been known for centuries that most glasses can be crystallised if they are subjected to heating for a sufficient length of time at a suitable temperature. There was no systematic development until the discovery of the first true glass-ceramics in 1957 by Dr. S. Donald Stookey [2] at Corning Glass Works. He found that it is possible to form glass objects by conventional methods and transform them to fine-grained ceramics by heat treatment. After that, he successfully invented photochromic glasses, machinable glasses and polychromatic glasses. These products have far more mechanical strength than their original glasses. The effective nucleating catalyst used in most of Stookey's system was TiO_2, and in 1970 McMillan et al. [3] reported that the use of metallic phosphates (P_2O_5) can promote controlled crystallisation in glasses. In addition to these, other oxides, such as ZrO_2, SnO_2, CrO_3 and V_2O_5 [4] were later discovered to be effective nucleating agents.

3.1.2 The science of glass-ceramics

Important aspects of glass-ceramics are nucleation and crystallisation. Glass-forming liquids are generally very viscous; therefore, processes of diffusion and atomic re-arrangement are slow, which enables control of nucleation and crystal growth. The rapid quenching process can be applied to the viscous liquids in order to avoid the crystallisation process during cooling and the resulting glass product can be used for further investigation of glass-ceramics. Another important phenomenon is amorphous phase separation, which can be important in both glass-ceramic formation and the stability of glasses. Because a glass melt is a good solvent for most oxides, a wide range of composition can be obtained, leading to the potential formation of glass-ceramics containing many crystal types, such as metastable phases and solid solutions within a variety of chemical environments. The ultra fine grains, typically less than one micrometer, of the glass-ceramics provide valuable material properties, such as good mechanical strength and good fracture toughness. These make glass-ceramics stronger than ordinary glasses and conventional ceramics. In addition, it is possible to control the degree of crystallinity in glass-ceramics, leading to the studies of mechanical failure and the investigation of the properties, involving diffusion, for example: ionic conductivity.

Normally, glass-ceramics are not transparent to visible light. However, transparent glass-ceramics can be derived if the crystals present are smaller than the wavelength of visible light or by minimising the difference between the refractive indices of the parent glasses and crystals.

3.1.3 Some applications of glass-ceramics

Apart from the early applications of glass-ceramics by Stookey and co-workers, more recent studies include:

- Glass-ceramics from the systems Li_2O-Al_2O_3-SiO_2 and CaO-Al_2O_3-SiO_2 having thermal expansion value near zero so they can be used as high temperature cookwares, cooker hot plates, laboratory bench tops and rotary heat exchangers for gas turbines.
- The magnesia-alumina-silica type or Cordierite glass-ceramics and glass-ceramics derived from ZnO-Al_2O_3-SiO_2 with addition of CaO, BaO or SrO, have low dielectric loss, high strength, good thermal shock resistance, high rain erosion resistance and are transparent to microwaves. They can be used in the production of radomes for missiles.
- Machinable glass-ceramics can be produced by crystallisation of fluorophlogopite mica ($KMg_3AlSi_3O_{10}F_2$) in glasses having wt % compositions of 30-50 % SiO_2, 3-20 % B_2O_3, 4-12 % K_2O, 15-25 % MgO and 4-10 % F.
- Glass-ceramics can be used in the biomedical field, such as for the production of artificial teeth from Li_2O-ZnO-SiO_2 glass systems. These products have a good acid resistance, high abrasion resistance and close thermal expansion matching between the glass-ceramics and the real tooth.
- Transparent glass-ceramics can be produced from many glass systems; such as Li_2O-MgO-ZnO-Al_2O_3-SiO_2, Al_2O_3-SiO_2 and ZnO-Al_2O_3-ZrO_2-SiO_2 with the corresponding major crystalline phases present being β-eucryptite , mullite and spinel respectively. They can be used in the large optical telescopes (eucryptite type) and the envelope materials for high-performance lamps (mullite and spinel type).
- Transparent ferroelectric glass-ceramics can be achieved with a variety of precipitated crystalline phases, such as $BaTiO_3$, $Pb_3MgNb_2O_9$, $Pb_5Ge_3O_{11}$

and $LaBGeO_5$. These glass-ceramics have electro-optical effects so they can be used in optical devices.

The next two sections summarise the theoretical background of glass formation and stability (non-silicate glasses), and, nucleation and crystallisation in glasses. The final section also provides a review of ferroelectric glass-ceramics in more detail.

3.2 Glass formation and stability (non-silicate glasses)

3.2.1 Glass definition

The most widely used definition of a glass, proposed by the A.S.T.M., is "a glass is an inorganic product of fusion, which has cooled to a rigid condition without crystallising." Organic substances, for example glucose and glycerol, would not be included in this definition, although they can be supercooled to a rigid condition without crystallising. Moreover, such a definition would exclude amorphous substances which are not prepared by melt cooling methods, but by other techniques, such as vacuum evaporation. [1]

A precise definition of glass is that "a glass or a substance in the glassy or vitreous state, is a material, formed by cooling from the normal liquid state, which has shown no discontinuous changes (such as crystallisation or separation into more than one phase at any temperature) but has become more or less rigid through a progressive increase in its viscosity." This definition regards viscosity as defining a natural boundary to the glassy state. It is useful because any material cooled below its liquidus, but whose viscosity has not reached this limiting value, is called a super-cooled liquid. There is no exact limiting value of viscosity but it can be assumed that the viscosity of the melt at the transformation temperature should be greater than about 10^{13} poises.

Glasses are characterised by many properties, which reflect their liquid-like structures. One of the most important properties of glasses is *transparency*, resulting from complete lack of grain boundaries or inclusions, which would cause the reflection of light. This property is usually found in the liquid state rather than in the solid crystalline state.

The relationship between liquid and solid can give a clearer understanding of the origin of the structure of a glass. The arrangement of atoms in a liquid has short-range order while that of a crystalline solid has both short-range and long-range order showing that the regularity in solid is almost complete. Thus, a glass, which has a liquid-like structure, exhibits a lack of long-range periodic order. [1]

Figure 3.1 shows the comparison of the radial distribution function of a hypothetical material in the glassy state with that of gas, liquid and crystalline state of the same composition.

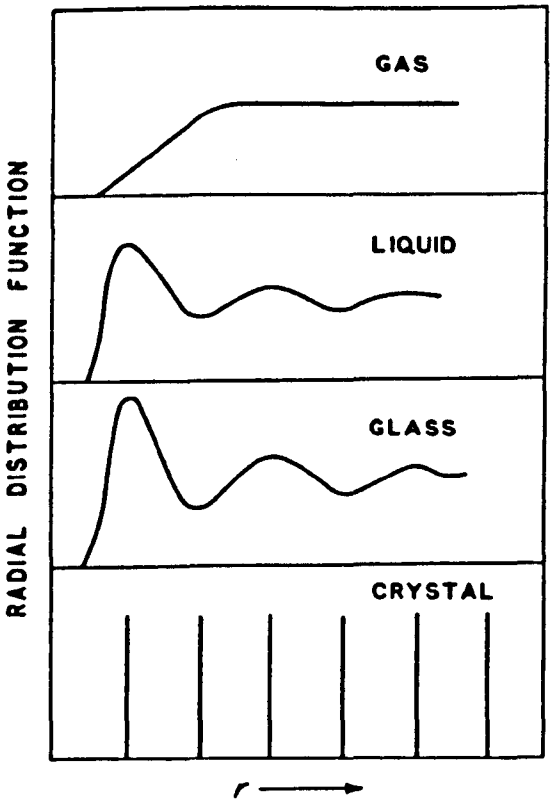

***Figure 3.1** Comparison of the radial distribution function of a glass with that of the gaseous, liquid and crystalline states.* [4]

The x-ray diffraction pattern of glass contains a few broad features reflecting the short range radial distribution of atoms while that of a crystalline substance has sharp lines indicating the long range 3D order. Glasses have broad melting behaviour unlike the sharp melting points of crystalline solids. Moreover, a glass does not cleave in any preferred direction. The final property of glass to be mentioned in this section is the electrolytic conduction associated with the liquid-like structure. This is because the structure of glass is permeable to small ions: for example, sodium. [4,5]

The phenomena, which occur during the cooling of melts, are very important for understanding the relationship between the glassy state and normal liquid and solid state. Figure 3.2 shows the relationship between these states by means of an enthalpy-temperature diagram. This diagram can also be presented in term of volume-temperature because enthalpy and volume behave in a similar manner.

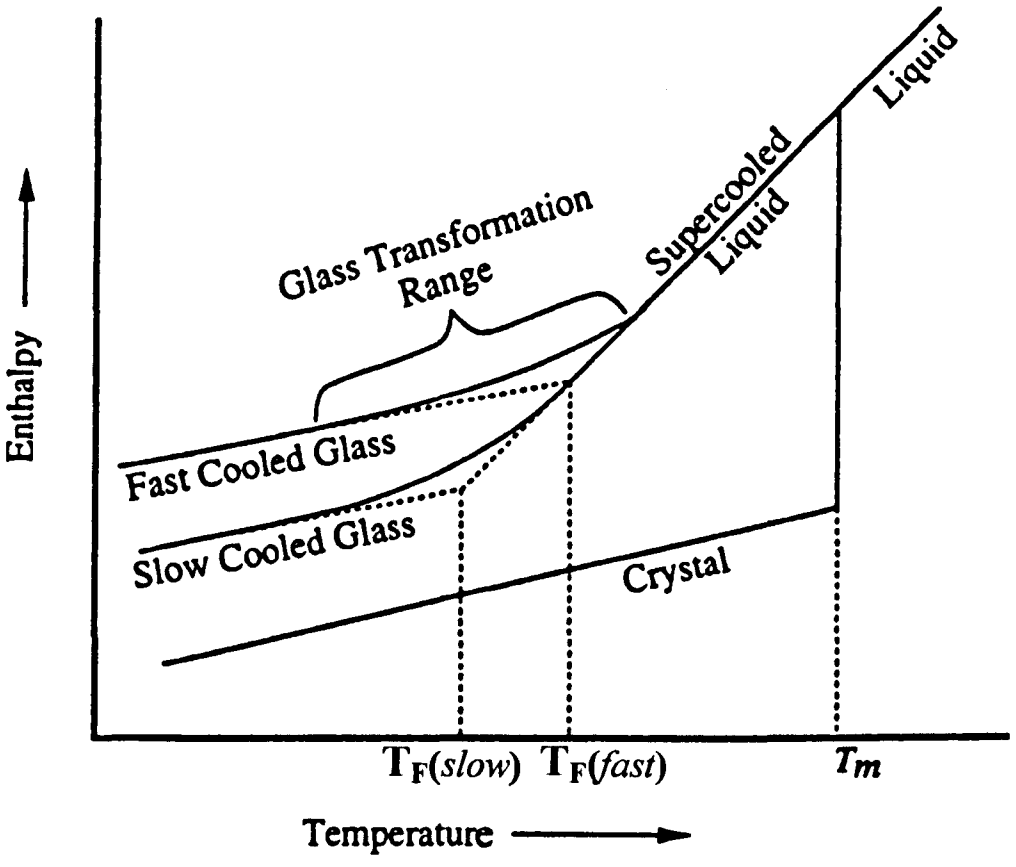

Figure 3.2 Effect of temperature on the enthalpy of a glass-forming melt. [6]

The liquid has a structure characteristic of the temperature at which the melt is held and, during cooling, the atomic structure of the melt will slowly change but still keep the characteristic short range order of the primary liquid. In general, when the melt is cooled below the melting temperature (T_m), crystallisation occurs and it becomes solid. As a result, a rapid decrease in enthalpy occurs to the appropriate value for the crystal. On continued cooling, the enthalpy will decrease slowly controlled by the heat capacity of the crystal. However, if the liquid can be cooled below the melting point by avoiding crystallisation, there will be an undercooling of the melt to give a supercooled liquid. No discontinuous rearrangement happens in this case as the temperature decreases, simply a gradual change in the overall enthalpy. Further cooling produces deviation from the equilibrium line since the viscosity of the melt greatly increases, inhibiting atom movement, leading to difficulty in the rearrangement of atoms to the equilibrium liquid structure. Then as the temperature decreases, the viscosity increases rapidly, resulting in frozen-in, liquid-like structure. The slope after this is determined by the heat capacity of the frozen liquid. The glass transformation region, appearing in the graph, may be defined as the temperature region joining the equilibrium liquid state and the frozen liquid state. Hence, the frozen liquid is a glass.

As shown in this figure, the intersection point between the glass and supercooled liquid lines is the fictive temperature (T_F), which may be defined as " the temperature at which the glass would find itself in equilibrium if suddenly brought to it from its given state". [6] The structure of equilibrium liquid at this temperature is similar to the structure of glass. Moreover, T_F can be changed by thermal history such as cooling rate. A high cooling rate freezes the liquid into a glassy state at lower density and higher specific volume than a lower cooling rate. The glass formed by slow cooling has a tendency to be more stable than that of fast cooling. This is because the atomic

arrangement of the slow cooled glass is closer to that characteristic of the equilibrium liquid than the more rapidly cooled glass.[6]

3.2.2 Glass former

A few elements in the Periodic Table, such as, phosphorus, oxygen, sulphur, selenium and tellurium, can form a glass by themselves. For instance, oxygen can be formed in the glassy state when liquid oxygen is cooled. However, most useful glasses are based on oxides and these can be divided into three types. The first type are glass-formers, which can form a glass on their own. They can produce the backbone in other mixed-oxide glasses since this type of oxide has strong directional bonds (iono-covalent) and prefers to form low coordination structures, such as tetrahedral. The commonly used glass-forming oxides are B_2O_3, SiO_2, GeO_2 and P_2O_5. [4]

The second type are called intermediate oxides, which are TeO_2, SeO_2, TiO_2, MoO_3, Bi_2O_3, Al_2O_3, Ga_2O_3 and V_2O_5. Such oxides cannot form glasses readily on their own as pure substances, but they can substitute for a network former giving more ionic bonds in the network and a tendency to higher coordination (e.g. octahedral). For example, tellurium-based glasses can be produced from a number of compositions containing a large amount of TeO_2 and a few mole percent of second oxides, such as, alkali or alkaline earth oxides and the oxides of a large number of tri-, tetra-, and pentavalent cations. Originally, some evidence showed that these glasses were composed of networks of tellurium-oxygen octahedra but recently a new model has been proposed, which is formed by the distortion of trigonal bipyramids.[7] The last type are network modifying oxides. These oxides break interpolyhedral linkages leading to weakening of the glass network. Examples of the modifying oxides are alkali metal oxides (e.g. Na_2O) and alkaline earth oxides. The properties of a glass also change upon addition of this oxide producing a decrease in hardness, and glass

transition temperature (T_g) and an increase in solubility. Moreover, glasses also become more difficult to produce. [8]

3.2.3 Atomic hypothesis of glass formation

In 1926, Goldschmidt pointed out that the glass-forming ability of an oxide might be related to the arrangement of the oxygen ions around the cations in order to form the unit cell of the crystal structure. By geometrical considerations, it could be shown that in an oxide M_xO_y, coordination of M by O would equal four if the radius ratio R_M/R_O is in the range of 0.225 to 0.414. The most probable arrangement of atoms in this case is tetrahedral with the oxygens at all corner positions and the cation at the central position. Furthermore, he found that many of the glass-forming oxides, such as SiO_2, GeO_2 and P_2O_5, have tetrahedral arrangements in the crystalline state and this can be a criterion of glass-forming ability. However, this postulate is not universally true so Zachariasen (1932) further developed the random network theory of glass structure. He suggested that, as in the crystal, the atoms in a glass must be linked in the form of a three-dimensional network but the arrangement of the structure in glass could not be long-range ordered as in a crystal. As a result of this, the x-ray diffraction pattern of a glass is not sharp like that of the crystal. He also deduced that the energy content of a substance in the glassy state must be slightly greater than that of the corresponding crystal network. Therefore, it could be assumed that the units of structure in a glass must be similar to those in the crystal. However, in the glass there is distortion of the bond angles so that the oxides form a random network, which is a non-periodic structure. Figures 3.3 (a) and (b) show the corresponding examples of a normal crystalline lattice and the random network of glass respectively. Both have the formula M_2O_3.[1]

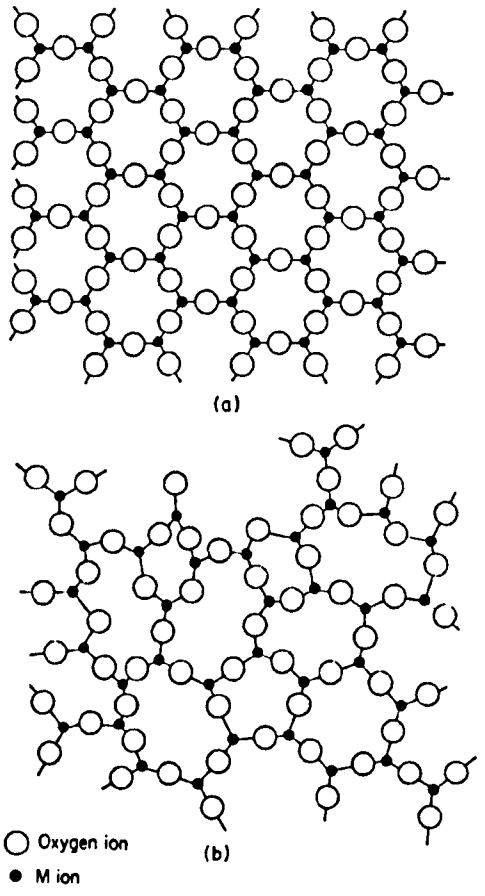

Figure 3.3 *Two-dimensional representation of an oxide M_2O_3 in (a) the crystalline form (b) the glassy form.* [1]

3.2.4 Glass formation and stability of GeO_2

For many years, silica (SiO_2), the principal glass-forming oxide, has been used for preparing numerous glasses. Because of its high softening temperature, its excellent resistance to chemical attack and its high transparency in the visible and ultra-violet, this glass is commercially available and can be used for many applications. [8] Nevertheless, glasses made from GeO_2 are better candidates for IR transmitting windows compared with glasses based on SiO_2. [9] Moreover, GeO_2 has a lower melting point than SiO_2 so it can be used instead of SiO_2 to provide information on the corresponding silicate glasses which have high liquidus temperatures and which are difficult to prepare. However germanate glasses show some detrimental features,

which do not occur in the silicate glasses (in particular attack by water) and this, plus the high cost of germanium oxide, means there is no widespread use of germanate glasses. [8] Germanium oxide (GeO_2) exists in three forms, two are crystalline and one is vitreous. The first crystalline form is tetragonal, having the rutile-type structure, with six oxygens around each germanium, giving the coordination number of Ge^{4+} as six. The second crystalline form is hexagonal, isostructural with α-quartz (i.e. four oxygens around each germanium, i.e. coordination number is 4). The radius ratio R_{Ge4+}/R_{O2-} is equivalent to 0.43, which can be used to determine the co-ordination number of the cation as in the range of 4-6. [8] Muller and Blank [10] and Laubengayer and Morton [11] have investigated the stability relationship of the two crystalline forms. The tetragonal form, having a density of 6.239 g/cm^3 at room temperature, is stable below 1033°C. It is nearly insoluble in water and does not react with HF and HCl. The second form, hexagonal, is stable from 1033°C to the melting point (1116°C), but it can be retained at room temperature because the transformation rate of one phase to the other is very slow. The density of this form is 4.228 g/cm^3 at 25°C. This oxide can be soluble in water and reacts with acids. Kotera and Yonemura [12] observed that the kinetics of the transformations of the hexagonal form to tetragonal form are increased only when mineralisers, such as alkali chlorides or carbonates are added.

Since germanium dioxide is a glass former, it can form glass on its own. The glass is a random network of germanium-oxygen tetrahedra. The density of glass is between 3.64-3.66 g/cm^2, which is nearer to that of the hexagonal crystal polymorph than that of the tetragonal form. In this case, the coordination number in germania glass is four, which is similar to silica glass. This has been confirmed by X-ray studies by Zarzycki (1957).[13] However, it is possible in some glass that the coordination number changes from four to six, i.e. an alkali germanate glass. [14] As the germanium

ion is larger than the silicon ion so the Ge-O distance is greater, at 0.173 nm and the bond angle Ge-O-Ge is smaller than Si-O-Si. The structure of vitreous germania is more compact than that of vitreous silica, giving rise to smaller free, or intersitial volume. However defects occur more in germanate glass than in silica glass such as the noticeable amount of Ge-Ge bonds present in the glass. [6]

3.3 Nucleation and crystallisation in glasses

3.3.1 Phase transformation in glasses

The diagram in Figure 3.4 shows the types of phase transformation, which usually occur in glasses.

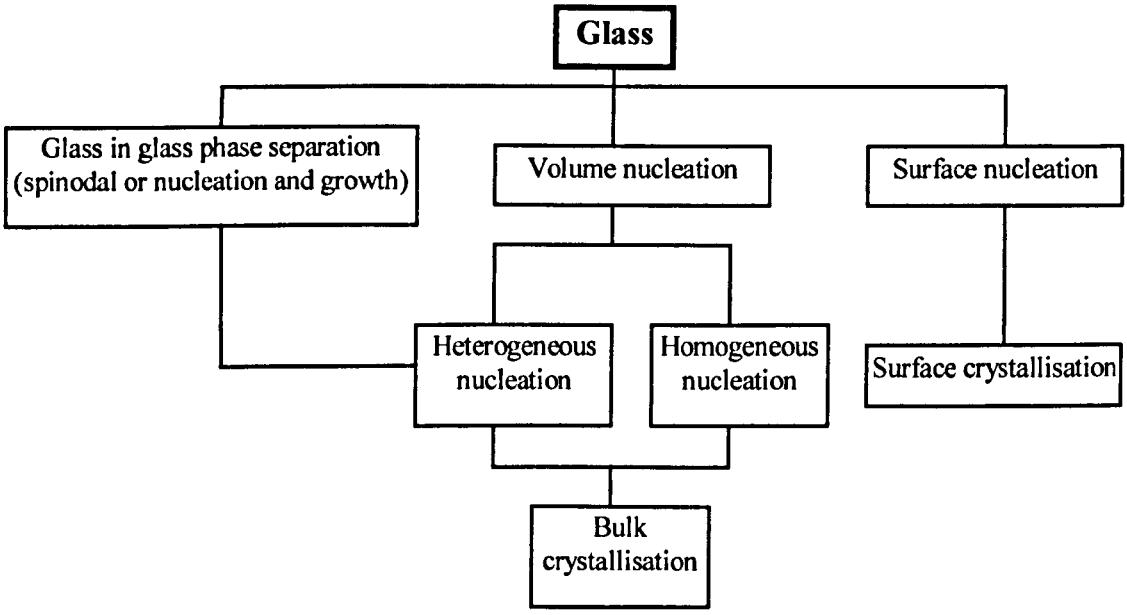

***Figure 3.4** Diagram of phase transformations in glasses.*

The descriptions of each transformation are presented as follows:

- *Crystallisation* is the process by which crystals are generated from the short-range ordered liquid structure. The composition of a crystalline phase might or might not be the same as the original liquid.

- *Surface crystallisation* is the growth of crystals from the glass/atmosphere interface and usually growing perpendicular to this interface.
- *Volume crystallisation* is the growth of crystals, from 'nucleation sites' in the body of the material. There are two types of the nucleation. The first type is *heterogeneous nucleation* where the initiating sites are pre-existing surfaces such as dust particles, crucible wall, etc. The second type is *homogeneous nucleation* where the nuclei are forming spontaneously within the melt. [6]
- *Spinodal decomposition* is the separation of a non-crystalline phase limited by diffusion only. This separation occurs in a region of the separation of two phases where there is no energy barrier to nucleation. [4]

3.3.2 Nucleation and crystallisation of glasses

Devitrification is the growth of crystals in glasses and, to make a glass, this phenomenon must be prevented. However, devitrification is important in the glass-ceramic process. This process must be controlled in order to have the correct microstructure and properties of final materials. [1] Crystallisation is the consequence of two individual kinetic processes, which are nucleation and crystal growth. In terms of nucleation, two contributions concerned with the stability of a particle in homogeneous nucleation are the free energy and the interfacial energy. At the melting point, the free energy of a material is the same in both the crystalline and liquid forms. When a melt of a single element is cooled below the melting point, the crystalline form will have the lower free energy and, if nuclei are available, the liquid will crystallise. The following equation shows the free energy change for the nucleation.

$$\Delta G = -\frac{4}{3}\pi r^3 \cdot \overline{\Delta G} + 4\pi r^2 \sigma \qquad (3.1)$$

where $\overline{\Delta G}$ = the change in free energy per unit volume for the crystal-liquid transformation

$\frac{4}{3}\pi r^3$ = the volume of the nucleus (r is the radius of nucleus or crystal)

σ = the surface tension or interfacial energy

$4\pi r^2$ = the surface area

$r^* = \frac{2\sigma}{\Delta G}$ is a critical radius where $\frac{d(\Delta G)}{dr} = 0$. If particles have radius smaller than r*, they are called embryos, $\frac{d^2(\Delta G)}{dr^2}$ is positive and thus they are unstable. On the other hand, if they have radius greater than r*, they are called nuclei, $\frac{d^2(\Delta G)}{dr^2}$ is negative and therefore they are stable.

The rate of nucleation is controlled by the production of critical-sized nuclei per unit volume and the rate at which atoms attach to the embryo. It can be shown in this following equation:

$$I = N_S \frac{kT}{h} \exp\left(-\frac{\Delta G_a}{kT}\right) \cdot N \exp\left(\frac{\Delta G^*}{kT}\right) \qquad (3.2)$$

The term: $N_S \frac{kT}{h} \exp\left(-\frac{\Delta G_a}{kT}\right)$ is the number of atoms crossing the interface per second, where N_S is the number of atoms adjacent to the surface of embryos, h is Planck's constant, kT/h is the vibrational frequency of the atom and ΔG_a is called the kinetic barrier to nucleation by Turnbull and Cohen. [15] In other words, the first term corresponds to the diffusion of matter during the formation of the nucleus. The second term ($N \exp\left(-\frac{\Delta G^*}{kT}\right)$) is the probability of forming a nucleus larger than the critical size at the temperature T where N is the number of atoms per unit volume and ΔG^* is the thermodynamic barrier to nucleation.

In terms of crystal growth, the rate of crystal growth is the rate at which atoms arrive and remain at the surface of the nucleus. The growth rate of the crystal, u, is given as follows:

$$u = \lambda \upsilon_0 \exp\left(-\frac{\Delta G_a}{kT}\right)\left(1-\exp\left(-\frac{\Delta G}{RT}\right)\right), \qquad (3.3)$$

where λ = the average interatomic spacing between atoms in the liquid and nucleus (crystal)

ν_0 = the frequency at which the atom in the liquid vibrates due to thermal energy

ΔG_a = the activation energy for an atom in the liquid to pass through the interface between the crystal and surrounding liquid.

R = the gas constant

ΔG = the energy change when an atom crosses the interface to the crystal

The first term $\lambda \upsilon_0 \exp\left(-\frac{\Delta G_a}{kT}\right)$ gives the probability of an atom having sufficient thermal energy to leave the liquid and join the nucleus. The second term $\left(1-\exp\left(-\frac{\Delta G}{RT}\right)\right)$ is the factor, which is formed by the consideration of the reduction in energy when the atom has crossed the interface to the crystal. [4]

The rates of homogeneous nucleation and crystal growth in a viscous liquid are shown in figure 3.5. From this figure, it can be noticed that, at the temperature at which the maximum nucleation rate takes places, the maximum possible number of crystal nuclei will be produced in a given length of time. Therefore, the optimum nucleation temperature can be selected for the production of glass-ceramics.

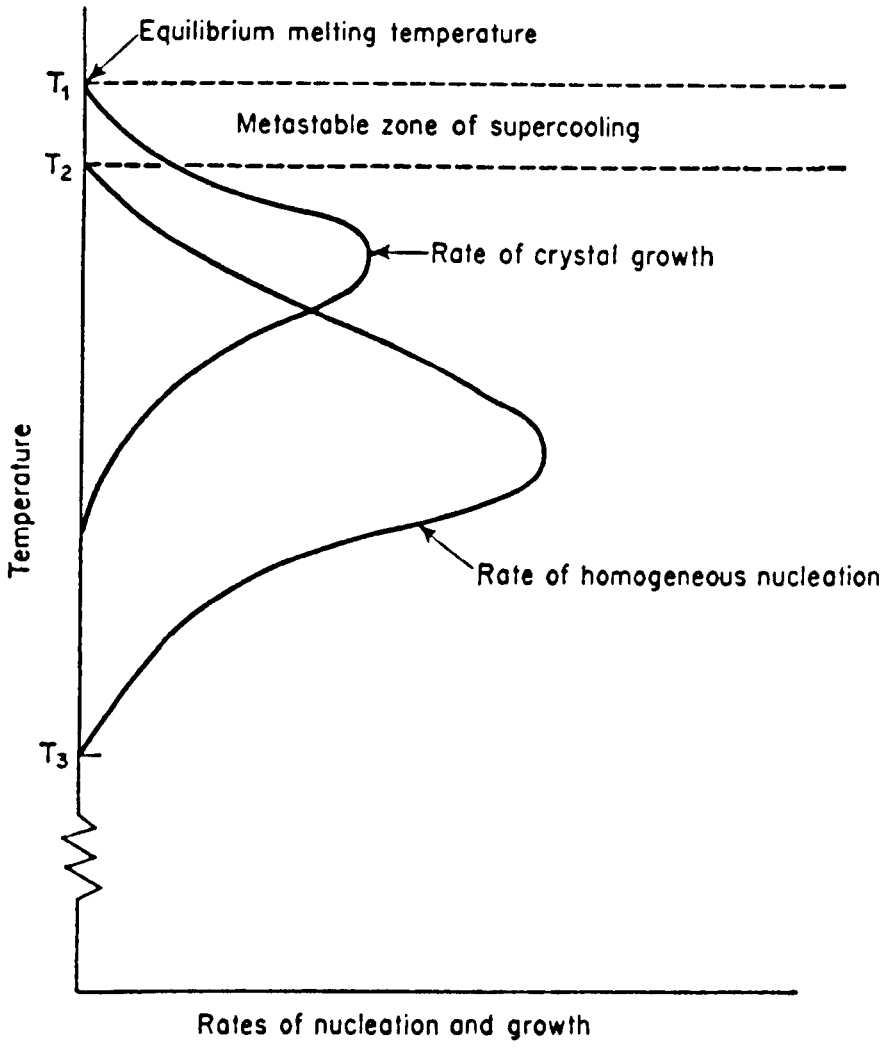

Figure 3.5 Rates of homogeneous nucleation and crystal growth in a viscous liquid.[1]

A glass is a metastable substance so either a low rate of crystal growth or a low rate of nucleation may encourage glass formation. In a normal glass, heterogeneous nucleation does not often occur because the glass melt is a good solvent for foreign particles. In addition, the homogeneous nucleation of a glass-forming liquid is difficult to achieve since the activation energy of diffusion is relatively high even at high temperature. As a result of this, it is possible to cool the glass melt through the critical temperature zone in which nucleation might take place. It is important to consider the time which the glass spends in this critical zone of temperature and glasses must usually be cooled quite quickly through this zone.[1,4]

3.3.3 Controlled crystallisation of glass to give a glass-ceramic

A controlled heat treatment is aimed at converting the glass into a glass-ceramic, which will have better properties than the original glass. Figure 3.6 shows the various stages of the heat-treatment process, which is presented as an idealised heat-treatment schedule for a glass-ceramic.

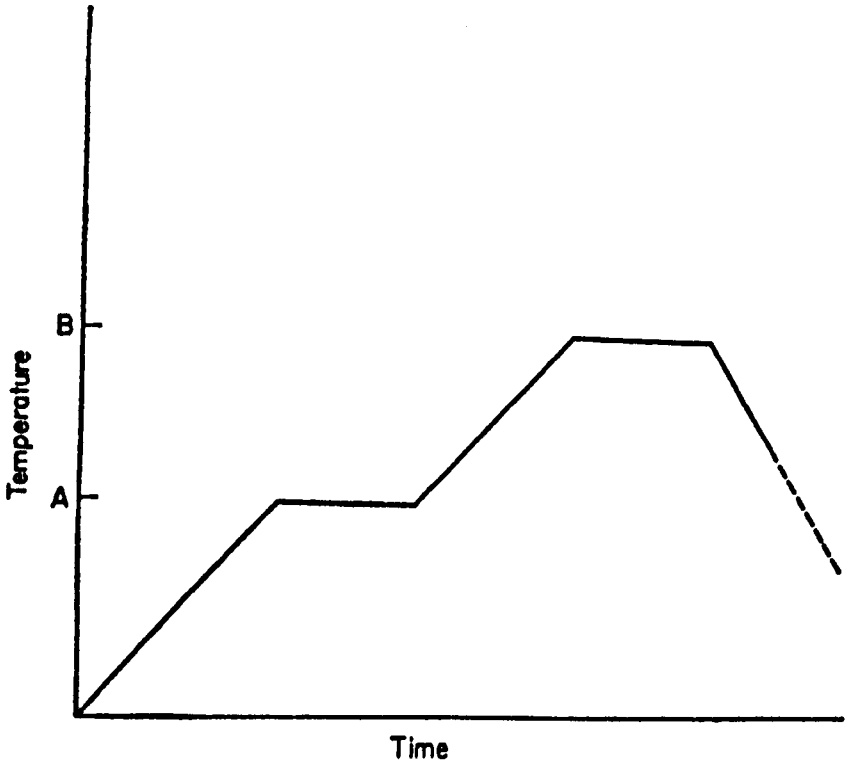

Figure 3.6 Idealised heat-treatment schedule for a glass-ceramic.[1]
(A = Nucleation temperature and B = Crystallisation temperature)

The optimum nucleation temperature should be between the Tg point and a temperature 50°C higher than this. In many instances, the nucleation stage can be omitted. Sufficient nucleation can be achieved during heating the glass to the crystallisation temperature at which crystals then grow upon the nuclei. The rate of increase of temperature should be carefully controlled in order to avoid deformation of the glass-ceramic and to ensure that crystallisation is complete. Generally, the heating rate is between 2°C and 5°C per minute even in thin glassware.

3.4 Review of ferroelectric glass-ceramics

The evolution of ferroelectric glass-ceramics began when the high dielectric constant materials were needed for high performance capacitors. In 1960, Thwin and co-workers [16] reported that $BaTiO_3$ crystals could be crystallised from a 90% $BaTiO_3$: 10% B_2O_3 glass and the maximum dielectric constant from this glass-ceramic was about 200 and the dissipation factor about 1 to 3%. Anderson and Friedberg [17] (1962) also succeeded achieving high permittivity materials by precipitating ferroelectric crystals of lead metaniobate ($PbNb_2O_6$), in a PbO-Nb_2O_5-SiO_2-Al_2O_3 glass. The maximum dielectric constant from the glass-ceramic, containing 57% ferroelectric orthorhombic + 2% paraelectric rhombohedral $PbNb_2O_6$, was about 160. However, these studies did not address the transparency of the ferroelectric glass-ceramics.

In 1963, a method to construct transparent high dielectric constant materials for electro-luminescent devices was reported by Allen and Herczog. [18] The high dielectric constant transparent semi-crystalline materials, containing sodium niobate, barium meta-niobate, and mixtures of them, with crystal size less than 1000 Å, could be achieved from BaO-Na_2O-Nb_2O_5-SiO_2 system. In 1967, Layton and Herczog [18] investigated transparent glass-ceramics containing $NaNbO_3$ as a major phase in the Na_2O-Nb_2O_5-SiO_2 system. They found that the transparency of the crystallised material was dependent on the particle size rather than on the amount of $NaNbO_3$ presented. The SiO_2 content also plays an important role in the transparency of glass-ceramics. The glass-ceramics containing <20 wt% have a high degree of transparency with the particle size ranging from 200 to 1000 Å. Borrelli et al (1965) [20-21] first reported the electro-optic effect of transparent niobate glass-ceramics, which they also claimed to be the first material exhibiting electro-optic activity in polycrystalline form.

Further investigation by Layton and Herczog (1969) [22] showed that it is possible to construct transparent glass-ceramics from low network-former content glasses (about 5-20 wt. % SiO_2 or GeO_2). The major crystalline phases from this work were mixtures of perovskite-type titanates or niobates: $BaTiO_3$, $NaNbO_3$, $Na_{0.7}Cd_{0.15}NbO_3$, $Na_{0.6}Sr_{0.2}NbO_3$, $Na_{0.7}Pb_{0.15}NbO_3$, $K_{0.2}Sr_{0.4}NbO_3$, $Ba_{0.16}Pb_{0.16}Sr_{0.17}NbO_3$, $Ba_{0.25}Pb_{0.25}NbO_3$. They also stated that, for low network-former glass-ceramics, a very high rate of nucleation was needed to get complete crystallisation of the crystals, which remain small enough to minimise light scattering. The dielectric, optical, and pyroelectric properties of these transparent glass-ceramics were described. [23-24] It has been shown that these properties were a function of the crystallite size. The larger the crystallite size, the better the dielectric or optical properties. However, crystallite size was limited to ≈ 2000 Å in order to get the transparent, low-light scattering specimens. Another method was recommended, which removes the limitation of crystallite size; (hence improving the dielectric and optical properties of glass-ceramics). The composition is altered in order to obtain a suitable refractive index match between the glass and the crystalline phase.

3.4.1 Ferroelectric glass-ceramics based on silicate glasses

In 1964, Herczog [25] reported the properties of ferroelectric glass-ceramics containing $BaTiO_3$ and $BaAl_2Si_2O_8$ as a major and minor phase respectively. The initial glass composition was $x(BaTiO_3)+(100-x)(BaAl_2Si_2O_8)$. The measured dielectric constant of glass-ceramics having 30 to 60 volume% of $BaTiO_3$ of about 1 μ grain size increased from 100 to 1200. They also stated that the minor phase $BaAl_2Si_2O_8$ acted as a grain-growth inhibitor of the major phase $BaTiO_3$ so an exact control of particle size is possible. Apart from $BaTiO_3$, there have been some attempts to construct glass-

ceramics consisting of other perovskite ferroelectrics such as $SrTiO_3$, $PbTiO_3$ and $LiNbO_3$ based on alumino-silicate glasses. The maximum dielectric constant of 520 at 33 K of $SrTiO_3$ glass-ceramics was reported by Lawless, in 1974.[26] The $SrTiO_3$ crystals of 5 μm in size were precipitated in alumino-silicate glasses. Subsequently, Siegwarth (1977) [27] reported some ferroelectric properties of the glass-ceramic at low temperature (between 4 to 77 K), such as a remanent polarisation and ferroelectric hysteresis loop. At around that time, Kokubo and Tashiro [28] studied the properties of the $PbTiO_3$ crystals crystallised from a $PbO\text{-}TiO_2\text{-}Al_2O_3\text{-}SiO_2$ glass as a function of grain size. They showed that the spontaneous deformation of the $PbTiO_3$ crystals surrounded by a glass matrix reduces from 0.055 to 0.000 when their grain size decreases from 2.5 μm to 160 Å. Additionally, the dielectric constant showed maxima at grain sizes of both 0.15 μm and 250 Å and was still considerably high at a grain size as small as 160 Å. Consequently, they suggested it was possible to produced a large electro-optic effect from very-fine-grained transparent ferroelectric glass-ceramic. In 1997, Todorović and Radonjić [29] found that transparent $LiNbO_3$ glass-ceramics based on $LiNbO_3\text{-}SiO_2\text{-}Al_2O_3$ could be obtained as good ferroelectric materials. The IR absorption spectra of these glasses showed that lithium-ions are located in the glass network closer to the NbO_6-octahedra than to the SiO_4-tetrahedra, thus enhancing the possibility for nucleation of the $LiNbO_3$ phase during heat treatment. Glass systems based on silicon oxide and boron oxide were also reported by Todrović et al.[30] It was found that the only way to prepare a glass from the system $BaO\text{-}TiO_2\text{-}SiO_2$ (or B_2O_3) was an extremely fast quenching method because these systems have a narrow glass-forming region. However, they found that the addition of a small amount of fluorine into these glass systems eased the preparation of homogeneous glasses and, from only

silica-based glass doped with fluorine; transparent $BaTiO_3$ glass-ceramics were produced with grain size of 200-400 nm.

3.4.2 Ferroelectric glass-ceramics based on tellurite glasses

In 1991 Komatsu et al. [31] suggested a new glass system of nonlinear optical glasses, which is based on tellurium oxide (TeO_2). Because the refractive indices of many perovskite ferroelectric crystals are similar to those of TeO_2-based glasses, these glasses are of interest to use as matrices for ferroelectric crystals. Moreover, tellurite glasses have low melting temperatures and good infrared transmission so they can be used successfully in non-linear optical devices. Many ferroelectric crystals such as $LiNbO_3$, $BaTiO_3$ and $KNbO_3$ were chosen to be the major phases. Komatsu et al. [31] reported that $LiNbO_3$ crystals were able to form through the transformation of a metastable pyrochlore-type compound above 500°C in $(100-x)TeO_2$-$xLiNbO_3$ ($x \geq 40$) and transparent TeO_2-based glasses containing ferroelectric $LiNbO_3$ mirocrystallites might be possible to achieve. In 1993, Komastsu et al [32] also reported the fabrication of transparent tellurite glasses containing potassium niobate ($KNbO_3$) crystals by an incorporation method. This method was done by directly incorporating $KNbO_3$ particles into TeO_2-K_2O-Nb_2O_5 and then a transparent glass-ceramic, consisting of $KNbO_3$ crystals with a diameter about 10 μm, was first successfully produced. In the same year, they introduced a controlled crystallisation method for the $70TeO_2$-15BaO-$15TiO_2$ glasses; hence $BaTiO_3$ crystals are grown with a diameter of about 5-10 μm.[33] However, there has been continued research by Tanaka et al, 1998, [34] which demonstrated that these glass-ceramics showed second-harmonic generation even though the precipitated $BaTiO_3$ crystals are the paraelectric cubic phase rather than the ferroelectric tetragonal one. Narazaki et al, introduced the poling-induced

crystallisation method in order to stabilise the tetragonal $BaTiO_3$ phase and improve the optical second-harmonic intensity in $BaO-TiO_2-TeO_2$ system in 1999. [35-36] This method was done by applying a direct current voltage in a range of 0.3-1kV to the original glass at around 400 °C and then the temperature was reduced to room temperature with the voltage constant throughout cooling. The $BaTiO_3$ crystals were precipitated in the near surface region with (101) or (110) preferred orientation and the resultant glass-ceramics exhibited second-harmonic generation. However, the glass forming region of TeO_2 based glasses for incorporating barium titanate is very narrow with a maximum amount of only 30 mol% BaO and 20 mol% TiO_2. [31] SrB_4O_7-BaO-TiO_2 glasses were then investigated by Shankar and Varma in 1999.[37] They founded that the optical properties of these glasses were improved.

3.4.3 Ferroelectric glass-ceramics based on phosphate and borate glasses

Various researchers also studied ferroelectric glass ceramics produced from other glass forming oxides, such as P_2O_5 and B_2O_3. In 1995, Araujo et al [38] reported the properties and crystallisation of $LiNbO_3$ in lithium niobophosphate glasses $[(xNb_2O_5:(0.5-x)P_2O_5):0.5Li_2O]:yFe_2O_3$. They found that the ferroelectric $LiNbO_3$ together with the additional phases: $LiPO_3$, $Li_4P_2O_7$ and Li_3PO_4 and Fe_2O_3 were formed by heat treatment of a glass with x = 0.1 in air at 700 °C for 1 hour. IR showed that increase of the ratio Nb_2O_5/P_2O_5 leads to niobium occupying octahedral sites, giving rise to the formation of ferroelectric $LiNbO_3$. Three years later Araujo et al [39] also reported the supportive result of Raman spectra of $LiNbO_3$ in the niobate glass-ceramics. Furthermore in 1999, the study of potassium niobophosphate glasses and glass-ceramics of the family $[x\ Nb_2O_5 - (50-x)\ P_2O_5 - 50K_2O]- y\ Fe_2O_3$ by Andrade et al,[40] using x-ray powder diffraction, infrared and Raman scattering spectroscopy,

showed related results concerning the role of Nb_2O_5 in the glass structure. They found that the increase of the ratio Nb_2O_5/P_2O_5 leads the niobium to sites of octahedral symmetry. Even though, in this work, they attempted to precipitate ferroelectric $KNbO_3$ crystals instead of $LiNbO_3$, a similar effect was still achieved.

Li_2O:B_2O_3 has been long known as an amorphous solid electrolyte system.[41] However, Singh et al reported that the addition of ferroelectric materials to this system enhanced the conductivity within the homogeneous glass formation region. They showed that glasses with 5 mol % $LiNbO_3$, $PbTiO_3$, $PbZrO_3$, 10 mol % $KNbO_3$ and 0.5 mol % $BaTiO_3$ have an increase in conductivity by an order of magnitude. The rapid quenching technique was used in this investigation.[42-43] Varma and his colleagues [44-46] used strontium tetraborate glass (SrB_4O_7) as a host matrix for dispersing ferroelectric materials. They found that precipitation of a ferroelectric crystalline phase of bismuth vanadate ($Bi_2VO_{5.5}$) and bismuth titanate ($Bi_4Ti_3O_{12}$) was accomplished by the controlled heat-treatment of glasses of the composition $2x\ Bi_2O_3$- $x\ V_2O_5$- $(100–3x)\ SrB_4O_7$ ($15 \leq x \leq 25$) and $2x\ Bi_2O_3$- $3xTiO_2$- $(1-5x)\ SrB_4O_7$ ($x = 0.10, 0.25$) respectively. Later in 1998, Shankar and Varma [47] showed that ferroelectric bismuth vanadate glass-ceramics had good electrical and optical properties which would be particularly useful for nonlinear optical applications. Recently, Murugan et al [48] successfully constructed the glass-ceramic of ferroelectric bismuth tungstate in lithium borate glass matrix of the system $(1-x)\ Li_2B_4O_7 - x\ Bi_2WO_6$ ($0.1 \leq x \leq 0.35$) via controlled heat-treatment. The initial substances were polycrystalline $Li_2B_4O_7$ and Bi_2WO_6 from solid state reaction route. They also found that an increase in x caused the dielectric constant to increase.

3.4.4 Solid solution in ferroelectric glass-ceramics

Solid solution in crystalline perovskite phases is important for controlling the properties of technological ferroelectrics. Therefore, considerable interest has been shown in materials in which ferroelectric solid solution crystals were precipitated in glasses to produce-pore free dielectrics. In 1970 Grossman and Isard [49] investigated glass-ceramic materials containing $PbTiO_3$ crystals in a $BaO-B_2O_3$ glass and were able to show that the dielectric properties of these materials obeyed a mixture formula. They found that the material had a disadvantageous high loss factor, which contributed to the conductivity of the $PbTiO_3$ crystals. Later in 1976, Isard et al attempted to make a ferroelectric solid solution glass-ceramic from the same system but with additions of small amounts of La_2O_3 and Nb_2O_5.[50] The same results were obtained, showing no effect of solid solution. However, they reported that (Pb, Ba)TiO_3 formed at 600°C from a mixture of $PbTiO_3$ crystals + $BaTiO_3$ crystals + 20% of a glass of composition $BaO{\cdot}PbO{\cdot}2B_2O_3$. X-ray diffraction showed a slight shoulder on the (200) peak indicating the formation of some $PbTiO_3$ and the peaks showed no effect of crystal clamping. As a result of this, they assumed that, under the conditions of glass-ceramic formation, there is no kinetic barrier against cation re-distribution, meaning that Pb^{2+} and Ba^{2+} can exchange between titanate crystal phase and borated glass at this temperature and $PbTiO_3$ must be the thermodynamic equilibrium phase in the glass-ceramic. In solid solution studies, especially for ferroelectrics, there can be confusion in identifying whether crystal clamping or solid solution causes the peak shifts in XRD. Crystal clamping is normally caused by lattice strain due to the restriction of the phase transition: paraelectric to ferroelectric, by the rigid glass matrix. This resulting strain can be strong enough to mask any shift in the diffraction pattern due to solid solution. Lynch and Shelby [51] suggested that the XRD technique alone was not sufficiently

unambiguous to conclude what caused the peak shifts. Therefore, they used the dilatometry method to prove their hypothesis and concluded that the peak shifts observed in XRD patterns actually resulted from crystal clamping rather than from (Pb, Ba)TiO_3 solid solution formation. In early 1999, Lee and his co-workers [52] investigated the glass-ceramic based on $30PbO\text{-}30TiO_2\text{-}(40\text{-}x)B_2O_3\text{-}xBaO$ (mol%, x=0-20) glass system, which is similar to Shelby's glasses. They reported that the BaO content affects the shift of the Curie temperature in the differential thermal analysis (DTA) and the added Ba ions substitute for Pb ions in the $PbTiO_3$ crystals. It is obvious that the conclusion of Lee is not consistent with that of Shelby. However, there was no mention of the XRD peak shifts in Lee's report.

3.4.5 Ferroelectric crystals containing glass-former(s)

In the last 25 years, there have been studies of a new system where there is no need to add any glass-former for glass making since it contains the good glass former GeO_2. Research into bismuth and lead germanate glasses has been stimulated by the unusual electronic properties of some of their crystalline counter parts. For instance, $Bi_4Ge_3O_{12}$ shows an electro-optic effect while $Pb_5Ge_3O_{11}$ exhibits optical and ferroelectric activity below 177°C. [53] In 1976 Hasegawa et al [54] also reported the crystallisations of $Pb_5Si_3O_{11}$ from the glass in the $PbO\text{-}SiO_2$ system but ferroelectric properties have not yet been investigated. Later in 1977, Glass and his colleagues [55] studied the evolution of ferroelectricity in ultrafine-grained $Pb_5Ge_3O_{11}$. They found that the high-density, highly polarisable $Pb_5Ge_3O_{11}$ glass could be successfully produced by rapid quenching method. By variation of controlled crystallisation glass-ceramics containing different grain sizes of $Pb_5Ge_3O_{11}$ could be formed. The large grained material ($\geq$ 1 μm) has normal ferroelectric properties. On the other hand, the fine-grained glass-ceramics with dimensions about 10 nm have unstable polarisation and

have no dielectric anomaly. This fine-grained material may be described as large dipolar clusters which can be frozen into ferroelectric-like order at low temperatures in the presence of an electric field but the clusters are too small to stabilise spontaneous ferroelectric order. However, this work has inspired many researchers who believe that the ease of preparing lead germanate ceramics by crystallisation from the glass and the possibility of modifying the properties by proper composition changes may make this type of material suitable for pyroelectric and ferroelectric applications. For examples, in 1994 Takahashi et al [56] investigated the pyroelectricity of $Pb_5Ge_3O_{11}$ thick-films prepared by rapid-quenching method and Cornejo and Haun, 1996 [57], studied the electrical properties of $Pb_5Ge_3O_{11}$– based ferroelectric glass-ceramics.

After the synthesis and structural study of lanthanide borogermanates $LnBGeO_5$ by Rulmont et al [58], in 1988, a hexagonal stillwellite-like phase, obtained where Ln = La, Pr and Nd (low-temperature phase), has been of interest especially in term of ferroelectric glass-ceramics because the crystal compositions already contain a glass-former (GeO_2). In 1995, Sigaev et. al.[59-60] investigated the crystallisation behaviour of ten glass compositions based on $LaBGeO_5$ and three glasses based on $PrBGeO_5$ using DTA, X-ray phase analysis and second harmonic generation techniques. The dielectric and nonlinear optical characteristics were obtained from this system. They found that both phases provided ferroelectric properties. The maximum of dielectric constant at T_C equals 520 °C for glass-ceramic based on $LaBGeO_5$ and 750 °C for $PrBGeO_5$ phase. Moreover, recently in 1999, Takahashi and his colleagues [61] successfully produced transparent surface crystallised glasses with optical non-linear $LaBGeO_5$ crystals. They found that the second harmonic intensity from the surface was in the order of 1/100 comparing with that of quartz. However, not only the stillwellite-like borogermanates phases were studied but stillwellite-like borosilicate

phases and structurally similar $ABPO_5$ (A = Ca, Sr, Ba, Pb) phases were also investigated in 1997.[62] They found that the borophosphates are piezoelectric and have no pyroelectric properties at room temperature because these compounds have higher symmetry (space group $P3_121$). On the other hand, $LaBSiO_5$ and $LaBGeO_5$ have space group $P3_1$ and exhibited both ferroelectric and pyroelectric properties. Therefore, the ternary systems Ln_2O_3-B_2O_3-SiO_2 (GeO_2) are of interest for formation of polar glass-ceramic textures with ferroelectric and pyroelectric properties. In 1999, Sigaev et al [63], introduced two new phases; tetragonal $KNbSi_2O_7$ (the potassium niobyl cyclotetrasilicate $K_2(NbO)_2Si_4O_{12}$) and orthorhombic $PbLiPO_4$, crystallised from K_2O-Nb_2O_5-SiO_2 and Li_2O-PbO-P_2O_5 glasses respectively. They found that by using controlled crystallisation under conditions suitable to hinder bulk glass nucleation the ferroelectric glass ceramic texture based on $KNbSi_2O_7$ and $LiPbPO_4$ were obtained and have possible applications as soft grain-oriented coatings. In addition, Pernice et al [64] reported that new transparent glass-ceramics based on potassium niobates ($KNbSi_2O_7$) with nonlinear optical properties were produced from K_2O-Nb_2O_5-$2SiO_2$ glass. The second harmonic generation was used to determine the ferroelectric properties of the glass-ceramics.

3.4.6 Other related materials

For the past twenty years, some scientists have studied new techniques for preparing glass-ceramics with oriented crystals. In this technique, glasses are recrystallised in a temperature gradient in order to grow the crystals in a preferred direction. Since very few ferroelectric materials are good glass formers, it is difficult to produce ferroelectric materials using glass-ceramics methods. Moreover, a glassy phase of low dielectric constant between the crystallites gives difficulty in electric poling. Gardopee et al. [65,66], demonstrated the possibility of producing a polar but

non-ferroelectric material by the glass-ceramic route. The needle-like crystals of $Li_2Si_2O_5$ were formed as a thin layer near the surface having their c-axes perpendicular to the glass surface. They showed that a high degree of orientation could be achieved if well-polished glass samples were heated in a large temperature gradient. These glass-ceramics have good pyroelectric properties but weak piezoelectric response. Halliyal et al [67-70], extensively investigated grain-oriented glass-ceramics in various glass systems, such as Li_2O-SiO_2, Li_2O-SiO_2-B_2O_3, BaO-SiO_2-TiO_2, SrO-SiO_2-TiO_2 and BaO-GeO_2-TiO_2. The crystalline phases recrystallised from these glass systems are $Li_2Si_2O_5$, $Li_2B_4O_7$, $Ba_2TiSi_2O_8$, $Sr_2TiSi_2O_8$ and $Ba_2TiGe_2O_8$ respectively, and all of them are non-ferroelectric but polar crystals. Glass-ceramics with good physical properties were obtained by compositional variation and by the addition of modifying oxides. The piezoelectric and pyroelectric properties of the glass-ceramics were also studied. In 1984, Halliyal et al [71] showed that grain-oriented glass-ceramics in the systems BaO-SiO_2-TiO_2, BaO-GeO_2-TiO_2 and SrO-SiO_2TiO_2 could be prepared by crystallising glasses of optimised compositions in a large temperature gradient. They found that the piezoelectric properties of these glass-ceramics are comparable to those of polyvinylidene fluoride ($(CH_2F_2)n$ =PVF_2) and PZT which were the commonly used piezoelectric materials. They showed that the piezoelectric voltage coefficients g_{33} and hydrostatic voltage coefficient g_h of these glass-ceramics are similar to those of PVF_2 and an order of magnitude higher than that of PZT. As a result, these glass-ceramics may offer several advantages over PVF_2 and other ferroelectric materials for application in piezoelectric devices. Recently, Zhang and his co-workers [72] produced the polar-nonferroelectric $(Ba_x, Sr_{2-x})TiSi_2O_8$ glass-ceramics with highly oriented crystallites by a gradient temperature heat treatment technique. These glass-ceramics have low dielectric constant, a high hydrostatic figure, no ageing or depoling problems

and good stability at high temperature and pressure so they can be used as hydrophones and high temperature infrared detectors.

Another topic of interest is glasses prepared by roller quenching with a reasonably high quenching rate of about 10^7 degrees per second. In 1980, Nassau [73] showed the possibility of producing glasses containing no glass-formers, such as $LiNbO_3$, $KTaO_3$, $Li_2Mo_2O_7$, $Y_3Fe_5O_{12}$, Li_5GaO_4, $Li_4CaK_2(SO_4)_4$ and $LiLa(SO_4)_2$. Attractively, these glasses have ferroelectric-like behaviour, antiferromagnetism and large ionic conductivities Moreover, in 1982 Torii et al [74] could form transparent $La_{0.33}NbO_3$ flakes, by the roller quenching method, with a high degree of crystallographic orientation which is useful in application of ferroelectric and electro-optic materials. The rapid quenching technique was not only of interest in term of transparent ferroelectric applications but also in the modification of the electric properties of amorphous solids. In 1984, Sekiya and Torii [75] studied Bi_2O_3-SiO_2 films using a twin-roller method (made by Chen et al [76]) in various compositions. They found that transparent films were obtained when the SiO_2 content was more than 10%. The grains of δ-Bi_2O_3 were almost perfectly oriented as the (111) was parallel with the film plane.

In general, ferroelectric materials can be produced in various forms such as single crystals, ceramics, thin films, polymer and glass-ceramics. However, Branunstein and his co-workers [77-79] presented an unusual ferroelectric material. They showed that glasses containing WO_6-octahedra in various glass-forming networks of Li_2O-B_2O_3, Na_2O-B_2O_3 and TeO_2 exhibit ferroelectric-like, electrochromic and photochromic behaviour. The local WO_6-octahedra provide the dielectric properties of these glasses and the dipole-dipole correlations contribute to the ferroelectric-like behaviour of these amorphous systems. A model was used to determine that the phase transition is related

to random "pseudo-spins" in a glass matrix. These glasses may be useful in applications of transducer, display and information storage devices.

References

1. McMillan, P.W. *Glass-Ceramics*, 1979 (Academic Press)
2. (2000, July 21), Our Successes [Online], Corning Incorporated, http://www.optical.corning.com/dev/t_t_b/innovation/index.html, [25 July 2000]
3. McMillan, P.W., Hodgson, B.P. and Partridge, G. 1970, *British Patent*, Service Number 943 599.
4. Paul, A. *Chemistry of Glasses*, 1982 (Chapman and Hall Ltd.)
5. Jones, G. O. *Glass*, 1971 (Chapman and Hall Ltd.)
6. Shelby, J. E. *Introduction to Glass Science and Technology*, 1997 (The Royal Society of Chemistry)
7. Yoko, T., Kamiya, K., Tanaka, K., Yamada, H. and Sakka, S. 1989, *Journal Ceramic Society Japan*, Volume 97, p. 289.
8. Rawson, H. *Inorganic Glass-forming Systems*, 1967 (Academic Press)
9. Sigaev, V. N., Stefanovich, Y., Sarkisov, P. D., Lopatina, E. V. (1995) *Materials Science and Engineering*, B32, p. 17.
10. Muller, J.H. and Blank, H.R. 1924, *Journal of American Chemistry Society*, Volume 46, p. 2358.
11. Laubengayer, A.W. and Morton, D.S. 1932, *Journal of American Chemistry Society*, Volume 54, p. 2303.
12. Kotera, Y. and Yonemura, M. 1963, *Trans. Faraday Soc.*, volume 59, p. 147.
13. Zarzycki, J. 1957, *Verres Réfract*, volume 11, p. 3.
14. Riebling, E.F. 1963, *J. Chem. Phys.*, volume 39, p. 3022.
15. Turnbull, D. and Cohen, M.H. *Modern Aspects of the Vitreous State 1*, 1960 (Butterworths, London)
16. Thwin, M.O., Kastenbein, E.L., Smoke, E.J. and DiVita, S. 1960, *American Ceramic Society Bulletin*, Volume 39, p. 197.
17. Anderson, R.C. and Friedberg, A.L. 1962, *Symposium on Nucleation and Crystallization in Glasses and Melts*, p. 29.
18. Allen, R.E. and Herczog, A. 1963, *US patent*, service Number 3,114,066.
19. Layton and Herczog, A. 1967, *Journal of American Ceramic Society*, Volume 50, Number 7, p. 369.
20. Borrelli, N.F., Herczog, A. and Maurer, R.D. 1965, *Applied Physics Letters*, Volume 7, Number 5, p. 117.
21. Borrelli, N.F. 1967, *Journal of Applied Physics*, Volume 38, Number 11, p. 4243.
22. Layton and Herczog, A. 1969, *Glass Technology*, Volume 10, Number 2, p. 50.
23. Borrelli, N.F. and Layton, M.M. 1971, *Journal of Non-Crystalline Solids*, Volume 6, p. 197.
24. Layton, M.M. and Smith, J.W. 1975, *Journal of American Ceramic Society*, Volume 58, Number 9-10, p. 435.
25. Herczog, A. 1964, *Journal of American Ceramic Society*, Volume 47, Number 3, p. 107.
26. Lawless, W.N. 1974, *Ferroelectrics*, Volume 7, p. 379.
27. Siegwarth, J.D. 1977, *Journal of Applied Physics*, Volume 48, Number 1, p. 1.
28. Kokubo, T. and Tashiro, M. 1973/74, *Journal of Non-Crystalline Solids*, Volume 13, p. 328.
29. Todorović, M., Radonjić, Lj. 1997, *Ceramics International*, Volume 23, p. 55.
30. Todorović, M., Radonjić, Lj. and Dumić, J. 1997, *Key Engineering Materials*, Voume 132-136, p. 193.

31. Komatsu, T., Tawarayama, H., Mohri, H. and Matusita, K. 1991, *Journal of Non-Crystalline Solids*, Volume 135, p. 105.
32. Komatsu, T., Shioya, K. and Matusita, K. 1993, *Journal of American Ceramic Society*, Volume 76, Number 11, p. 2923.
33. Komatsu, T., Shioya, K. and Matusita, K. 1993, *Journal Ceramic Society Japan*, Volume 76, p. 2923.
34. Tanaka, K., Kuroda, H., Narazaki, A., Hirao, K. and Soga, N. 1998, *Journal of Material Science Letters*, Volume 17, p. 1063.
35. Narazaki, A., Tanaka, K. and Kirao, K, 1999, *Applied Physics Letters*, Volume 75, Number 21, p. 3399.
36. Narazaki, A., Tanaka, K. and Kirao, K. 1999, *Journal of Material Research*, Volume 14, Number 9, p. 3641.
37. Shankar, M.V. and Varma, K.B.R. 1999, *Physics and Chemistry of Glasses*, Volume 40, Number 1, p. 44.
38. Araujo, E. B., Paiva, J. A. C. and Sombra, A. S. B. 1995, *Journal of Physics: Condensed Matter*, Volume 7, p. 9723.
39. Araujo, E. B., Paiva, J. A. C., Freitas JR. J. A. and Sombra, A. S. B. 1998, *Journal of Physics Chem Solids*, Volume 59, Number 5, p. 689.
40. Andrade, J. S., Pinheiro, A. G., Vasconcelos, I. F., Sasaki, J. M., Paiva, J. A. C., Valente, M. A. and Sombra, A. S. B. 1999, *Journal of Physics: Condens. Matter*, Volume 11, p. 4451.
41. Otto, K. 1966, *Physics and Chemistry of Glasses*, Volume 7, p. 29.
42. Singh, K. and Rokde, S. 1984, *Journal of Power Sources*, Volume 13, p. 151.
43. Singh, K., Gandhi, P. R. and Chaudhari, B. M. 1988, Solid State Ionics, Volume 28-30, p. 752.
44. Varma, K. B. R., Shankar, M. V. and Subbanna, G. N. 1996, *Material Research Bulletin*, Volume 31, Number 5, p. 475.
45. Varma, K. B. R. and Shankar, M. V. 1996, *IEEE International Symposium on Application of Ferroelectrics*, Volume 2, p. 813.
46. Shankar, M. V. and Varma, K. B. R. 1996, *IEEE International Symposium on Application of Ferroelectrics*, Volume 2, p. 817.
47. Shankar, M. V. and Varma, K. B. R. 1998, *Journal of Non-Crystalline Solids*, Volume 226, p. 145.
48. Murugan, G. S., Subbanna, G. N. and VarMa, B. R. 1999, *Journal of Materials Science Letters*, Volume 18, p. 1687.
49. Grossman, D.G. and Isard, J.O. 1970, *Journal of Physics D: Applied Physics*, Volume 4, p. 1058.
50. Isard, J.O., Keight, D.V. and Minshull, J.L. 1976, *Ferroelectrics*, Volume 11, p. 445.
51. Lynch, S.M. and Shelby, J.E. 1984, *Journal of American Ceramic Society*, Volume 67, Number 6, p.424.
52. Lee, S.W., Shim, K.B., Auh, K.H. and Knott, P. 1999, *Materials Letters*, Volume 38, p. 356.
53. Riebling, E. G. 1975, *Materials Research Bulletin*, Volume 10, p. 23.
54. Hasegawa, H., Shimada, M., Kanamaru, F. and Koizumi, M. (1977) *Bulletin Chemistry Society Japan*, Volume 50, Number 2, p.529.
55. Glass, A. M., Nassau, K. and Shiever, J. W. 1977, *Journal of Applied Physics*, Volume 48, Number 12, p. 5213.
56. Takahashi, K., Ueda, H. and Suzuki, T. and Kakegawa, K. 1994, *Ferroelectrics*, Volume 154, p. 41.

57. Cornejo, I. A. and Haun, M. J. 1996, *Materials Research Society Symposium Proceedings*, Volume 400, p. 353.
58. Rulmont, A. and Tarte, P. 1988, *Journal of Solid State Chemistry*, Volume 75, p. 244.
59. Sigaev, V. N., Stefanovich, S. Yu., Sarkisov, P. D. and Lopatina, E. V. 1995, *Fizika Khimiya Stekla*, Volume 20, p. 590.
60. Sigaev, V. N., Stefanovich, S. Yu., Sarkisov, P. D. and Lopatina, E. V. 1995, *Materials Science and Engineering*, Volume B32, p. 17.
61. Tkahashi, Y., Benino, Y., Dimitrov, V. and Komatsu, T. 1999, *Journal of Non-Crystalline Solids*, Volume 260, p. 155.
62. Stefanovich, S., Mill, B. and Sigaev, V. 1997, *Ferroelectrics*, Volume 201, p. 285.
63. Sigaev, V. N., Sarkisov, P. D., Stefanovich, S. Yu., Pernice, P. and Aronne, A. 1999, *Ferroelectrics*, Volume 233(3-4), p. 165.Pernice, P., Aronne A., Sigaev, V. N., Sarkisov, P.D., Molev, V. I. and Stefanovich, S. Yu. 1999, *Journal of American ceramic society*, Volume 82, p. 3447.Gardopee, G., Newnham, R. E., Halliyal, A. and Bhalla, A. S. 1980, *Applied Physics Letters*, Volume 36, p. 817.
66. Gardopee, G., Newnham, R. E. and Bhalla, A. S. 1981, *Ferroelectrics*, Volume 33, p. 155.
67. Halliyal, A., Bhalla, A. S., Newnham, R. E. and Cross, L. E. 1981, *Journal of Materials Science*, Volume 16, p. 1023.
68. Halliyal, A., Bhalla, A. S., Newnham, R. E. and Cross, L. E., 1981, *Ferroelectrics*, Volume 38, p. 781.
69. Halliyal, A., Bhalla, A. S., Newnham, R.E. and Cross, L. E. 1981, *Ultrasonic Symposiums*, p. 315.
70. Halliyal, A., Bhalla, A. S. and Newnham, R. E., 1983, *Materials Research Bulletin*, Volume 18, Number 8, p. 1007.
71. Halliyal A., Safari, A., Bhalla A.S., Newnham R.E., and Cross L. E. 1984, *Journal of American ceramic society*, Volume 67, No. 5, pp. 331-335.
72. Zhang, J., Lee, B. I. And Schwartz, R. W. 1999, *Journal of Applied Physics*, Volume 85, Number 12, p. 8343.
73. Nassau, K. 1980, *Journal of non-crystalline Solids*, Volume 42, p. 423.
74. Torii, Y., Sekiya, T. and Yamamoto, T. 1982, *Materials Research Bulletin*, Volume 17, p. 727.
75. Sekiya, T. and Torii, Y. 1984, *Materials Research Bulletin*, Volume 19, p. 885.
76. Chen, H. S. and Miller, C. E. 1970, *Review of Scientific Instruments*, Volume 41, p.1237.
77. Braunstein, R., Lefkowitz, I. And Snare, J. 1978, *Solid State Communication*, Volume 28, Number 10, p. 843.
78. Braunstein, R. and Barner, K. 1978, *Solid State Communication*, Volume 28, Number 10, p. 847.
79. Braunstein, R. and Lefkowitz, I. 1980, *Ferroelectrics*, Volume 27, p. 225.

Chapter 4

Experimental materials and techniques

4.1 Glass-ceramics development

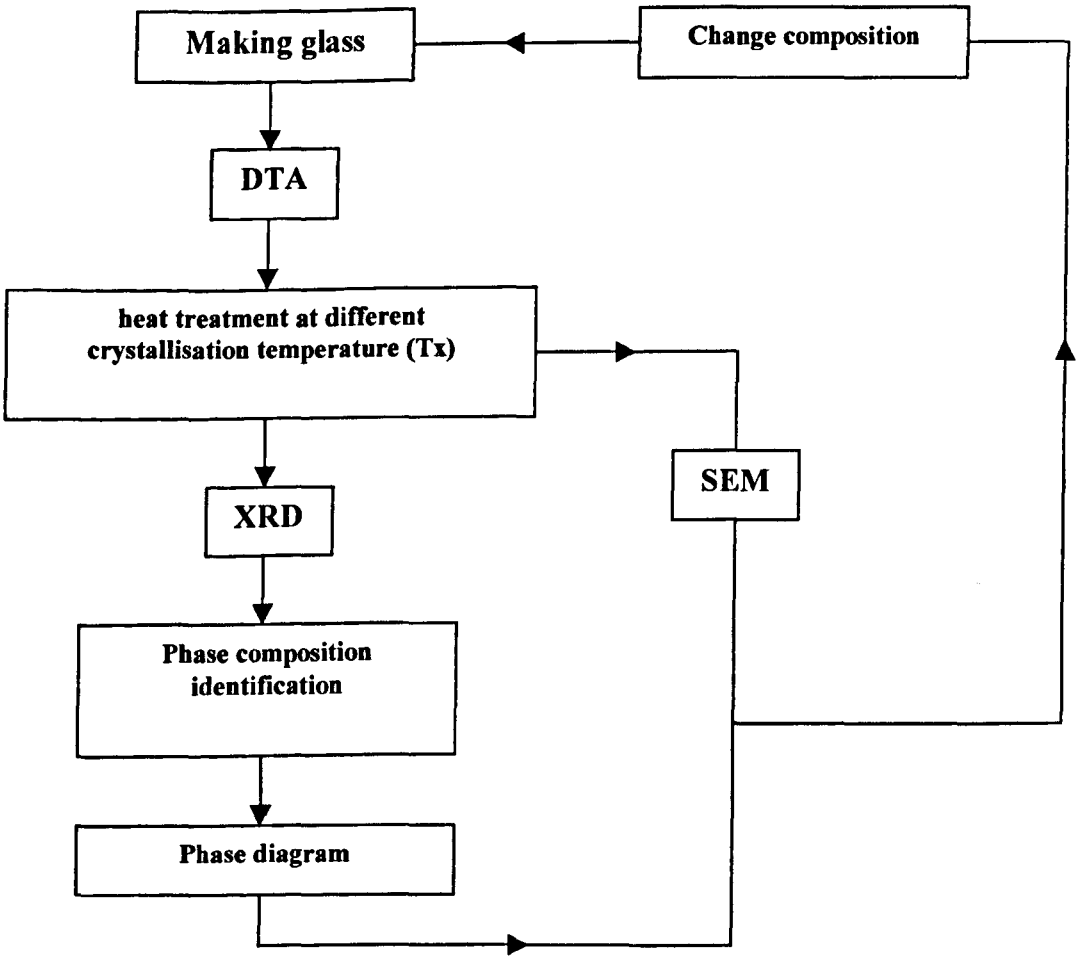

***Figure 4.1** Diagram of glass-ceramic development.*

The above diagram shows the important stages in developing new glass-ceramics. First, a glass composition of interest is chosen and the glass is melted and quenched. Then phase transformations, including crystallisation temperatures and melting points, are identified using DTA (Differential Thermal Analysis). After that,

heat treatments are applied corresponding to each crystallisation temperature, and the phase composition of the crystallised samples is determined by X-Ray Diffraction Analysis (XRD). In addition, the microstructure of the resulting glass-ceramic is investigated using Scanning Electron Microscopy (SEM). Consequently, if the analysed glass-ceramic is unsatisfactory, other compositions are considered. The following sections describe the backgrounds of the techniques and experimental methods employed.

4.2 Preparation of a homogeneous glass

In this work, glass compositions from the systems of interest: $BiO_{1.5}$-GeO_2, $BiO_{1.5}$-GeO_2-B_2O_3, $BiO_{1.5}$-GeO_2-TeO_2, PbO-GeO_2, PbO-Nb_2O_5-GeO_2, $Pb_5Ge_3O_{11}$-$PbNb_2O_6$-SiO_2 were chosen. About 25-30 gram batches of each composition were then melted in a 90Pt/10Rh crucible and held for melt-homogenisation at various melting temperatures in an electric furnace for about 15-30 minute depending on individual composition. The crucible was covered by an alumina sheet lid in order to reduce volatilisation of PbO and Bi_2O_3 from the melt. After that, the glasses were quenched between stainless-steel plates, either at room temperature or liquid-nitrogen temperature depending on the viscosity of the melts. This yielded plates of about 0.5 to 1mm thickness.

4.3 Differential thermal analysis (DTA)

This technique gives important information, such as phase transformations including crystallisation temperatures. The concept is that the difference in temperature, ΔT, between the sample and a reference material is measured in the same heating schedule and atmosphere by means of a differential thermocouple. Figure 4.2 shows a schematic diagram of the DTA construction.

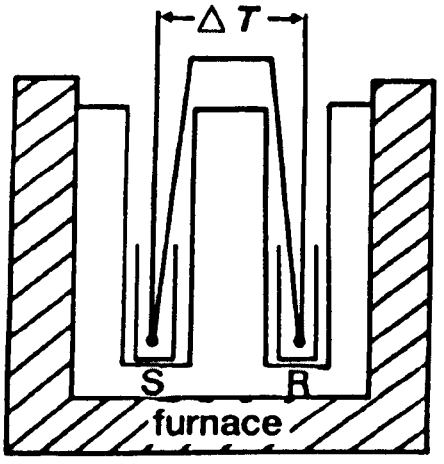

Figure 4.2 Classical apparatus (S = sample; R = reference). [1]

From figure 4.2, a block, with two symmetrical holes, is used for positioning the sample and reference holder. The material used for the holder should have low thermal conductivity in order to give sufficient differential signal. In general, when an endothermic thermal event, such as melting, occurs in the sample the difference in enthalpy (ΔH) is positive as the sample internal energy increases. On the other hand, in DTA, ΔT is measured from the surroundings so the value is negative in an endotherm.

The changes in structure of a glassy substance involve the evolution or absorption of energy in the form of heat. For example, an exotherm occurs at the temperature where the glass crystallises or a metastable crystal phase transforms and an endotherm occurs at the melting temperature. An idealised DTA curve of a glassy material is presented in figure 4.3. A represents the glass transition point, B and C refer to exothermic peaks due to formation of crystal phases and D is an endothermic event due to first melting.

In this work, a Stanton Redcroft DTA model 673-4 was used. Finely powdered glass of about 0.2-0.3 g depending on the density of the glass, was placed in a small capsule made from platinum. Another capsule was used to contain a reference powder

such as alumina or silica. Ideally, the heat capacities of sample plus holder and the reference plus holder should be similar. The thermocouples connected with the two capsules are connected in opposition in order to obtain an e.m.f corresponding to the differential temperature between the test powder and standard powder when the two capsules are heated at a constant rate about 5 °C/min. The graph of differential temperature versus temperature is then plotted.

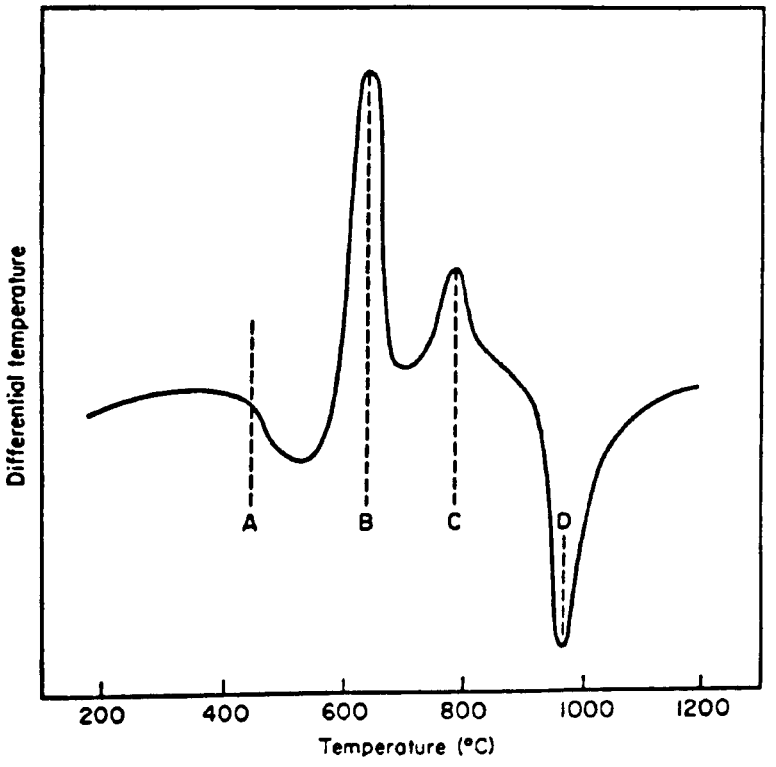

***Figure 4.3** Differential thermal analysis curve for a devitrifiable glass. (After McMillan[2].*

4.4 Controlled heat treatment to produce the glass-ceramics

This treatment is aimed at converting the glass into a crystalline ceramic, which will have better properties than the original glass. The various stages of the heat-treatment process, are presented as an idealised heat-treatment schedule in figure 3.6 (chapter 3).

The glasses from all systems were subjected to heat treatment schedules at different crystallisation temperatures (from DTA). The normal schedule for most samples is shown in figure 4.4 which omits the nucleation stage. The heating and cooling rate used were 5°C/min and 10°C/min respectively with 4 hours of dwell time for complete crystallisation.

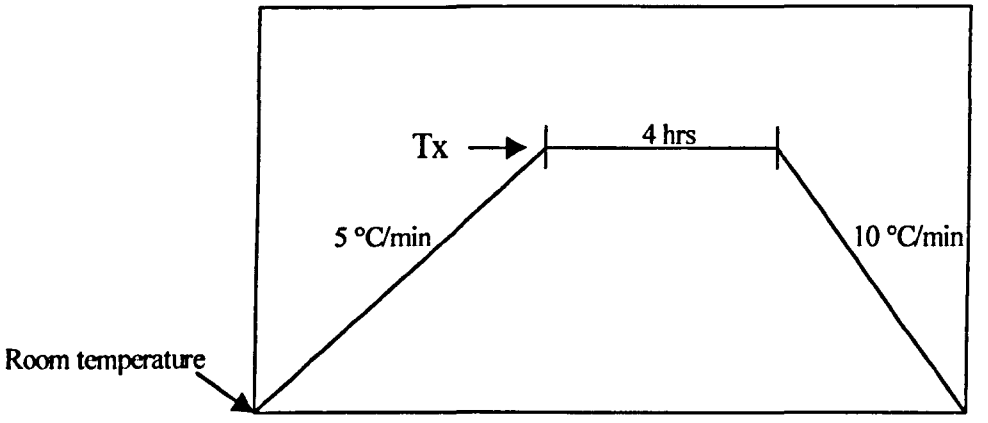

***Figure 4.4** The diagram of the heat treatment schedule used in this study.*

4.5 X-ray diffraction analysis (XRD)

X-ray diffraction is used to investigate the crystallisation of glasses. A diffuse X-ray diffraction pattern, with complete absence of sharp lines, is found in glass samples. On the other hand, crystalline materials will give an X-ray diffraction spectrum containing sharp peaks. By using Bragg's law ($2d\sin\theta = n\lambda$) and 2θ values from the spectrum, d-spacings can be calculated and used to identify the phases by comparing with standard data, such as the JCPDS files complied by the International Centre for Diffraction Data (ICDD). [3] The diagrams in figure 4.5 (a) and (b) illustrate θ and 2θ. Figure 4.5 (a) shows the reflection of X-rays from two lattice planes belonging to the family (hkl) and d is the interplanar spacing. From figure 4.5 (b), it

can be seen that a diffraction maximum can only be obtained when a reciprocal lattice vector or scattering vector ($\mathbf{r_H^*}$ or $\Delta\mathbf{k}$) crosses the Ewald sphere where $r_H^* = ha^* + kb^* + lc^*$.

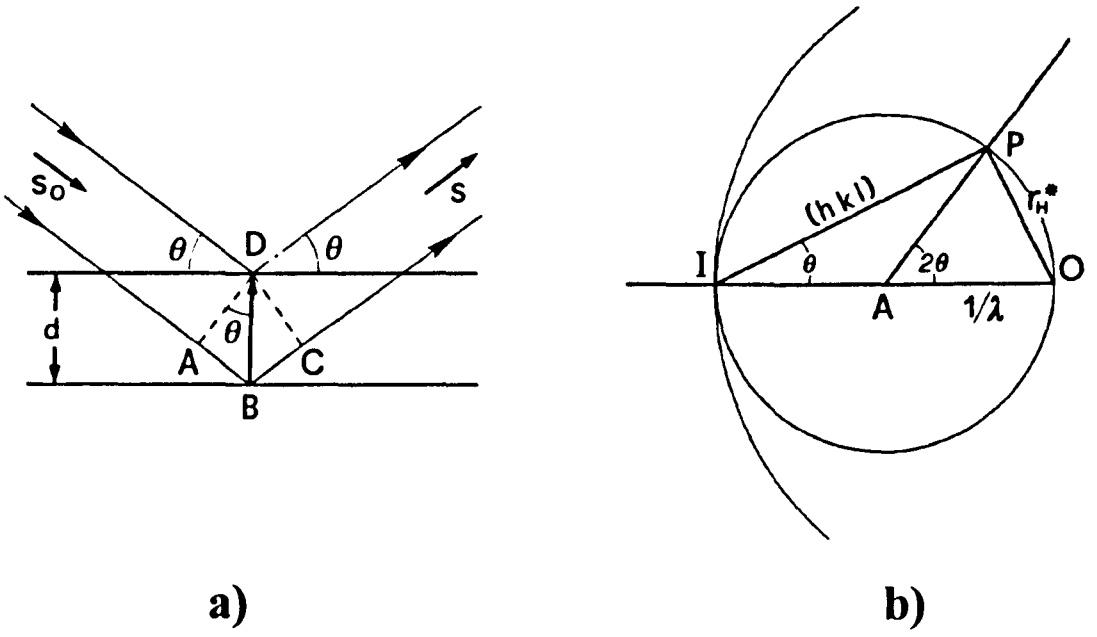

Figure 4.5 *(a) Simple illustration of Bragg's law construction*[4] *(b) Ewald sphere*

X-ray powder diffraction using an automatic diffractometer is used to collect the powder diffraction patterns. The diagram in figure 4.6 shows the diffractometer equatorial geometry. The detector rotates about the instrument main axis. Reflections will always be detected in the plane containing the incident beam and an electronic counter is used to record the diffracted intensity at each value of two-theta. The sample is loaded in a recess in a flat-plate aluminium holder. The scan mode is theta-2-theta and the source is CuKα.

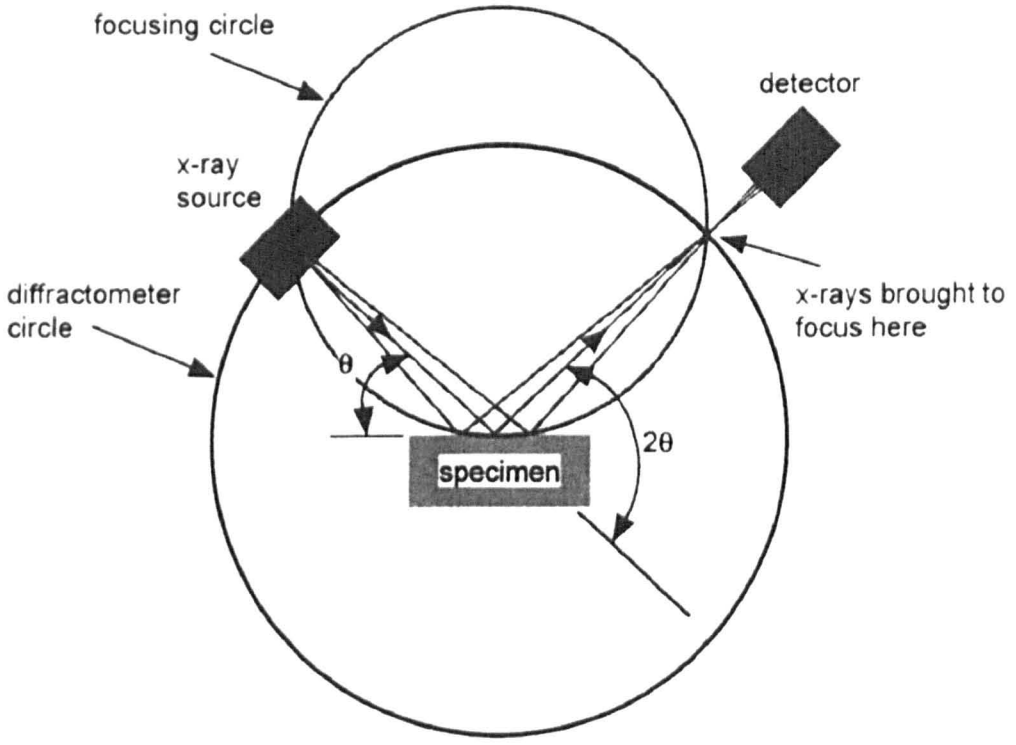

Figure 4.6 *The diffractometer equatorial geometry.*[5]

The diffraction pattern, in fact, acts like "a finger print" of phases in crystalline samples, which might contain only one phase or more. The relation between intensity of a diffraction peak from one phase in a mixture of phases and the concentration of that phase is non-linear because the diffracted intensity depends noticeably on the absorption coefficient of the mixture, which again depends on the concentration of the phase. Equation 4.1 presents the intensity of the diffracted beam from a single-phase polycrystalline powder specimen containing randomly oriented grains.

$$I = \left(\frac{I_0 A\lambda^3}{32\pi r}\right)\left[\left(\frac{\mu_0}{4\pi}\right)^2 \frac{e^4}{m^2}\right]\frac{1}{v^2}\left[F^2 p\left(\frac{1+\cos^2 2\theta}{\sin^2\cos\theta}\right)\right]\frac{e^{-2M}}{2\mu} \qquad (4.1)\ ^{(5)},$$

where I is the integrated intensity of diffraction peak, I_0 is the incident beam intensity, A is the incident beam cross-sectional area, λ is the incident beam wavelength, r is the radius of the diffractometer circle, $\mu_0 = 4\pi \times 10^{-7}\,\mathrm{mkgC^{-2}}$, e is the electron charge, m

is the electron mass, v is the unit cell volume, F is the structure factor, p is the multiplicity factor, θ is the Bragg angle, $M = B((\sin\theta)/\lambda)^2$, where B is temperature factor and μ is the linear absorption coefficient. This equation is essential to the quantitative analysis. The intensity of a reflection of the α phase in the mixture of phases (α, β, ...) can be written as

$$I_\alpha = \frac{K_1 c_\alpha}{\mu_m} \qquad (4.2)^{(5)},$$

where K_1 is constant, c_α is the volume fraction of the α phase in the mixture and μ_m is the linear absorption coefficient for the mixture. The weight of a unit volume of the mixture is ρ_m and the weight of α in the mixture is $w_\alpha \rho_m$, where w_α is the weight fraction of α phase in the mixture. Therefore, the volume of α in the mixture (c_α) is equal to $w_\alpha \rho_m / \rho_\alpha$. Similar expressions are obtained for others phases such as β.

Equation 4.2 can be rewritten as equation 4.3 below.

$$I_\alpha = \frac{K_1}{\mu_m}\frac{w_\alpha}{\rho_\alpha}\rho_m$$

or

$$I_\alpha = \frac{K_1 w_\alpha}{\rho_\alpha (\mu/\rho)_m} \qquad (4.3)$$

Practically, there are three methods for calculation of c_α:

1. External standard method (a reference peak from pure α)
2. Direct comparison method (a reference peak from another phase in the mixture)
3. Internal standard method (a reference peak from a foreign material mixed with specimen)

In this study, the *direct comparison method* is of interest as this method can be used to determine the phase proportions in the glass-ceramics. For simple calculation, equation 4.1 can be rewritten as

$$I = \frac{K_2 R}{2\mu} \tag{4.4}$$

where

$$K_2 = \frac{I_0 A \lambda^3}{32\pi r}\left[\left(\frac{\mu_0}{4\pi}\right)^2 \frac{e^4}{m^2}\right] \tag{4.5}$$

and

$$R = \frac{1}{v^2}\left[F^2 p\left(\frac{1+\cos^2 2\theta}{\sin^2 \cos\theta}\right)\right] e^{-2M}. \tag{4.6}$$

K_2 is constant and dependent only on the diffractometer but R depends on the nature of the phase, θ and hkl values. The two diffracted intensities of two different phases α and β can be expressed as

$$I_\alpha = \frac{K_2 R_\alpha c_\alpha}{2\mu_m} \tag{4.7}$$

$$I_\beta = \frac{K_2 R_\beta c_\beta}{2\mu_m} \tag{4.8}$$

Eventually, c_α / c_β can be obtained from the following equation:

$$\frac{c_\alpha}{c_\beta} = \frac{R_\beta I_\alpha}{R_\alpha I_\beta} \tag{4.9}$$

I_α/I_β can be measured from the diffraction peaks and R_α and R_β can be calculated by using the information on the crystal structure and lattice parameters of the two phases. If the powder specimen contains only two phases α and β, the value of c_α or c_β will be found by the additional relationship:

$$c_\alpha + c_\beta = 1. \tag{4.10}$$

However, the calculated peaks from the powder diffraction patterns should be carefully selected. Firstly, α and β reflections should be well separated from each

other. Secondly, the volume of the unit cell should be calculated from the observed lattice parameter in order to avoid the confusion of solid solutions or impure components. Finally, the intensity used should be the integrated intensity not the peak height because of peak broadening due to the crystallite size and lattice strain in the sample. [5]

In this work, the X-ray powder diffraction method was used to identify the crystalline phases of all glass and glass-ceramic samples. Samples were ground to fine powder using an agate pestle and mortar and mounted in aluminium sample holders. All samples were run on the Philips powder diffractometer using Cu Kα (λ = 1.54178 Å) radiation. The 2θ-step size was 0.02 and time constant 1 second for all samples. Then the phases were identified by comparing the experimental diffraction patterns with the powder diffraction database (JCPDS files) using the PDF Maint version 3.0 program.[3] The direct comparison method was used to determine the phase proportion in some glass-ceramics.

4.6 Scanning Electron Microscopy (SEM)

Many structural features of glass-ceramics are often not observable using a simple optical microscope. Particularly, nucleation particles can be less than 10 nm in dimension and crystals of the order of microns. Therefore, the high magnification of SEM or TEM is required. The SEM (Scanning electron microscope) can be compared to a closed-circuit TV. In the SEM the object is scanned with the electron beam and the electrons emitted or scattered from the surface are collected and amplified to form the video signal corresponding to the image. Electron lenses are used to magnify the image. When an electron beam of high energy (from 1 to 50 kV) penetrates into a specimen, most energy is lost by ionising the atoms of the solid and some important interactions may occur as illustrated in figure 4.7. [6]

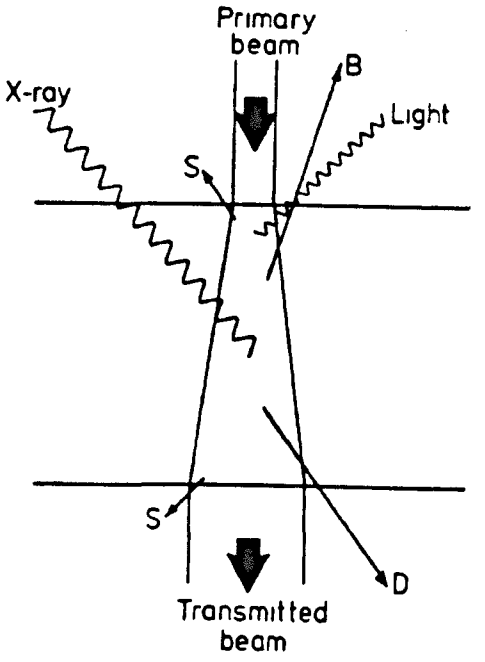

***Figure 4.7** A summary of the effects which may be detected when a primary beam of high energy electrons hits specimen. S = secondary electrons; B = backscattered electrons; D = diffracted electrons.* [7]

The main imaging mode is of secondary electrons of energy less than 100 eV. The emitted intensity of these electrons is sensitive to the angle of inclination of the specimen surface so it can give 'topographic contrast' revealing surface shape at high resolution. In addition, the backscattering image, which uses back-scattered electrons of energy near to that of the incident electron beam in SEM, can show the atomic contrast of phases in the sample. As a result, the scattered intensity is sensitive to atomic number and provides a mapping of compositional differences within the specimen. Therefore, it is useful for observing the microstructure of the glass-ceramics or glass samples. In addition, Energy Dispersive Analysis (EDS) can be used to quantify the composition of each phase shown in the backscattering image. The energy of each X-ray photon corresponding to the transition energy between orbital shells in the atom can be presented as $E = hc/\lambda$. The phenomenon of diffraction can be used to separate the wavelengths according to Bragg's law: $n\lambda = 2d\sin\theta$. The ED spectrometer

measures X-ray energy directly, producing a spectrum of counts versus energy in keV. Hence, it can be used to quantify the composition of an element in a specific area, which is equivalent to the probe size. Several features of EDS analysis make them usable in both TEM (transmission electron microscopes) and SEM. [8]

The estimation of the amount of an element occurring in the bulk sample is made by comparison with a standard of known composition. Equation 4.11 expresses the concentration of the element in the specimen, C_{spec}.

$$C_{spec} = k \times C_{std} \qquad (4.11)^{(7)}$$

A complication of this analysis arises because the specimen is not the same as the standard. Therefore, the equation 4.11 may need a matrix (ZAF) correction. These three factors (ZAF) are known as the atomic number correction Z, the absorption correction A and the fluorescence F. The ZAF technique is performed by measuring X-ray counts from an element in both specimen and standard. The k value is the ratio of the specimen intensity and the standard intensity. C_{spec} is given by:

$$C_{spec} = k \times Z \times A \times F \qquad (4.12)$$

The values of Z, A and F depend on several factors, including the mean atomic weight of the specimen. [7] They are only accurate if the specimen and standard matrices are very similar in composition. Moreover, there is a major problem with the large excitation volume in SEM EDS, where several phases may be sampled unknowingly. The simple diagram of this situation is depicted in figure 4.8. It can be seen that x-rays, seemingly coming from phase A, also can come from unexpected phases B, C and M.

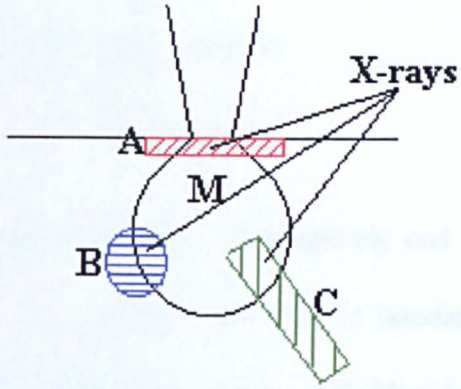

Figure 4.8 *Simple diagram of the excitation volume in SEM.*

The specimens used in the SEM analysis were prepared as follows. The glass-ceramic pieces were cut in cross-section and then they were put into a plastic mould. Each mould was filled with a mixture of 20ml METSET RESIN and 5 drops of METSET HARDENER. Finally the mould was dried in air for 1 day to make it hard enough to polish. Each specimen was polished using a series of silicon carbide papers and different grade of diamond spray to 0.5 μm. Carbon paste was used to paint around the resin mould, excluding the specimen area, in order to make a conductive contact. After the paste was dried, the surface was sputter coated with gold. A JEOL 6100 electron microscope was used to record the backscattering images and examine the microstructure of the glass-ceramic bulk and the EDS analysis was used for compositional analysis of the bulk and of individual features.

4.7 Thermal expansion

The instrument used for measuring thermal expansion is known as a dilatometer, which can give information on volume or length of a substance as a function of temperature. [9] For solids, the most common parameter for this

measurement is the length, which normally increases on heating. The linear relationship between L (length) and T (temperature) is given by

$$L_2 = L_1(1 + \int_{T_1}^{T_2} \alpha dT) \qquad (4.13)$$

where L_1 and L_2 are the length at T_1 and T_2 respectively and α is linear expansion coefficient which depends on the structure and type of bonding in the solid and is normally constant over a small temperature interval, ΔT. Therefore, the equation 4.13 can be assumed as

$$L_2 - L_1 = \Delta L = L_1 \alpha \Delta T \qquad (4.14)$$

or

$$\Delta L / L_1 = \alpha \Delta T \qquad (4.15)$$

The value of α is normally low for the stronger bonded solids. For example, α of covalent and ionic materials < that of metals < that of molecularly bonded materials. In crystalline material, α changes in different crystallographic direction (anisotropic behaviour). [2]

The experimental was carried out using a homemade, vertical, fused silica dilatometer, which was calibrated with a platinum standard as shown in figure 4.9. [10] The LVDT unit (a linear variable displacement transducer) is also illustrated in figure 4.10.

The selected glass sample of 0.5×0.25×2.5 cm dimension was measured from room temperature to the softening point of the glass with a heating rate of 2°C/min. When the temperature increased, expansion occurred and the silica rod was pushed upwards. Therefore, the displacement (ΔL) was detected by LVDT. The graph ΔL versus temperature was then plotted and the thermal expansion coefficient (α) was calculated using equation 4.15.

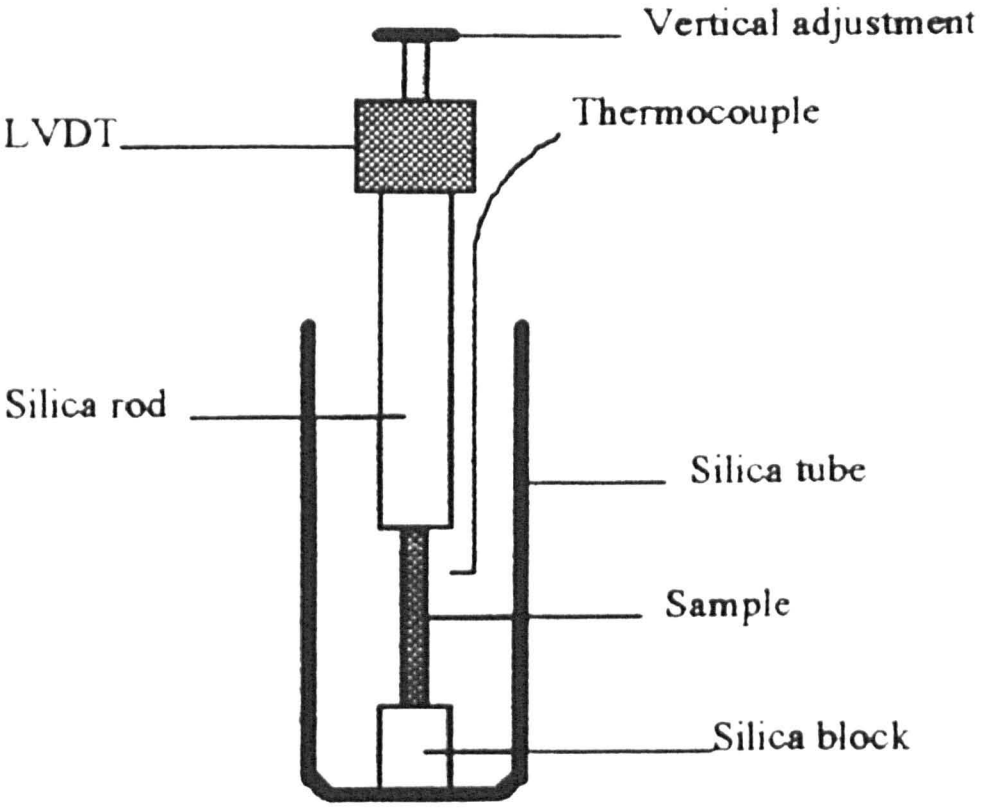

Figure 4.9 *Cross section of the inside of the quartz dilatometer.* [10]

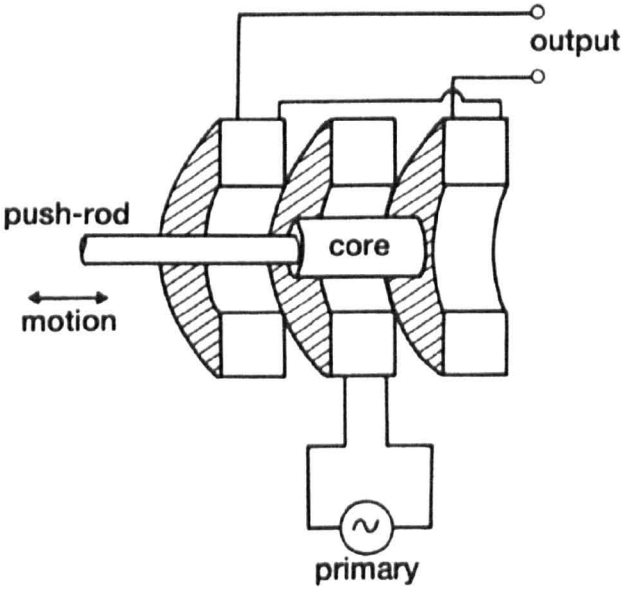

Figure 4.10 *A simple diagram of a linear variable differential transformer (LVDT).* [2]

4.8 Density and Molar volume

Density is one of the important properties of glass and glass-ceramics. The density is mostly dependent on the overall chemical composition and the volume and, the change in volume on going from glass to glass-ceramic is generally small so the densities of glass-ceramics are in a similar range to those of glasses or conventional ceramics. Moreover, the influence of various oxides on the densities of glass-ceramics would be analogous to those of conventional glasses. Archimedes' principle is used to determine the density (ρ), which can be expressed by the equation below.

$$\rho = \rho_L \frac{W_A}{W_A - W_L}, \qquad (4.16)$$

where W_A is the weight of the sample in air, W_L is the weight in the immersion fluid and ρ_L is the density of the immersion fluid. Then the molar volume can be calculated by

$$V_m = \frac{M}{\rho}, \qquad (4.17)$$

where M is the molecular weight calculated from the glass composition.

In this work, the densities of all glasses and selected glass-ceramics were measured using a digital density balance (Precisa 125A) as shown in figure 4.11.

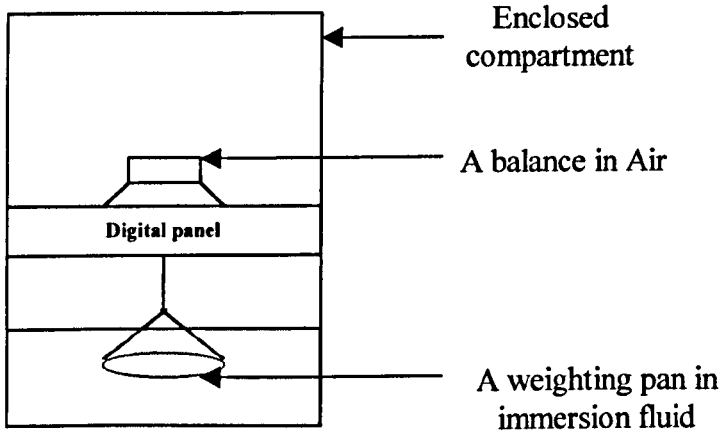

Figure 4.11 The simple diagram of a digital density balance (Precisa 125A).

The samples were first weighed in air and then were cleaned using acetone and distilled water. After that, they were placed in a weighing pan, which was suspended in immersion fluid (degassed distilled water). Finally, the density and molar volume of each sample were calculated using equations 4.16 and 4.17 respectively.

4.9 Dielectric measurement

The dielectric properties are of interest, especially in the field of ferroelectric materials. The simplest circuit for measuring the dielectric properties of any dielectric material is a parallel-plate capacitor with a dielectric material in an alternating field (e.m.f.). More details on the basic background in dielectrics are described in sections 2.13 and 2.14. From the equation 2.16:

$$\varepsilon_r^*(\omega) = \varepsilon_r'(\omega) - j\varepsilon_r''(\omega), \qquad (4.18)$$

the complex permittivity ε_r^* is an important parameter from which the dielectric loss is determined. Therefore, the most popular parameters for presenting dielectric properties of materials are ε_r' and ε_r''. Moreover, as those parameters are frequency and temperature dependent for dielectric and ferroelectric materials, the relationships between them are of interest.

For measuring the complex dielectric constant at low frequencies, an electrical bridge method is employed. This method is a common method, which is used to measure ε_r' and $\tan\delta$ or dissipation factor (D). For the various ranges of frequency such as ultra low frequency (from 0.01 Hz to 200 Hz) and audio-frequency (from 20 Hz to 3MHz), several bridges with different circuits are used.[11] The most common audio-frequency bridge is the Schering bridge[12] as shown in figure 4.12 because it can

accurately measure both the capacitance C and $\tan\delta$ at the same time and ε_r' and ε_r'' can be calculated by equation 4.18 and 4.19 respectively from these data.

$$\varepsilon_r' = C\frac{d}{\varepsilon_0 A} \tag{4.19}$$

where *d* is the thickness of the sample and *A* is the electrode area.

$$\varepsilon_r'' = \varepsilon_r' \tan\delta \tag{4.20}$$

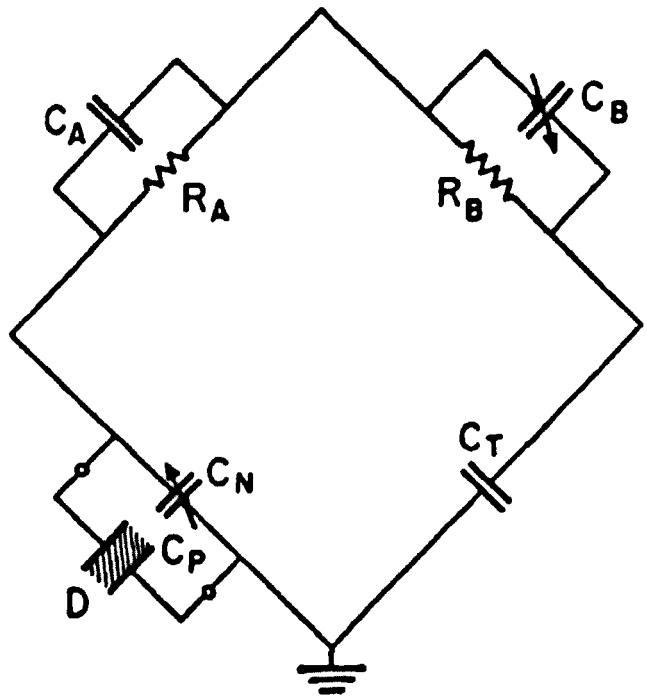

Figure 4.12 Schering bridge. [12]

From the above figure, the capacitance bridges used for dielectric measurements usually have equal ratio arms R_A and R_B. C_A is a fixed stray capacitor for a dissipation factor reading, C_B is a variable capacitor for balancing the bridge, C_N is a standard variable air capacitor and C_T is a balancing capacitor. The dielectric specimen of Cp and D value is connected in parallel with the standard capacitor to make the bridge balance. The Schering bridge is generally used in more than ten different models of the digital impedance analyser because it can be used to high frequency with

insignificant error and the resistive control can be calibrated directly in dissipation factor. [12]

In this experiment, the homemade high temperature rig was used to control the temperature of the sample between room temperature and ~500°C. An LCR meter (Hewlett-Packard 4192A LF Impedance Analyser) was also used for C and **tan**δ measurement over the frequency range from 5Hz to 13MHz. Figure 4.13 shows the simple diagram for the experimental set up.

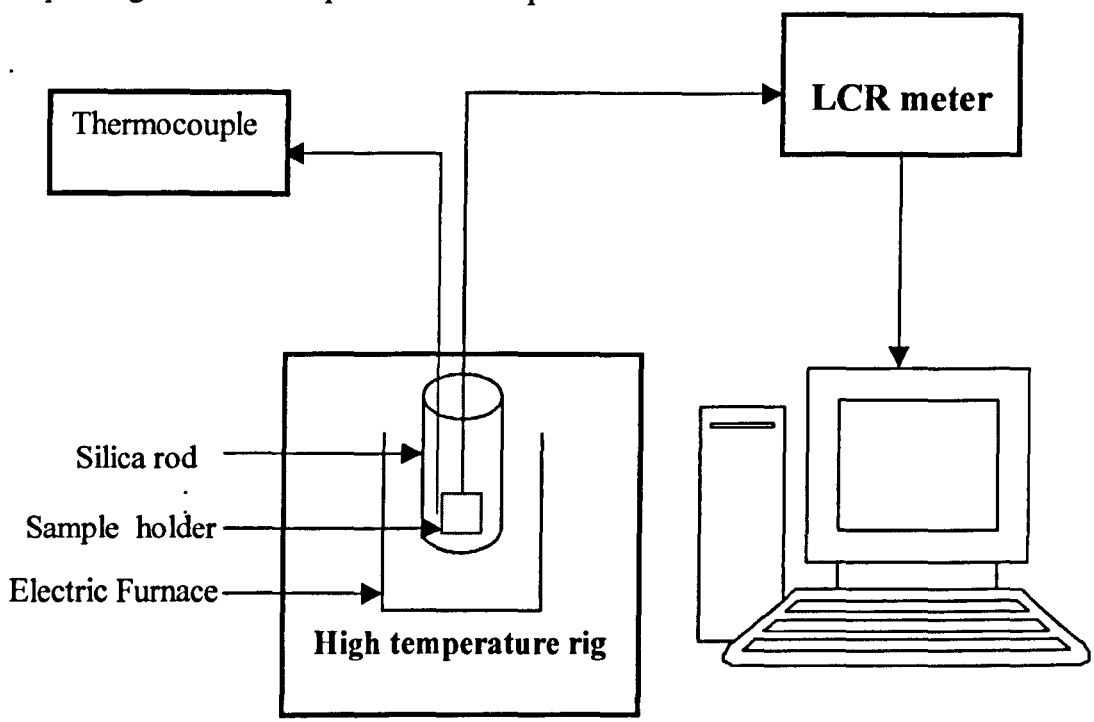

***Figure 4.13** The diagram for dielectric measurement.*

The selected glass-ceramic samples of various sizes were prepared. Both surfaces were polished using 1200 SiC paper. After that, the sample was sputter coated with platinum in order to make an electrode of 3 mm diameter for both sides. Then it was placed into the high temperature rig. At each constant temperature ranging from room temperature up to about 500°C (increment of 10°C), the measurement of C and D values was carried out over the frequency range from 5 Hz to 13 MHz using the LCR meter, which was connected to a computer in order to collect the data.

4.10 Ferroelectric hysteresis loop measurement

The conventional methods of recording the ferroelectric hysteresis loop are based on the work of Sawyer and Tower (1930).[13] Their circuit diagram is shown in figure 4.14.

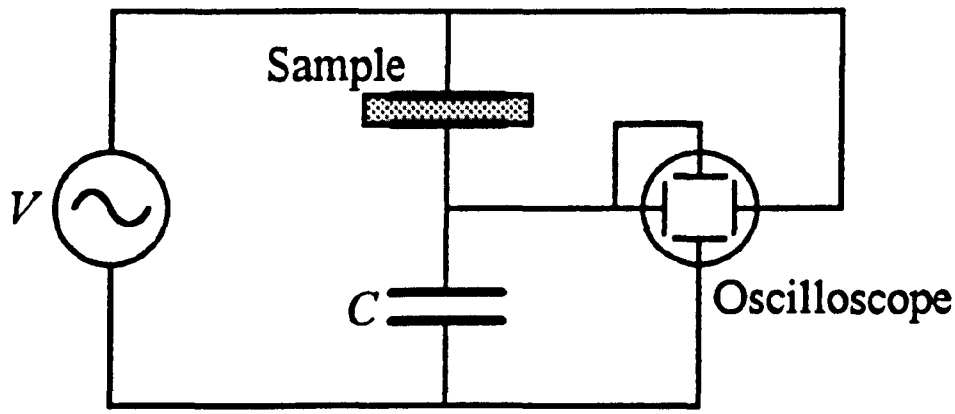

Figure 4.14 *Circuit for investigation of the hysteresis loop. (After Sawyer and Tower, 1930)*[13]

The sample is in the form of a parallel plate connected to the circuit with electrodes. Polarisation field loops are displayed on a cathode-ray oscilloscope. The horizontal plates measure the voltage across the crystal, which is proportional to the field. On the other hand, the vertical plates measure the voltage across a capacitor C in series with the crystal, which is proportional to the charge on the crystal and the displacement. [14] When using this circuit, however, it is usually assumed that the material has a low loss and high polarisation. Thus, a circuit which provides cancellation for resistive losses and stray capacitance is needed, especially with lossy samples. Figure 4.15 shows the basic compensation circuits added to remove effects caused by resistive losses in the sample and stray capacity across it. [15]

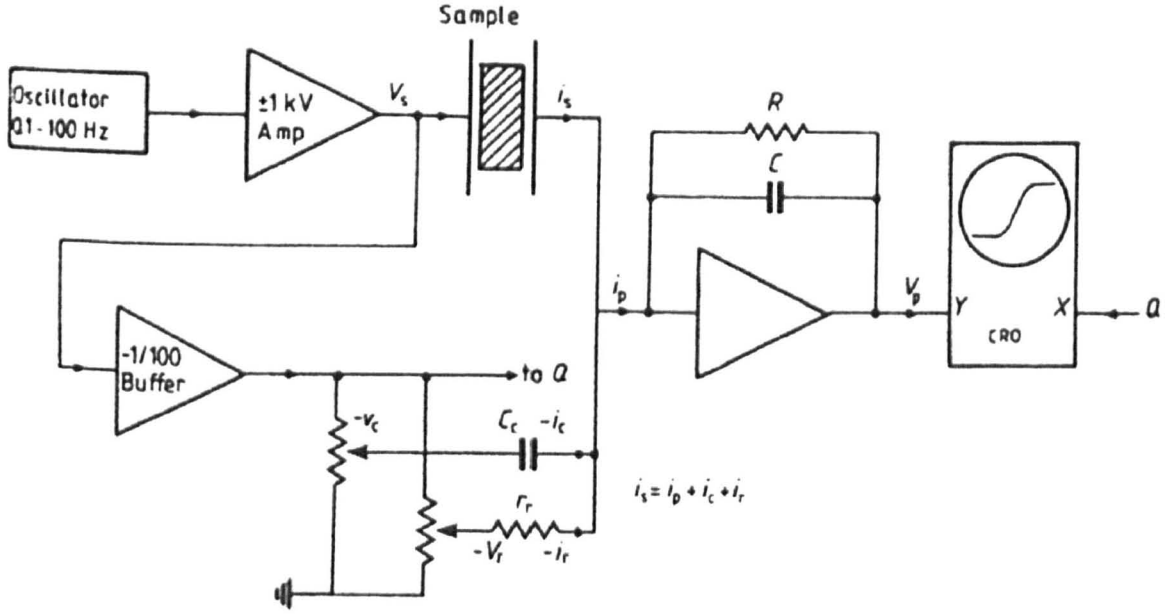

Figure 4.15 *Circuit with compensation added.*[15]

From the above diagram, the circuit description is summarised as follow. An oscillator generates the potential difference between the sample and the X input of the oscilloscope. The resulting polarisation (P) of the sample, giving rise to a charge Q which is fed to the amplifier, is obtained from P = Q/A (A = the electrode area of the sample). By assuming that the amplifier is ideal, with large inverting gain, the output from the operational amplifier then equals to V = -Q/C, which is proportional to the polarisation. Because the large gain of the amplifier makes its input a virtual earth, the field can be detected directly from the oscilloscope voltage. Moreover, the stray capacitance from input to ground can be negligible. The total current (i_S) of the sample is the sum of the current from polarisation (i_P), from stray capacitance across the sample (i_C) and from sample conduction (i_r) as shown in equation 4.21.

$$i_S = i_P + i_C + i_r \qquad (4.21)$$

However, the unwanted signal can be cancelled by feeding $-i_C$ and $-i_r$ into the amplifier giving a net input of i_P. These currents ($-i_C$ and i_r) are produced from the adjustable resistors $-v_c$ and $-V_r$ across C_C and r_r respectively as can be seen from figure 4.15.

In this experiment, the circuit used is based on the circuit diagram from figure 4.15. The samples were polished to 0.3 mm thickness and silver-paste electrodes of 2 mm diameter were applied on both sides of the samples. The samples were then placed into the high voltage protective instrument which connected to the circuit. The input voltages were in the range of 1-1.5 kV at 50-100 Hz. The data was collected via a computer program. Finally, the hysteresis loops were plotted.

References

1. Brown, M.E. *Introduction to Thermal Analysis: Techniques and Applications*, 1988 (Chapman and Hall).
2. McMillan, P.W. *Glass Ceramics*, 1979 (Academic Press).
3. Bruker AXS INC., *PDF Maint version 3.0*-Powder Diffraction Database,1997 (Bruker Analytical X-ray Systems).
4. Giacovazzo, C., Monaco, H. L., Viterbo, D., Scordari, F., Gilli G., Zanotti, G. and Catti M. *Fundamentals of Crystallography*, 1992 (Oxford Science Publications)
5. Suryanarayana, C. and Norton, M.G. *X-ray Diffraction- A Practical Approach*, 1998 (Plenum Press, New York and London).
6. Thornton, P.R. *Scanning Electron Microscopy*, 1968 (Chapman and Hall LTD).
7. Goodhew, P. J. and Humphreys F. J. *Electron Microscopy and Analysis*, 1988 (Taylor & Francis, London).
8. Lewis, M.H. and Hall, C.R. *Lecture in Electron Imaging and Analyis: MSc*, 1995 (Department of Physics, the University of Warwick).
9. Wunderlich, B. *Thermal Analysis*, 1990 (Academic Press, INC.)
10. Karim M.MA. *Ph. D thesis*, 1995 , Department of Physics, The University of Warwick.
11. Xu, Y. *Ferroelectric Materials and Their Applications*, 1991 (North-Holland)
12. Hippel, A.R.V. *Dielectric Materials and Applications*, 1954 (The M.I.T. Press)
13. Sawyer, C.B. and Tower, C.H. 1930, *Phys. Rev.*, volume 57, p. 54.
14. Helen, D.M. *Ferroelectricity in Crystals*, 1957 (Methuen & Co LTD)
15. Glazer, A.M., Groves, P. and Smith, D.T. 1984, *J. Physics E:Sci Instruments*, volume 17, pp. 95-97.

Chapter 5

The bismuth germanate system

5.1 Introduction

Over the past four decades, the bismuth germanate system has provided some most interesting materials, because a number of bismuth germanate crystals, such as $Bi_4(GeO_4)_3$ and $Bi_{12}GeO_{20}$, possess valuable properties. Single crystals of bismuth germanate $Bi_4(GeO_4)_3$, having an eulytine structure, were grown by Nitsche, in 1965.[1] He suggested that, even though its electro-optic coefficient (r_{41}= 1.03×10^{-10}cm/V) is not as high as that of other optical materials, one benefit for applications is that its large single crystals are easy to obtain by classical pulling techniques. Later, in 1967, another bismuth germanium oxide, $Bi_{12}GeO_{20}$, was grown as a large single crystal by the Czochralski technique. The crystal structure is cubic with space group I23 and has strongly piezoelectric properties with large electromechanical coupling constant and electro-optic effects.[2-3] For this particular phase $Bi_{12}GeO_{20}$, there has been some disagreement between two groups of researchers who have presented the phase diagram of the Bi_2O_3-GeO_2 system as shown in figure 5.1.[4-5] The Bi_2O_3-rich end of the Bi_2O_3-GeO_2 phase diagram is shown in figure 5.1(a), from Levin et al. [4] Figure 5.1(b) is the Bi_2O_3-GeO_2 full phase diagram according to Speranskaya and Arshakun [5]. It can be seen that the composition $6Bi_2O_3$:$1GeO_2$ from Levin's diagram, is formulated as $Bi_{14}GeO_{23}$ by Speranskaya and Arshakun. Abrahams et al [3] performed a complete structural determination and reported the crystal structure of piezoelectric bismuth germanate of composition $Bi_{12}GeO_{20}$, which is consistent with Levin's work[4].

In the Bi_2O_3-GeO_2 system, four phases with different stoichiometries of 6/1, 1/1, 2/3 and 1/3 have been reported. The phases 6/1 and 2/3, are thermodynamically stable as

can be seen from the phase diagrams (figure 5.1). However, in the field of ferroelectric glass-ceramics, the Bi_2GeO_5 phase (1/1), having a high probability of being ferroelectric, is of particular interest.[6-8] Its composition contains 50 mole % GeO_2 and, since this is a good glass forming oxide, there is no need to add any further glass former as in the case of other ferroelectric glass-ceramics. Moreover, as this phase is metastable, it is difficult to form pure Bi_2GeO_5 by conventional ceramic methods.

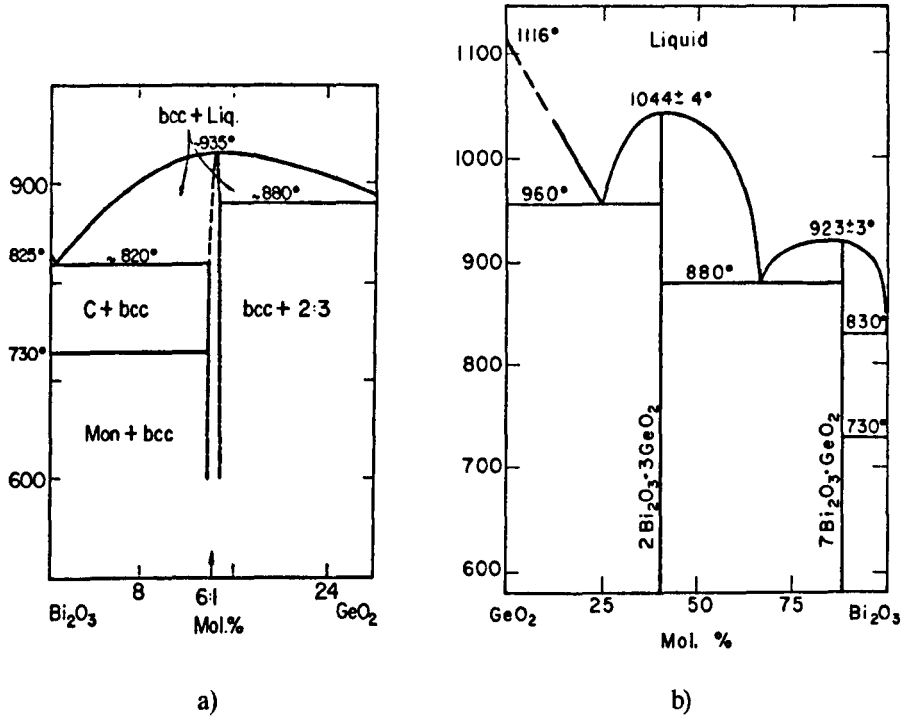

Figure 5.1 *Bi_2O_3-GeO_2 phase diagrams.*
a) by Levin and Roth [4] b) by Speranskaya and Arshakun. [5]
bcc = body centred cubic phase, C = cubic Bi_2O_3, Mon = monoclinic Bi_2O_3

This chapter concentrates on the preparation of glasses and glass ceramics in this system. Crystallisation information is obtained using differential thermal analysis (DTA) and x-ray powder diffraction (XRD). Scanning Electron Microscopy (SEM) has been used in phase identification and microstructure analysis. In addition, physical properties including density and thermal expansion of selected glasses are presented.

5.2 Glass preparation

The work has been aimed at maximising the amount of Bi_2GeO_5 in the finished glass-ceramics. Stoichiometric Bi_2GeO_5 glass was prepared using 66.67 mol % of bismuth oxynitrate ([I]$BiONO_3.H_2O$) and 33.33 mol % of Puratronic germanium oxide ([II]GeO_2). In addition, selected compositions of glasses from the system $BiO_{1.5}$-GeO_2-$BO_{1.5}$ were produced by melting appropriate combinations of bismuth oxynitrate ([I]$BiONO_3.H_2O$), puratonic germanium dioxide ([II]GeO_2), and boric oxide ([III]B_2O_3). Glasses from the system $BiO_{1.5}$-GeO_2-TeO_2 were also formed by the same method but using tellurium oxide ([IV]TeO_2) instead of boric oxide ([III]B_2O_3). Approximately 25 g of each composition were melted, in a 90Pt/10Rh crucible, in an air atmosphere, using an electric furnace. The melt temperature was between 1000 and 1050°C for samples from the $BiO_{1.5}$-GeO_2-$BO_{1.5}$ system, between 1050 and 1100°C for the $BiO_{1.5}$-GeO_2-TeO_2 system and 1050°C for the stoichiometric composition. The melts were held at those temperatures for homogenisation around 15 to 30 minutes. Then they were splat-quenched between liquid-nitrogen cooled copper plates or room temperature steel plates. In addition, ceramic pieces of 50 mol % Bi_2O_3 and 50 mol % GeO_2, with diameter of 10 mm and thickness of about 3mm, have b[II]een prepared by powder sintering at 710°C for 24 hours.

5.3 Bi_2O_3-GeO_2

Some devitrification, giving Bi_2GeO_5, $Bi_4(GeO_4)_3$ and β-Bi_2O_3 occurred in the stoichiometric composition, if $BiONO_3.H_2O$ was used. Interestingly, if Bi_2O_3 is used instead as the precursor, a devitrified solid consisting of $Bi_4(GeO_4)_3$ and $Bi_{12}GeO_{20}$ was

---

[I] $BiONO_3 \cdot H_2O$ – 98% Bismuth Subnitrate (Aldrich)
[II] GeO_2 – 99.999% Puratronic Germanium (IV) oxide (Alfa Aesar)
[III] B_2O_3 – 98% Boric Oxide (BDH Chemicals Ltd)
[IV] TeO_2 – 99+% Tellurium dioxide (Aldrich)

formed without any trace of Bi_2GeO_5. The comparison of the XRD patterns of the devitrified solids produced from different precursors is shown in figure 5.2. It may be said that the use of bismuth oxynitrate eases the formation of the Bi_2GeO_5 phase. As this experiment is aimed at preparing Bi_2GeO_5 glass-ceramics, the bismuth oxynitrate precursor was used thereafter. From the phase diagram in figure 5.1 (b), at 50 mol% of Bi_2O_3, if the melt is cooled slowly from the liquid state, the equilibrium solid produced should be a mixture of $Bi_4(GeO_4)_3$ and $Bi_{14}GeO_{23}$. However, from the XRD pattern of the devitrified solid, a noticeable amount of $B_{12}GeO_{20}$ phase was detected rather than the $Bi_{14}GeO_{23}$ phase. Therefore, it may be assumed that the correct stoichiometric ratio of this phase should be 6/1. Firsov et al [6] also reported that the solid, crystallised from a melt of Bi_2GeO_5 composition, contained the phases 2/3, 1/1 and 6/1.

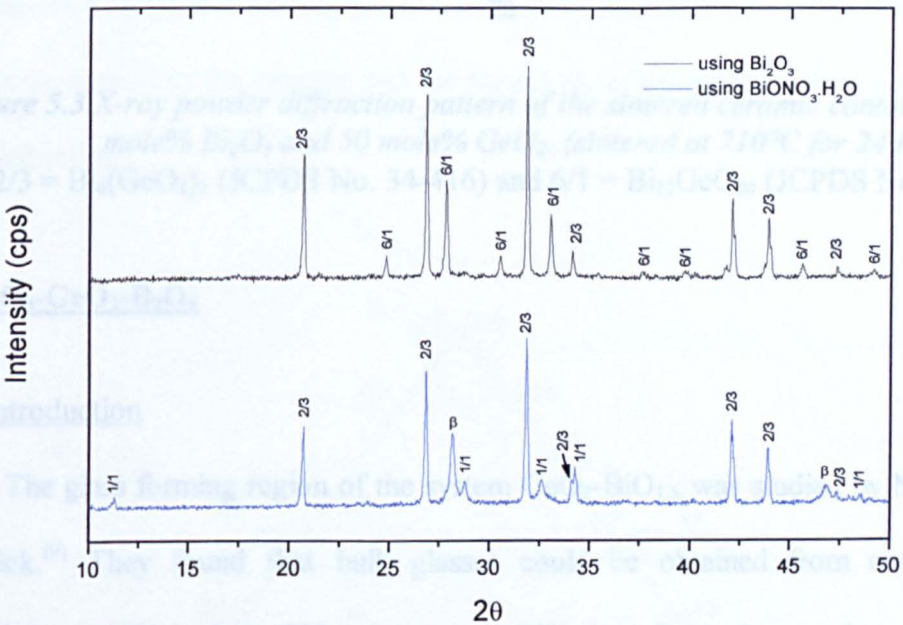

Figure 5.2 *The comparison of devitrified glasses produced from different initial substances.*

Note: 2/3 = $Bi_4(GeO_4)_3$ (JCPDS No. 34-416), 6/1 = $Bi_{12}GeO_{20}$ (JCPDS No. 34-36), 1/1 = Bi_2GeO_5 (JCPDS No. 39-3) and β = β-Bi_2O_3 (JCPDS No. 18-244)

The X-ray powder diffraction pattern of the sintered ceramic is shown in figure 5.3 and the sharp peaks have been indexed as two phases - $Bi_4(GeO_4)_3$ (2/3) and $Bi_{12}GeO_{20}$ (6/1) - with no trace of Bi_2GeO_5. Therefore, it can be assumed that the Bi_2GeO_5 cannot be formed easily by the conventional ceramic sintering method.

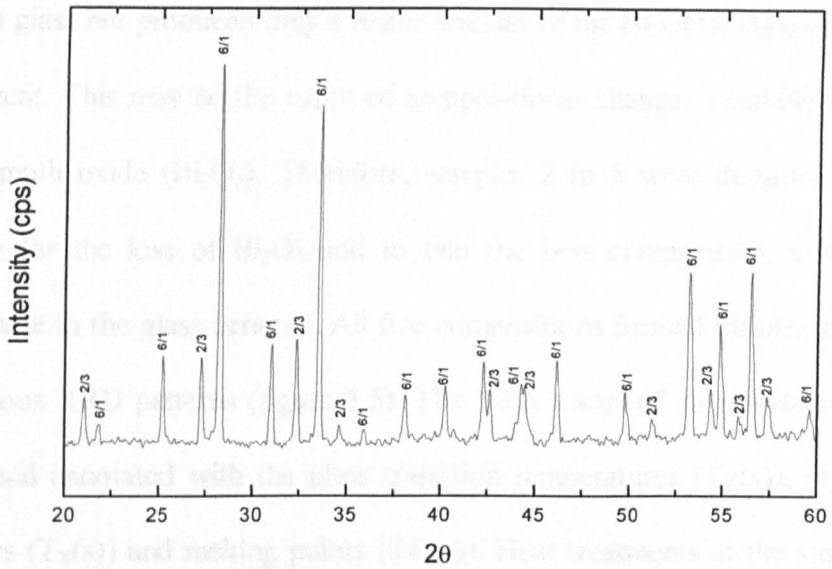

Figure 5.3 *X-ray powder diffraction pattern of the sintered ceramic containing 50 mole% Bi_2O_3 and 50 mole% GeO_2. (sintered at 710°C for 24 hours)*
Note: 2/3 = $Bi_4(GeO_4)_3$ (JCPDS No. 34-416) and 6/1 = $Bi_{12}GeO_{20}$ (JCPDS No. 34-36)

5.4 Bi_2O_3-GeO_2-B_2O_3

5.4.1 Introduction

The glass forming region of the system GeO_2-$BiO_{1.5}$ was studied by Nassau and Chadwick.[9] They found that bulk glasses could be obtained from compositions containing up to 50 mole % $BiO_{1.5}$ but it was difficult to form glasses where the $BiO_{1.5}$ content was between 60 and 70 mole %. As a result, new systems have been prepared containing an additional glass former ($BiO_{1.5}$-GeO_2-$BO_{1.5}$) and ($BiO_{1.5}$-GeO_2-TeO_2). Note that the phase diagram in figure 5.4 has been drawn with respect to $BiO_{1.5}$ and $BO_{1.5}$ to illustrate the effect of compositional change based on individual polyhedra.

B_2O_3 and TeO_2 do not increase the melting temperature of glass and are therefore preferable to the use of SiO_2. This is important in bismuth germanate systems because bismuth oxide is relatively volatile.

The seven compositions of the samples studied in the system $BiO_{1.5}$-GeO_2-$BO_{1.5}$ are presented in the ternary diagram in Figure 5.4 and Table 5.1. The $BiGeB_1$ sample was a good glass but produced only a minor amount of the Bi_2GeO_5 crystalline phase on heat treatment. This may be the result of compositional changes resulting from loss of volatile bismuth oxide (Bi_2O_3). Therefore, samples 2 to 5 were designed in order to compensate for the loss of Bi_2O_3 and to find the best composition, with maximum Bi_2GeO_5 phase in the glass-ceramic. All five compositions formed glasses, as shown by the amorphous XRD patterns (figure 5.5). The DTA traces of all glasses are shown in figure 5.6 and annotated with the glass transition temperatures (Tg(s)), crystallisation temperatures (T_X(s)) and melting points (Tm(s)). Heat treatments at the various values of T_X were applied to the samples and the crystal phase information was obtained using x-ray diffraction.

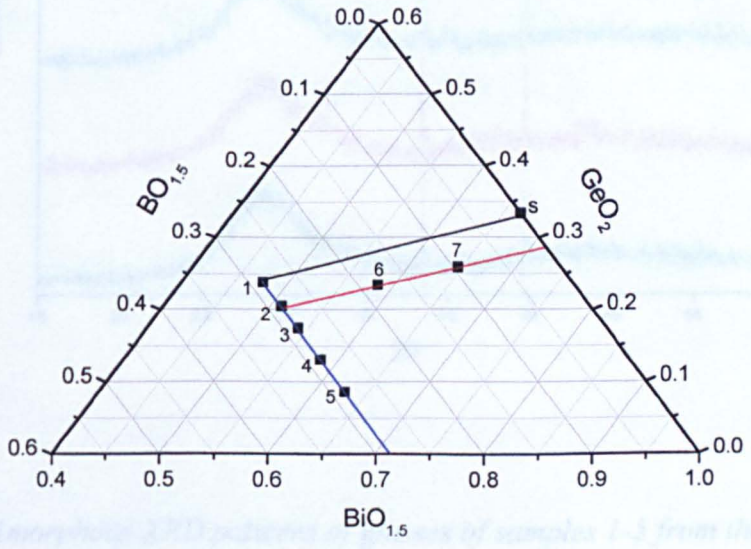

Figure 5.4 *The seven samples in the phase diagram of the $BiO_{1.5}$-GeO_2-$BO_{1.5}$ system.*

Table 5.1 *The nominal compositions prepared from the $BiO_{1.5}$-GeO_2-$BO_{1.5}$ system.*

Sample	$BiO_{1.5}$ (mol%)	GeO_2 (mol%)	$BO_{1.5}$ (mol%)
$BiGe_S$(S)	66.67	33.33	0
$BiGeB_1$(1)	47.62	23.80	28.58
$BiGeB_2$(2)	51.02	20.40	28.58
$BiGeB_3$(3)	54.09	17.33	28.58
$BiGeB_4$(4)	58.34	13.08	28.58
$BiGeB_5$(5)	62.85	8.57	28.58
$BiGeB_6$(6)	58.44	23.38	18.18
$BiGeB_7$(7)	64.62	25.86	9.52

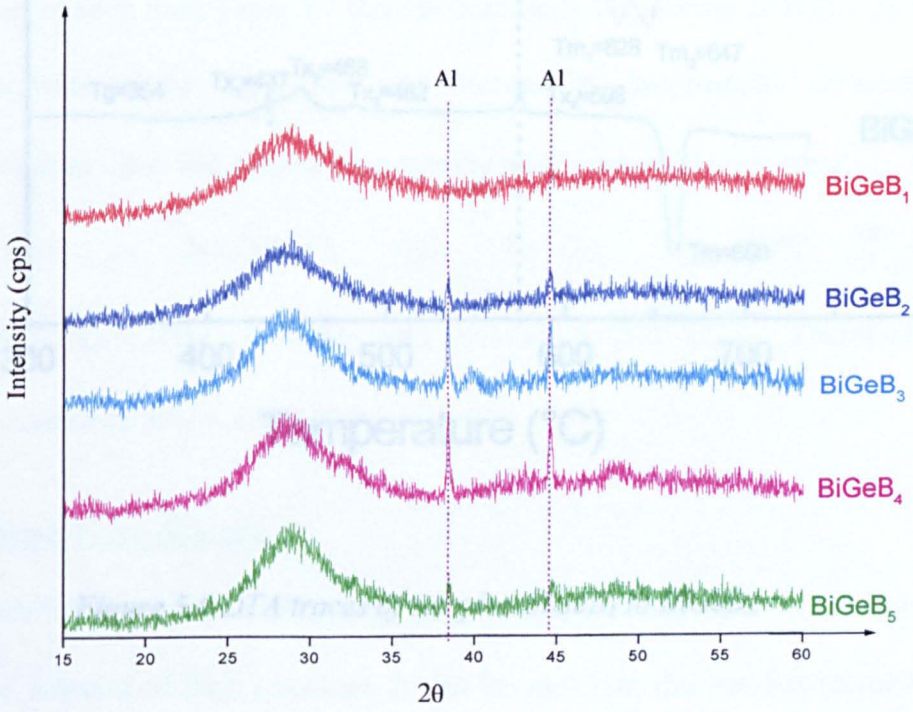

Figure 5.5 *Amorphous XRD patterns of glasses of samples 1-5 from the $BiO_{1.5}$-GeO_2-$BO_{1.5}$ system.*

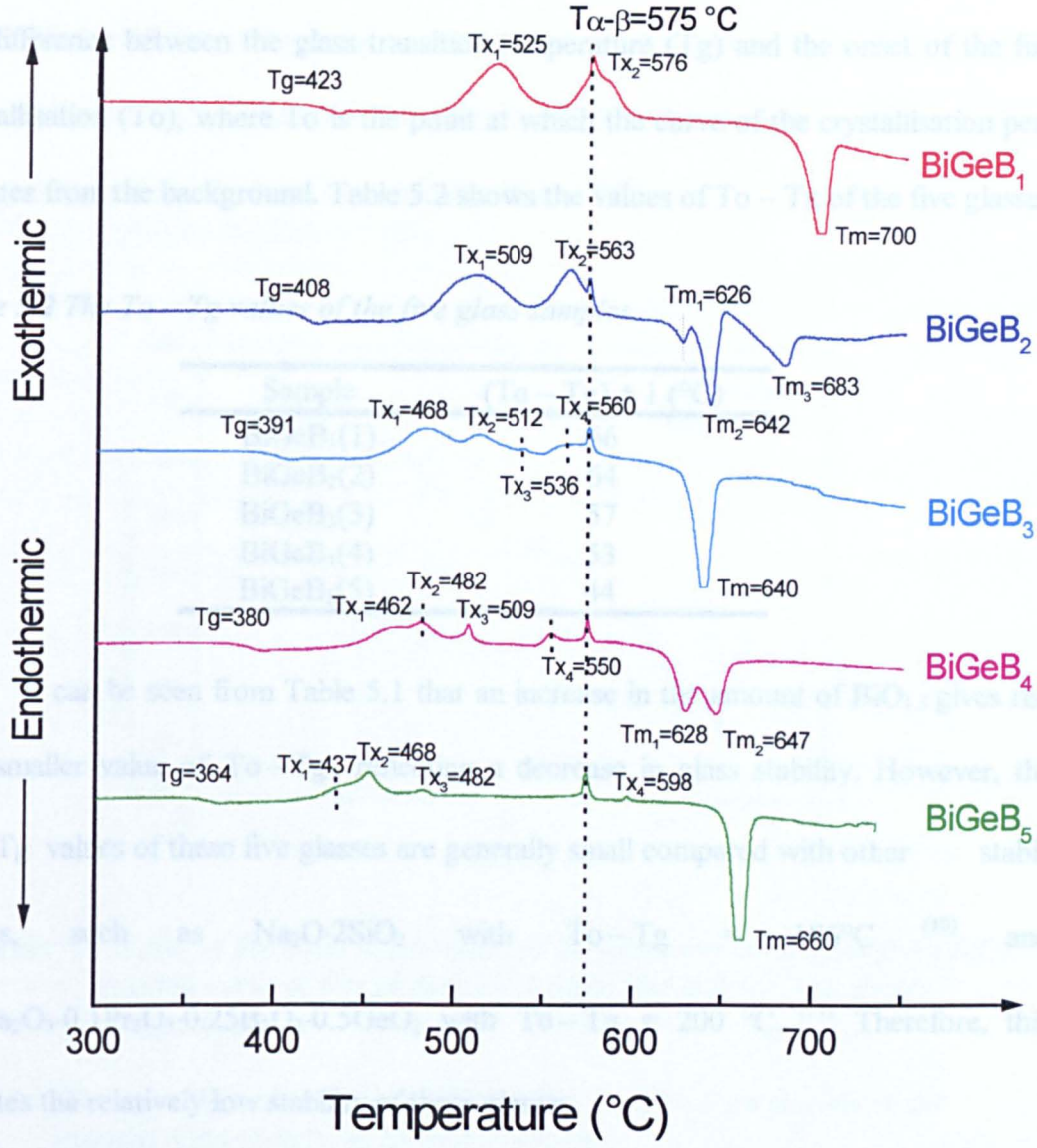

Figure 5.6 *DTA traces of samples $BiGeB_1$ to $BiGeB_5$.*

5.4.2 The stability of glasses

The XRD patterns of glasses (1)-(5) in figure 5.5 illustrate the random distribution patterns of amorphous materials. The stability of glasses can be expressed by the difference between the glass transition temperature (Tg) and the onset of the first crystallisation (To), where To is the point at which the curve of the crystallisation peak deviates from the background. Table 5.2 shows the values of To – Tx of the five glasses.

***Table 5.2** The To – Tg values of the five glass samples.*

Sample	(To – Tg) ± 1 (°C)
$BiGeB_1(1)$	66
$BiGeB_2(2)$	64
$BiGeB_3(3)$	57
$BiGeB_4(4)$	53
$BiGeB_5(5)$	44

It can be seen from Table 5.1 that an increase in the amount of $BiO_{1.5}$ gives rise to a smaller value of $To-Tg$, reflecting a decrease in glass stability. However, the $To-Tg$ values of these five glasses are generally small compared with other stable glasses, such as $Na_2O{\cdot}2SiO_2$ with $To-Tg$ = 186°C [10] and $0.15La_2O_3{\cdot}0.1Pr_2O_3{\cdot}0.25B_2O_3{\cdot}0.5GeO_2$ with $To-Tg$ = 200 °C. [11] Therefore, this indicates the relatively low stability of these glasses.

5.4.3 The simple phase diagram

Figure 5.7 shows a plot of liquidus temperature, obtained from the DTA cooling curves, as a function of $BiO_{1.5}$ content. It can be seen that the liquidus temperatures from the cooling curve are different from the melting points from the heating curve. This is because the melting points from the heating curve correspond to the melting point of the crystals which have previously been formed in glass on heating and the liquidus temperatures from cooling curve relate to the thermodynamic stable phase formed

during cooling from the glass melt. In this case, the crystals crystallised in the glass are not necessarily the same as the thermodynamic crystal phase resulting in the difference between the melting points from heating curve and liquidus temperature from cooling curve. Figure 5.7 cannot be compared with the phase diagrams in figure 5.1 since this is a ternary system ($BO_{1.5}$ added) and there is also likely to be some $BiO_{1.5}$ loss on melting. Such problems have also been reported elsewhere. [12,13]

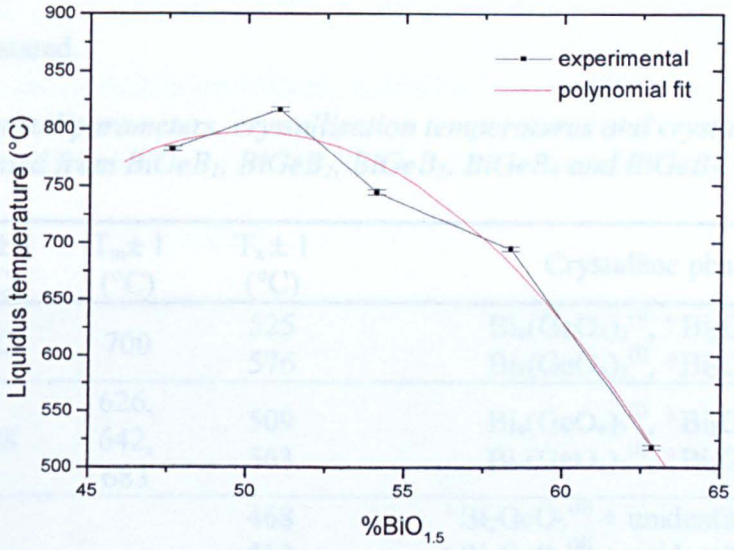

Figure 5.7 *A plot of the onset temperature of the first exothermic peak from DTA cooling curve of five glasses 1 – 5. (Red line is fitted by a simple polynomial)*

Table 5.3 *The crystalline phases formed by cooling the melt from just above the liquidus temperatures of samples (1) to (5)*

Sample	Mol% $BiO_{1.5}$	$T_L \pm 1$ (°C)	Crystalline phase
$BiGeB_1$	47.62	782	$Bi_4(GeO_4)_3$*
$BiGeB_2$	51.02	816	$Bi_4(GeO_4)_3$*
$BiGeB_3$	54.09	744	$Bi_4(GeO_4)_3$*, $Bi_4B_2O_9$**
$BiGeB_4$	58.34	695	$Bi_4(GeO_4)_3$*, $Bi_4B_2O_9$**
$BiGeB_5$	62.85	518	$Bi_4(GeO_4)_3$*, $Bi_4B_2O_9$**

* JCPDS No. 34-416, **JCPDS No. 25-1089

X-ray diffraction patterns of solids, produced by cooling from just above the liquidus temperature of these five glasses, give the phases as shown in Table 5.3. It can be seen that, in the $BiO_{1.5}$ content range from about 47 to 51 mol% the bismuth ions prefer to form the bismuth germanate phase until at about 51 mol% of $BiO_{1.5}$ excess Bi^{3+} joins isolated BO_3 groups and produces a $Bi_4B_2O_9$ phase as shown in Table 5.3.

5.4.4 Phase formation in glass-ceramics

Table 5.4 summarises the phases formed by devitrification of these glasses at the temperatures stated.

Table 5.4 *Thermal parameters, crystallisation temperatures and crystalline phases formed from $BiGeB_1$, $BiGeB_2$, $BiGeB_3$, $BiGeB_4$ and $BiGeB_5$.*

Sample	$T_g \pm 1$ (°C)	$T_m \pm 1$ (°C)	$T_x \pm 1$ (°C)	Crystalline phase
$BiGeB_1$	423	700	525	$Bi_4(GeO_4)_3^{(I)}$, $*Bi_2GeO_5^{(II)}$
			576	$Bi_4(GeO_4)_3^{(I)}$, $*Bi_2GeO_5^{(II)}$
$BiGeB_2$	408	626, 642, 683	509	$Bi_4(GeO_4)_3^{(I)}$, $*Bi_2GeO_5^{(II)}$
			563	$Bi_4(GeO_4)_3^{(I)}$, $*Bi_2GeO_5^{(II)}$
$BiGeB_3$	391	640	468	$*Bi_2GeO_5^{(II)}$ + unidentified phase
			512	$*Bi_2GeO_5^{(II)}$ + unidentified phase
			536	$*Bi_2GeO_5^{(II)}$ + unidentified phase
			560	$*Bi_2GeO_5^{(II)}$ + unidentified phase
$BiGeB_4$	378	625, 645	462	$*Bi_2GeO_5^{(II)}$, unidentified phase
			482	$*Bi_2GeO_5^{(II)}$, $BiBO_3^{(III)}$
			509	$*Bi_2GeO_5^{(II)}$, $BiBO_3^{(III)}$
			552	$*Bi_2GeO_5^{(II)}$, $BiBO_3^{(III)}$
$BiGeB_5$	364	660	437	$*Bi_2GeO_5^{(II)}$, $Bi_4B_2O_{9(IV)}$, Bi_2O_3-$Bi_{24}GeO_{38}^{(V)}$
			468	$*Bi_2GeO_5^{(II)}$, $Bi_4B_2O_9^{(IV)}$
			482	$*Bi_2GeO_5^{(II)}$, $Bi_4B_2O_9^{(IV)}$
			598	$*Bi_2GeO_5^{(II)}$, $Bi_4B_2O_9^{(IV)}$

(I), (II), (III), (IV) and (V) refer to JCPDS No 34-416, 36-289, 27-320, 25-1089 and 42-190 respectively.

*Some unidentified peaks at high angle were observed in every XRD pattern containing Bi_2GeO_5. Therefore, it may be assumed that the JCPDS pattern is incomplete or the phase here is a new polymorph of Bi_2GeO_5.

It can be seen that the Bi_2GeO_5 phase predominantly crystallises from $BiO_{1.5}$-GeO_2-$BO_{1.5}$ glasses in a wide composition range. SEM analysis was used to observe the unidentified phase in the $BiGeB_3$ sample. Figure 5.8 illustrates the cross-section backscattering image of $BiGeB_3$ heat treated at 468°C. The spherulites of Bi_2GeO_5 phase can be observed but the expected unidentified phase, separated by different contrast in the backscattering image, cannot be detected. The other glass-ceramics heat treated at other crystallisation temperatures give similar XRD patterns containing Bi_2GeO_5 phase plus unidentified phase. After all the heat treatments, these glass-ceramics were easily broken into pieces, indicating low strength. This may be caused by the high porosity near the surface of the glass-ceramics as can be seen in the backscattering image (Figure 5.8).

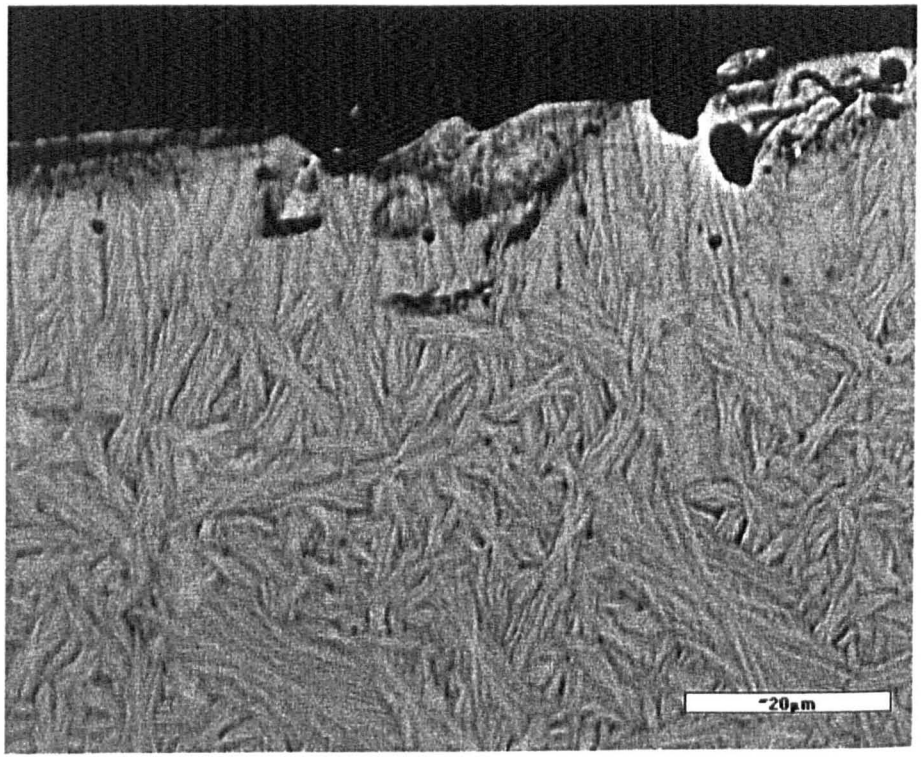

Figure 5.8 *SEM backscattering image of $BiGeB_3$ cross-sectional glass-ceramic heat treated at 468°C for four hours.*

5.4.5 Metastable phase formation

Figure 5.9 shows the DTA trace of $BiGeB_4$ glass powder. There are one broad and three sharp exothermic peaks at T_{X1}, T_{X2}, T_{X3} and T_{X4} which relate to the formation of different crystal phases. However, as seen in figure 5.10, the XRD patterns of those glass-ceramics produced at T_{X2}, T_{X3}, and T_{X4} are identical, containing Bi_2GeO_5 (plus attendant unidentified peaks at high angle) and $BiBO_3$. The phases formed at T_{X1} are Bi_2GeO_5 (plus attendant unidentified peaks at high angle) and some additional unidentified phases. The trace obtained by cooling from above the liquidus also indicates the existence of two thermodynamically stable phases at low temperature which are $Bi_4(GeO_4)_3$ and $Bi_4B_2O_9$ as discussed in section 5.4.3. This suggests that the broad peak at T_{X1} is due to devitrification of the glass giving Bi_2GeO_5 and an unknown phase.

Samples heat treated at T_{X2} produce Bi_2GeO_5 and $BiBO_3$. The unidentified phase in T_{X1} may be an unidentified bismuth oxide phase which, when the glass was heated to T_{X2}, reacted with B_2O_3 to produce $BiBO_3$. Alternatively, the unidentified phase at T_{X1} might be a bismuth germanate phase which decomposes by reaction with B_2O_3 producing $BiBO_3$ at T_{X2}. As the XRD patterns of T_{X2}, T_{X3} and T_{X4} are identical, it may be assumed that, at T_{X3} and T_{X4}, phases are produced which revert to $BiBO_3$ on cooling. High temperature XRD is needed to characterise these two metastable phases. A similar problem of metastable phase formation is seen in sample $BiGeB_5$ but with a different stable phase ($Bi_4B_2O_9$) as shown in Table 5.4.

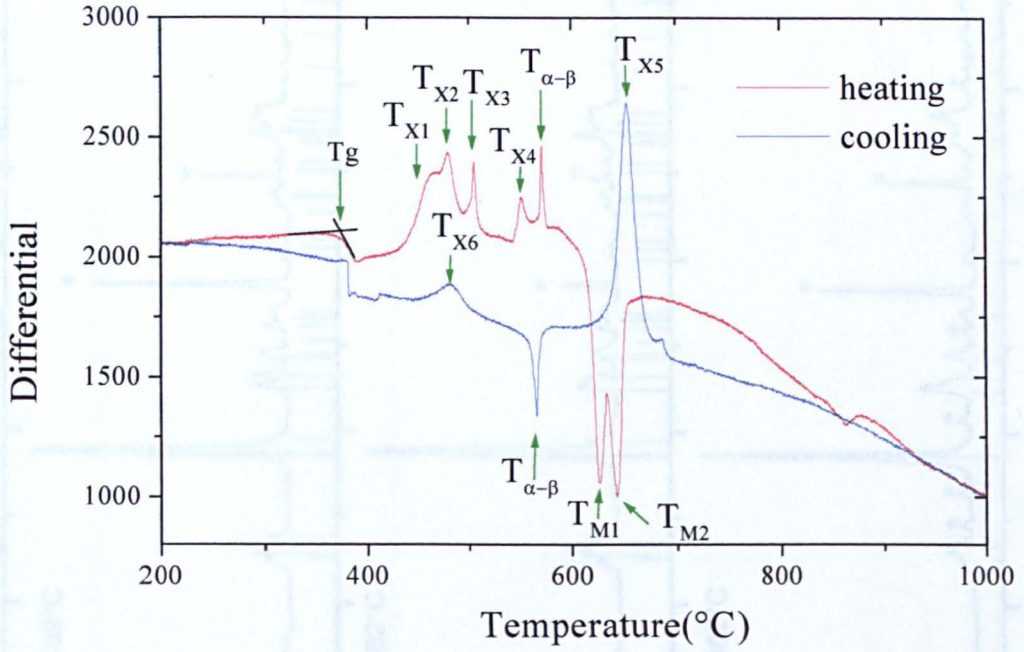

$T_g \pm 1$	$T_{X1} \pm 1$	$T_{X2} \pm 1$	$T_{X3} \pm 1$	$T_{X4} \pm 1$	$T_{X5} \pm 1$	$T_{X6} \pm 1$	$T_{M1} \pm 1$	$T_{M2} \pm 1$
380°C	462°C	482°C	509°C	552°C	655°C	485°C	628°C	647°C

Figure 5.9 *The DTA trace of $BiGeB_4$ sample shows the metastable sharp peaks (T_{X2} - T_{X4}).*

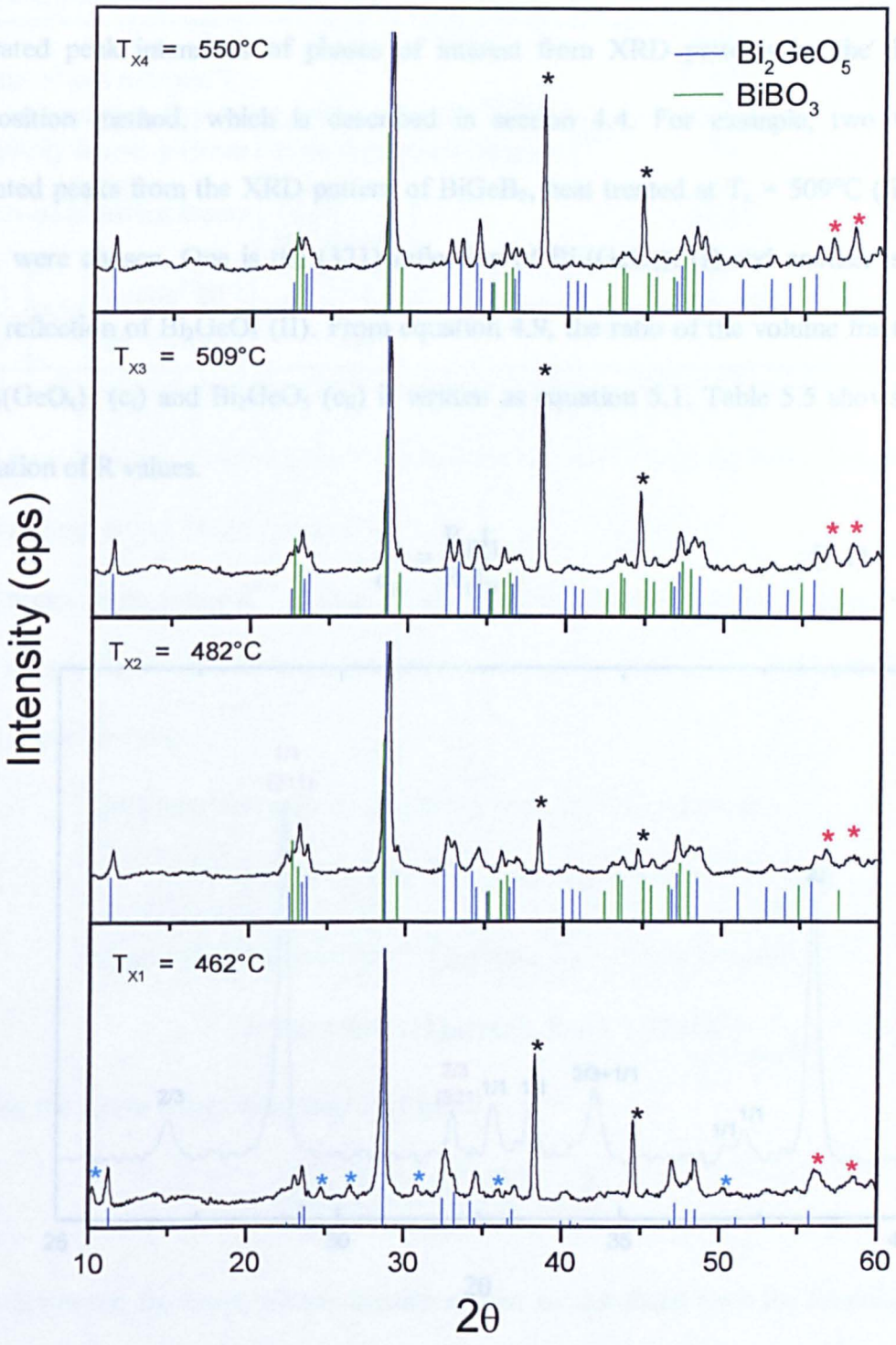

Figure 5.10 *The XRD patterns of $BiGeB_4$ sample heated at four different temperatures: T_{X1}, T_{X2}, T_{X3} and T_{X4}.*

*Note: * = Al, * = unidentified phase, * = unidentified peaks related to Bi_2GeO_5, Bi_2GeO_5 - JCPDS No. 36-289 and $BiBO_3$ - JCPDS No. 27-320*

5.4.6 The calculation of volume fraction ratios

The relative proportions of each phase can be calculated using selected integrated peak intensities of phases of interest from XRD patterns by the direct composition method, which is described in section 4.4. For example, two well-separated peaks from the XRD pattern of $BiGeB_2$, heat treated at T_x = 509°C (figure 5.11), were chosen. One is the (321) reflection of $Bi_4(GeO_4)_3$ (I) and another is the (311) reflection of Bi_2GeO_5 (II). From equation 4.9, the ratio of the volume fractions of $Bi_4(GeO_4)_3$ (c_I) and Bi_2GeO_5 (c_{II}) is written as equation 5.1. Table 5.5 shows the calculation of R values.

$$\frac{c_I}{c_{II}} = \frac{R_{II} I_I}{R_I I_{II}} \qquad (5.1)$$

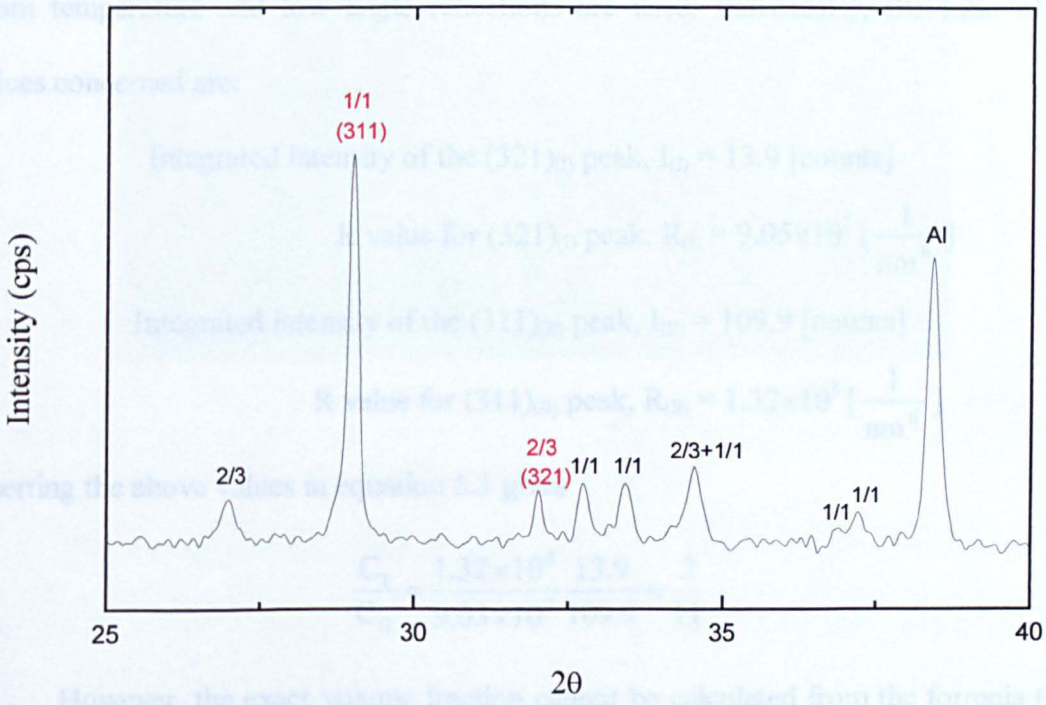

Figure 5.11 *XRD pattern of $BiGeB_2$. (Tx = 509°C)*
Note: 2/3 = (I) $Bi_4(GeO_4)_3$ (JCPDS No. 34-416), 1/1 = (II) Bi_2GeO_5 (JCPDS No. 36-89) and Al = aluminium holder (JCPDS No. 4-787)

Table 5.5 Calculation of R values of $Bi_4(GeO_4)_3$ (R_I) and Bi_2GeO_5 (R_{II}).

Phase and Reflection	I (321)	II (311)
2θ (°)	31.80	28.77
Volume of unit cell (nm^3), v	1.16382	0.46511
F^2 (calculated from Crystallographica program *)[14]	214160	241060
Multiplicity factor, p (from Crystallographica program)[14]	24	4
Lorentz-polarisation factor $\left[\frac{1+\cos^2 2\theta}{\sin^2\theta\cos\theta}\right]$	23.85	29.57
$R = \frac{1}{v^2}\left[F^2 p\left[\frac{1+\cos^2 2\theta}{\sin^2\theta\cos\theta}\right]\right]e^{-2M}\ [\frac{1}{nm^6}]$**	9.05×10^7	1.32×10^8

* The atomic positions (x,y,z) of each atom in each phase, used for F^2 calculation, were found from Inorganic Crystal Structure Database (ICSD)[15] with the collection codes: 39227 (phase I) and 49685 (phase II).

** The temperature factor e^{-2M} is ignored because the diffraction pattern is recorded at room temperature and low-angle reflections are used. Particularly, the ratio of R values concerned are:

Integrated intensity of the $(321)_{(I)}$ peak, $I_{(I)} = 13.9$ [counts]

R value for $(321)_{(I)}$ peak, $R_{(I)} = 9.05\times10^7\ [\frac{1}{nm^6}]$

Integrated intensity of the $(311)_{(II)}$ peak, $I_{(II)} = 109.9$ [counts]

R value for $(311)_{(II)}$ peak, $R_{(II)} = 1.32\times10^8\ [\frac{1}{nm^6}]$

Inserting the above values in equation 5.1 gives

$$\frac{C_I}{C_{II}} = \frac{1.32\times10^8}{9.05\times10^7}\frac{13.9}{109.9} \approx \frac{2}{11}$$

However, the exact volume fraction cannot be calculated from the formula ($C_I + C_{II} = 1$) because the glass-ceramic does not contain only two phases ($Bi_4(GeO_4)_3$ and Bi_2GeO_5) but also borogermanate or borate residual glass. Figure 5.12 shows the SEM picture of a cross-section of the $BiGeB_2$ glass-ceramic heat treated at 509°C for four hours.

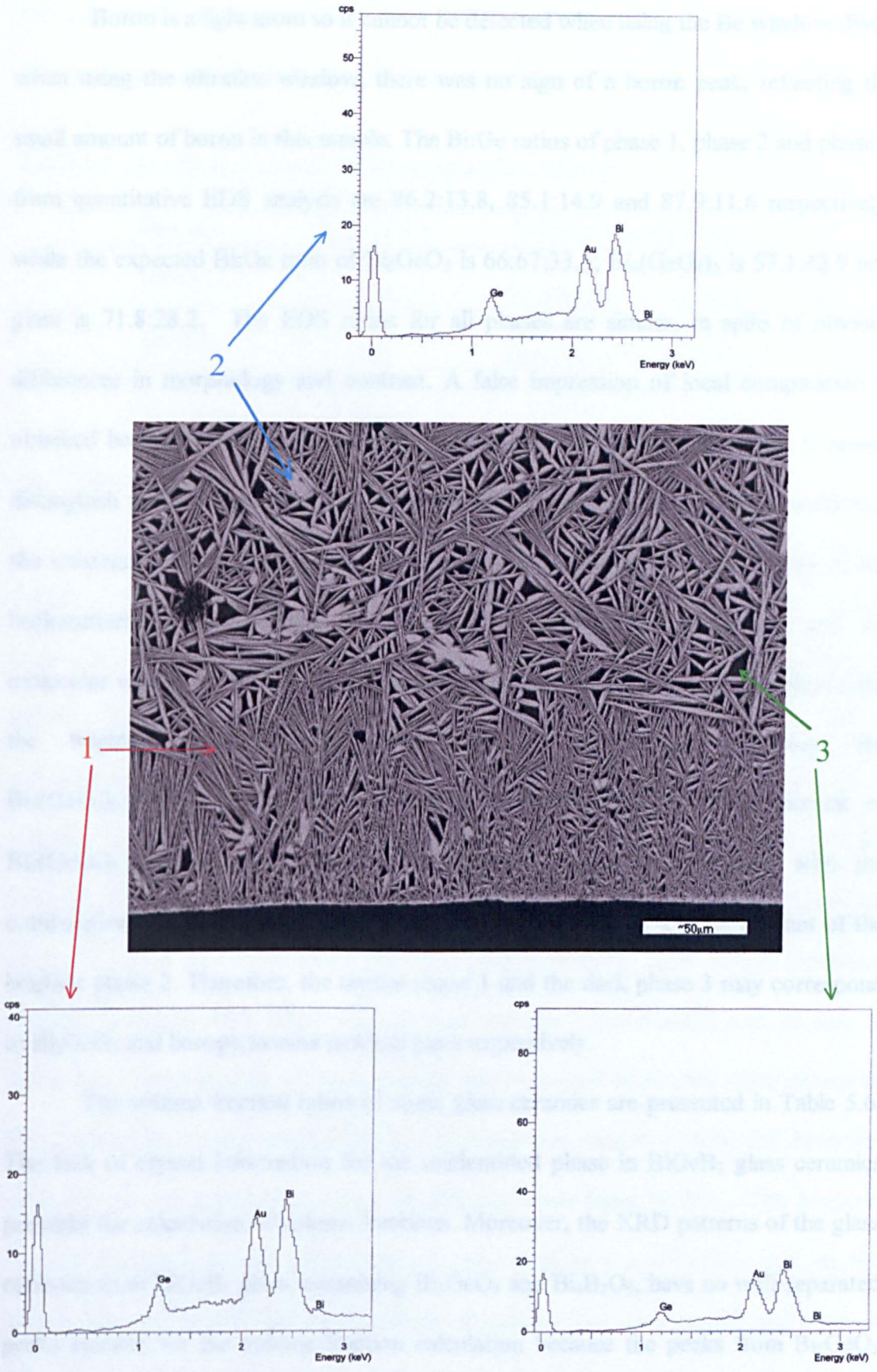

Figure 5.12 *SEM backscattering image and EDS spectra of each phase in $BiGeB_2$ cross-sectional glass-ceramic heat treated at 509°C for four hours.*

Boron is a light atom so it cannot be detected when using the Be window. Even when using the ultrafine window, there was no sign of a boron peak, reflecting the small amount of boron in this sample. The Bi:Ge ratios of phase 1, phase 2 and phase 3 from quantitative EDS analysis are 86.2:13.8, 85.1:14.9 and 87.9:11.6 respectively, while the expected Bi:Ge ratio of Bi_2GeO_5 is 66.67:33.3; $Bi_4(GeO_4)_3$ is 57.1:42.9 and glass is 71.8:28.2. The EDS ratios for all phases are similar, in spite of obvious differences in morphology and contrast. A false impression of local composition is obtained because of the large excitation volume of EDS analysis, therefore, it cannot distinguish phase 1 from phase 2. However, the X-ray diffraction analysis confirmed the existence of Bi_2GeO_5 and Bi_4GeO_3 phases. Knowing that the brightness of the backscattering image depends on the electron density of a compound, and the molecular weight of $Bi_4(GeO_4)_3$ is larger than that of Bi_2GeO_5, it may be inferred that the brighter phase 2 may correspond to $Bi_4(GeO_4)_3$. Moreover, the $Bi_4(GeO_4)_3$:Bi_2GeO_5 ratio, equal to 2:11, shows that only a small amount of $Bi_4(GeO_4)_3$ crystals are present in the sample, which is consistent with the compositional image or backscattering image which show only a small amount of the brighter phase 2. Therefore, the crystal phase 1 and the dark phase 3 may correspond to Bi_2GeO_5 and borogermanate residual glass respectively.

The volume fraction ratios of some glass ceramics are presented in Table 5.6. The lack of crystal information for the unidentified phase in $BiGeB_3$ glass ceramics prevents the calculation of volume fractions. Moreover, the XRD patterns of the glass ceramics from $BiGeB_5$ glass, containing Bi_2GeO_5 and $Bi_4B_2O_9$, have no well-separated peaks suitable for the volume fraction calculation because the peaks from Bi_2GeO_5 largely superimpose on the peaks of $Bi_4B_2O_9$. Furthermore, the ratios of

$BiBO_3$:Bi_2GeO_5 of glass-ceramics from $BiGeB_4$ sample at T_{X2}, T_{X3}, T_{X4}, cannot be calculated because there is no crystal information from JCPDS file (No. 27-320)[16].

***Table 5.6** The volume fraction ratios of some glass ceramics.*

Sample	$T_X \pm 1$ (°C)	Volume fraction ratio ± 0.05
$BiGeB_1$	525	$Bi_4(GeO_4)_3^{(I)}$: $*Bi_2GeO_5^{(II)}$ = 3:4
	576	$Bi_4(GeO_4)_3^{(I)}$: $*Bi_2GeO_5^{(II)}$ = 9:2
$BiGeB_2$	509	$Bi_4(GeO_4)_3^{(I)}$: $*Bi_2GeO_5^{(II)}$ = 2:11
	563	$Bi_4(GeO_4)_3^{(I)}$: $*Bi_2GeO_5^{(II)}$ = 7:2

Note: (I), (II) refer to JCPDS No 34-416 and 36-289 respectively.

5.4.7 Glass density

The densities of the $BiGeB_1$-$BiGeB_5$ glasses are presented in Table 5.7 and the variation of density with mol% $BiO_{1.5}$ is illustrated in figure 5.13. The molar volume cannot be calculated because accurate composition data is needed. The densities of $BiGeB_2$, $BiGeB_6$, (the optimum composition described in the next section), $BiGeB_7$ and additional glasses are shown in Table 5.8 and plotted as a function of mol% $BO_{1.5}$ – figure 5.14. As would be expected, density increases with increasing $BiO_{1.5}$ content because of the substitution of heavy Bi^{3+} for the light Ge and decreases with addition of $BO_{1.5}$ which introduces extra network units comprising light atoms. However, increase in density with $BiO_{1.5}$ content goes through a maximum as can be seen in figure 5.13. Consideration of the crystalline phases formed by heating these glasses to the crystallisation temperature (Table 5.4) shows that sample $BiGeB_4$ (58.34 mol% $BiO_{1.5}$) is the first sample to produce the bismuth borate phase ($BiBO_3$). This suggests that, at this point, the excess bismuth ion now acts as a modifier ion and, as the bismuth ions are larger than the interstices of isolated BO_3, they modify and increase the size of the interstices giving a decrease in glass density as shown in figure 5.13. From figure 5.14, it can be seen that the relationship between the mol% of $BO_{1.5}$ and

density of glasses is linear. This is similar to the binary systems, B_2O_3-GeO_2, where the density varies almost linearly with composition.[17]

***Table 5.7** The density of $BiGeB_1$-$BiGeB_5$ glasses*

Samples	Mol% $BiO_{1.5}$	Density (ρ) g/cm^3	Density error
$BiGeB_1$	47.62	7.172	± 0.060
$BiGeB_2$	51.02	7.607	± 0.074
$BiGeB_3$	54.09	8.025	± 0.046
$BiGeB_4$	58.34	8.295	± 0.094
$BiGeB_5$	62.85	8.177	± 0.102

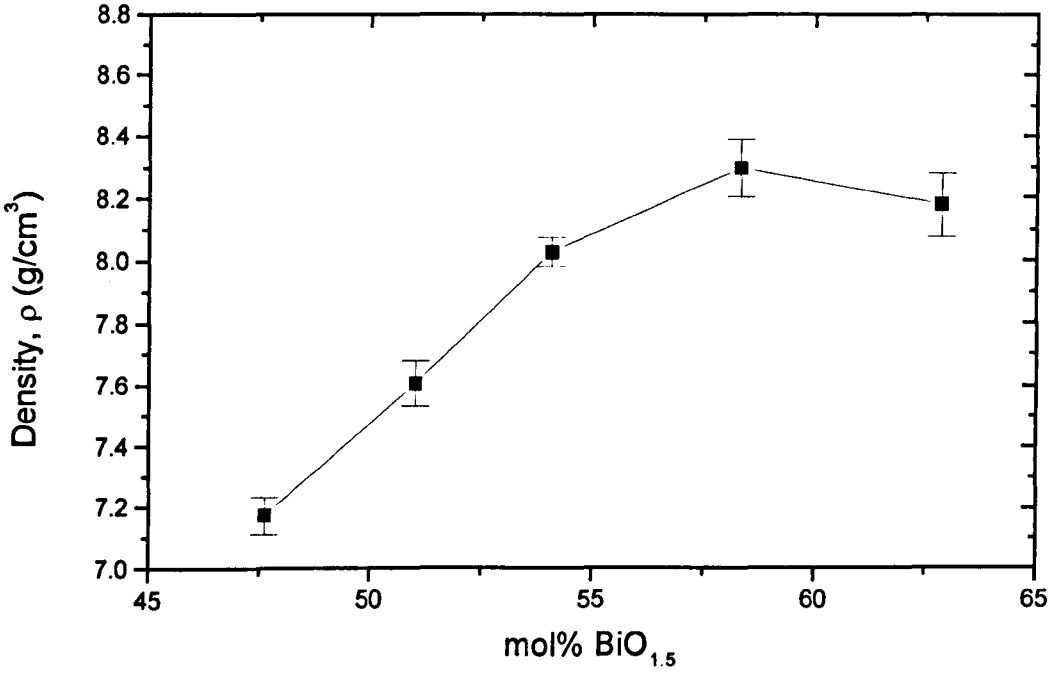

***Figure 5.13** Density of $BiGeB_1$-$BiGeB_5$ samples (constant amount of 28.58 mol% $BO_{1.5}$) as a function of $BiO_{1.5}$ content.*

Table 5.8 *The density of other $BiO_{1.5}$-GeO_2-$BO_{1.5}$ glasses*

Samples	Mol% $BO_{1.5}$	Density (ρ) g/cm^3	Density error
$BiGeB_7$	9.52	8.722	± 0.243
$BiGeB_6$	18.18	7.834	± 0.099
$BiGeB_2$	28.58	7.607	± 0.174
20%B_2O_3	33.33	7.316	± 0.149
25%B_2O_3	40	7.022	± 0.069
50%B_2O_3	66.67	5.083	± 0.07

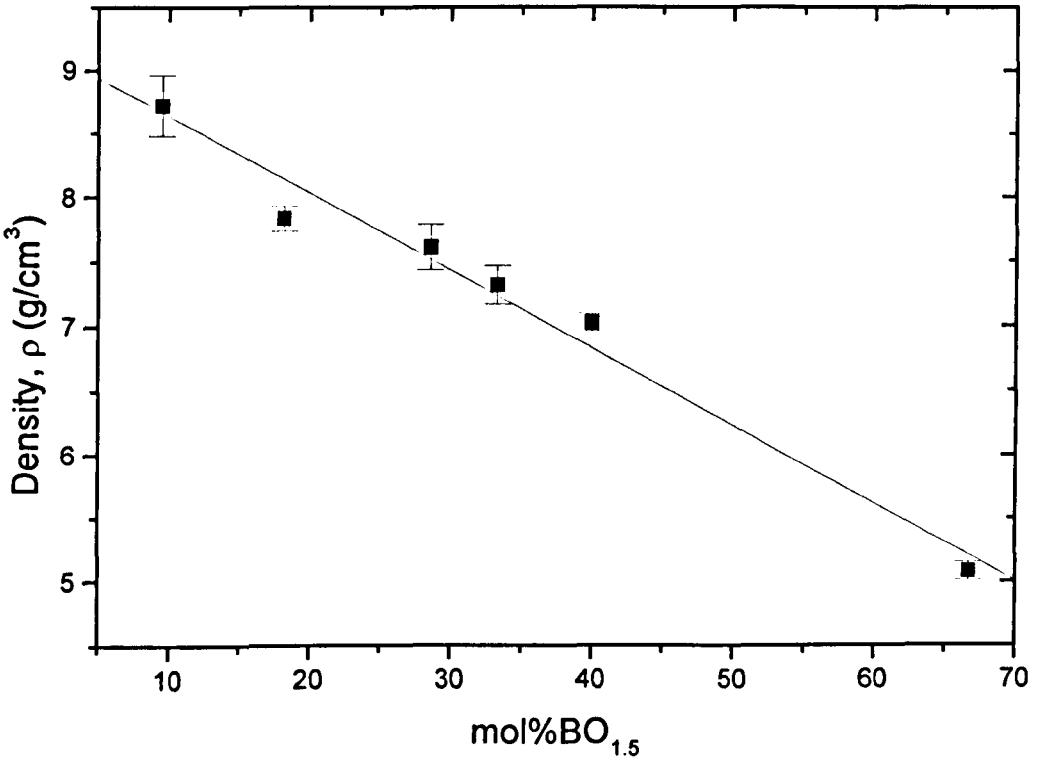

Figure 5.14 *Density of $BiGeB_2$, $BiGeB_6$, $BiGeB_7$ and additional glasses as a function of $BO_{1.5}$ content.*

5.4.8 Optimisation of composition

Samples $BiGeB_6$ and $BiGeB_7$, as shown in figure 5.4, were also investigated to optimise composition. The ratio $BiO_{1.5}$:GeO_2 was kept equal to that of sample $BiGeB_2$ because, among the five glasses (1-5), this composition contained the largest amount of Bi_2GeO_5. Moreover, this glass-ceramic contains two identifiable bismuth germanate phases while the glass-ceramics from sample $BiGeB_3$ to $BiGeB_5$ contain unidentified phases. The $BO_{1.5}$ content was reduced to 18.8 mol % in sample $BiGeB_6$ and 9.52 mol% in sample $BiGeB_7$. The XRD patterns of the melt-quenched $BiGeB_6$ and $BiGeB_7$ are presented in figure 5.15.

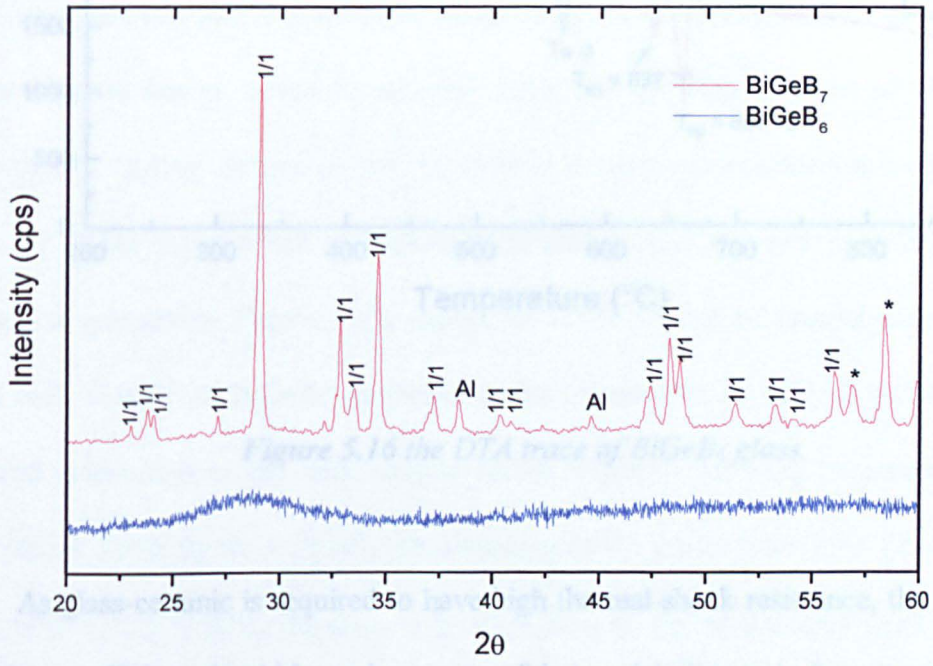

Figure 5.15 *XRD patterns of melted glasses of sample $BiGeB_6$ and $BiGeB_7$. Note: 1:1 = Bi_2GeO_5 (JCPDS No. 36-289) and * = unidentified peaks at high angle*

From figure 5.15, it can be seen that $BiGeB_7$ devitrified while cooling, giving rise to Bi_2GeO_5 crystals, but $BiGeB_6$ is a good glass as confirmed by the amorphous XRD pattern. The devitrified $BiGeB_7$ sample disintegrated into pieces while cooling.

The DTA trace of $BiGeB_6$ glass is illustrated in figure 5.16. The value of To-Tg equals 54 °C which is similar to that of $BiGeB_4$ (53 °C) from Table 5.1. Since the amount of $BO_{1.5}$ in $BiGeB_6$ sample was reduced to 18.18% and the ratio $BiO_{1.5}$:GeO_2 was the same as that of $BiGeB_2$, it may be assumed that reducing the amount of $BO_{1.5}$ lowers the glass stability resulting in devitrification at 9. 52 mol% $BO_{1.5}$.

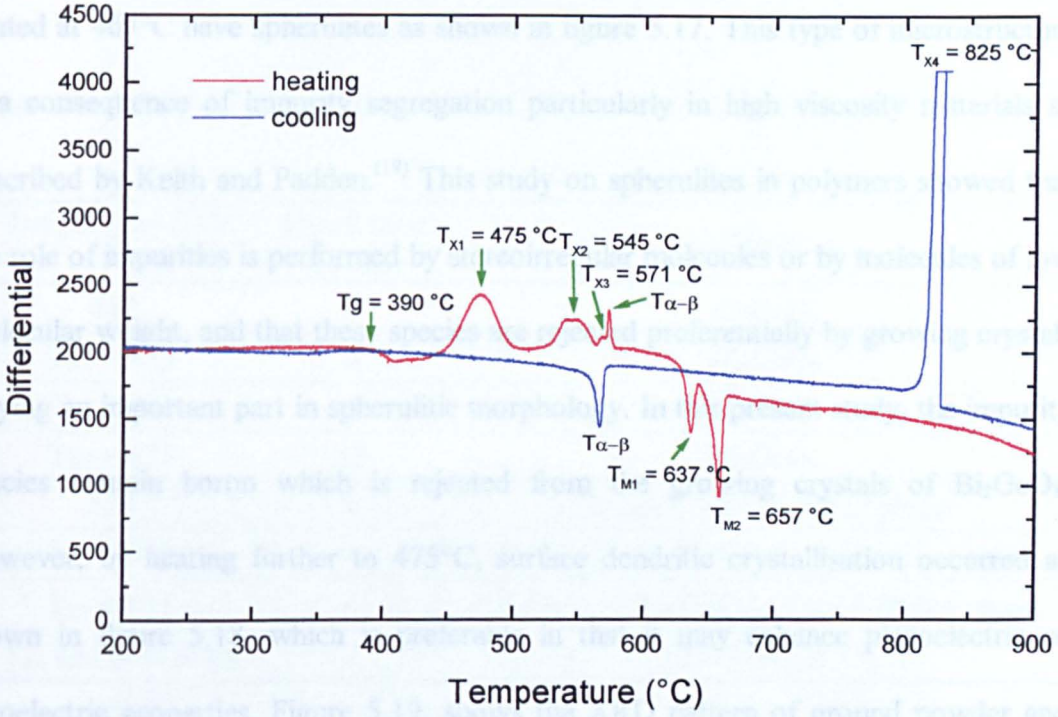

***Figure 5.16** the DTA trace of $BiGeB_6$ glass.*

As glass-ceramic is required to have high thermal shock resistance, the thermal expansion coefficient should be as low as possible to minimise strain from temperature gradients within materials. The linear thermal expansion coefficient (α_L) of $BiGeB_6$ glass in the 25-300 °C temperature range was found to be ~ 8.0 MK^{-1}. Topping et al [18] reported thermal expansion coefficients in the range 8.5 to 9 MK^{-1}, for bismuth germanate glasses containing 95 to 75 mol% GeO_2. Therefore, the value α_L of $BiGeB_6$

glass is in good agreement with that of Topping et al. The slightly different value may be caused by the addition of B_2O_3 oxide.

The crystal phase information in $BiGeB_7$ glass-ceramics for different heat treatment is summarised in Table 5.9. Figures 5.17 and 5.18 show the SEM backscattering images of glass-ceramics $BiGeB_6$ heated at 467°C and at 475°C for four hours. Both glass-ceramics contain the Bi_2GeO_5 crystal phase. The glass-ceramics heated at 467°C have spherulites as shown in figure 5.17. This type of microstructure is a consequence of impurity segregation particularly in high viscosity materials as described by Keith and Padden.[19] This study on spherulites in polymers showed that the role of impurities is performed by stereoirregular molecules or by molecules of low molecular weight, and that these species are rejected preferentially by growing crystals playing an important part in spherulitic morphology. In this present study, the impurity species contain boron which is rejected from the growing crystals of Bi_2GeO_5. However, by heating further to 475°C, surface dendritic crystallisation occurred as shown in figure 5.18, which is preferable in that it may enhance piezoelectric or pyroelectric properties. Figure 5.19, shows the XRD pattern of ground powder and also a bulk sample of $BiGeB_6$ subjected to heat treatment at 475 °C for 4 hours. Preferred orientation in the bulk sample shows Bi_2GeO_5 growing perpendicular to (311) planes. From figure 5.19 (b), the d-spacing of the unidentified peak (?) at 59.58 ± 0.2, is d = 1.55 ± 0.01. As $d_{(311)} = 3.105 \approx 2d_{(?)}$ so the unidentified peak may be identified as the (622) plane which was not indicated in JCPDS file number 36-289.[20] By using the algebraic expressions of d-spacing (d_{hkl}) for the orthorhombic system:

$$\frac{1}{d_{hkl}^2} = \frac{h^2}{a^2} + \frac{k^2}{b^2} + \frac{l^2}{c^2}, \qquad (5.2)$$

where the lattice parameters: a = 15.698 Å, b = 5.5 Å, and c = 5.387 Å, the unidentified peaks at 56.44 and 58.04 (figure 5.19 (a)), may be indexed. The comparison between the calculated (d_{cal}) and experimental (d_{exp}) values of d-spacing(s) at 56.44, 58.04 and 59.58 (°2θ) are shown in table 5.10. From this table, the reasonably low % error and the consistency with the reflection rule give an acceptable identification of these peaks.

Table 5.9 *The crystal phases formed from different heat treatments of $BiGeB_6$ glass.*

Temperature (°C)	Dwell time (Hours)	Phase
467	4	*Bi_2GeO_5
$T_{X1} = 475$	0	*Bi_2GeO_5
$T_{X1} = 475$	4	*Bi_2GeO_5
$T_{X1} = 475$	12	*Bi_2GeO_5
533	4	*Bi_2GeO_5 + unidentified phase
$T_{X2} = 545$	4	*Bi_2GeO_5 + $Bi_4(GeO_4)_3$ + unidentified phase
$T_{X3} = 571$	4	*Bi_2GeO_5 + $Bi_4(GeO_4)_3$ + unidentified phase
> T_{X4} and cool down	-	$Bi_4(GeO_4)_3$

Note: $Bi_4(GeO_4)_3$ (JCPDS No. 34-416) and Bi_2GeO_5 (JCPDS No. 36-289)
*Bi_2GeO_5 + unidentified peaks at high angle (described in section 5.4.4)

Table 5.10 *The calculated and experimental values of the three unidentified peaks.*

2θ ± 0.1	(h,k,l)	d_{cal}	d_{exp} ± 0.002	% Error	Reflection rule*
56.50	(3,1,3)	1.622	1.627	0.30	hkl: h+k = 2n
58.10	(5,3,0)	1.581	1.586	0.31	hk0: h+k = 2n
59.58	(6,2,2)	1.552	1.550	0.13	hkl: h+k = 2n

Note: The values d_{cal}(s) are calculated from equation 5.2.

% Error is the deviation of experimental value from calculation value.

* The reflection rule of space group $Cmc2_1$ (Number 36) is from the International Tables for Crystallography.[21]

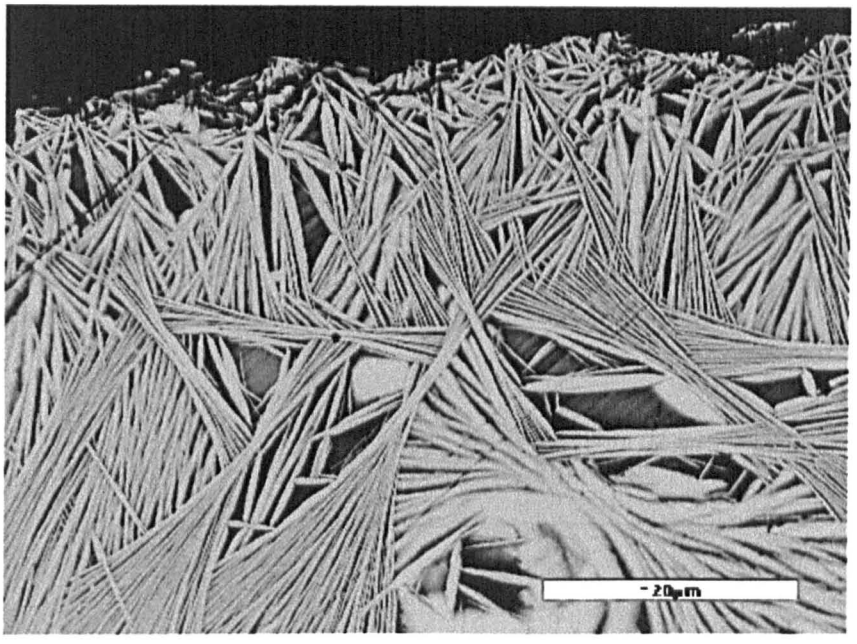

Figure 5.17 *SEM backscattering image of $BiGeB_6$ cross-sectional glass-ceramic heat treated at 467°C for four hours.*

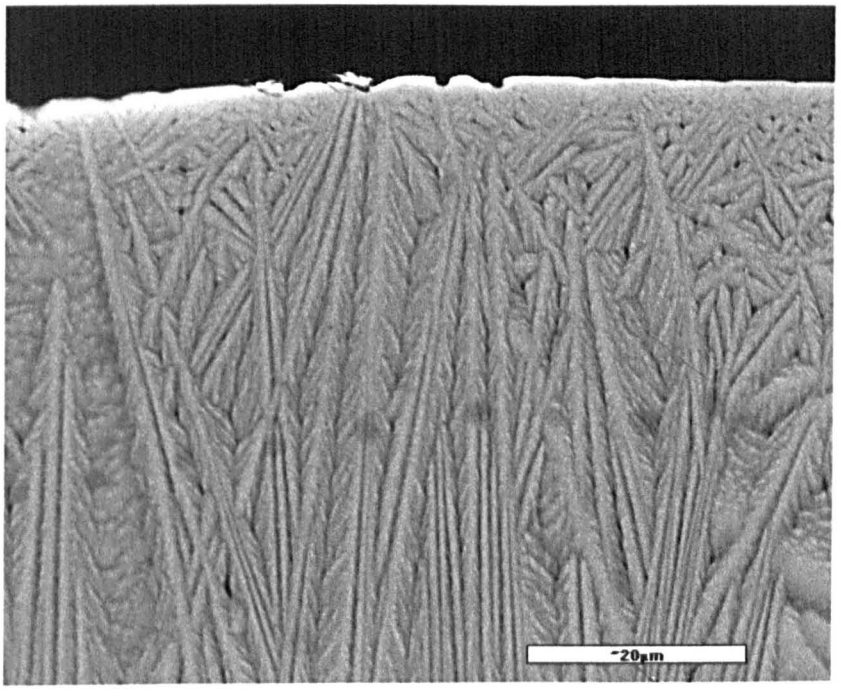

Figure 5.18 *SEM backscattering image of $BiGeB_6$ cross-sectional glass-ceramic heat treated at T_{X1} = 475°C for four hours.*

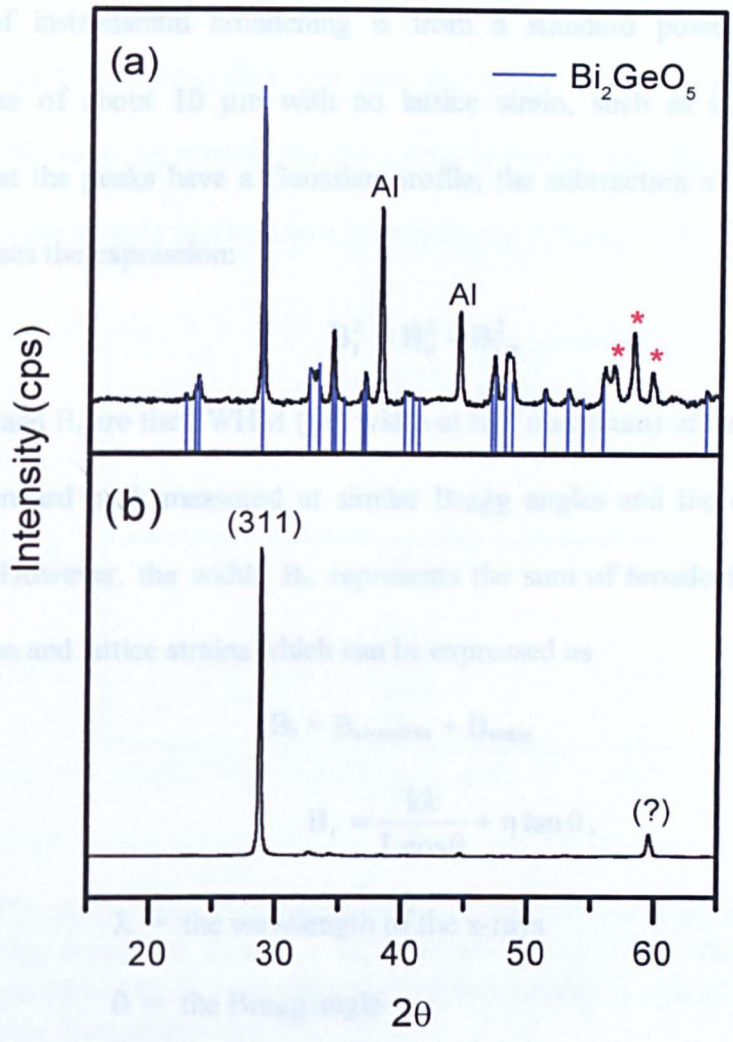

Figure 5.19 *The XRD pattern of $BiGeB_6$ glass-ceramics heat treated at 475 °C for 4 hours. (a) ground powder and (b) bulk piece.*
Note: JCPDS No. of Bi_2GeO_5 is 36-289.

5.4.9 The calculation of crystallite size

The broadening of x-ray diffraction peaks can lead to values for the average crystallite size in glass-ceramics. Small crystallites contain insufficient number of parallel planes to build a sharp diffraction maximum and the peaks in the diffraction pattern become broadened. However, the factors that control peak broadening are not only *crystallite size* but also *instrumental effects* and *lattice strain*. Therefore, the

individual contributions of small crystallite size and lattice strain can be determined after subtracting the broadening from instrumental effects. The estimation of the magnitude of instrumental broadening is from a standard powder, having large crystallite size of about 10 μm with no lattice strain, such as silicon powder.[20] Assuming that the peaks have a Gaussian profile, the subtraction of the instrumental broadening uses the expression:

$$B_r^2 = B_o^2 - B_i^2, \qquad (5.3)$$

where B_o, B_i and B_r are the FWHM (full width at half maximum) of the observed x-ray peak, the standard peak measured at similar Bragg angles and the remaining width respectively. However, the width, B_r, represents the sum of broadening due to small crystallite sizes and lattice strains which can be expressed as

$$B_r = B_{crystallite} + B_{strain} \qquad (5.4)$$

or

$$B_r = \frac{k\lambda}{L\cos\theta} + \eta\tan\theta, \qquad (5.5)$$

where λ = the wavelength of the x-rays

θ = the Bragg angle

L = the average crystallite size

k = a constant (at the best assumption, k = 1.0)

η = the strain in the material. [22]

The expression $B_{crystallite} = \frac{k\lambda}{L\cos\theta}$ is known as the Scherrer equation and is derived based on Gaussian line profiles. By multiplying equation (5.5) by cos θ, it can be rewritten as

$$B_r\cos\theta = \frac{k\lambda}{L} + \eta\sin\theta, \qquad (5.6)$$

therefore, by plotting $B_r \cos\theta$ against $\sin\theta$, a straight line with slope = η and interception at $\frac{k\lambda}{L}$ can be achieved. From equation 5.5, it can be seen that the peak broadening due to the crystallite size and the lattice strain increases rapidly with increasing θ. However, at small θ, the separation is clearer. The idea of how the values η and L affect the straight line is shown schematically in figure 5.20.

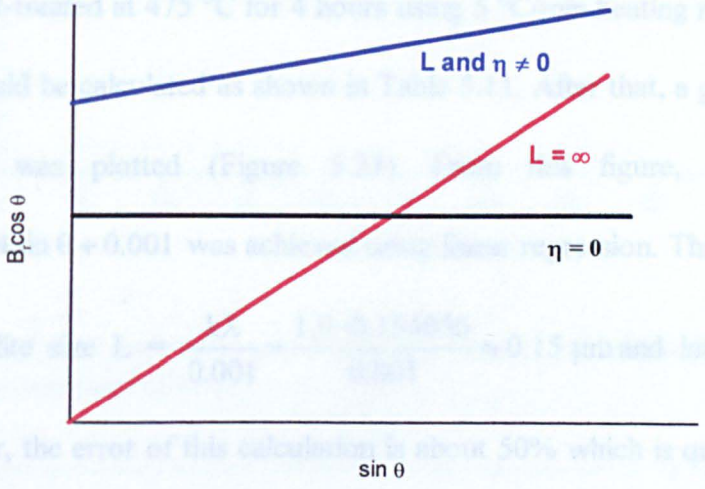

Figure 5.20 *The typical plots illustrating the positions of the straight lines of very large crystallite sizes (L = ∞), no strain ($\eta = 0$) and when crystallite size and lattice strain contribute to peak broadening (L and $\eta \neq 0$). (After Suryanarayana)* [22]

Silicon powder was used as a standard for the correction of instrumental effects. The XRD pattern of the standard powder was collected from 2θ = 20 to 50 because at small diffraction angles the effects of crystallite size and lattice strain are well separated. By using computational analysis based on a Gaussian fit, the FWHM of each peak was found. Figure 5.21 shows FWHM versus 2θ for the silicon standard. Assuming that this relationship is linear, the equation Y = 0.0027X + 0.071 can be estimated using linear regression [23]. Therefore, this equation can be used for the optimum approximation of FWHM (°) or B_i (rad). The XRD patterns of the $BiGeB_6$

glass-ceramics from various heat treatments were investigated from 20 to 70 degrees. In one pattern, well-separated peaks were chosen and again by Gaussian fit, the FWHM (°) or B_o (rad) of each reflection were estimated. Figure 5.22 illustrates the example of a Gaussian fit. By using equation 5.3, the B_r of each peak can be calculated and the function $B_r\cos\theta$ versus $\sin\theta$ plotted and a linear fit applied.

For example, by carefully choosing well separated peaks from the XRD pattern of $BiGeB_6$, heat-treated at 475 °C for 4 hours using 5 °C/min heating rate, $B_r\cos\theta$ and $\sin\theta$ values could be calculated as shown in Table 5.11. After that, a graph of $B_r\cos\theta$ versus $\sin\theta$ was plotted (Figure 5.23). From this figure, the expression $B_r\cos\theta = 0.004\sin\theta + 0.001$ was achieved using linear regression. This then gives the average crystallite size $L = \frac{k\lambda}{0.001} = \frac{1.0 \cdot 0.154056}{0.001} \approx 0.15$ μm and lattice strain $\eta \approx$ 0.004. However, the error of this calculation is about 50% which is quite high, giving the inaccuracy of determining the real crystallite size. However, SEM backscattering image of the same sample (figure 5.18), does not give precise measure of the crystal size because of the surface crystallisation in this glass-ceramic. However, the trend of how heat treatment schedules affect the crystallite size may still be informative.

Table 5.11 *Calculations for $BiGeB_6$ heat-treated at 475 °C for 4 hours (heating rate 5°C/min)*

Peak	2θ (°)	sin θ	hkl	B_i (rad) (±2%)	B_o (rad) (±2%)	$B_r^2 = B_o^2 - B_i^2$	$B_r\cos\theta$ (±3%)
1	28.719	0.248	311	0.00259	0.00363	6.45×10^{-6}	0.00246
2	51.051	0.431	621	0.00364	0.00471	8.87×10^{-6}	0.00269
3	63.922	0.529	332	0.00425	0.00624	20.9×10^{-6}	0.00388

Note: $\lambda_{Cu\,K\alpha} = 0.154056$ nm

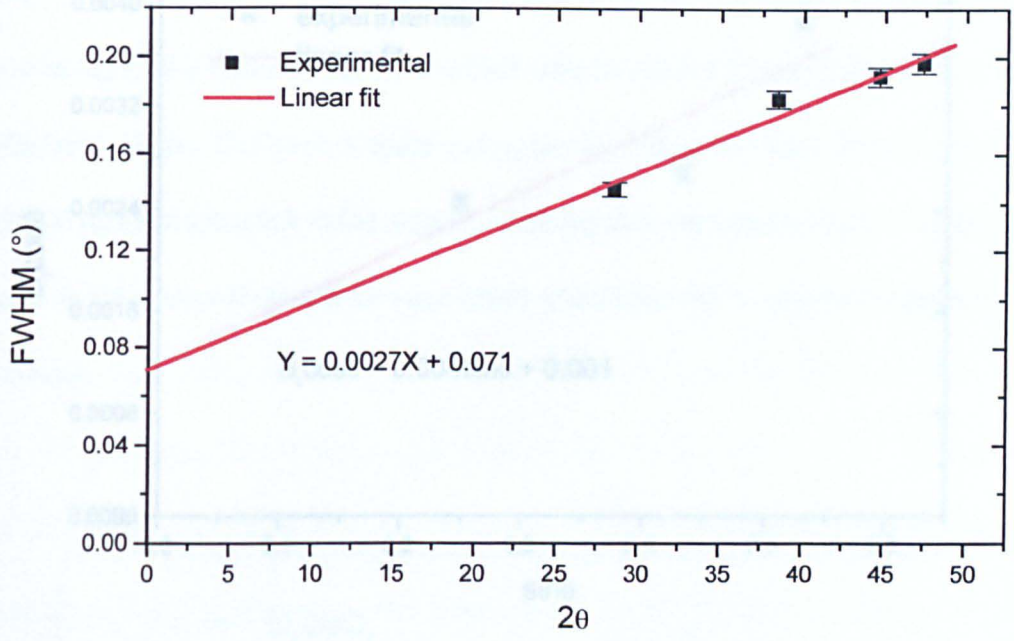

Figure 5.21 *The linear regression of FWHM of silicon standard for the correction of instrumental effects.*

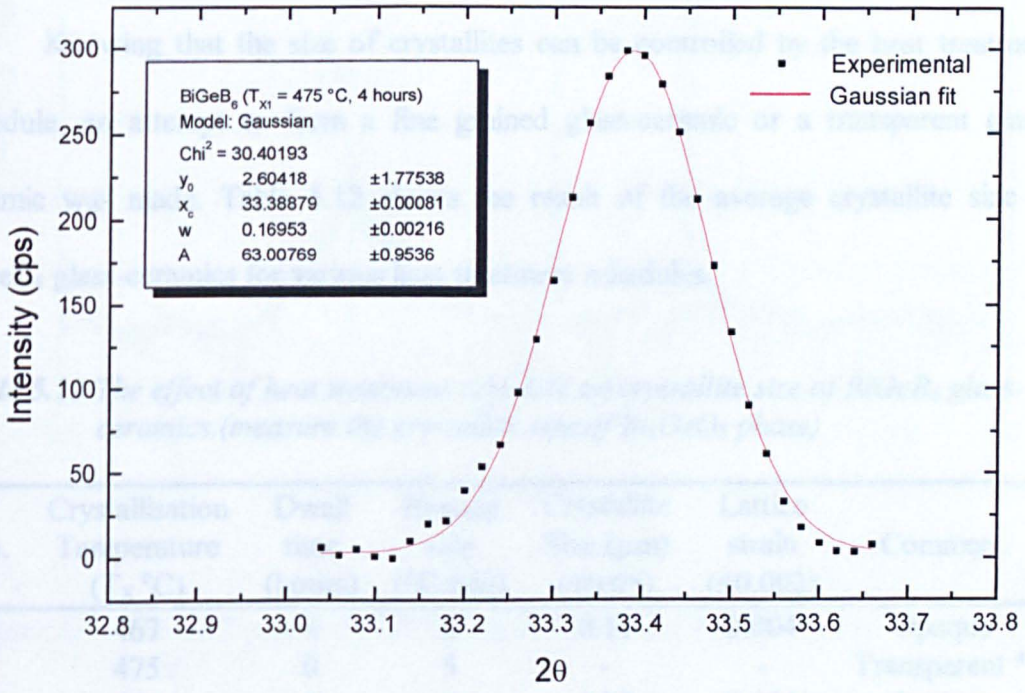

Figure 5.22 *The Gaussian fit of the peak from XRD pattern of $BiGEB_6$ of T_{X1} = 475 °C for 4 hours, the heating rate = 5 °C/min.*

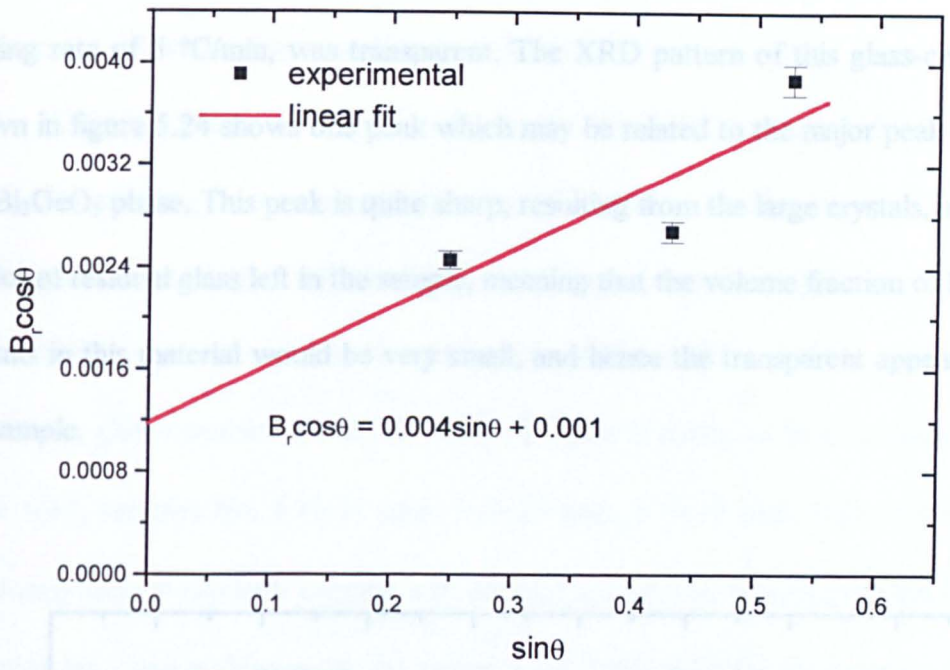

Figure 5.23 *The linear regression of $B_r\cos\theta$ versus $\sin\theta$ using three reflections from the XRD pattern of $BiGeB_6$ glass-ceramic of T_{X1} = 475 °C, hold for 4 hours and heating rate = 5 °C/min.*

Knowing that the size of crystallites can be controlled by the heat treatment schedule, an attempt to form a fine grained glass-ceramic or a transparent glass-ceramic was made. Table 5.12 shows the result of the average crystallite size of $BiGeB_6$ glass-ceramics for various heat treatment schedules.

Table 5.12 *The effect of heat treatment schedule on crystallite size of $BiGeB_6$ glass-ceramics.(measure the crystallite size of Bi_2GeO_5 phase)*

No.	Crystallisation Temperature (T_X °C)	Dwell time (hours)	Heating rate (°C/min)	Crystallite Size (μm) (±0.05)	Lattice strain (±0.002)	Comment
1	467	4	5	0.11	0.004	Opaque
2	475	0	5	-	-	Transparent *
3	475	4	5	0.15	0.004	Opaque
4	475	12	5	0.20	0.005	Opaque
5	475	0	1	0.17	0.002	Opaque
6	475	0	0.5	0.16	0.003	Opaque
7	545	4	5	0.17	0.001	Opaque
8	571	4	5	0.25	0.006	Opaque

* The $BiGeB_6$ glass-ceramic subjected to heat treatment at 475 °C for 0 hour using a heating rate of 5 °C/min, was transparent. The XRD pattern of this glass-ceramic as shown in figure 5.24 shows one peak which may be related to the major peak (311) of the Bi_2GeO_5 phase. This peak is quite sharp, resulting from the large crystals, and there is a lot of residual glass left in the sample, meaning that the volume fraction of Bi_2GeO_5 crystals in this material would be very small, and hence the transparent appearance of the sample.

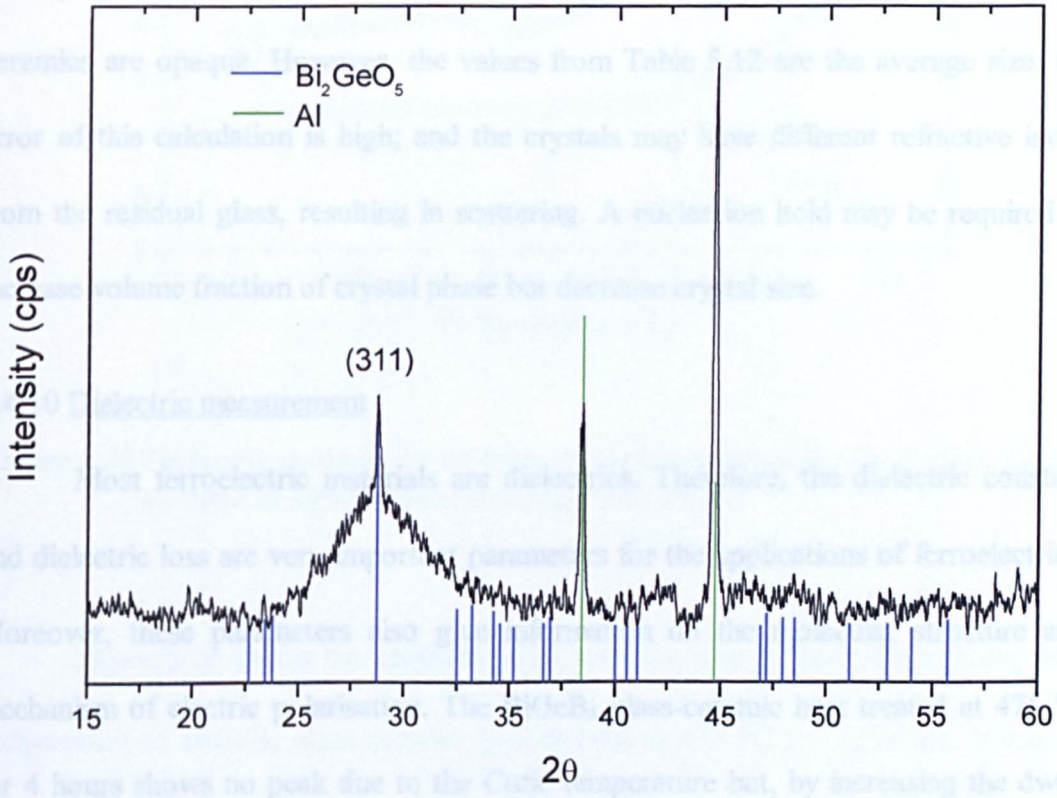

Figure 5.24 *The XRD pattern of $BiGeB_6$ glass-ceramics heat treated at 475 °C for 0 hour.*

From table 5.12, it can be seen that the crystallisation temperature is the important parameter in controlling crystallite size in these glass-ceramics and the

crystallite size of the Bi_2GeO_5 phase increases with increase in crystallisation temperature. However, the error is large (~30%)

When the glass was heated to T_{X1} = 475 °C at 5°C/min (no hold), nucleation was poor, resulting in low volume fraction of Bi_2GeO_5. Heating rates of 0.5 and 1 °C/min gave rise to higher volume fraction and larger crystals. Layton et al [24], stated that crystallite sizes of common ferroelectrics crystals, such as $BaTiO_3$, $NaNbO_3$, and $PbTiO_3$, in glass-ceramics should be below 0.2 μm in order to be transparent. From Table 5.12, samples No. 1 (0.11 μm), 3 (0.15 μm), 5 (0.17 μm), 6 (0.16 μm) and 7 (0.17 μm) contain Bi_2GeO_5 crystals with average size smaller than 0.2 μm but all glass-ceramics are opaque. However, the values from Table 5.12 are the average size; the error of this calculation is high; and the crystals may have different refractive index from the residual glass, resulting in scattering. A nucleation hold may be required to increase volume fraction of crystal phase but decrease crystal size.

5.4.10 Dielectric measurement

Most ferroelectric materials are dielectrics. Therefore, the dielectric constant and dielectric loss are very important parameters for the applications of ferroelectrics. Moreover, these parameters also give information on the molecular structure and mechanism of electric polarisation. The $BiGeB_6$ glass-ceramic heat treated at 475 °C for 4 hours shows no peak due to the Curie temperature but, by increasing the dwell time to 12 hours, the peak started to show at about 407 °C as seen in figure 5.25. This is because the Bi_2GeO_5 crystals in the glass-ceramics heat-treated at 475°C for 12 hours are larger than in glass-ceramics heat-treated at the same temperature for 4 hours. This is consistent with the work done by Borrelli and Layton [25], who reported that a cadmium-doped sodium niobate glass-ceramic, which contained the largest

crystals, showed a sharp peak in the dielectric constant but, with decrease in crystallite size, the apparent Curie temperature and peak permittivity decreased.

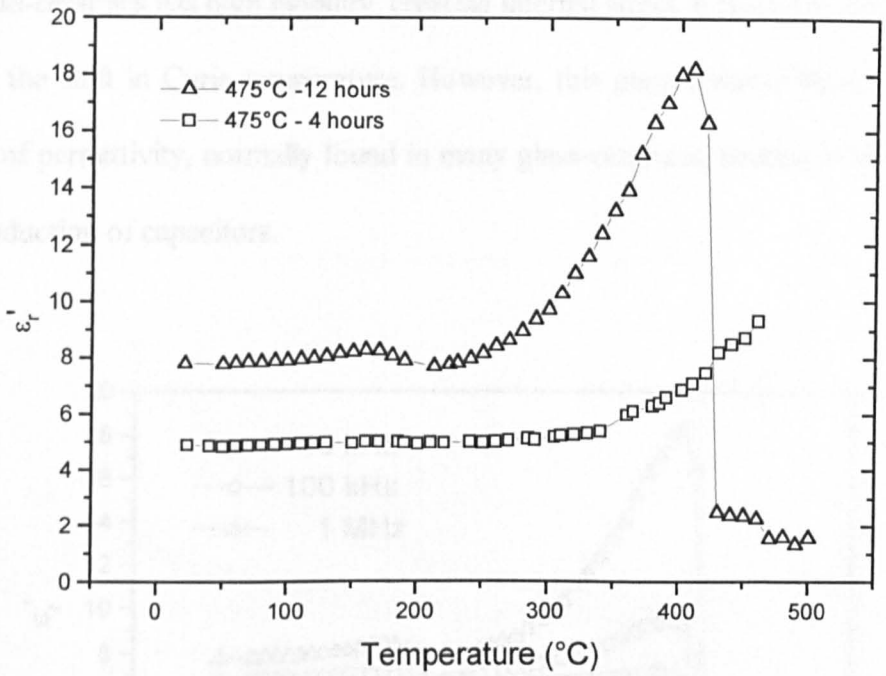

Figure 5.25 *Dielectric constant (at 10 kHz) versus temperature for the $BiGeB_6$ glass-ceramic at different heat treatment schedules.*

Figure 5.26 shows the variation of (ε_r') and (ε_r''), at different frequencies, with temperature of $BiGeB_6$ glass-ceramic heat-treated at 475 °C for 12 hours. It can be seen that ε_r' increases with increase in temperature at all frequencies from 10 kHz to 1 MHz. A peak in ε_r' and ε_r'' is observed around 407 °C. The peak in dielectric constant ε_r' of this glass-ceramic may be attributed to the phase-transition temperature of crystalline Bi_2GeO_5. Firsov et al.[6] suggested that the single crystal of Bi_2GeO_5 phase can be ferroelectric with $T_C > 800$ K (527 °C). Therefore a shift in Curie temperature of the glass-ceramic may arise from the effects of the elastic and the electrostrictive

forces exerted by the surrounding glass matrix on the crystallites contributing in the phase transition. Moreover, from the DTA heating trace of $BiGeB_6$ glass (figure 5.16), the glass transition temperature is around 390 °C which is near the Curie temperature of this glass-ceramic, so at this temperature, it may be possible that the residual glass in the glass-ceramics has high mobility, creating internal stress in Bi_2GeO_5 crystals, giving rise to the shift in Curie temperature. However, this glass-ceramic has relatively low values of permittivity, normally found in many glass-ceramics, making it unsuitable for the production of capacitors.

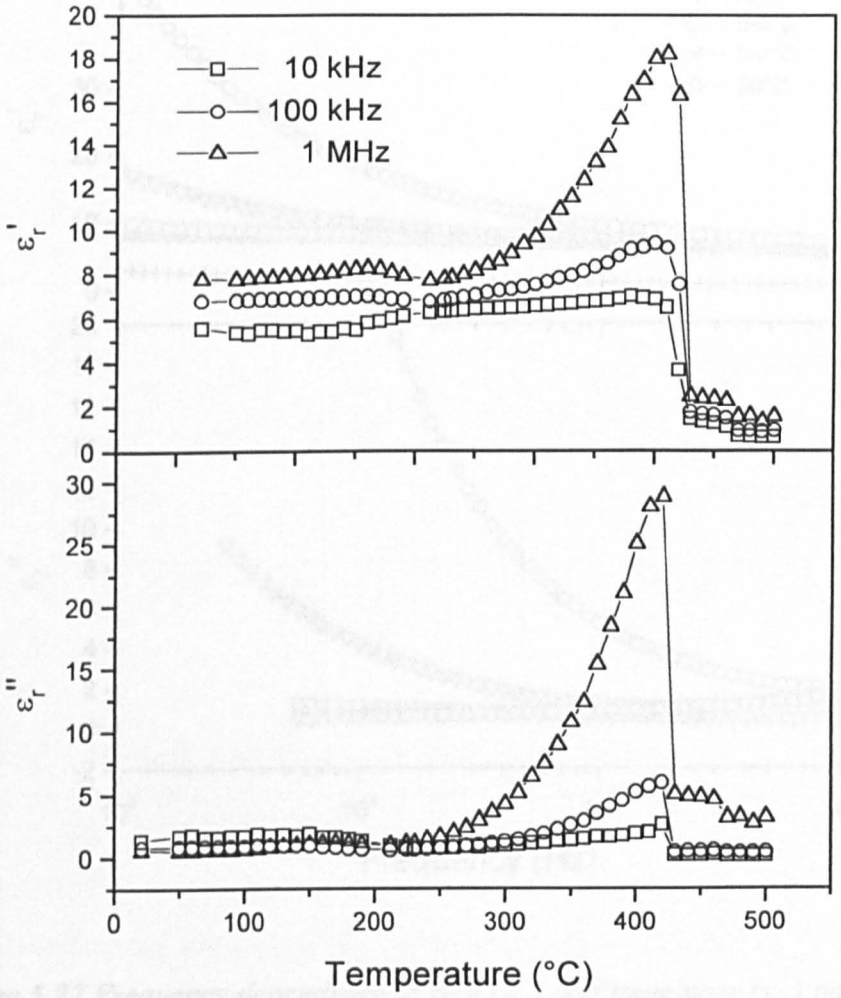

Figure 5.26 *Temperature dependence of real (ε_r') and imaginary (ε_r'') parts of the complex permittivity of a $BiGB_6$ thin sample (heat-treated at 475°C for 12 hours).*

The frequency responses of the of real ($\varepsilon_r^{'}$) and imaginary ($\varepsilon_r^{''}$) parts of the complex permittivity of a $BiGeB_6$ thin sample heat-treated at 475°C for 12 hours, are illustrated in figure 5.27. ε_r' and ε_r"decrease with increasing frequency in the 1 kHz to 1 MHz frequency range at all temperatures and increase with increasing temperature from 50 to 400 °C but at 500 °C (after the Curie temperature ≈ 407 °C) ε_r' and ε_r" values drop.

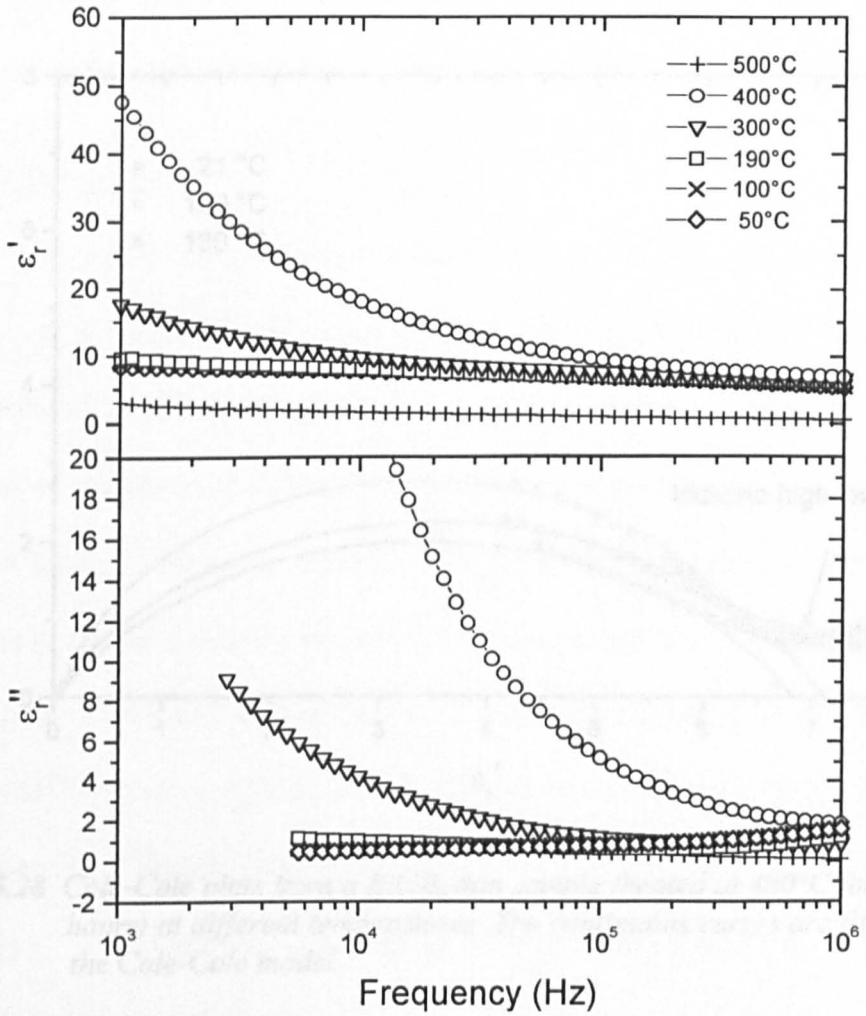

Figure 5.27 *Frequency dependence of real ($\varepsilon_r^{'}$) and imaginary ($\varepsilon_r^{''}$) parts of the complex permittivity of a $BiGB_6$ thin sample (heat-treated at 475°C for 12 hours).*

The permittivity dispersion of this glass-ceramic occurs at around 10^3 to 10^5 Hz. However, there are instrumental limitations in measuring the dissipation factor ε_r'' at low frequency, therefore peaks of ε_r'' at a relaxation frequency cannot be observed. Cole-Cole plots at different temperatures (figure 5.28) show a tail in the distribution, indicating a large distribution of relaxation times which may be attributed to multiple polarisation mechanisms or losses due to conduction. A low loss dielectric would have a Cole-Cole plot approximating to a semicircle.[26]

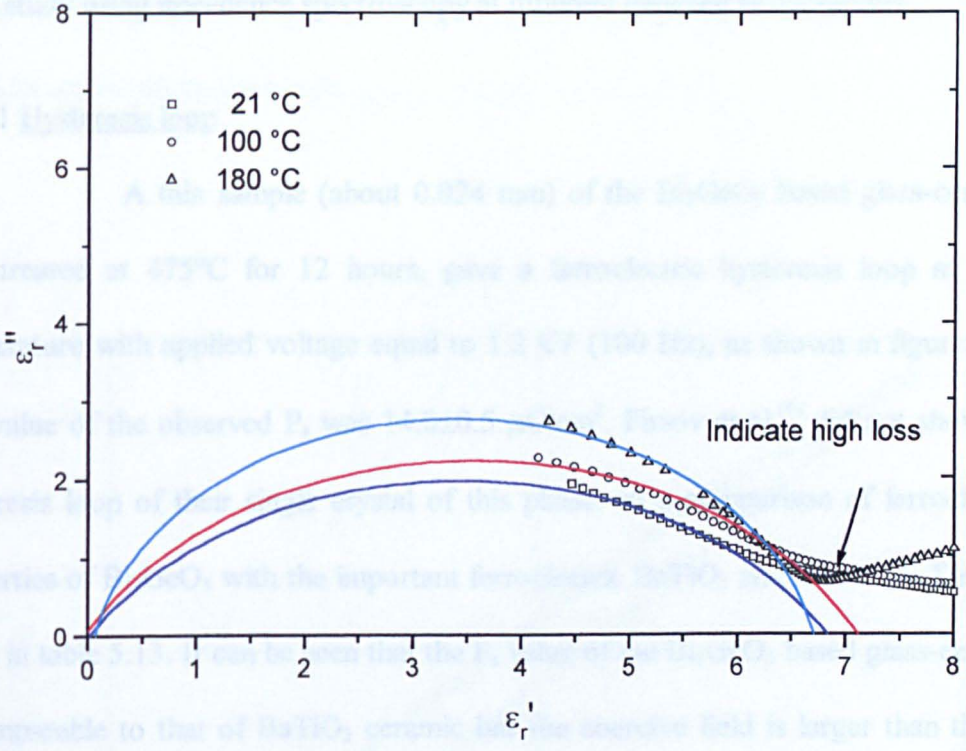

Figure 5.28 *Cole-Cole plots from a $BiGB_6$ thin sample (heated at 480°C for 12 hours) at different temperatures. The continuous curves are fitted with the Cole-Cole model.*

The relaxation process of this glass-ceramic may be related to the interfacial or space charge mechanism which is a phenomenon of the glass-electrode interface.[27] This may result from poor contacts during measurement. The sample was coated by platinum but gold plates were used to connect the sample to the circuit, so gold

diffusion may have occurred into the glass-ceramics, causing the space charge polarisation. Dielectric and mechanical losses are often due to movement of mobile ions under the influence of an external electric field. This may explain the high loss in this glass-ceramic by assuming that there is a glassy phase of low dielectric constant left after crystallisation which provides some mobile ions. In this case, the interfacial polarisation may result from the mobile ions. However, further investigation is needed in order to conclude which cause: electrode or mobile ion, contributes to the interfacial polarisation. In order to fully evaluate this behaviour, it would be necessary to carry out a study using impedance spectroscopy at different elevated temperatures.

5.4.11 Hysteresis loop

A thin sample (about 0.024 mm) of the Bi_2GeO_5 based glass-ceramic, heat treated at 475°C for 12 hours, gave a ferroelectric hysteresis loop at room temperature with applied voltage equal to 1.2 kV (100 Hz), as shown in figure 5.29. The value of the observed P_s was 14.0±0.5 $\mu C/cm^2$. Firsov et al.[6] did not show any hysteresis loop of their single crystal of this phase, so a comparison of ferroelectric properties of Bi_2GeO_5 with the important ferroelectric $BaTiO_3$ and related $Bi_4Ti_3O_{12}$ is made in table 5.13. It can be seen that the P_s value of the Bi_2GeO_5 based glass-ceramic is comparable to that of $BaTiO_3$ ceramic but the coercive field is larger than that of $BaTiO_3$ ceramic. Bismuth titanate ($Bi_4Ti_3O_{12}$) has a layer structure of [TiO_6] octahedra and a $Bi_2O_2^{2+}$ layer. Ge atoms in the Bi_2GeO_5 crystal structure prefer to form chains of [GeO_4] tetrahedra as illustrated in figure 2.13 (chapter 2). Consider the general formula of the perovskite-type structure, ABO_3, where O is oxygen, A is a cation with a larger ionic radius and B is a cation with a smaller ionic radius. A tolerance factor t can be defined where $t = (R_A + R_O)/(2)^{1/2}(R_B+R_O)$, and R_A, R_B and R_O are the ionic radii of A, B and O ions respectively. The value t where A = Bi (R_{Bi} = 1.7 and B = Ge

(R_{Ge} = 1.37) O = O (R_O = 0.65) can be calculated equal to 0.82. To form a stable perovskite structure, the value t has to be between 0.9 and 1.1[28], thus it is impossible to form perovskite bismuth germanate. However, Bi_2GeO_5 phase can be ferroelectric. A thin film of $Bi_4Ti_3O_{12}$ was grown along its c-axis, giving rise to Ps = 5.7 $\mu C/cm^2$ [29], which is smaller than that of the Bi_2GeO_5 based glass-ceramic. However, P_s of $Bi_4Ti_3O_{12}$ single crystal grown along its a-axis is quite high, up to 50 $\mu C/cm^2$. Regarding the similar layer structures of $Bi_4Ti_3O_{12}$ and Bi_2GeO_5, in appears that, since this Bi_2GeO_5 glass-ceramic has preferred orientation perpendicular to its (311) planes, it may not have the best electrical properties which might be obtained if the crystals could be grown along the a-axis.

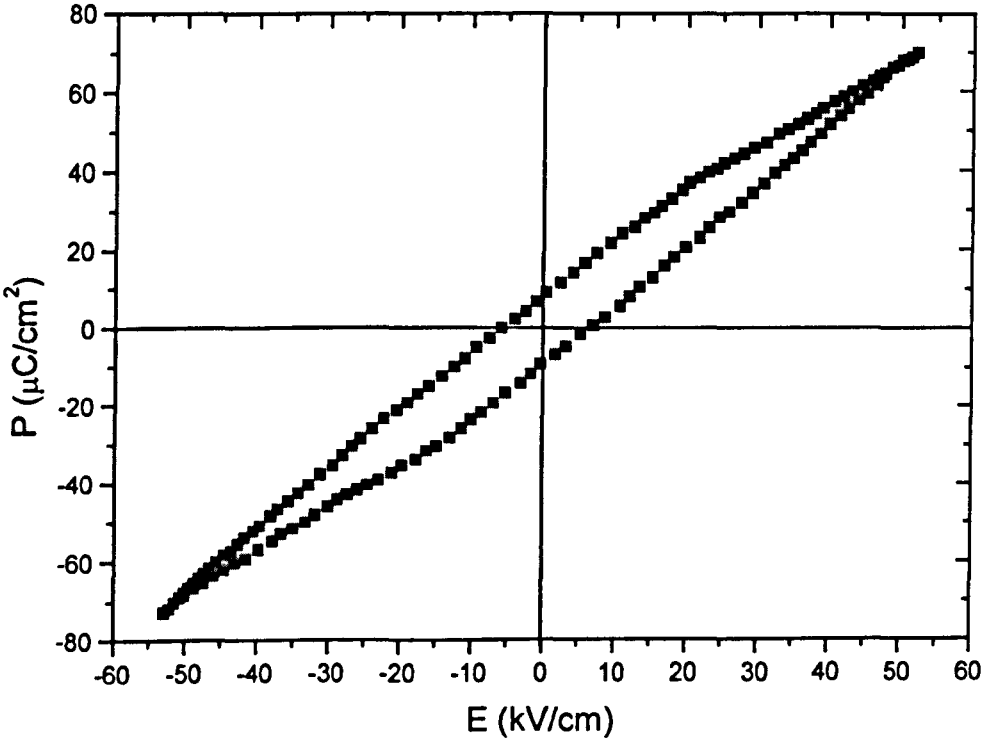

***Figure 5.29** Hysteresis loop at room temperature (100 Hz) of a $BiGeB_6$ glass-ceramic of 0.024±0.002 cm thickness, heated at 480°C for 12 hours.*

Table 5.13 *The comparison of T_C (Curie temperature), P_s (spontaneous polarisation) and E_r (coercive field) of Bi_2GeO_5 and some well-known ferroelectrics.*

Ferroelectrics	T_C (°C)	P_s (at room temperature) ($\mu C/cm^2$)	E_r (kV/cm)
Bi_2GeO_5 (Glass-ceramic)	407±1	14.0±0.5	5.6±0.2
$BaTiO_3$ [30] (Ceramic)	≈120	≈13	≈0.3
$Bi_4Ti_3O_{12}$ [29] (c-axis thin film)	≈675	≈5.7	≈130

5.5 $BiO_{1.5}$-GeO_2-TeO_2

Figure 5.30 and Table 5.14, show five compositions from the $BiO_{1.5}$-GeO_2-TeO_2 system. The stoichiometric composition, s, devitrified on cooling.

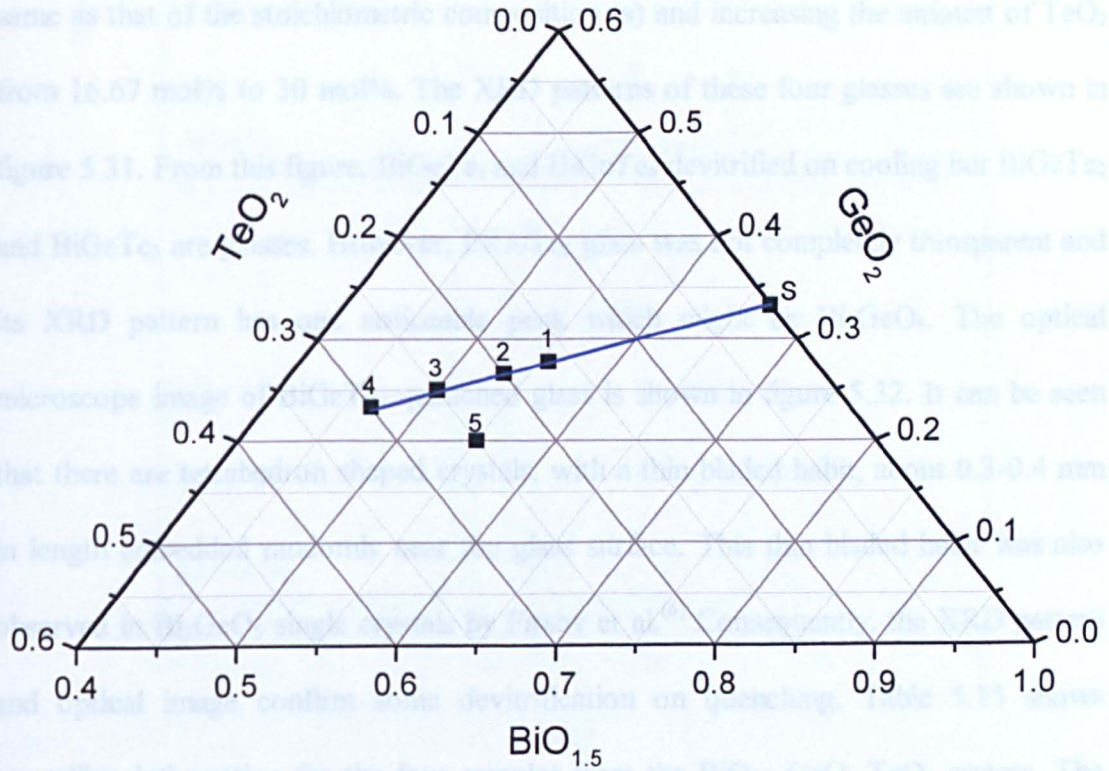

Figure 5.30 *The five samples prepared from the $BiO_{1.5}$-GeO_2-TeO_2 system.*

Table 5.14 The nominal compositions prepared from the $BiO_{1.5}$-GeO_2-TeO_2 system.

Sample Number	$BiO_{1.5}$ (mol%)	GeO_2 (mol%)	TeO_2 (mol%)
S	66.67	33.33	0
$BiGeTe_1$(1)	55.56	27.77	16.67
$BiGeTe_2$(2)	53.33	26.67	20
$BiGeTe_3$(3)	50	25	25
$BiGeTe_4$(4)	46.67	23.33	30
$BiGeTe_5$(5)	55	20	25

The first four compositions were chosen to keep the ratio of $BiO_{1.5}$:GeO_2 the same as that of the stoichiometric composition (s) and increasing the amount of TeO_2 from 16.67 mol% to 30 mol%. The XRD patterns of these four glasses are shown in figure 5.31. From this figure, $BiGeTe_1$ and $BiGeTe_4$ devitrified on cooling but $BiGeTe_2$ and $BiGeTe_3$ are glasses. However, $BiGeTe_2$ glass was not completely transparent and its XRD pattern has one noticeable peak which might be Bi_2GeO_5. The optical microscope image of $BiGeTe_2$ quenched glass is shown in figure 5.32. It can be seen that there are tetrahedron shaped crystals, with a thin bladed habit, about 0.3-0.4 mm in length embedded randomly near the glass surface. This thin bladed habit was also observed in Bi_2GeO_5 single crystals by Firsov et al.[6] Consequently, the XRD pattern and optical image confirm some devitrification on quenching. Table 5.15 shows crystalline information for the four samples from the $BiO_{1.5}$-GeO_2-TeO_2 system. The DTA traces of $BiGeTe_2$ and $BiGeTe_3$ glasses are illustrated in figure 5.33.

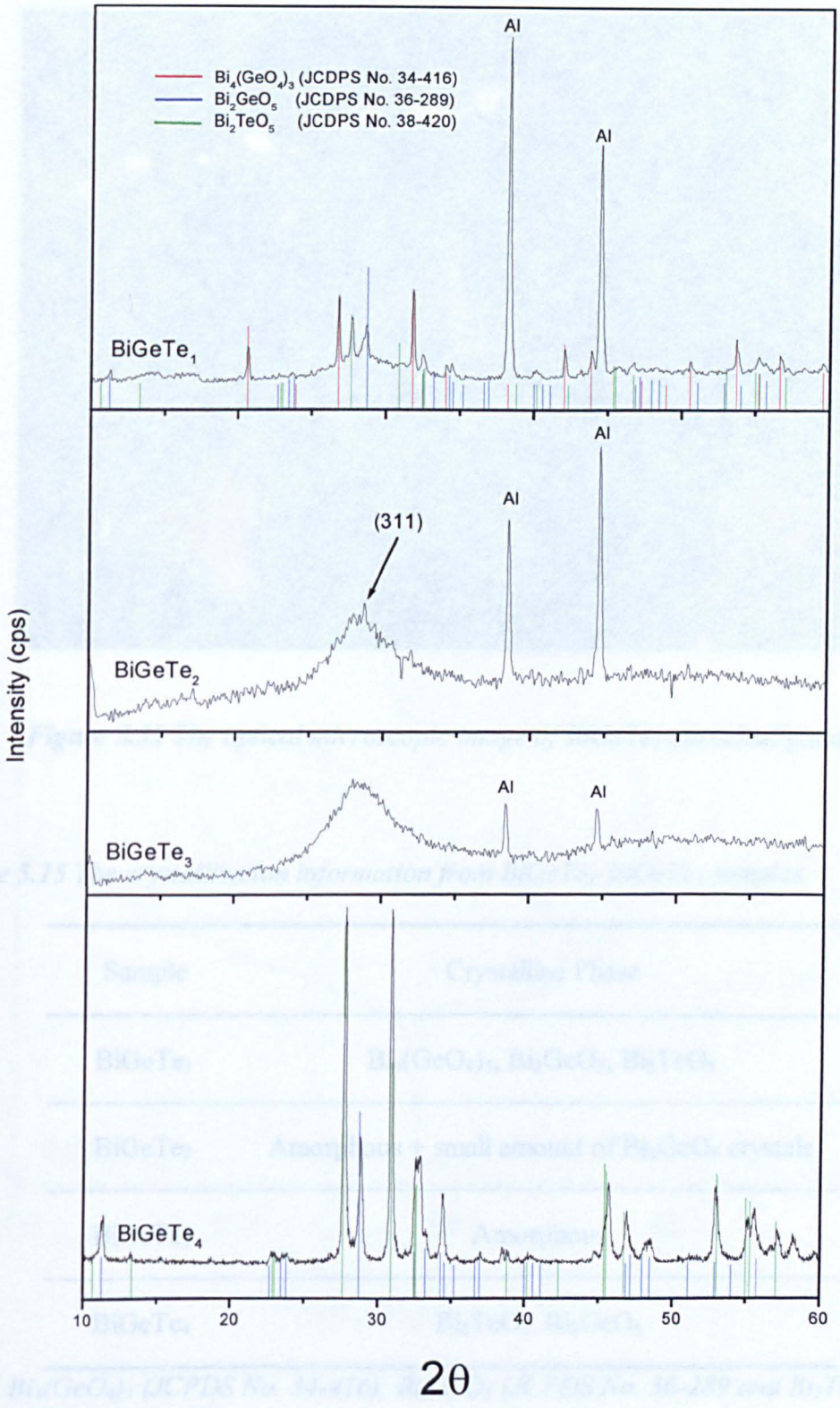

Figure 5.31 *XRD patterns of glasses of samples 1-4 from the $BiO_{1.5}$-GeO_2-TeO_2 system.*

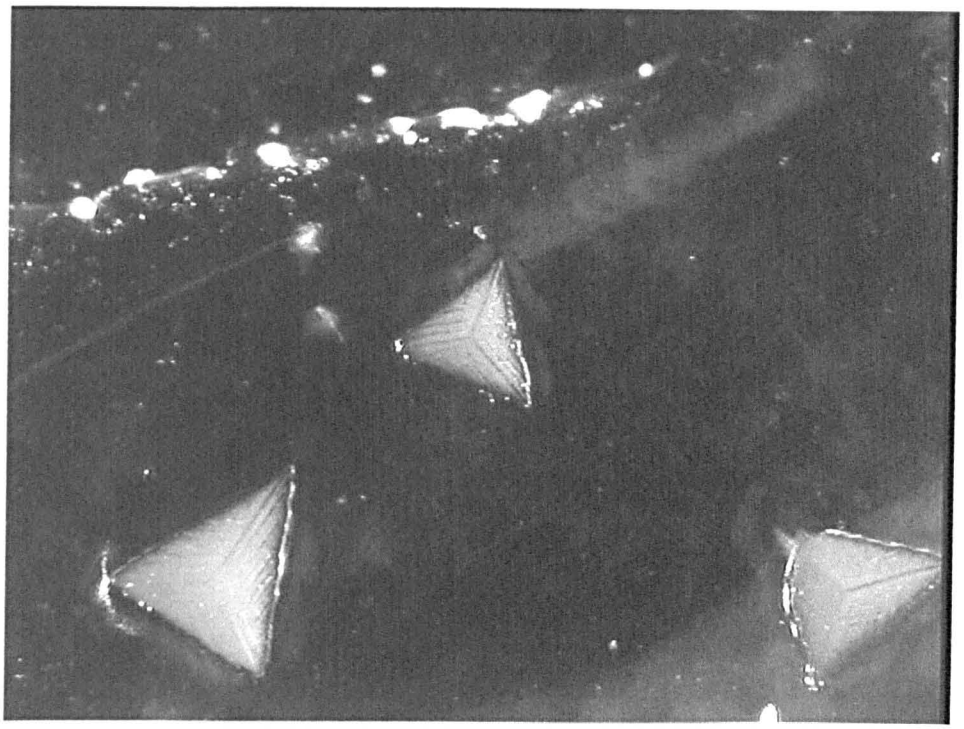

Figure 5.32 *The optical microscopic image of $BiGeTe_2$ quenched glass.*

Table 5.15 *The crystallisation information from $BiGeTe_1$-$BiGeTe_5$ samples.*

Sample	Crystalline Phase
$BiGeTe_1$	$Bi_4(GeO_4)_3$, Bi_2GeO_5, Bi_2TeO_5
$BiGeTe_2$	Amorphous + small amount of Bi_2GeO_5 crystals
$BiGeTe_3$	Amorphous
$BiGeTe_4$	Bi_2TeO_5, Bi_2GeO_5

Note: $Bi_4(GeO_4)_3$ (JCPDS No. 34-416), Bi_2GeO_5 (JCPDS No. 36-289 and Bi_2TeO_5 (JCPD No. 38-420)

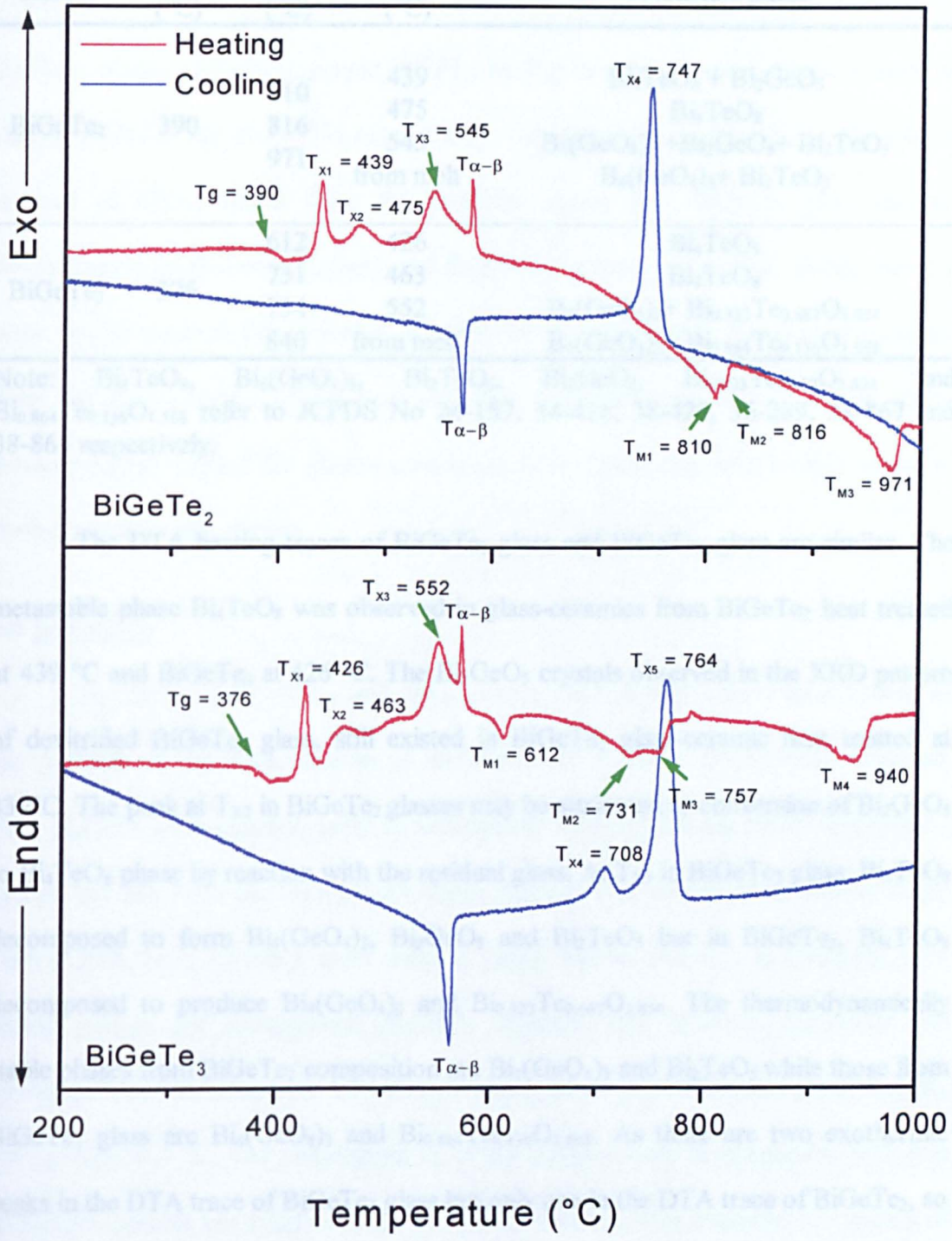

Figure 5.33 *The comparison of DTA traces of $BiGeTe_2$ and $BiGeTe_3$ glasses.*

Table 5.16 Thermal parameters, crystallisation temperatures and crystalline phases of all glass-ceramics from $BiGeTe_2$ and $BiGeTe_3$ glasses.

Sample	$T_g \pm 1$ (°C)	$T_m \pm 1$ (°C)	$T_x \pm 1$ (°C)	Crystalline phase
$BiGeTe_2$	390	810	439	$Bi_4TeO_8 + Bi_2GeO_5$
		816	475	Bi_4TeO_8
		971	545	$B_4(GeO_4)_3 + Bi_2GeO_5 + Bi_2TeO_5$
			from melt	$B_4(GeO_4)_3 + Bi_2TeO_5$
$BiGeTe_3$	376	612	426	Bi_4TeO_8
		731	463	Bi_4TeO_8
		754	552	$B_4(GeO_4)_3 + Bi_{0.333}Te_{0.667}O_{1.834}$
		840	from melt	$B_4(GeO_4)_3 + Bi_{0.864}Te_{0.136}O_{1.568}$

Note: Bi_4TeO_8, $Bi_4(GeO_4)_3$, Bi_2TeO_5, Bi_2GeO_5, $Bi_{0.333}Te_{0.667}O_{1.834}$ and $Bi_{0.864}Te_{0.136}O_{1.568}$ refer to JCPDS No 24-157, 34-416, 38-420, 36-289, 38-867 and 38-865 respectively.

The DTA heating traces of $BiGeTe_2$ glass and $BiGeTe_3$ glass are similar. The metastable phase Bi_4TeO_8 was observed in glass-ceramics from $BiGeTe_2$ heat treated at 439 °C and $BiGeTe_3$ at 426 °C. The Bi_2GeO_5 crystals observed in the XRD pattern of devitrified $BiGeTe_2$ glass, still existed in $BiGeTe_2$ glass-ceramic heat treated at 439°C. The peak at T_{X2} in $BiGeTe_2$ glasses may be attributed to conversion of Bi_2GeO_5 to Bi_4TeO_8 phase by reaction with the residual glass. At T_{X3} in $BiGeTe_2$ glass, Bi_4TeO_8 decomposed to form $Bi_4(GeO_4)_3$, Bi_2GeO_5 and Bi_2TeO_5 but in $BiGeTe_3$, Bi_4TeO_8 decomposed to produce $Bi_4(GeO_4)_3$ and $Bi_{0.333}Te_{0.667}O_{1.834}$. The thermodynamically stable phases from $BiGeTe_2$ composition are $Bi_4(GeO_4)_3$ and Bi_2TeO_5 while those from $BiGeTe_3$ glass are $Bi_4(GeO_4)_3$ and $Bi_{0.864}Te_{0.136}O_{1.568}$. As there are two exothermic peaks in the DTA trace of $BiGeTe_3$ glass but only one in the DTA trace of $BiGeTe_2$, so it may be assumed that the exothermic peak at T_{X4} is related to the formation of the $Bi_{0.864}Te_{0.136}O_{1.568}$ phase.

The values of To – Tg of $BiGeTe_2$ and $BiGeTe_3$ are about 37 and 38 respectively, smaller than from glasses from $BiO_{1.5}$-GeO_2-$BO_{1.5}$, indicating lower glass

stability. $BiGeTe_3$ is the only composition that offers a good glass from the $BiO_{1.5}$-GeO_2-TeO_2 system. $BiGeTe_2$ is largely amorphous but also has indications of devitrification of Bi_2GeO_5. However, $BiGeTe_3$ glass-ceramics show no trace of Bi_2GeO_5 phase. Therefore, sample $BiGeT_5$, having the same amount of TeO_2 oxide as that of $BiGeTe_3$ but about 5% more $BiO_{1.5}$, was prepared, expecting that the excess amount of $BiO_{1.5}$ might form the Bi_2GeO_5 phase. The $BiGeTe_5$ glass showed devitrification to Bi_2TeO_5, Bi_2GeO_5 and $Bi_4(GeO_4)_3$ phases on cooling, giving rise to a poor, fragile material. Consequently, it is difficult to form $BiGeO_5$ based glass-ceramics from the $BiO_{1.5}$-GeO_2-TeO_2 system and this, combined with a very limited glass-forming region (typical for glasses containing TeO_2 oxide) has been a disincentive to further work on this system.

5.6 Summary

The $BiO_{1.5}$-GeO_2-$BO_{1.5}$ and $BiO_{1.5}$-GeO_2-TeO_2 systems were investigated as the problem of the devitrification of stoichiometric Bi_2GeO_5 from binary occurred. Pure Bi_2GeO_5 glass-ceramic could be successfully formed from the $BiO_{1.5}$-GeO_2-$BO_{1.5}$ system but not from the $BiO_{1.5}$-GeO_2-TeO_2 system. The glass-forming region of the $BiO_{1.5}$-GeO_2-TeO_2 system is quite narrow, giving rise to difficulty in obtaining good parent glasses for precipitating Bi_2GeO_5 crystals. The dielectric behaviour and hysteresis loop confirmed the ferroelectric character of Bi_2GeO_5 based glass-ceramic, having T_C = 407 °C. The polarisation P_s of this glass-ceramic is comparable with that of $BaTiO_3$ ceramic but a high voltage was used for poling. The preferred orientation of this glass-ceramic is perpendicular to its (311) planes but a-axis orientation may be preferable, in order to enhance the electrical properties. Therefore the grain-oriented glass-ceramic method should be attempted in future work.

References

1. Nitsche, R. 1965, *Journal of Applied Physics*, Volume 36, Number 8, p. 2358.
2. Ballman, A. A., 1967, *Journal of Crystal Growth*, Volume 1, p. 37.
3. Abrahams, S. C., Jamieson, P. B. and Bernstein, J. L. 1967, *Journal of Chemical Physics*, Volume 47, Number 10, p. 4034.
4. Levin, E. M. and Roth, R. S. 1964, *J. Research Natl. Bur Standards*, Volume 68A, Number 2, p. 201.
5. Speranskaya, E. I. and Arshakun, A. A. 1964, *Zh. Neorgan. Khim.*, Volume 9, Number 2, p. 417.
6. Firsov, A. V., Skorokhodov, N. E., Astaf'ev, A. V., Stefanovich, S. Yu., and Venevtsev, Yu. N., 1984, *Kristallografiya*, Volume 29, p. 509.
7. Auriviltius B., Lindblom C. I., and Stenson, P., 1964 *Acta Chemica Scandinavica*, Volume 18, p. 1556.
8. Hahn, T. 1987, *International Tables for Crystallography*, Volume A: space-group symmetry (D. Reidel Publishing Company).
9. Nassau, K. and Chadwick, D. L., 1982, *Journal of the American Ceramic Society*, Volume 65, p. 197.
10. Mortuza, M. G., 1989, *Ph. D Thesis*, Department of Physics, The University of Warwick.
11. Sigaev, V. N., Stefanovich, S. Yu., Sarkisov, P. D. and Lopatina, E. V. 1995, *Materials Science and Engineering*, Volume B32, p. 17.
12. Riebling, E. F. 1974, *Journal of Materials Science*, Volume 9, p. 753.
13. Nitsche, R. 1965, *Journal of Applied Physics*, Volume 36, p. 2358.
14. Oxford Cryosystems, 1995-99, *Crystallographica*, Version 1.52.
15. FIZ Karlsruhe and Gmelin-Institut, 1990, *Inorganic Crystal Structure Database (ICSD)*.
16. Pottier, M. 1974, *Bull. Soc. Chim. Belg.*, Volume 83, p. 235.
17. Shelby, J. E. *Introduction to Glass Science and Technology*, 1997 (The Royal Society of Chemistry)
18. Topping, J. A., Cameron, N. and Murthy, M. K. 1974, *Journal of the American Ceramic Society*, Volume 57, p. 519.
19. Keith, H. D. and Padden F. J. 1961, *Journal of Applied Physics*, Volume 35, Number 4, p. 1270.
20. Eysel, C. 1984, *ICDD Grant-in-Aid*, Mineralogisch-Petrographisches Institut, Universitat Heidelberg, Germany.
21. Hahn T. *International Tables for Crystallography, Volume A:space-group symmetry*, 1987 (D. Reidel Publishing Company).
22. Suryanarayana, C. and Norton, M.G. *X-ray Diffraction- A Practical Approach*, 1998 (Plenum Press, New York and London).
23. Microcal Software, *Microcal Origin, Version 5.1*, 1991-1997 (Microcal Software, Inc.)
24. Layton, M.M. and Smith, J.W. 1975, *Journal of American Ceramic Society*, Volume 58, Number 9-10, p. 435.
25. Borrelli, N.F. and Layton, M.M. 1971, *Journal of Non-Crystalline Solids*, Volume 6, p. 197.
26. Hench, L. L. and West, J. K. *Principles of Electronic Ceramics*, 1990 (John Wiley & Son).

27. Tomozawa, M. and Doremus, R. H. *Treatise on Materials Science and Techonology: Volume 12*, 1977 (Academic Press)
28. Xu, Y. *Ferroelectric Materials and Their Applications*, 1991 (North-Holland).
29. Wu, S. Y. 1979, *Journal of Applied Physics*, Volume 50, p. 4314.
30. Moulson, A. J. and Herbert, J. M. *Electroceramics*, 1990 (Chapman & Hall).

Chapter 6

The lead germanate and lead niobate systems

6.1 Introduction

$Pb_5Ge_3O_{11}$ has been the subject of much interest, as a result of its low processing temperature and possible applications as a pyroelectric sensor and nonvolatile ferroelectric memory.[1] Pb^{2+} has a high electronic polarisability, therefore high refractive indices and large electro-optic effects can be achieved from materials containing lead ions. Since 1971 the ferroelectric properties of $Pb_5Ge_3O_{11}$ single crystals were discovered by Iwasaki and Sugii [2] and many scientific workers have investigated $Pb_5Ge_3O_{11}$-based ferroelectric materials with high transparency in various forms, such as single crystals, thin films and glass-ceramics. [1-11]

The glass-ceramic method has been considered as a fabrication route since this phase (62.5 mole% PbO : 37.5 mole% GeO_2) contains a good glass former (GeO_2) which plays an important role in the formation of glasses. However, there are some obstacles to make a glass with the stoichiometric composition since this is close to the glass-forming boundary and has a tendency to be unstable during the glass-making process. Moreover, the fluidity of the melt and the thermal expansion of the glass are quite high, thus devitrification of the $Pb_5Ge_3O_{11}$ phase easily occurs and the quenched sample breaks due to the resulting stresses.

In this project, two systems were considered, as follows:

1. The addition of SiO_2 to the binary (PbO-GeO_2) glass system. [12-15]
2. The addition of another corresponding ferroelectric phase to the $Pb_5Ge_3O_{11}$ phase.

Hasegawa et al [14] prepared highly transparent glass-ceramics in which the solid solution ferroelectric phases $Pb_5Ge_{3-x}Si_xO_{11}$ ($0 \leq x \leq 1.75$) were crystallised with

small particle size, < 3000 Å. The observed Curie temperatures (T_Cs) were 175°C, 115°C and 65°C for glass-ceramics of $Pb_5Ge_{3-x}Si_xO_{11}$ with x = 0, 0.5 and 1 respectively. Therefore, it can be assumed that increase of the SiO_2 content lowers the Curie point of the ferroelectric glass-ceramic in addition to stabilising glass formation.

Some groups have tried to add an additional ferroelectric phase to $Pb_5Ge_3O_{11}$ in order to produce multiple ferroelectric glass-ceramics. For example, Cornejo and Haun [11] studied glass compositions in the $Pb_5Ge_3O_{11}$-$PbTiO_3$ (PG-PT) and $Pb_5Ge_3O_{11}$-$Pb(Zr_{1/2}Ti_{1/2})O_3$ (PG-PZT) systems. It has been found that the addition of PT and PZT to PG enhanced the electrical properties of the materials. Consequently, this work suggested a new ferroelectric glass-ceramic system, based on the lead germanate $Pb_5Ge_3O_{11}$ phase with the addition of lead niobate. Lead niobate ($PbNb_2O_6$) was considered to be interesting because it possesses ferroelectric properties, making it one of the most important commercial piezoelectric-ceramics. In this case, it should be interesting to mix these two phases, $Pb_5Ge_3O_{11}$ and $PbNb_2O_6$, in the form of glass-ceramic, in order to investigate the extended properties of the new ferroelectric materials for various applications.

6.2 $Pb_5Ge_3O_{11}$ (PG)

Initially the base glass of stoichiometric composition (5PbO: $3GeO_2$), was prepared using 99% red lead oxide (Pb_3O_4) and Puratronic 99.999% germanium (IV) oxide (GeO_2). An ~40 gram batch was mixed and melted, in a Pt/10Rh crucible, in an air atmosphere at 750°C for about 30 minutes. The melt was then quenched by pressing between liquid-N_2 cooled copper plates. As a result of this, broken pieces of partly glassy material, with thickness of about 0.5 mm were obtained. X-ray diffraction showed some devitrification, giving the $Pb_5Ge_3O_{11}$ (JCPDS No. = 24-0576) phase. It was noticed that the viscosity of the melt was quite low, which was

also observed by Cornejo and Haun [11]. Hence, the problem of controlled formation of the glass-ceramics has been underlined since a good base glass was itself difficult to achieve. However, the attempt to fabricate multiple glass-ceramics (PG-PN) continued in the belief that the addition of Nb_2O_5 might ease the formation of the glass.

6.3 $Pb_5Ge_3O_{11}$:$PbNb_2O_6$ (PG-PN)

Five different compositions on the tieline from the system figure 6.1 have been studied.

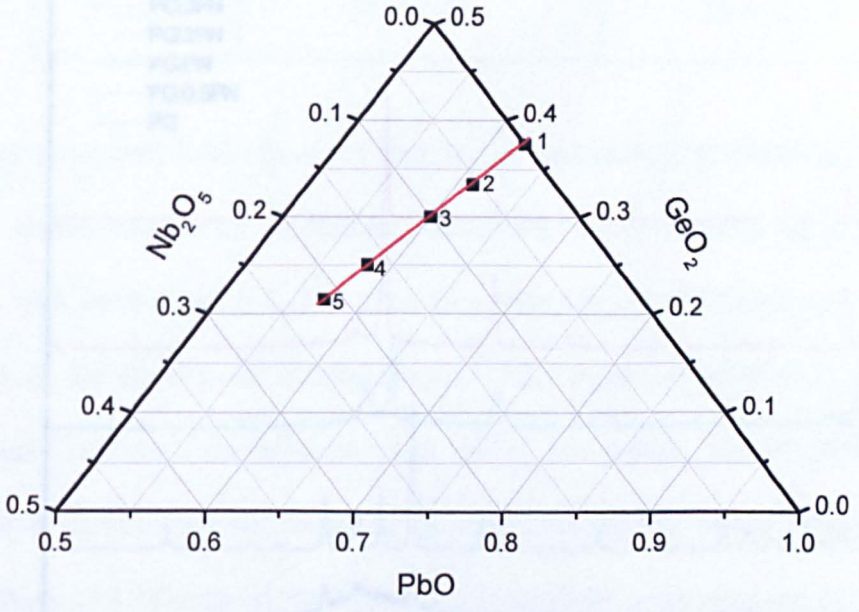

Sample Number	The ratio of PG/PN	PbO (mol%)	GeO_2 (mol%)	Nb_2O_5 (mol%)
1	PG	62.5	37.5	0
2	PG:0.5PN	61.1	33.4	5.5
3	PG:PN	60	30	10
4	PG:2PN	58.3	25	16.7
5	PG:3PN	57.2	21.4	21.4

Figure 6.1 *Five compositions from the PbO-GeO_2-Nb_2O_5 system.*

The starting materials: reagent-grade red lead oxide ([I]Pb_3O_4), germanium oxide ([II]GeO_2) and niobium(V) oxide ([III]Nb_2O_5)were mixed. Each batch, of about 30 g, was then melted in the electric furnace at temperatures in the range 1000 to 1150 °C. Unfortunately, the melts had noticeably low viscosity, giving rise to the crystallisation of unwanted phases upon quenching on the liquid-N_2 cooled stainless steel plate. The powder diffraction patterns of these samples are shown in figure 6.2 and Table 6.1 contains the crystallisation information.

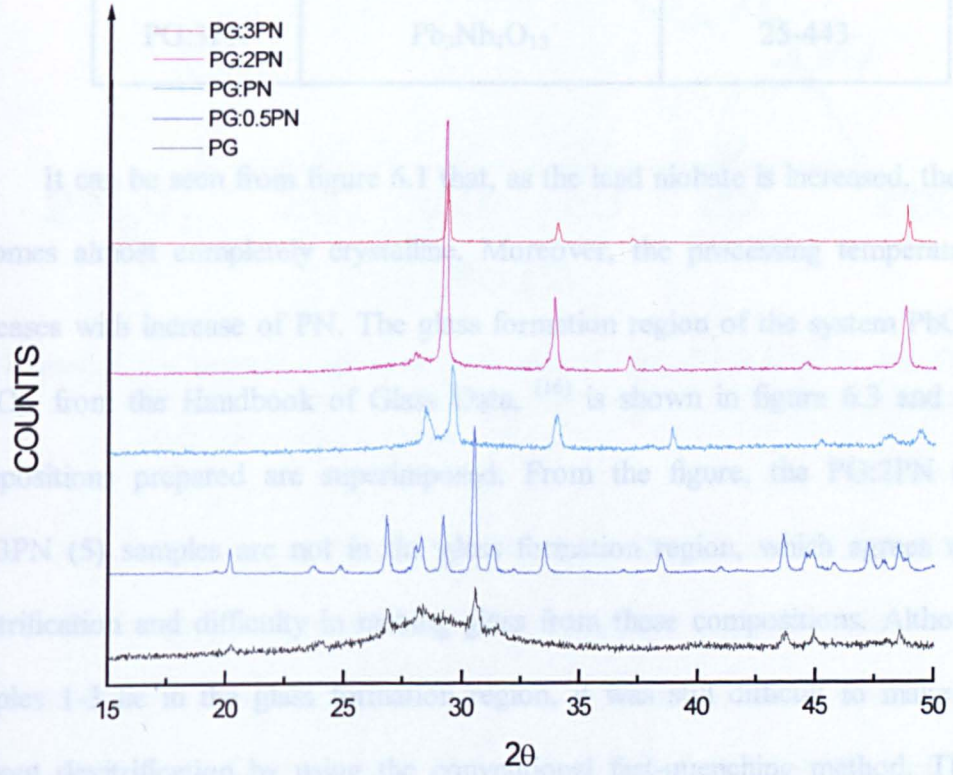

Figure 6.2 *The comparison of the X-ray diffraction patterns of the PG-PN quenched samples.*

[I] Pb_3O_4 – 99% red lead oxide (Aldrich)
[II] GeO_2 – 99.999% Puratronic Germanium (IV) oxide (Alfa Aesar)
[III] Nb_2O_5 – 99.99% Niobium (V) oxide (Aldrich)

Table 6.1 *The crystallisation information for PG, PG:0.5PN, PG:PN, PG:2PN and PG:3PN samples.*

Sample	Devitrification phase	JCPDS Number
PG	$Pb_5Ge_3O_{11}$	24-576
PG:0.5PN	$Pb_5Ge_3O_{11}$ & $Pb_2Nb_2O_7$	24-576 & 40-829
PG:PN	$Pb_2Nb_2O_7$	43-960
PG:2PN	$Pb_5Nb_4O_{15}$	46-637
PG:3PN	$Pb_3Nb_4O_{13}$	25-443

It can be seen from figure 6.1 that, as the lead niobate is increased, the sample becomes almost completely crystalline. Moreover, the processing temperature also increases with increase of PN. The glass formation region of the system PbO-GeO_2-Nb_2O_5, from the Handbook of Glass Data, [16] is shown in figure 6.3 and the five compositions prepared are superimposed. From the figure, the PG:2PN (4) and PG:3PN (5) samples are not in the glass formation region, which agrees with the devitrification and difficulty in making glass from these compositions. Although the samples 1-3 lie in the glass formation region, it was still difficult to make glasses without devitrification by using the conventional fast-quenching method. This may result from compositional change during melting, as lead oxide is fairly volatile. The alumina-sheet lid was placed onto the Pt-crucible and the time at temperature for homogenisation of the glass, was reduced to about 15-20 minutes. The observed weight losses are in fact quite low, between 0.7% and 1.2%. In order to cope with this problem, a more rapid quenching technique, such as the apparatus used for the quenching of refractory oxide melts (quenching rate about 10^7 degrees sec^{-1}) might be

needed. [17] Another possible way is to add a small amount of either glass-forming oxide (GeO_2) or volatilised oxide (PbO) to the compositions.

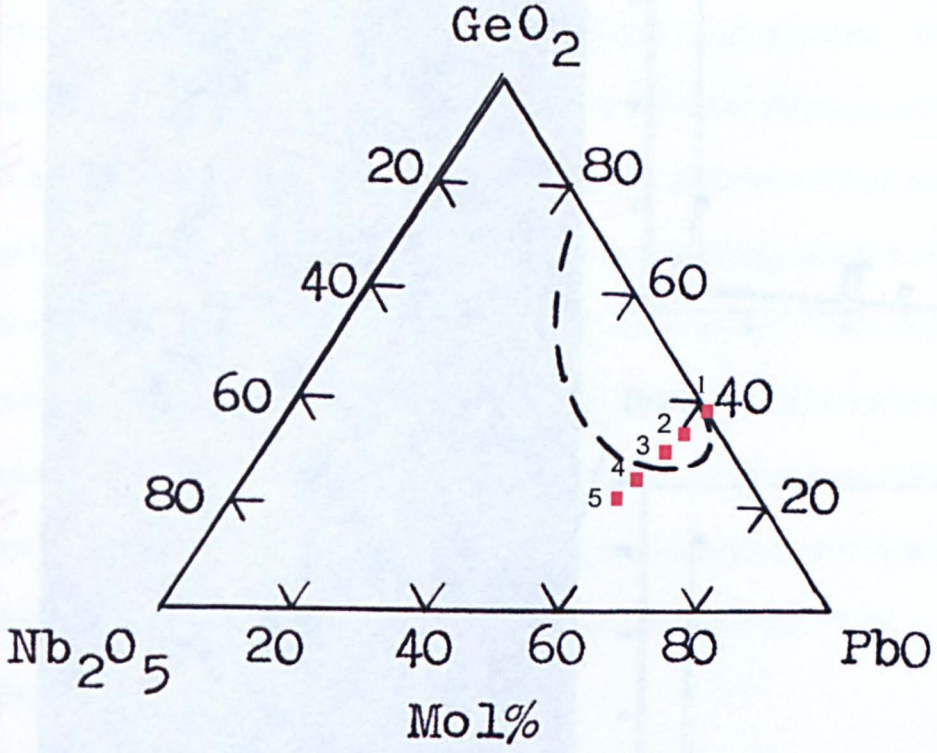

Figure 6.3 *The location of five compositions: PG (1), PG:0.5PN (2), PG:PN (3), PG:2PN (4) and PG:3PN (5), with the glass formation region in $PbO:GeO_2:Nb_2O_5$ system.* [16]

Quenched samples of PG (1), PG:PN (3), PG:2PN (4) and PG:3PN (5) were of limited use for property measurement since they had fragmented due to thermal shock. However, sample PG:0.5PN (2) could be quenched into a sizeable piece of glass-ceramic. Using XRD and EDS analysis, it was confirmed that this glass-ceramic contains the two interesting phases: $Pb_5Ge_3O_{11}$ and $Pb_2Nb_2O_7$. The SEM backscattering image of the PG:0.5PN cross-section is illustrated in figure 6.4. It can be seen that the crystallisation of $Pb_2Nb_2O_7$ with crystallites between 1 to 10 μm in size, occurred randomly in the sample. These in turn were surrounded by a thin layer about 0.5-1 μm of $Pb_5Ge_3O_{11}$ phase. The explanation is that the $Pb_2Nb_2O_7$ precipitates first followed by surface nucleation and growth of the $Pb_5Ge_3O_{11}$ phase.

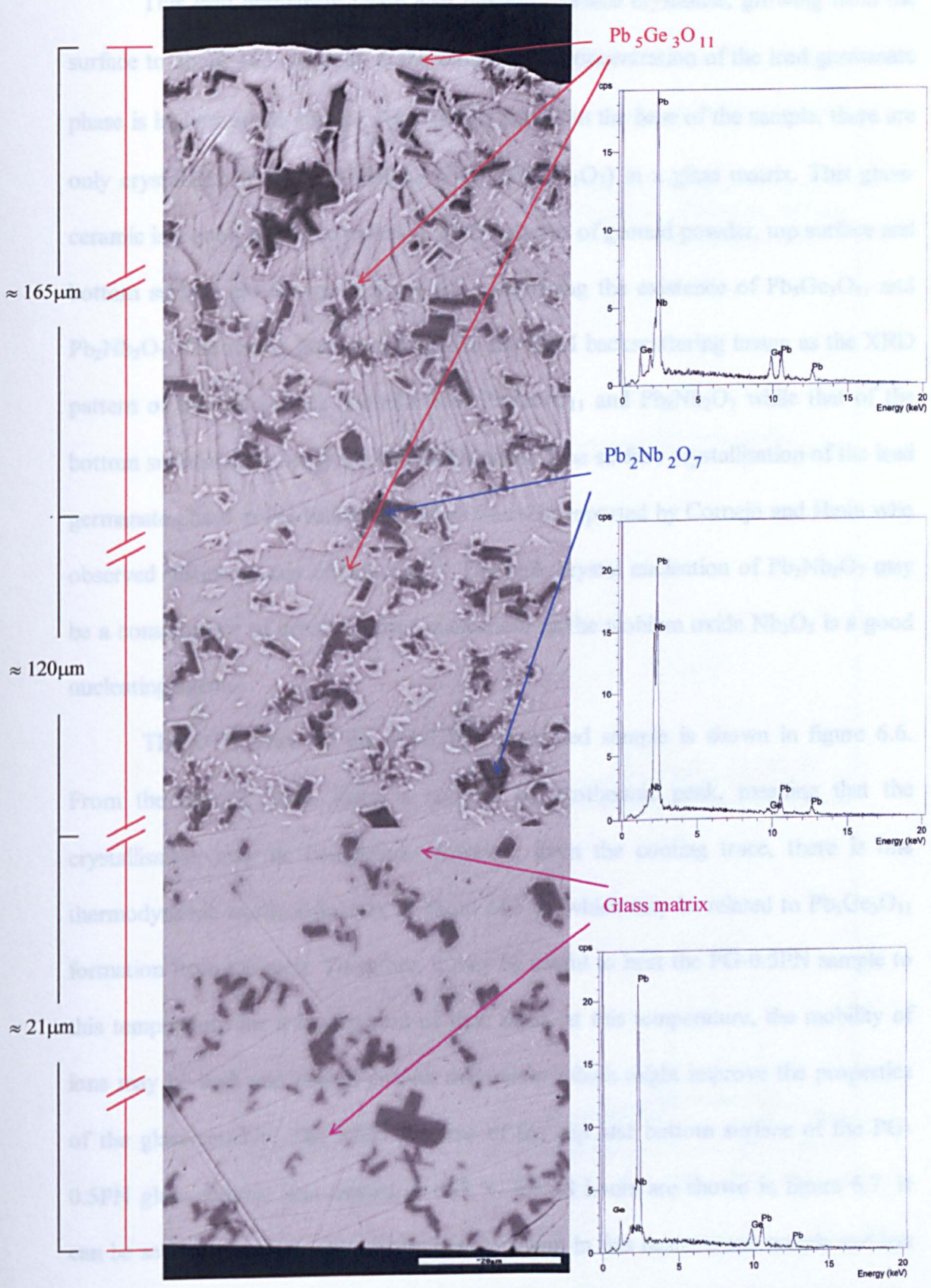

Figure 6.4 *The electron back-scattering image and EDS spectra of the PG-0.5PN quench-melt cross-section of 306μm in thickness.*

This lead germanate phase also tends to surface crystallise, growing from the surface to about 165 μm deep in the sample. The concentration of the lead germanate phase is highest at the surface. At about 21 μm from the base of the sample, there are only crystallites of the lead niobate phase ($Pb_2Nb_2O_7$) in a glass matrix. This glass-ceramic is a good pore-free material. XRD patterns of ground powder, top surface and bottom surface are shown in figure 6.5, confirming the existence of $Pb_5Ge_3O_{11}$ and $Pb_2Nb_2O_7$. The results are consistent with the SEM backscattering image as the XRD pattern of the top surface contains both $Pb_5Ge_3O_{11}$ and $Pb_2Nb_2O_7$ while that of the bottom surface shows only the $Pb_2Nb_2O_7$ phase. The surface crystallisation of the lead germanate phase in PG-based thick films was also reported by Cornejo and Haun who observed distinct c-axis orientation.[11] The bulk crystal nucleation of $Pb_2Nb_2O_7$ may be a consequence of heterogeneous nucleation, as the niobium oxide Nb_2O_5 is a good nucleating agent.

The DTA trace of the PG-0.5PN quenched sample is shown in figure 6.6. From the heating trace, there is no sign of exothermic peak, meaning that the crystallisation may be completed. However, from the cooling trace, there is one thermodynamic exothermic peak at about 667 °C which may be related to $Pb_5Ge_3O_{11}$ formation from the melt. Therefore, it may be useful to heat the PG-0.5PN sample to this temperature for a long period of time since, at this temperature, the mobility of ions may be high and crystal growth may occur which might improve the properties of the glass-ceramic. The XRD patterns of the top and bottom surface of the PG-0.5PN glass-ceramic heat-treated at 667 °C for 48 hours are shown in figure 6.7. It can be seen that surface crystallisation is dominant in this heat-treated sample and has specific orientation perpendicular to the (h00) planes, i.e. crystallographic a-axis orientation. However, the mechanical strength of this heat-treated sample was quite poor and the sample was easily broken.

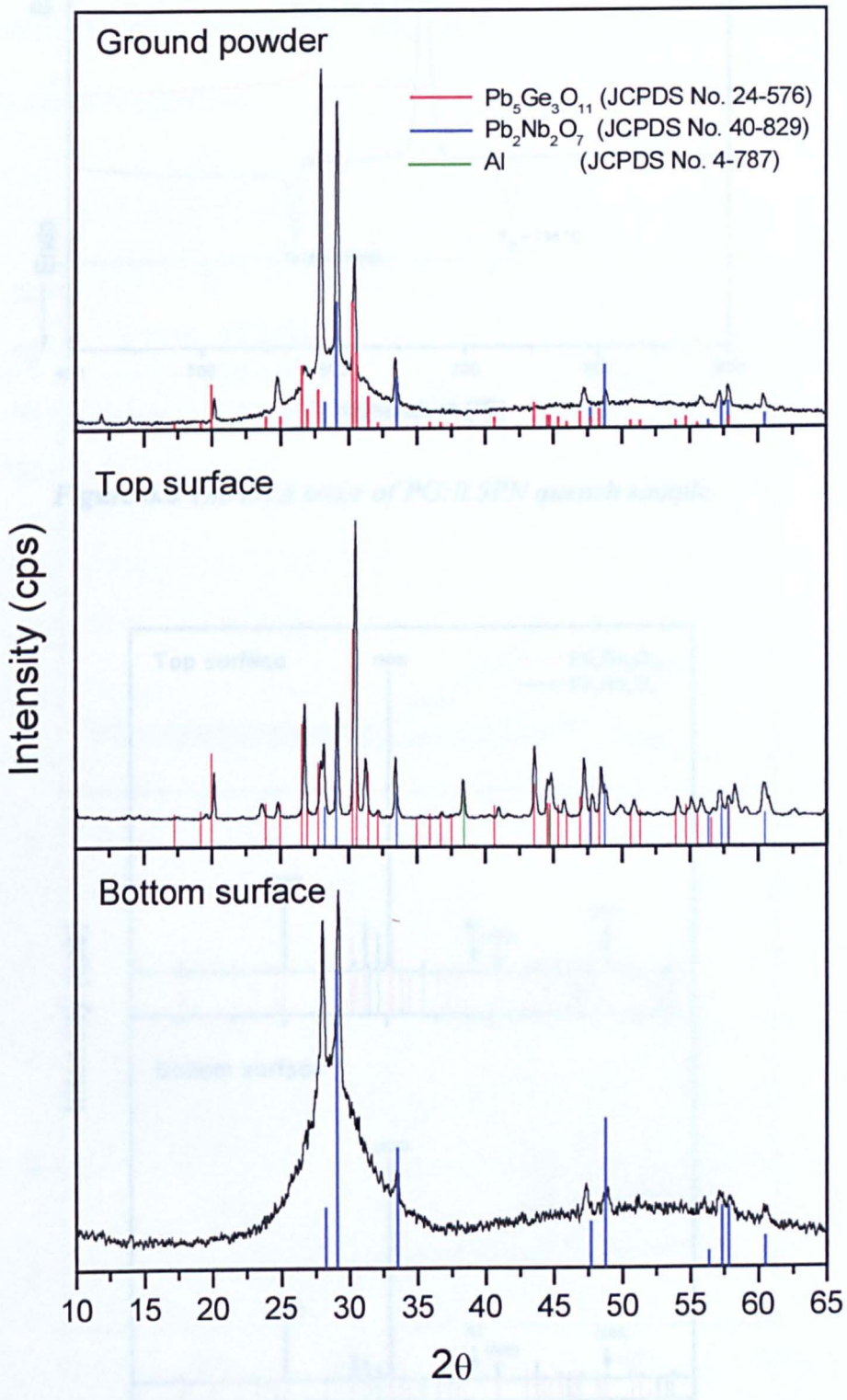

Figure 6.5 *The XRD pattern of ground powder and top and bottom surface of PG:0.5PN quenched sample.*

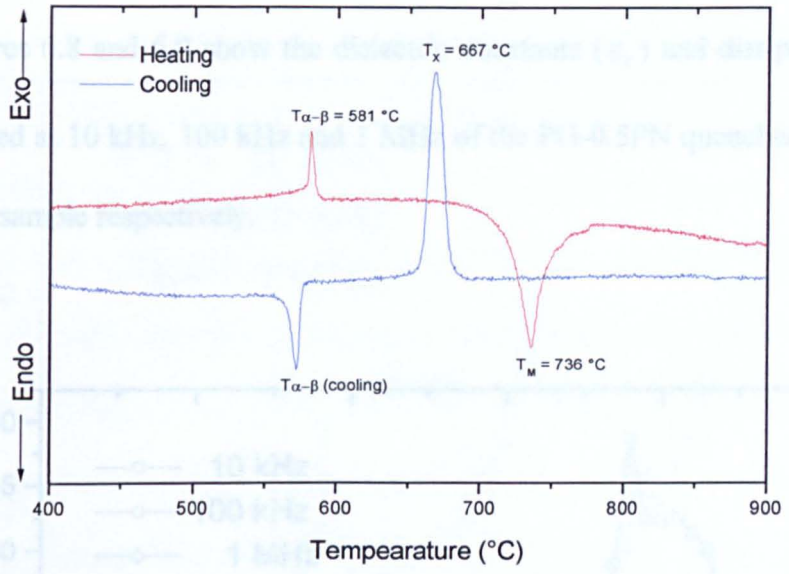

Figure 6.6 *The DTA trace of PG:0.5PN quench sample.*

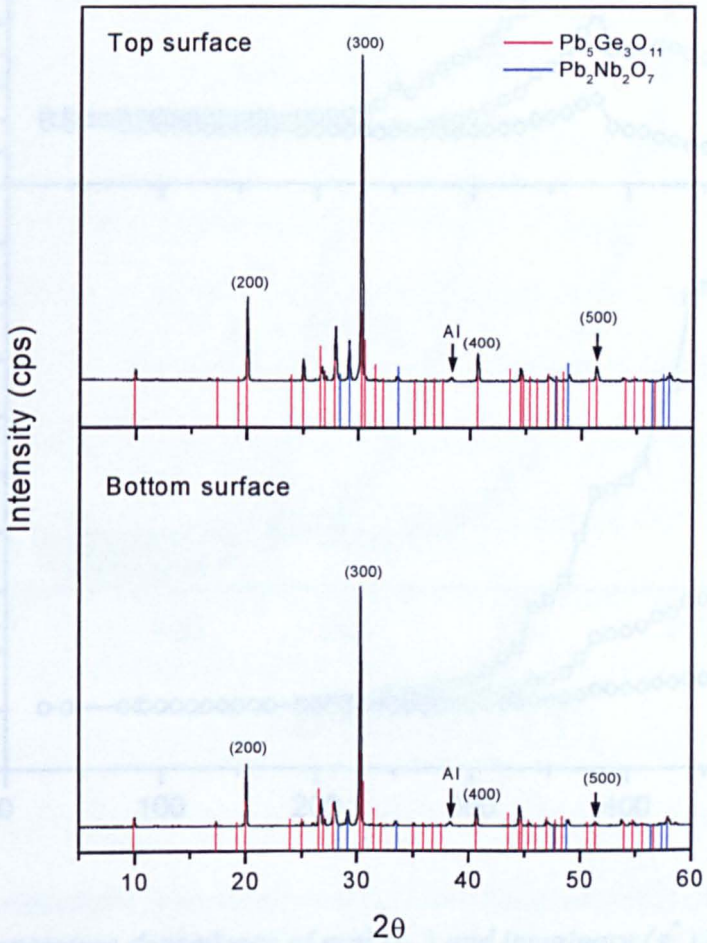

Figure 6.7 *The XRD pattern of the top and bottom surface of PG-0.5PN subjected to heat treatment at 667°C for 48 hrs.*

6.4 Dielectric measurement

Figures 6.8 and 6.9 show the dielectric constants (ε_r') and dissipation factors (ε_r'') measured at 10 kHz, 100 kHz and 1 MHz of the PG-0.5PN quenched sample and heat-treated sample respectively.

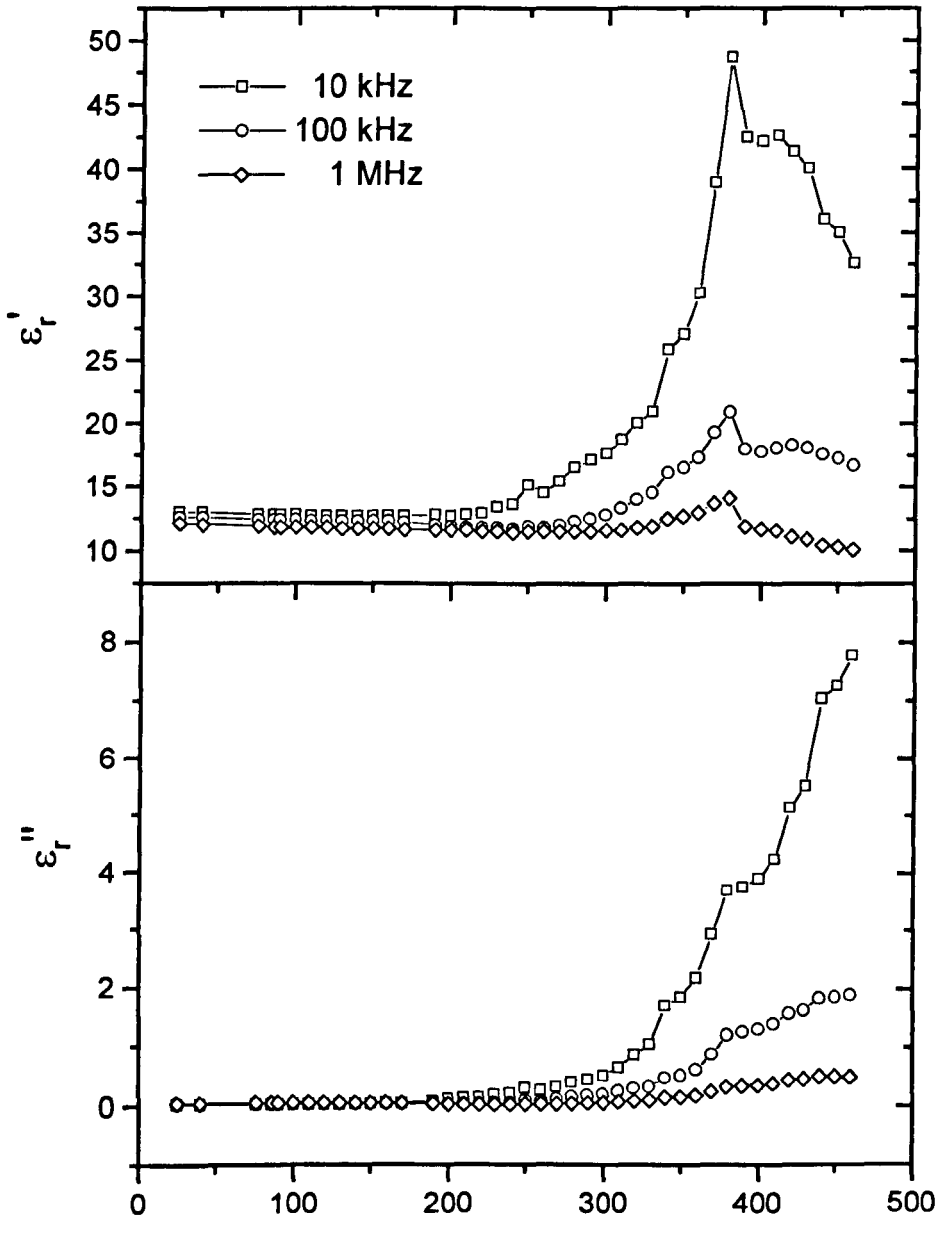

Figure 6.8 *Temperature dependence of real (ε_r') and imaginary (ε_r'') part of complex permittivity of PG-0.5PN quenched sample of about 0.040±0.002 cm in thickness.*

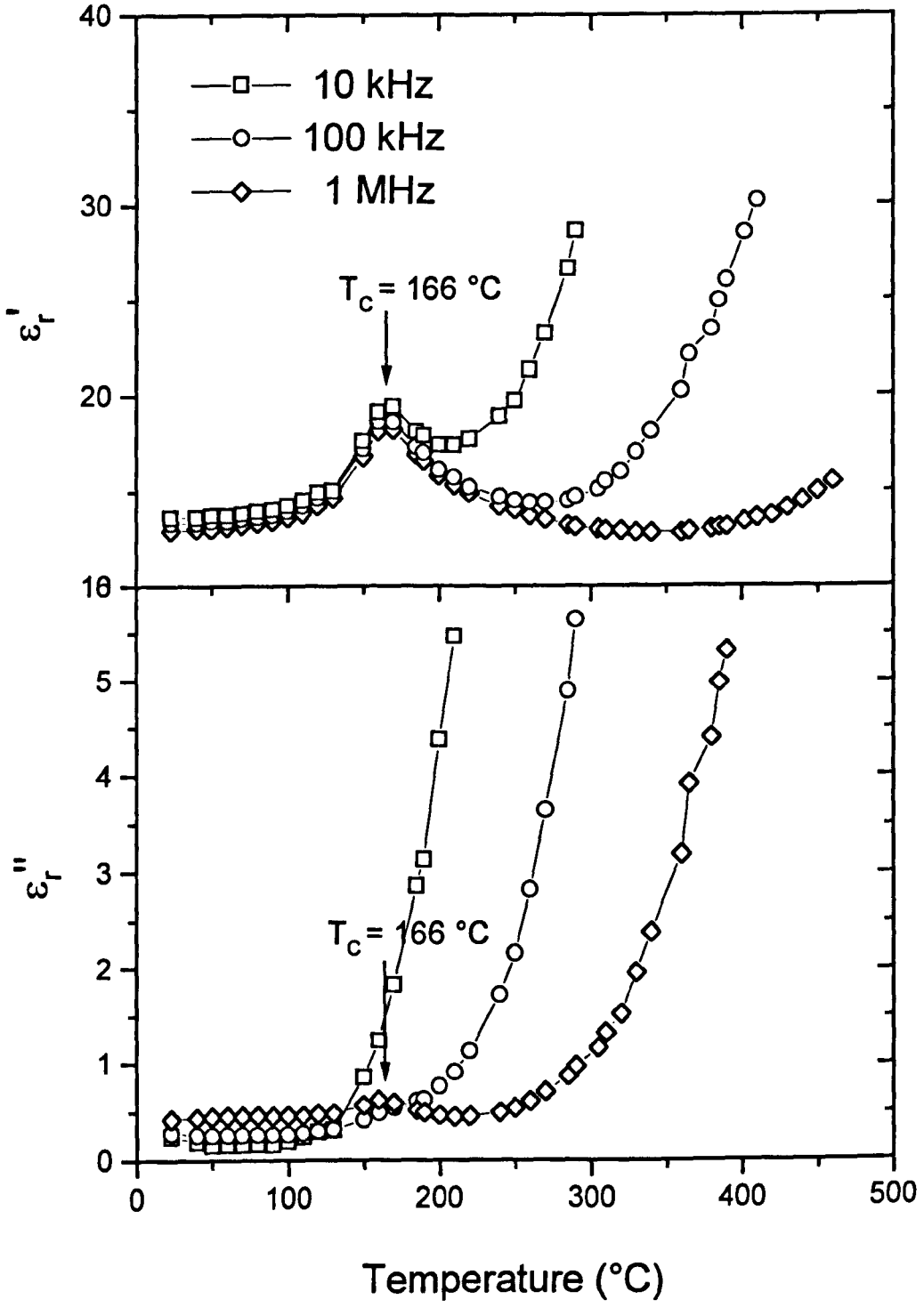

Figure 6.9 Temperature dependence real (ε_r') and imaginary (ε_r'') part of complex permittivity of PG-0.5PN subjected to heat treatment at 667°C for 48 hrs of about 0.140±0.002 cm in thickness.

From figure 6.8, there is a noticeable peak at about 380 °C. This does not correspond to the Curie point of $Pb_5Ge_3O_{11}$ which, in the single crystal of this phase has T_C = 177 °C. This sample was very thin (about 0.042 cm) so the $Pb_5Ge_3O_{11}$ phase from the surface could be polished off and in that case the $Pb_2Nb_2O_7$ phase was dominant. Therefore, this peak may be attributed to some transition of the $Pb_2Nb_2O_7$ phase that affects the decrease in dielectric constant. However, if there is a phase transition of $Pb_2Nb_2O_7$, the DTA heating trace should have some noticeable exothermic peak but, as can be seen from figure 6.6, no such peak occurs. It is possible that the activation energy of this transition is very small, rendering the exotherm from a small volume fraction unobserved by conventional DTA analysis. Even though this phase has been investigated by many researchers [18-25], there is no information on phase transitions of this phase at high temperature. The study of dielectric properties and phase transition of $Pb_2Nb_2O_7$ at low temperature by Cook et al [18], Shirane et al [19] and Hulm [20] suggested that, in this lead pyroniobate ($Pb_2Nb_2O_7$), the dielectric constant peak at around 15 K might be associated with an antiferroelectric phase transition. However, they stated that it is difficult to reconcile either ferroelectric or antiferroelectric behaviour with the negative Curie-Weiss temperature. Moreover, Siegwarth et al [21] also studied the dielectric and thermal properties of pyrochlore $Pb_2Nb_2O_7$ at low temperature and showed that there was no evidence for a phase transition at 15 K, which is contrary to previous suggestions, and the peak in the dielectric constant may be due to relaxation phenomena. Consequently, there has not yet been agreement as to whether this phase is antiferroelectric. $Pb_2Nb_2O_7$ has been of interest because its structure is pyrochlore type; similar to ferroelectric $Cd_2Nb_2O_7$ which shows a Curie temperature at about 170 K.[22] However, the crystal structure of cadmium niobate is a face-centered cubic lattice while the structure of $Pb_2Nb_2O_7$ formed by conventional ceramics method,

which has been used for low temperature studies [18-22], is rhombohedral.[23,24] This may make its properties different from $Cd_2Nb_2O_7$. Additionally, high-pressure studies on the lead pyroniobate by Jayaraman et al,[25] showed the rhombohedral structure could be changed to the cubic pyrochlore structure at 13 GPa. In addition to this cubic $Pb_2Nb_2O_7$ there is also a monoclinic polymorph. Since, the $Pb_2Nb_2O_7$ observed in this work is rhombohedral; there may be a phase transition from rhombohedral to another structure at about 380 °C as mentioned above. However, extensive study of this particular $Pb_2Nb_2O_7$ phase transition is needed.

From the dielectric parameters in Figure 6.9, the Curie point (T_C) of the PG-0.5PN heat-treated at 667°C for 48 hours was observed to be about 166 °C which is somewhat lower than the single crystal value of 177°C. This type of behaviour may be caused by two mechanisms: internal stress and impurities. The internal stresses may be attributed to small grain size, residual matrix or combination of both.[26-27] However, if internal stress actually occurred, it would shift the XRD peaks, which was not observed in the PG-0.5PN subjected to heat treatment at 667 °C for 4 hours (figure 6.9). Therefore, the decrease in T_C may result from impurities because, according to Cornejo,[28] impurities in PG have a large effect in shifting T_C, especially when lead is replaced. At 1 MHz (room temperature), the dielectric constant (ε_r') of this sample was about 13 whereas, that of the PG ($Pb_5Ge_3O_{11}$) bulk sample from Cornejo and Haun[11] was about 27. The bulk sample from Cornejo and Haun had c-axis orientation but the PG-0.5PN glass-ceramic, heat treated at 667°C for 48 hours, has a-axis orientation, so this may be the cause of the lower value of dielectric constant. Furthermore, the PG-0.5PN glass-ceramic not only contains ferroelectric $Pb_5Ge_3O_{11}$ phase but also rhombohedral $Pb_2Nb_2O_7$, it may be assumed that the addition of this lead pyroniobate gives the decrease in dielectric properties.

6.5 Hysteresis loop

Hysteresis loops and electrical poling of the quenched sample PG-0.5PN were not achieved with electric fields up to 25 kV/cm. However, the PG-0.5PN sample of 0.026 cm thickness, heat treated at 667 °C for 48 hours, gives a noticeable ferroelectric hysteresis loop at room temperature (figure 6.10) with voltage supply equal to 1 kV (50 Hz), which is expected because this heat treated sample contains a greater amount of the $Pb_5Ge_3O_{11}$ ferroelectric phase than the untreated sample.

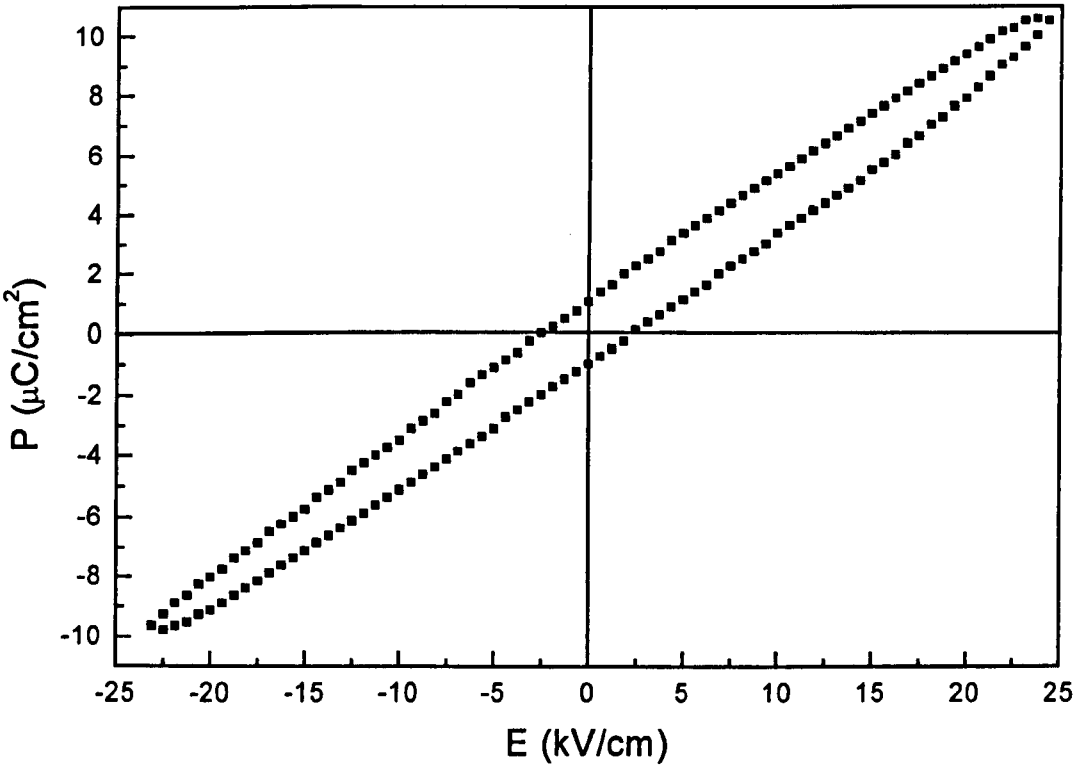

***Figure 6.10** Hysteresis loop at room temperature (50 Hz) of PG-0.5PN glass-ceramic of 0.026±0.002 cm thickness, heated at 667°C for 48 hours.*

Table 6.2 shows a comparison of the important ferroelectric parameters of the heat-treated PG-0.5PN sample and some related materials. The spontaneous polarisation value (Ps) at room temperature of the PG-0.5PN sample is quite small

compared to that of a single crystal but slightly higher than the Ps value of the thick film (60 μm), with 28% c-axis orientation of the $Pb_5Ge_3O_{11}$ crystals, prepared by Takahashi et al [29], using the rapid-quenching method. They suggested that, by increasing the fraction of c-plane orientation, electric properties would be improved, judging from the data from the single crystal. The orientation of the surface crystallisation in the PG-0.5PN heat treated sample is along the a-axis so giving a lower P_s value than that of single crystal. Consequently, attempts at preparing PG-based glass-ceramic with c-axis orientation together with ferroelectric $PbNb_2O_6$ should be carried forward. However, good parent glasses from $PbO:GeO_2:Nb_2O_5$ system for forming this particular glass-ceramic are needed.

Table 6.2 *The comparison of T_C (curie temperature), P_s (spontaneous polarisation) and E_r (coercive field) of the PG-0.5PN sample and some related ferroelectrics.*

Ferroelectrics	T_C (°C)	P_s (at room temperature) ($\mu C/cm^2$)	E_r (kV/cm)
PG-0.5PN (Glass-ceramic)	≈166	≈1	≈2.5
$Pb_5Ge_3O_{11}$ [30] (Single crystal)	177	4.8	14
PG [29] (Thick film)	155-177	0.2-0.8	-

6.6 Further investigation of the $PbO:GeO_2:Nb_2O_5$ system

Attempts to fabricate $Pb_5Ge_3O_{11}$-based glasses progressed with the preparation of samples 6 to 10, as shown in the ternary $PbO:GeO_2:Nb_2O_5$ diagram of (figure 6.11). Table 6.3 shows the nominal compositions of these glasses.

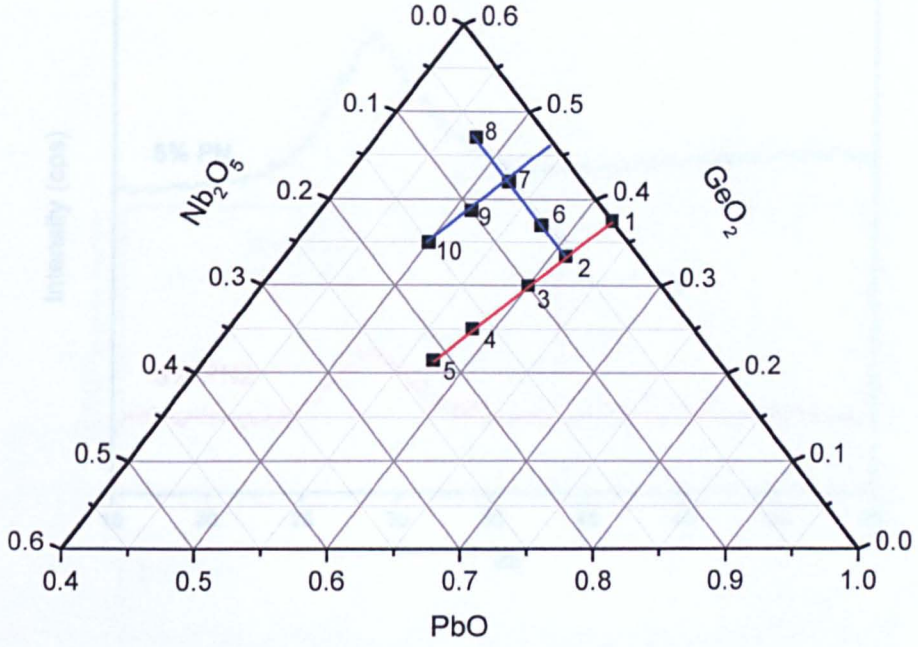

Figure 6.11 *Additional samples in the $PbO:GeO_2:Nb_2O_5$ system.*

Table 6.3 *The nominal compositions of the samples 6-7 from the $PbO:GeO_2:Nb_2O_5$ system.*

Sample Number	The ratio of PG/PN	PbO (mol%)	GeO_2 (mol%)	Nb_2O_5 (mol%)
6	5%PN1	56.9	37.6	5.5
7	5%PN	52.5	42	5.5
8	5%PN2	47.5	47	5.5
9	10%PN	51.4	38.6	10
10	15%PN	50	35	15

Only 5%PN (7) and 5%PN2 (8) glasses were made successfully by quenching from about 1000°C processing temperature. The rest show some devitrification on quenching. The phase crystallised from 5%PN1, 10%PN and 15% PN was $Pb_2Nb_2O_7$ (JCPDS No. 40-829) and the samples were in a poor mechanical state.

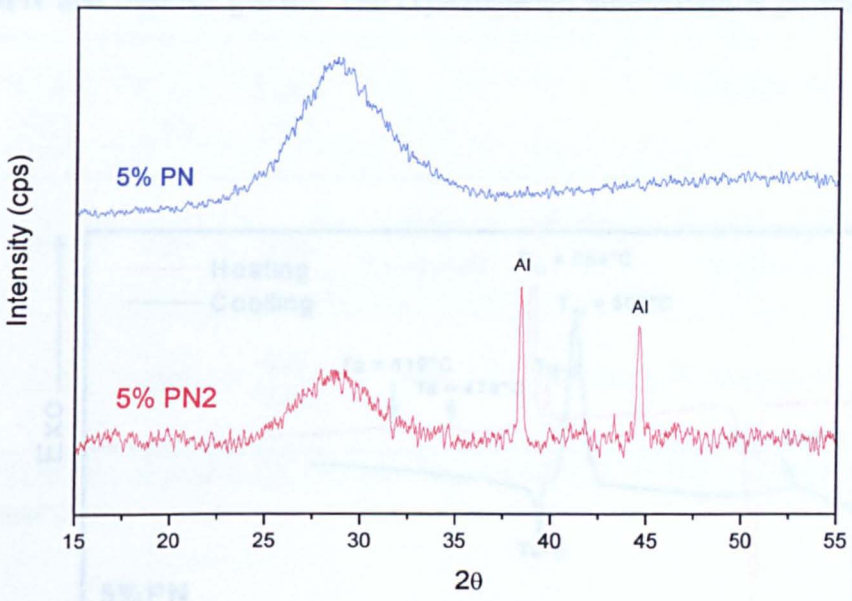

Figure 6.12 *The amorphous powder diffraction patterns of the 5%PN (7) and 5%PN2 (8).*

The amorphous XRD patterns and DTA traces of 5%PN and 5% PN2 glasses are shown in figure 6.12 and figure 6.13 respectively. From the DTA traces, it can be seen that 5%PN2 glass is more stable than 5%PN glass as the cooling curve of 5%PN2 shows no exothermic peaks while that of 5%PN shows two peaks. Moreover, the melting point of 5%PN2 is less than that of 5%PN. The increased addition of GeO_2 reduces the melting temperature and enhances the stability of 5%PN2 glass. Note that the cooling trace of 5%PN2 has no $T_{\alpha-\beta}$ quartz transition because, during DTA analysis this sample was heated to 1500 °C while 5%PN was heated only to 1100 °C. According to the phase transitions of SiO_2 as shown in figure 6.14, the tridymite ↔ quartz transition is slow and the endothermic peak at 220 °C in the 5%PN2 cooling trace should be related to $T_{\alpha-\beta}$ (tridymite). This was confirmed by the XRD pattern of SiO_2 powder, after similar DTA analysis, which matched the tridymite phase.

Heat treatments at all crystallisation temperatures ($T_X(s)$) were then applied to both 5%PN and 5%PN2 glasses. The crystallisation information is presented in table 6.4.

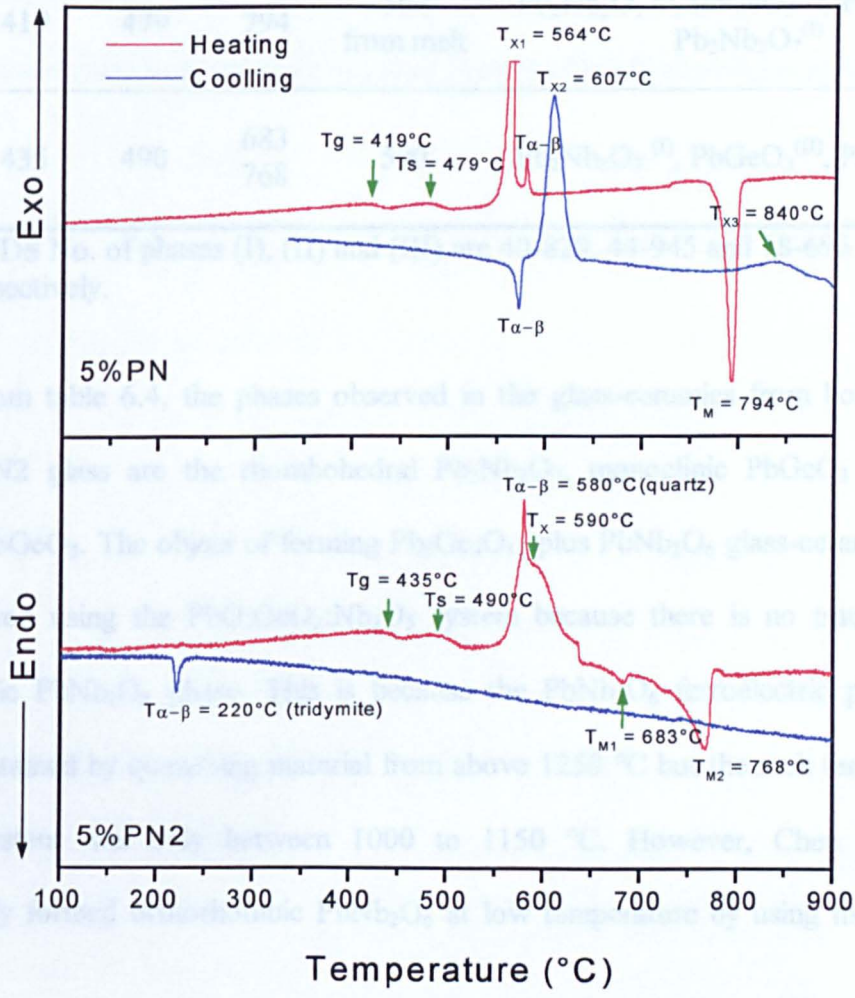

Figure 6.13 *The Differential Thermal Analysis (DTA) trace of 50%PbO: 40%GeO_2: 5%Nb_2O_5 (10%$NbO_{2.5}$) glass powder with 5°C/min heating rate.*

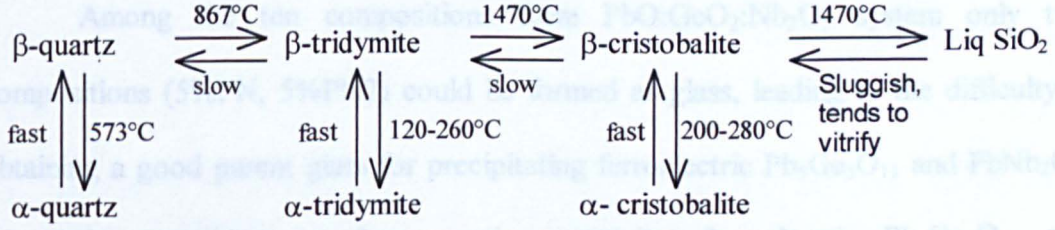

Figure 6.14 *The phase transitions diagram of SiO_2. (after Greenwood and Earnshaw).*[31]

Table 6.4 Thermal parameters, crystallisation temperatures and crystalline phases of all glass-ceramics from 5%PN and 5%PN2 glasses.

Sample	$T_g \pm 1$ (°C)	$T_s \pm 1$ (°C)	$T_m \pm 1$ (°C)	$T_x \pm 1$ (°C)	Crystalline phase
5%PN	419	479	794	564 from melt	$Pb_2Nb_2O_7$ [(I)], $PbGeO_3$[(II)], $PbGeO_3$[(III)] $Pb_2Nb_2O_7$[(I)]
5%PN2	435	490	683 768	590	$Pb_2Nb_2O_7$ [(I)], $PbGeO_3$[(II)], $PbGeO_3$[(III)]

Note: JCPDS No. of phases (I), (II) and (III) are 40-829, 44-945 and 18-696 respectively.

From table 6.4, the phases observed in the glass-ceramics from both 5%PN and 5%PN2 glass are the rhombohedral $Pb_2Nb_2O_7$, monoclinic $PbGeO_3$ and non indexed $PbGeO_3$. The object of forming $Pb_5Ge_3O_{11}$ plus $PbNb_2O_6$ glass-ceramics, was not achieved using the $PbO:GeO_2:Nb_2O_5$ system because there is no trace of any ferroelectric $PbNb_2O_6$ phase. This is because the $PbNb_2O_6$ ferroelectric phase can only be obtained by quenching material from above 1250 °C but the melt temperature of this system was only between 1000 to 1150 °C. However, Chen et al [23] successfully formed orthorhombic $PbNb_2O_6$ at low temperature by using molten salt synthesis.

6.7 Summary

Among the ten compositions from $PbO:GeO_2:Nb_2O_5$ system only two compositions (5%PN, 5%PN2) could be formed as glass, leading to the difficulty in obtaining a good parent glass for precipitating ferroelectric $Pb_5Ge_3O_{11}$ and $PbNb_2O_6$. By rapid quenching, a glass-ceramic containing ferroelectric $Pb_5Ge_3O_{11}$ and rhombohedral $Pb_2Nb_2O_7$ phase could be obtained from the PG-0.5PN composition. SEM and XRD analysis confirmed the surface crystallisation of $Pb_5Ge_3O_{11}$ with a-

axis orientation and the bulk crystallisation of $Pb_2Nb_2O_7$ phase. By applying the heat treatment at 667 °C for 48 hours, $Pb_5Ge_3O_{11}$ could be grown further in this glass-ceramic with a higher degree of a-axis orientation. A hysteresis loop was obtained from this heat treated sample, confirming the ferroelectricity of this glass-ceramic. However, the desired $PbNb_2O_6$ phase has not been observed, and $Pb_5Ge_3O_{11}$-$PbNb_2O_6$ based glass-ceramics have not been obtained from the PbO-GeO_2-Nb_2O_5 system.

References

1. Canale, J. E., Condrate, R. A., Nassau, K. and Cornilsen, B. C. 1987, *Materials Research Society Symposia Proceedings*, Volume 88, pp. 169-175.
2. Iwasaki, H. and Sugii, K. 1971, *Applied Physics Letters*, Volume 19, Number 4, p. 92.
3. Sugii, K., Iwsaki, H. and Miyazawa, S. 1971, *Materials Research Bulletin*, Volume 6, p. 503.
4. Iwata, Y., Koizumi, H., Koyano, N., Shibuya, I. and Niizeki, N. 1973, *Journal of Physics Society JAPAN*, Volume 35, p. 314.
5. Iwata, Y., Koyano, N., and Shibuya, I. 1973, *Journal of Physics Society JAPAN*, Volume 35, p.1269.
6. Hasegawa, H., Shimada, M., Koizumi, M. 1973, *Journal of Material Science*, Volume 8, p. 2923.
7. Schmitt, H. and Kleer, G. 1985, *Materials Research Bulletin*, Volume 20, p. 829.
8. Ying, X. L. and Chen, L. J. 1985, *Prog. Crystal Growth and Charact.*, Volume 11, p. 237.
9. Kim, J. H., Kim, J. B. and Lee, K. S. 1993, *Solid State Communications*, Volume 88, p. 727.
10. Kageyama, Y.Sakata, J. and Taga, Y. 1995, *Japanese Journal of Applied Physics*, Volume 34, p. 5158.
11. Cornejo, A. I. and Haun, M.J. 1996, *Materials Research Society Symposia Proceedings*, Volume 400, p.353.
12. Eysel, W., Wolfe, R. W. and Newnham, R. E. 1973, *Journal of the American Ceramic Society*, Volume 56, No. 4, p.185.
13. Topping, J. A., Fuchs, P. and Murthy, M. K. 1974, *Journal of the American Ceramic Society*, Volume 57, Number 5, p. 205.
14. Hasegawa, H., Shimada, M., Kanamaru, F. and Koizumi, M. 1977, *Bulletin Chemistry Society Japan*, Volume 50, Number 2, p.529.
15. Hasegawa, H., Shimada, M. and Koizumi, M. 1982, *Ceramics International*, Volume 8, Number 4, p.141.
16. Mazurin, O. V., Streltsina, M. V. and Shvsiko-Shvaikovskaya, T. P. *Handbook of Glass Data, Part D: ternary non-silicate glasses*, 1991 (ELSEVIER)
17. Nassau, K. 1980, *Journal of non-crystalline Solids*, Volume 42, p. 423.
18. Cook, W. R. and Jaffe, H. 1953, *Physics Review*, Volume 89 p. 1297.
19. Shirane, G. and Pepinsky, R. 1953, *Physics Review*, Volume 92, p. 504.
20. Hulm, J. K. 1953, *Physics Review*, Volume 92, p. 504.
21. Siegwarth, J. D., Lawless, W. N. and Morrow, A. J. 1976, *Journal of Applied Physics*, Volume 47, Number 9, p. 3789.
22. Cook, W. R. and Jaffe, H. 1952, *Physics Review*, Volume 88 p. 1426.
23. Li C. C., Chiu, C. C. and Desu, S. B. 1991, *Journal of the American Ceramic Society*, Volume 74, Number 1, p. 42.
24. Lu, C. H. and Lo, S. Y. 1997, *Materials Research Bulletin*, Volume 32, Number 3, p. 371.
25. Jayaraman, A. Kourouklis, G. A., Cooper, A. S. and Espinosa, G. P. 1990, *Journal of Physical Chemistry*, Volume 94, p. 1091.
26. Grossman, D. G. and Isard, J. O. 1969, *Mater. Sci.*, Volume 4, p. 1059.
27. Herczog, A. 1964, *Journal of the American Ceramic Society*, Volume 47, Number 3, p. 107.
28. Cornejo, I. A. 1994, *Ph.D. Thesis*, T-4631, Colorado School of Mines, Golden, Co, USA.

29. Takahashi, K., Ueda, H., Suzuki, T., and Kakegawa, K. 1994, *Ferroelectric*, Volume 154, p. 41.
30. Xu, Y., *Ferroelectric Materials and Their Applications*, 1991 (North-Holland).
31. Greenwood, N. N. and Earnshaw, A. *Chemistry of the Elements*, 1984 (Pergamon Press)

Chapter 7

The $Pb_5Ge_3O_{11}$: $PbNb_2O_6$: $SiO_2 + Al_2O_3$ system

7.1 Introduction

According to the findings in chapter 6, it is difficult to form $Pb_5Ge_3O_{11}$+$PbNb_2O_6$ based glass from the PbO:GeO_2:Nb_2O_5 system. However, the discovery of the highly transparent $Pb_5Ge_{3-x}Si_xO_{11}$ ($0 \leq x \leq 1.75$) ferroelectric glass-ceramics by Hasegawa et.al. [1], together with the possibility of constructing the high dielectric constant materials by crystallising ferroelectric lead metaniobate ($PbNb_2O_6$) from the PbO: Nb_2O_5: SiO_2+15%Al_2O_3 glass system as reported by Anderson and Friedberg, [2] suggested a new system ($Pb_5Ge_3O_{11}$: $PbNb_2O_6$: SiO_2 + 15%Al_2O_3). The six samples along the tieline were investigated as shown in figure 7.1. The tieline was designed by joining the two chosen points at 62.5 mol%PbO: 25 mol%GeO_2: 12.5 mol%SiO_2 (the stoichiometric of $Pb_5Ge_{3-x}Si_xO_{11}$ (x =1) solid solution) and 40% $PbNb_2O_6$: 60%SiO_2. Both ends were selected by consideration of the optimum compositions from previous work [1,2].

In this chapter, a preliminary study of $Pb_5Ge_3O_{11}$: $PbNb_2O_6$: SiO_2+ 15%Al_2O_3 is reported. DTA analysis was used to investigate the thermal behaviour of each glass and to design the glass-ceramic heat treatment. Crystallisation information on glass-ceramics from this system was obtained using XRD analysis.

7.2 Glass preparation

Six glasses were produced from the $Pb_5Ge_3O_{11}$: $PbNb_2O_6$: SiO_2+ 15%Al_2O_3 system as shown in figure 7.1 and a glass of 87.5%$Pb_5Ge_3O_{11}$: 12.5%SiO_2.

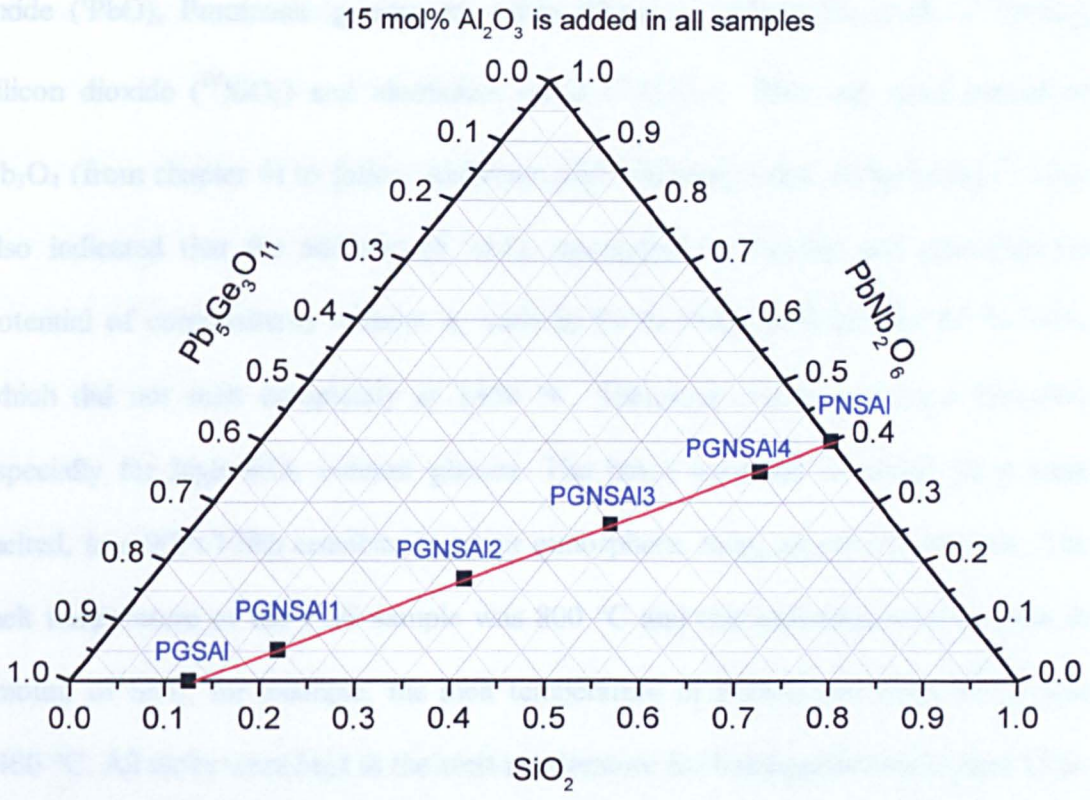

Figure 7.1 *The position of samples along the designed tieline in the ternary diagram (axis labels are presented in mole fraction).*

Table 7.1 *The nominal compositions prepared from the of $Pb_5Ge_3O_{11}$: $PbNb_2O_6$: SiO_2+ 15%Al_2O_3 system.*

Sample	PbO (mol%)	GeO_2 (mol%)	Nb_2O_5 (mol%)	SiO_2 (mol%)	+ Al_2O_3 (mol%)
PGS	62.50	25.00	-	12.50	-
PGSAl	62.50	25.00	-	12.50	15.00
PNSAl	20.00	-	20.00	60.00	15.00
PGNSAl1	49.80	28.30	2.60	19.30	15.00
PGNSAl2	39.70	18.80	8.50	33.00	15.00
PGNSAl3	31.90	11.20	13.20	43.70	15.00
PGNSAl4	23.75	3.75	17.50	55.00	15.00

Note: 15 % Al_2O_3 is an additional content.

The compositions of the glasses from Table 7.1 were prepared using lead oxide ([I]PbO), Puratronic germanium oxide ([II]GeO_2), niobium(V) oxide ([III]Nb_2O_5), silicon dioxide ([IV]SiO_2) and aluminium oxide ([V]Al_2O_3). PbO was used instead of Pb_3O_4 (from chapter 6) to follow Anderson and Friedberg's best composition.[2] They also indicated that the addition of Al_2O_3 decreased the fluidity and crystallisation potential of compositions without it, such as 20 % PbO: 20% Nb_2O_5: 60 % SiO_2, which did not melt completely at 1450 °C. Therefore Al_2O_3 was used thereafter especially for high SiO_2 content glasses. The batch materials of about 30 g were melted, in a 90Pt/10Rh crucible, in an air atmosphere, using an electric furnace. The melt temperature of the PGS sample was 800 °C and this increased with increase in amount of SiO_2, for example, the melt temperature of PNSAl (60 mo% SiO_2) was 1400 °C. All melts were held at the melt temperature for homogenisation around 15 to 30 minutes. After this, they were splat-quenched between room temperature stainless steel plates.

7.3 The amorphous XRD patterns and immiscibility

Figure 7.2 shows the amorphous XRD patterns of all glasses from the $Pb_5Ge_3O_{11}$: $PbNb_2O_6$: SiO_2+ 15%Al_2O_3 system. However, only PGS and PGNSAl3 are clear glasses, the others, such as PGSAl, PGNSAl1, and PGNSAl2 are not transparent, showing some small distinct regions having different refractive index from that of the main glass body. This is indicative of glass-in glass phase separation. On the other hand, the samples PNSAl, chosen from Anderson and Friedberg[2], and

[I] PbO – 99.9+% lead (II) oxide (Aldrich)
[II] GeO_2 – 99.999% Puratronic Germanium (IV) oxide (Alfa Aesar)
[III] Nb_2O_5 – 99.99% Niobium (V) oxide (Aldrich)
[IV] SiO_2 – Wacomsil Japan Quartz, reagent grade silica
[V] Al_2O_3 – 99.8% Aluminium oxide (Aldrich)

PGNSAl4 produced large areas of clear glass but with a little opalescence near the surface during air quenching.

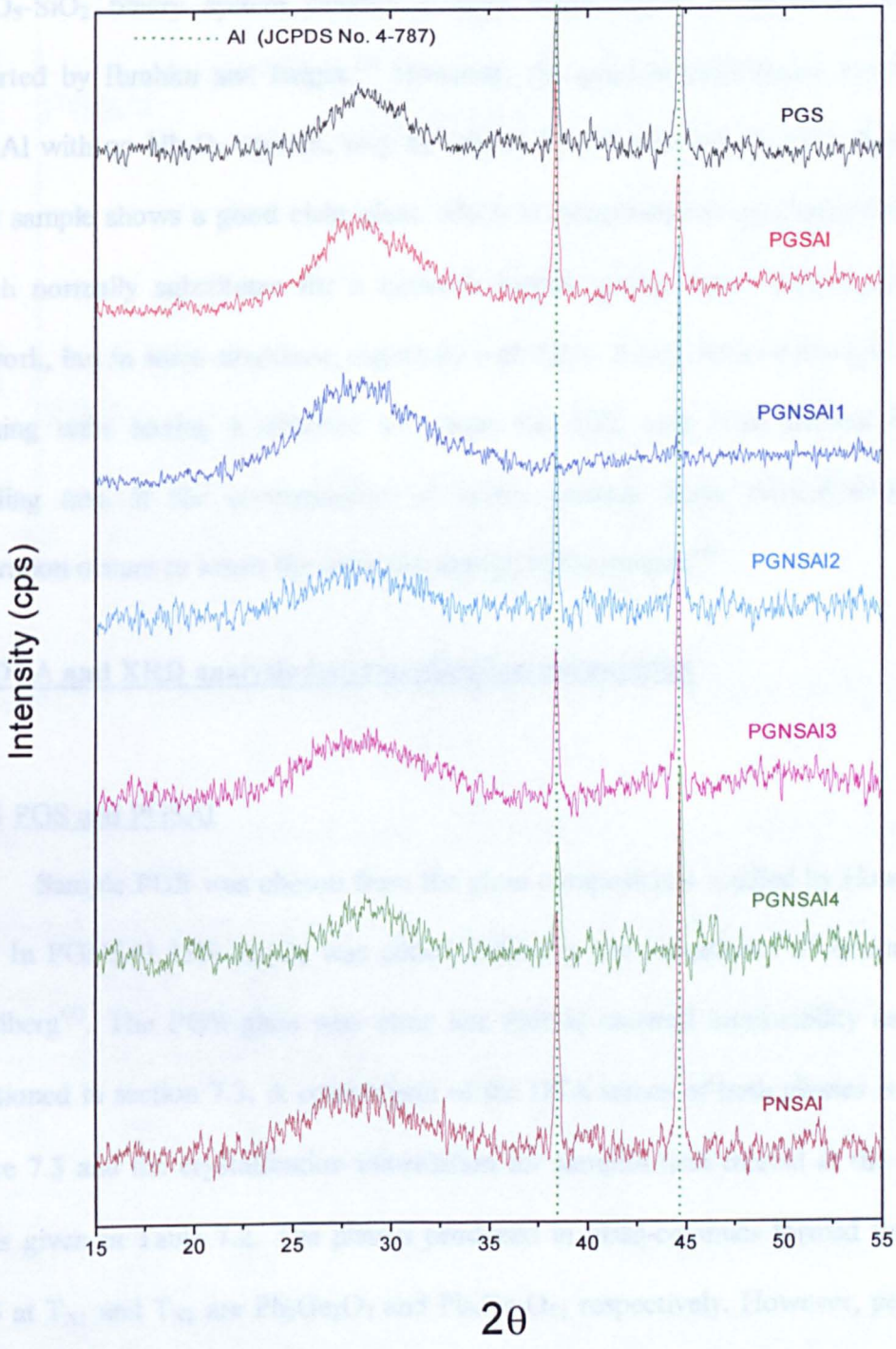

***Figure 7.2** XRD patterns of six glasses from the $Pb_5Ge_3O_{11}$: $PbNb_2O_6$: SiO_2+ 15%Al_2O_3 system and PGS glass (no addition of Al_2O_3).*

These glasses have a high mechanical strength. The problem of this trace opalescence also occurred in most of the glasses, containing 5-20 mol % Al_2O_3, from Anderson and Friedberg.[2] Phase separation in this system is expected, since the Nb_2O_5-SiO_2 binary system exhibits a large stable liquid immiscibility region as reported by Ibrahim and Bright.[3] However, the glass-in glass phase separation in PGSAl with no Nb_2O_5 content, may be caused by the addition of Al_2O_3 because the PGS sample shows a good clear glass. Al_2O_3 is categorised as an intermediate oxide which normally substitutes for a network former giving more ionic bonds in the network, but in some situations, especially with SiO_2, it may act as a foreign network, forming units having a different size from the SiO_4 unit. This distorts the Si-O bonding and, if the concentration of Al_2O_3 exceeds some critical limit, phase separation occurs to lower the total free energy of the system.[4]

7.4 DTA and XRD analysis for crystallisation information

7.4.1 PGS and PGSAl

Sample PGS was chosen from the glass compositions studied by Hasegawa et al.[1] In PGNSAl 15% Al_2O_3 was added following the procedures of Anderson and Friedberg[2]. The PGS glass was clear but PGSAl showed immiscibility as already mentioned in section 7.3. A comparison of the DTA traces of both glasses is made in figure 7.3 and the crystallisation information for samples heat treated at the different T_X is given in Table 7.2. The phases produced in glass-ceramics formed from glass PGS at T_{X1} and T_{X2} are $Pb_3Ge_2O_7$ and $Pb_5Ge_3O_{11}$ respectively. However, peak shifts from the JCPDS phases in both samples were observed as shown in figures 7.4 (a) and (b), indicating the formation of solid solutions $Pb_3(Ge,Si)_2O_7$ and $Pb_5(Ge,Si)_3O_{11}$.

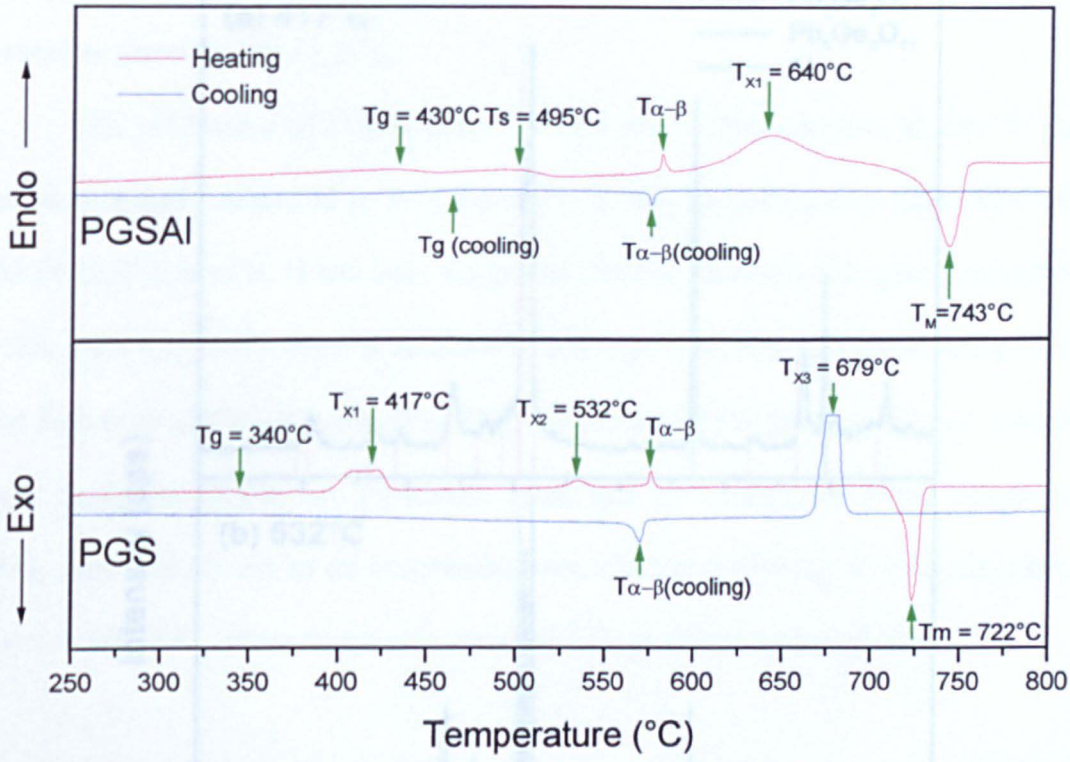

Figure 7.3 *The comparison between the DTA trace of PGS and PGSAl glass.*

Table 7.2 *Thermal data and crystalline phases of glass-ceramics formed from PGS and PGSAl glasses.*

Sample	$T_g \pm 1$ (°C)	$T_m \pm 1$ (°C)	$T_x \pm 1$ (°C)	Crystalline phase
PGS	340	722	417 532 from melt	$Pb_3Ge_2O_7$ [$Pb_3Ge_{2-x}Si_xO_7$ (x = 1)] $Pb_5Ge_3O_{11}$ [$Pb_3Ge_{5-x}Si_xO_{11}$ (x = 1)] $Pb_5Ge_3O_{11}$ [$Pb_3Ge_{5-x}Si_xO_{11}$ (x = 1)]
PGSAl	430 495	743	640	Pb_5GeO_7, $PbAl_2SiO_6$

Note: JCPDS No. of $Pb_3Ge_2O_7$, $Pb_3Ge_5O_{11}$, Pb_5GeO_7 and $PbAl_2SiO_6$ are 27-1188, 24-576, 39-850 and 30-689 respectively.

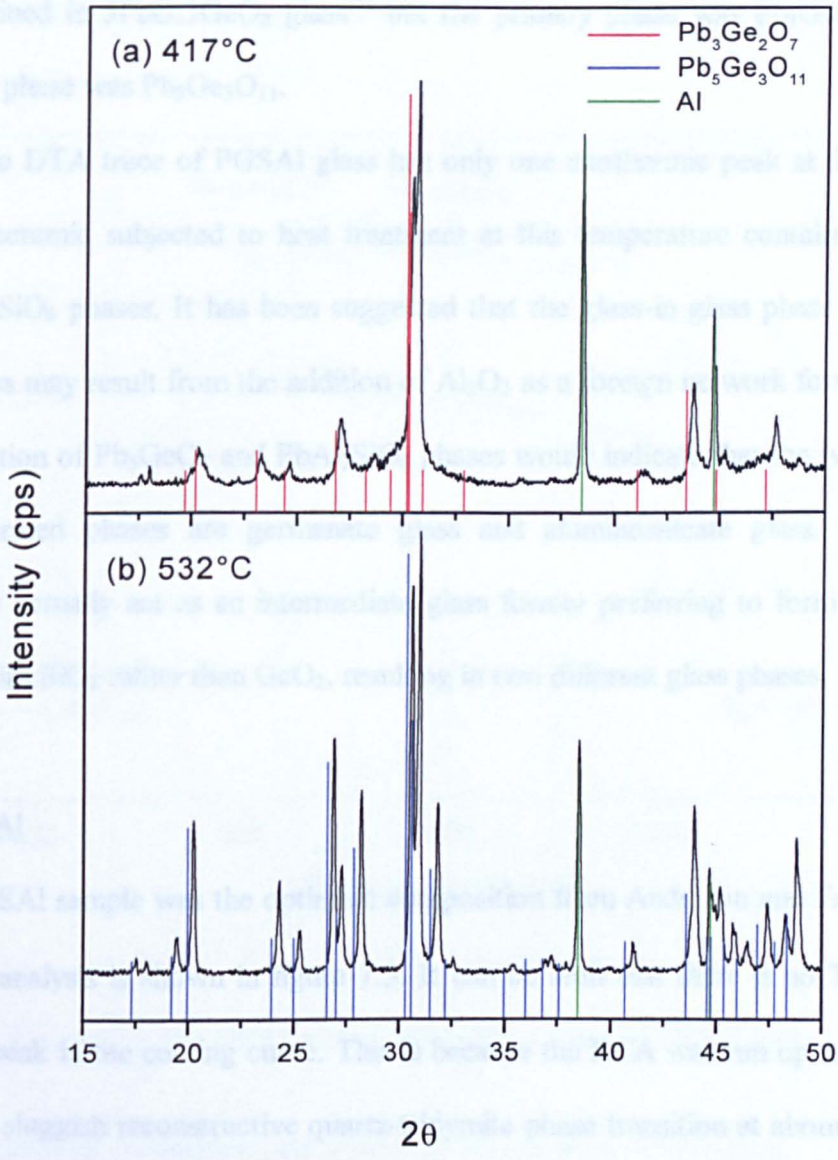

Figure 7.4 *The XRD patterns of PGS glass-ceramics: (a) T_{X1} = 417 °C and (b) T_{X2} = 532 °C.*

The lattice parameters a = 10.098, c = 19.37 for $Pb_3Ge_{2-x}Si_xO_7$(x = 1) and a = 10.115, c = 10.597 for $Pb_3Ge_{5-x}Si_xO_{11}$ (x = 1) were observed, which is consistent with the lattice parameters from Vegard's plots by Hasegawa et al.[1] Both phases are hexagonal. The exothermic peak at T_{X1} = 417°C resulted from the formation of primary phase $Pb_3Ge_{2-x}Si_xO_7$ (x = 1) whereas that at T_{X2} = 532°C is due to reaction of the primary crystalline phase with residual glass to give ferroelectric $Pb_3Ge_{5-x}Si_xO_{11}$

(x = 1) phase, which is consistent to the work by Hasegawa[1]. Similar DTA results were obtained in $5PbO:3GeO_2$ glass[5] but the primary phase was Pb_3GeO_7 and the secondary phase was $Pb_5Ge_3O_{11}$.

The DTA trace of PGSAl glass has only one exothermic peak at 640 °C and the glass-ceramic subjected to heat treatment at this temperature contains Pb_5GeO_7 and $PbAl_2SiO_6$ phases. It has been suggested that the glass-in glass phase separation in this glass may result from the addition of Al_2O_3 as a foreign network forming units. The formation of Pb_5GeO_7 and $PbAl_2SiO_6$ phases would indicate that the two glass-in glass separated phases are germanate glass and aluminosilicate glass. Therefore, Al_2O_3 may actually act as an intermediate glass former preferring to form the glass-network with SiO_2 rather than GeO_2, resulting in two different glass phases.

7.4.2 PNSAl

PNSAl sample was the optimum composition from Anderson and Friedberg.[2] The DTA analysis is shown in figure 7.5. It can be seen that there is no $T_{\alpha-\beta}$ quartz transition peak in the cooling curve. This is because the DTA was run up to 1500 °C, passed the sluggish reconstructive quartz-tridymite phase transition at about 1470 °C. Therefore, on slow cooling, the $T_{\alpha-\beta}$ (tridymite) transition occurred at about 220°C. The phase transition diagram of SiO_2 is shown in figure 6.12 (Chapter 6). From the DTA heating curve, it is difficult to identify whether or not the endothermic feature at about 755 °C is related to a second glass transition event because it should not appear after the crystallisation temperature at T_{X1}. As phase separation was observed in this glass, so it may be possible to have separate glass transitions for each phase, one at Tg = 644 °C and another at T? = 755°C. Figure 7.6 shows the XRD patterns of the glass-ceramics heat treated at T_{X1} and T_{X2}. It can be seen that there is only one distinctive peak of $AlNbO_4$ phase from the XRD pattern of the glass-ceramic from T_{X1}= 684 °C

while the XRD pattern of the glass-ceramic from T_{X2} = 866 °C contains sharper peaks of $AlNbO_4$ together with the peaks of $PbNb_2O_6$.

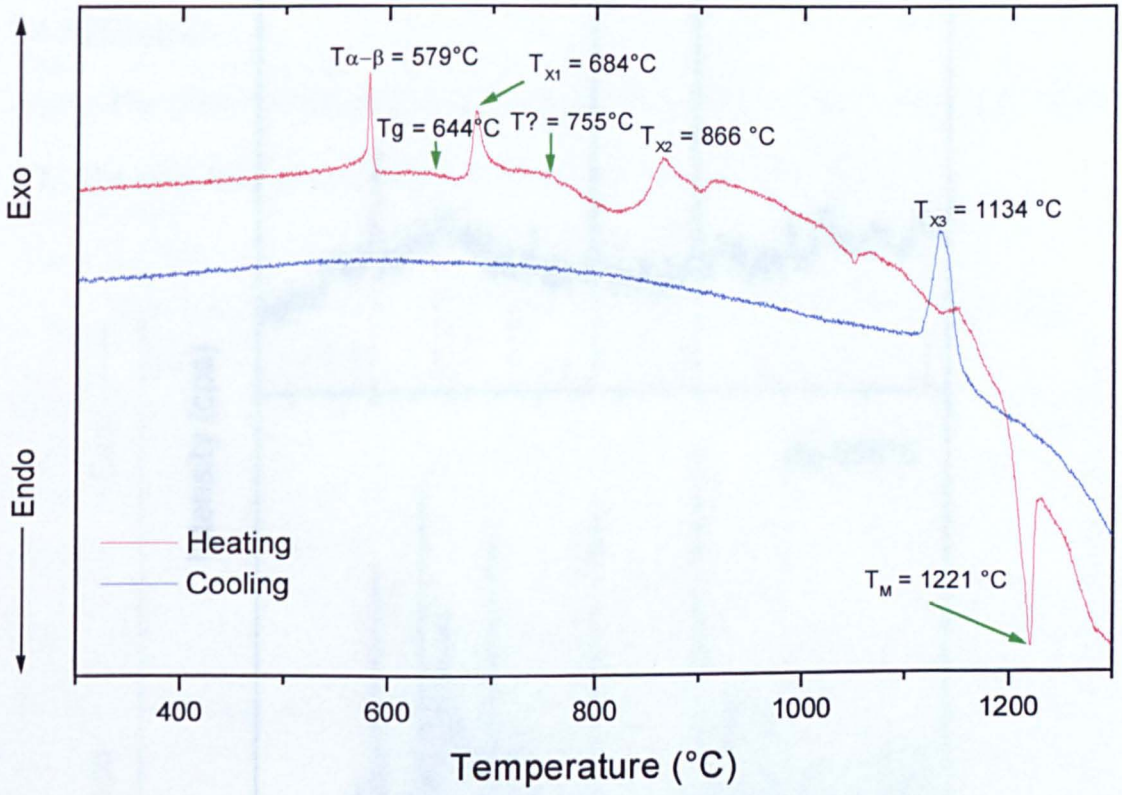

Figure 7.5 *The DTA heating and cooling trace of PNSAl glass.*

Table 7.3 *Thermal parameters and crystalline phases from PNSAl glass.*

$T_g \pm 1$ (°C)	$T_m \pm 1$ (°C)	$T_x \pm 1$ (°C)	Crystalline phase
		684	$AlNbO_4$
644	1221	866	$AlNbO_4$, $PbNb_2O_6$
		from melt	$AlNbO_4$, $PbNb_2O_6$, Pb_6GeO_8

Note: JCPDS No. of $AlNbO_4$, $PbNb_2O_6$ and Pb_6GeO_8 are 41-347, 11-122 and 35-1103 respectively.

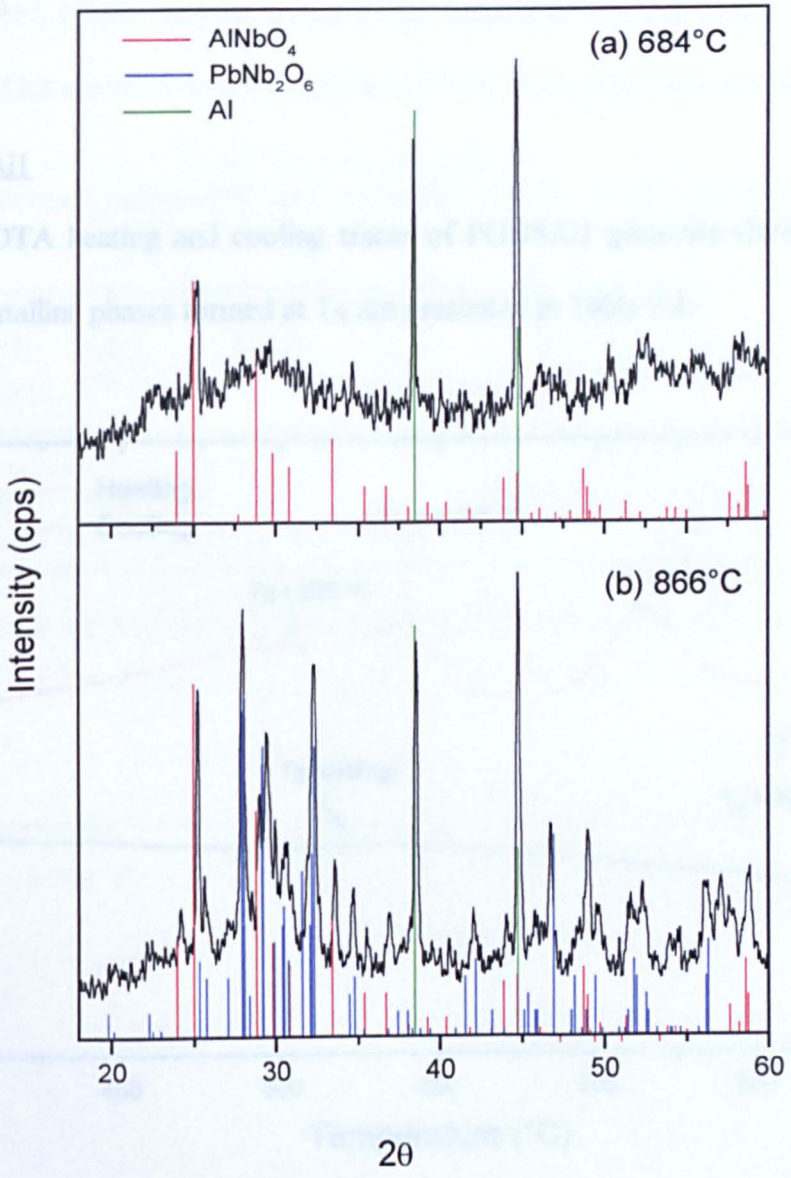

***Figure 7.6** The XRD patterns of PNSAl glass-ceramics: (a) T_{X1} = 684 °C and (b) T_{X2} = 866 °C.*

Consequently, it can be found that a small amount of $AlNbO_4$ phase was formed in the PNSAl glass-ceramic heat treated at 684 °C for 4 hours, and this may be related to the small region of glass in glass phase separation of the parent glass. After increase of the crystallisation temperature to 866°C the orthorhombic ferroelectric phase ($PbNb_2O_6$) was successfully produced along with $AlNbO_4$. This glass-ceramic is different from that of Anderson and Friedberg who observed the orthorhombic

$PbNb_2O_6$ together with the rhombohedral $PbNb_2O_6$, which is paraelectric at room temperature[6]

7.4.3 PGNSAl1

The DTA heating and cooling traces of PGNSAl1 glass are shown in figure 7.7. The crystalline phases formed at T_X are presented in Table 7.4.

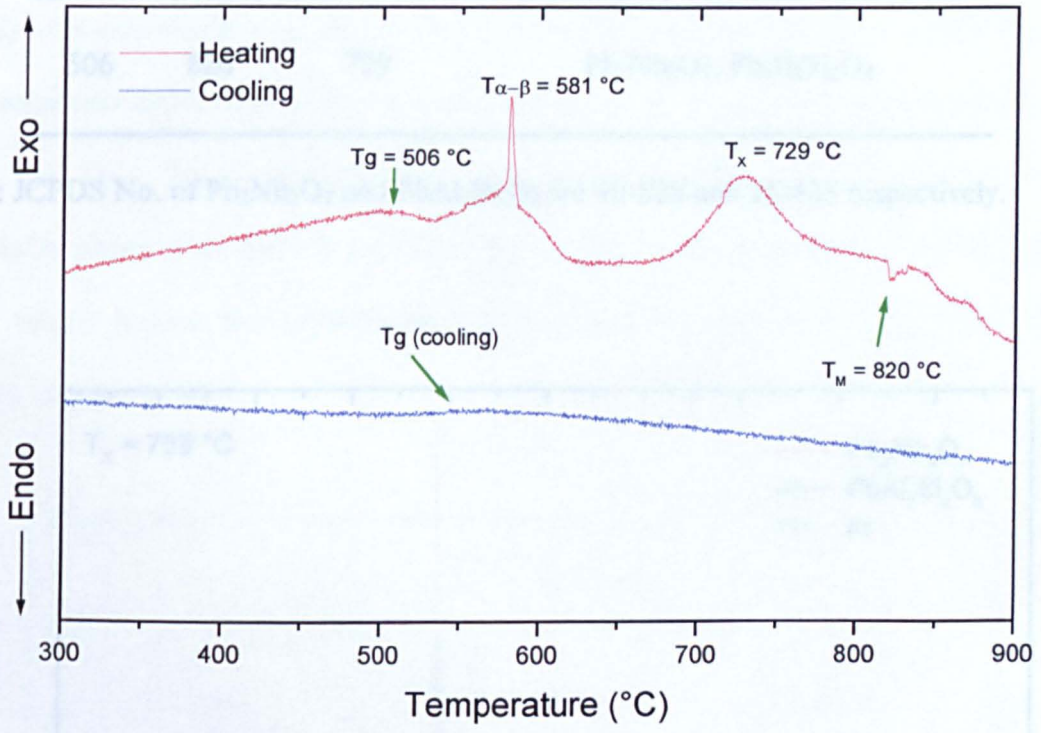

***Figure 7.7** The DTA heating and cooling trace of PGNSAl1 glass.*

It can be seen that there is only one broad exothermic peak at 729 °C on heating which is related to the formation of $Pb_2Nb_2O_7$ and $PbAl_2Si_2O_8$. The XRD pattern of this glass-ceramic powder is shown in figure 7.8. Interestingly, the $Pb_2Nb_2O_7$ crystallised from this glass is monoclinic which is different from the rhombohedral $Pb_2Nb_2O_7$ formed in the glass-ceramic PG-0.5PN from Chapter 6. Again, the DTA was run up to 1500°C, therefore no peak of $T_{\alpha\text{-}\beta}$ quartz shows in the cooling trace as described in section 7.4.2. As mentioned above, this glass also

suffered phase separation. Since Nb_2O_5 is a good nucleating agent, the addition of about 2.6 mol% Nb_2O_5 may influence phase separation as well as the presence of Al_2O_3 oxide. This occurs whether Nb_2O_5 or Al_2O_3 is alone or in combination.

Table 7.4 *Thermal parameters and crystalline phases in the glass-ceramic from PGNSA11 glass.*

$T_g \pm 1$ (°C)	$T_m \pm 1$ (°C)	$T_x \pm 1$ (°C)	Crystalline phase
506	820	729	$Pb_2Nb_2O_7$, $PbAl_2Si_2O_8$

Note: JCPDS No. of $Pb_2Nb_2O_7$ and $PbAl_2Si_2O_8$ are 40-828 and 25-428 respectively.

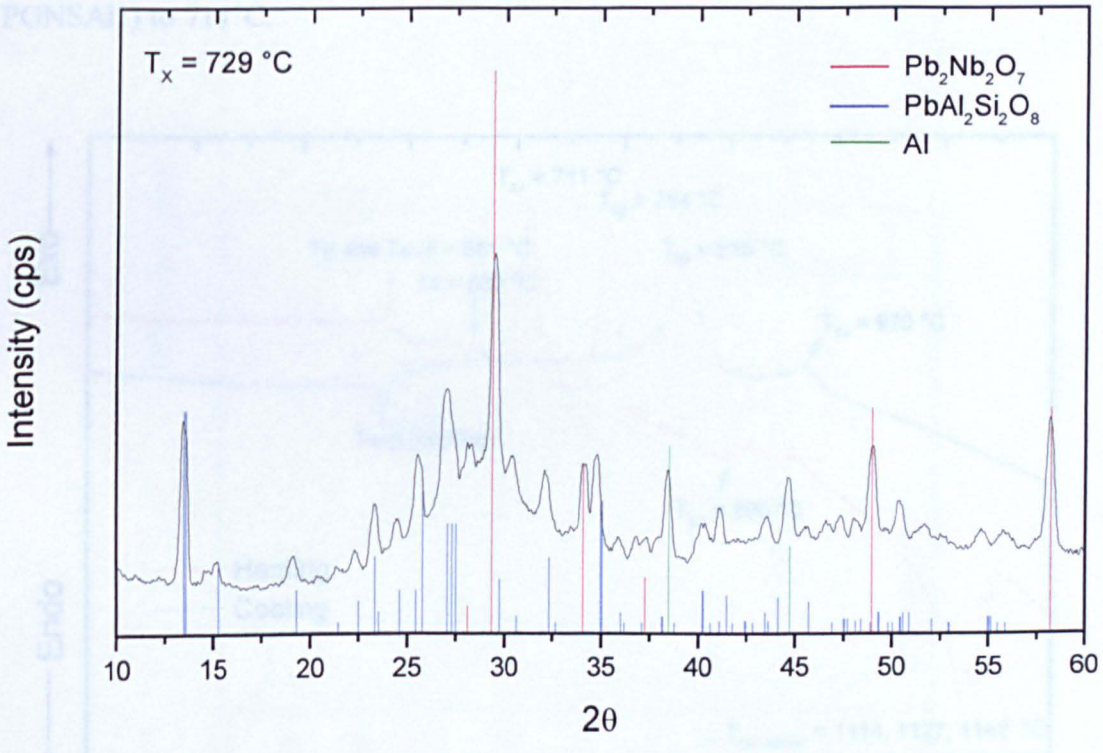

Figure 7.8 *The XRD patterns of PGNSA11 glass-ceramics at T_X = 729 °C.*

7.4.4 PGNSAl2

The DTA trace and crystallisation summary for this glass are shown in figure 7.9 and Table 7.5 respectively. The XRD patterns of the glass-ceramics at T_{X1} and T_{X2} are also shown in figure 7.10. It can be seen that the phases produced in the glass-ceramics from this glass are similar to those of PGNSAl1. The DTA run of this glass was up to 1400 therefore $T_{\alpha-\beta}$ quartz is retained in the cooling trace. Although, the phases formed by PGNSAl1 and PGNSAl2 are similar, in the case of PGNSAl1 there is only one exothermic peak on heating and cooling whereas PGNSAl2 shows two well-separated exothermic peaks on heating. Moreover, the glass-ceramic produced from the T_{X1}= 711°C crystallisation temperature contains only the monoclinic $Pb_2Nb_2O_7$ phase. This may be explained by the higher Nb_2O_5 content in PGNSAl2 glass which lowers the crystallisation temperature of $Pb_2Nb_2O_7$ from 729 °C (PGNSAl1) to 711°C.

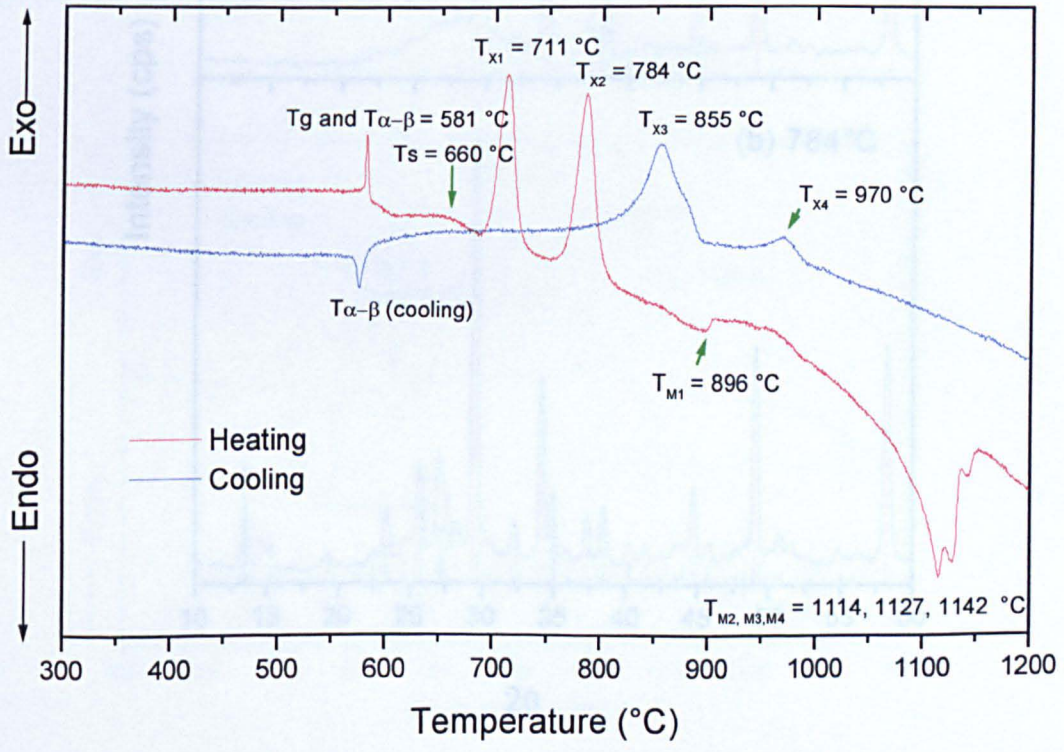

***Figure 7.9** The DTA heating and cooling trace of PGNSAl2 glass.*

Table 7.5 *Thermal parameters, crystallisation temperatures and crystalline phases of glass-ceramics for PGNSAl2 glass.*

$T_g \pm 1$ (°C)	$T_m \pm 1$ (°C)	$T_x \pm 1$ (°C)	Crystalline phase
660	896	711	$Pb_2Nb_2O_7$
	1114	784	$Pb_2Nb_2O_7$, $PbAl_2Si_2O_8$
	1127	from melt	$Pb_2Nb_2O_7$, $PbAl_2Si_2O_8$
	1142		

Note: JCPDS No. of $Pb_2Nb_2O_7$ and $PbAl_2Si_2O_8$ are 40-828 and 25-428 respectively.

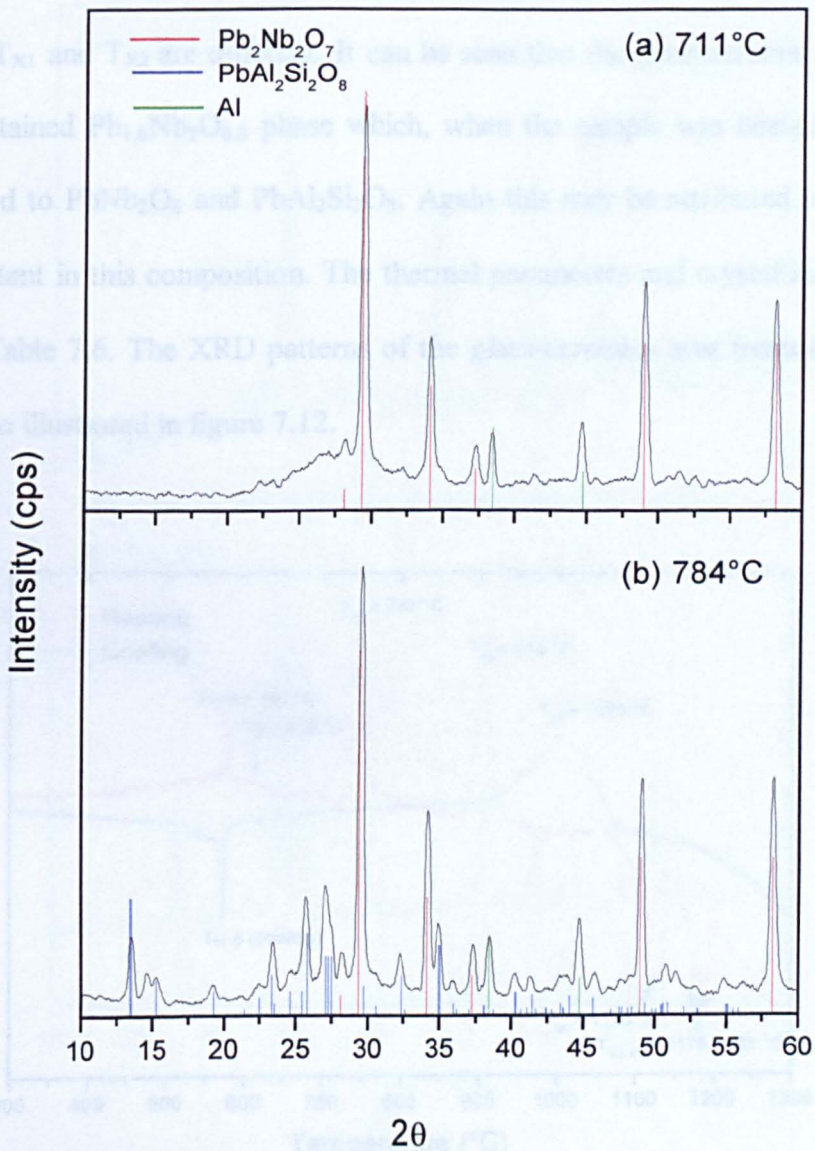

Figure 7.10 *The XRD patterns of PGNSAl2 glass-ceramics: (a) T_{X1} = 711 °C and (b) T_{X2} = 784 °C.*

The crystal phases formed in glass-ceramics from PGNSAl1 and PGNSAl2 are $Pb_2Nb_2O_7$ and $PbAl_2Si_2O_8$. As these two glasses have glass-in glass phase separation, it may be assumed that one glass phase contains more Nb_2O_5 and the other is rich in Al_2O_3. Therefore, after heat treatment, the first separated glass produced $Pb_2Nb_2O_7$ and the $PbAl_2Si_2O_8$ phase is formed in the second.

7.4.5 PGNSAl3

The DTA heating trace of PGNSAl2 glass as shown in figure 7.11 is similar to that of PGNSAl2 glass. However, the phases formed in these glass-ceramics heat treated at T_{X1} and T_{X2} are different. It can be seen that the glass-ceramic heat treated at T_{X1} contained $Pb_{1.6}Nb_2O_{6.6}$ phase which, when the sample was heated up to T_{X2}, decomposed to $PbNb_2O_6$ and $PbAl_2Si_2O_8$. Again this may be attributed to the higher Nb_2O_5 content in this composition. The thermal parameters and crystalline phases are shown in Table 7.6. The XRD patterns of the glass-ceramics heat treated at T_{X1} and T_{X2} are also illustrated in figure 7.12.

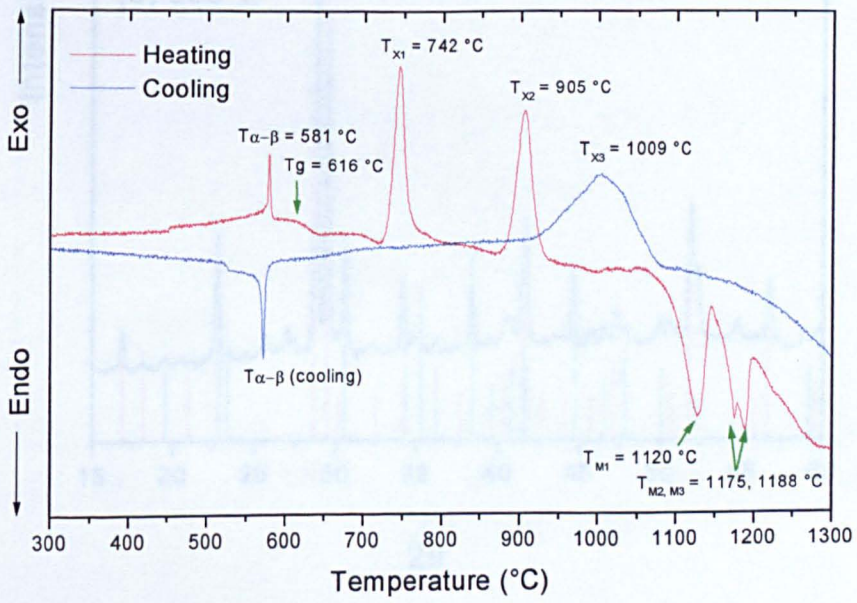

***Figure 7.11** The DTA heating and cooling trace of PGNSAl3 glass.*

Table 7.6 *Thermal parameters and crystalline phases of glass-ceramics from PGNSAl3 glass.*

$T_g \pm 1$ (°C)	$T_m \pm 1$ (°C)	$T_x \pm 1$ (°C)	Crystalline phase
	1120	742	$Pb_{1.6}Nb_2O_{6.6}$
616	1175	905	$PbNb_2O_6$, $PbAl_2Si_2O_8$
	1188	from melt	$PbNb_2O_6$, $PbAl_2Si_2O_8$

Note: JCPDS No. of $Pb_{1.6}Nb_2O_{6.6}$, $PbNb_2O_6$ and $PbAl_2Si_2O_8$ are 46-984, 29-780 and 14-326 respectively.

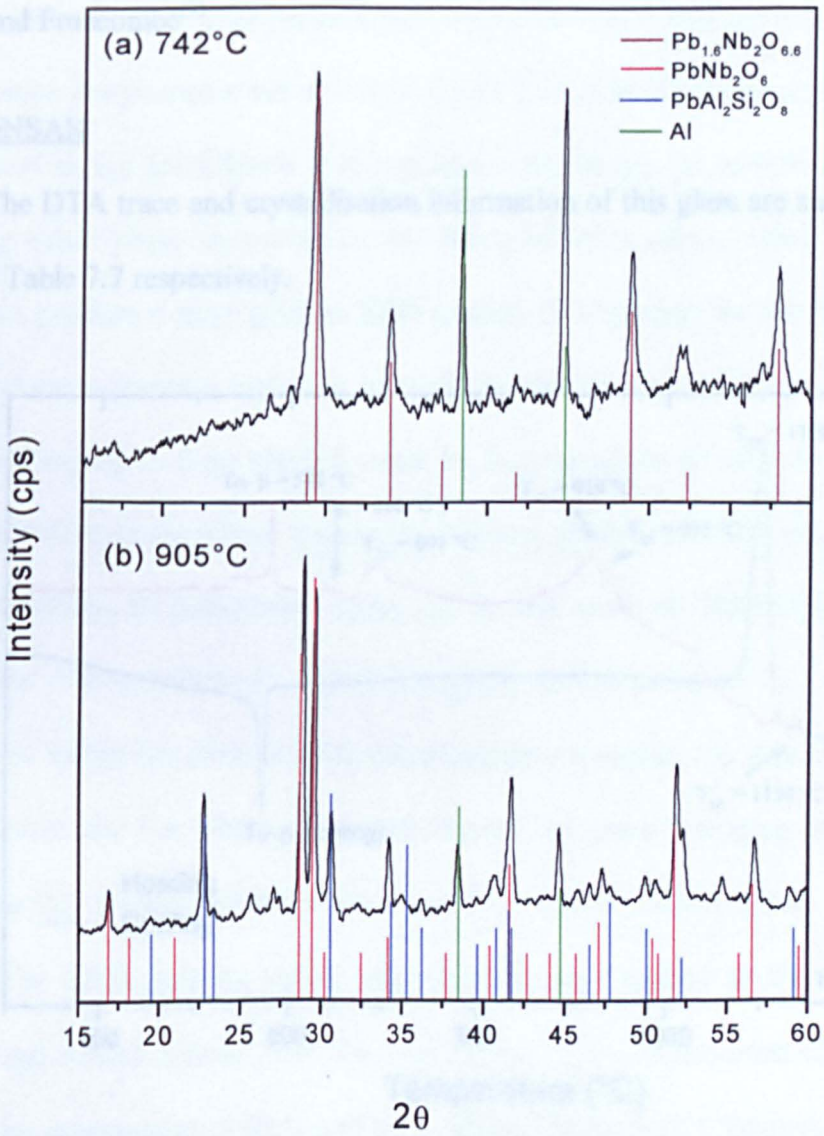

Figure 7.12 *The XRD patterns of PGNSAl2 glass-ceramics: (a) T_{X1} = 742 °C and (b) T_{X2} =905 °C.*

This PGNSAl3 glass differs from other glasses in this system in that there is no visible phase separation. The DTA cooling trace shows only one exothermic peak which may be related to the crystallisation of $PbNb_2O_6$ and $PbAl_2Si_2O_8$ on cooling. It should be noted that, even though the glass was heated up to 1400 °C the ferroelectric orthorhombic $PbNb_2O_6$ phase was not obtained as expected, considering that orthorhombic $PbNb_2O_6$ is stable at 1250 °C.[7] However, the cooling rate of the sample from the melt was about 10-15 °C/min which may be too slow to form this orthorhombic lead metaniobate phase since rapid cooling is required as reported by Roth[8] and Francombe[9].

7.4.6 PGNSAl4

The DTA trace and crystallisation information of this glass are shown in figure 7.13 and Table 7.7 respectively.

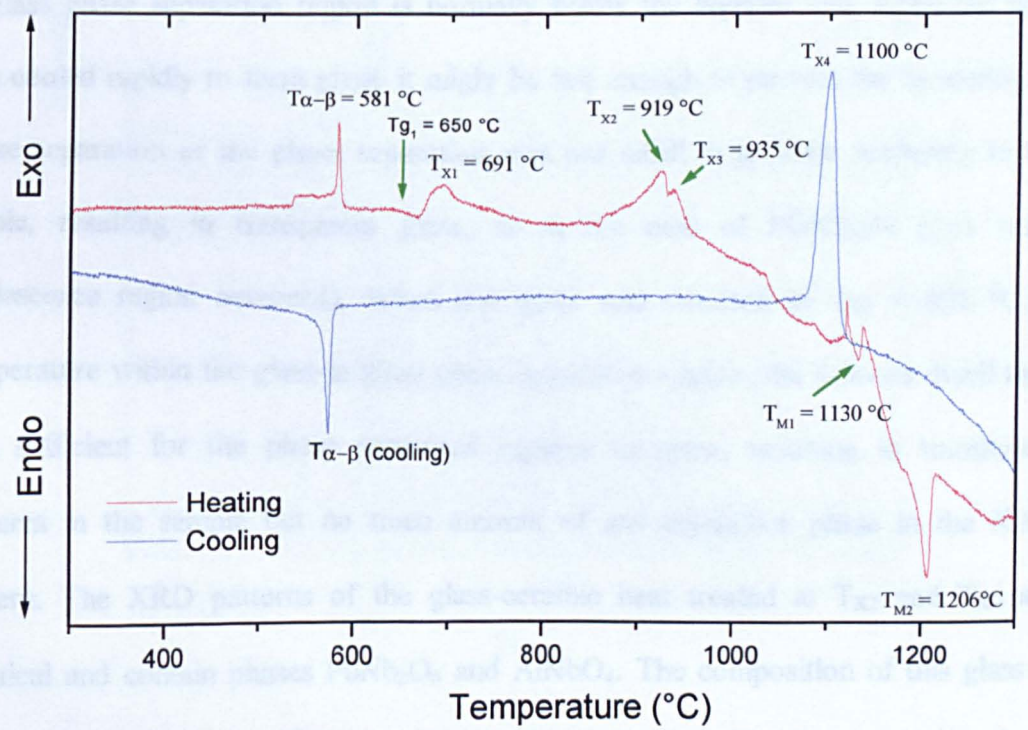

Figure 7.13 *The DTA heating and cooling trace of PGNSAl4 glass.*

Table 7.7 Thermal parameters and crystalline phases of glass-ceramics for PGNSAl4 glass.

$T_g \pm 1$ (°C)	$T_m \pm 1$ (°C)	$T_x \pm 1$ (°C)	Crystalline phase
		691	No trace of crystals
650	1130	919	$PbNb_2O_6$, $AlNbO_4$
691	1206	935	$PbNb_2O_6$, $AlNbO_4$
		from melt	$PbNb_2O_6$, $AlNbO_4$

Note: JCPDS No. of $PbNb_2O_6$ and $AlNbO_4$ are 29-780 and 41-347 respectively.

From the DTA heating curve, there are three distinctive exothermic peak at T_{X1}, T_{X2} and T_{X3}. The XRD patterns of the glass-ceramics heat treated at these three crystallisation temperatures are shown in figure 7.14. The XRD pattern of the sample heat treated at T_{X1} for 4 hours is amorphous even though the sample is translucent, indicating either phase separation or nucleation of some phase, which is very small and cannot produce a sharp peak in XRD pattern. Considering, the fact that the glass-in glass phase separation region is normally below the liquidus line, when the melt was cooled rapidly to form glass, it might be fast enough to prevent the formation of phase separation or the phase separation was too small to produce scattering in the visible, resulting in transparent glass, as in the case of PGNSAl4 (just small opalescence region occurred). When this glass was reheated to T_{X1} = 691 °C, a temperature within the glass-in glass phase separation region, the 4 hours dwell time was sufficient for the phase separated regions to grow, resulting in translucent features in the sample but no trace amount of any crystalline phase in the XRD pattern. The XRD patterns of the glass-ceramic heat treated at T_{X2} and T_{X3} are identical and contain phases $PbNb_2O_6$ and $AlNbO_4$. The composition of this glass is near to the composition PNSAl and both glasses have similar features, such phase separation. Since the first crystallisation peak in PNSAl is related to the formation of $AlNbO_4$, it may be assumed that the first crystallisation peak T_{X1} of glass PGNSAl4 is

also due to $AlNbO_4$ but of very small crystallite size. This may be another different explanation of the exothermic peak T_{X1} = 691 °C from that mentioned above. The $PbNb_2O_6$ phase formed in PGNSAl4 is rhombohedral while in PNSAl it is the ferroelectric orthorhombic phase.

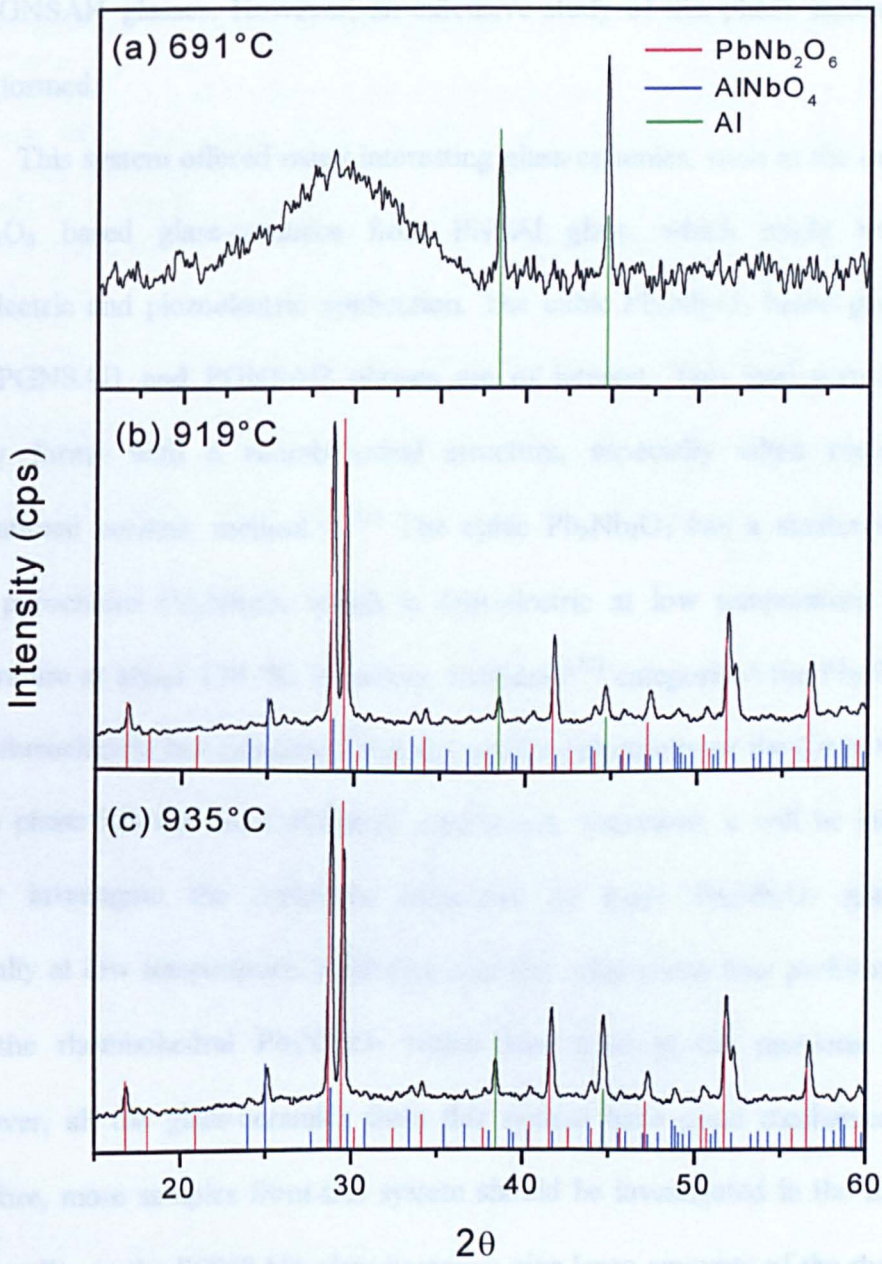

Figure 7.14 *The XRD patterns of PGNSAl4 glass-ceramics: (a) T_{X1} = 691 °C, (b) T_{X2} = 919 °C and (c) T_{X3} = 935 °C.*

7.5 Summary

Most of the glasses from this system exhibit some glass- in glass phase separation. From DTA analysis and subsequence crystallisation information, the most likely possible parameters, which control the glass-in glass phase separation, may be the Nb_2O_5/SiO_2 ratio for PGNSAl1-PGNSAl3 glasses and Al_2O_3 for PNSAl, PGSAl and PGNSAl4 glasses. However, an extensive study of this phase separation should be performed.

This system offered many interesting glass-ceramics, such as the orthorhombic $PbNb_2O_6$ based glass-ceramics from PNSAl glass, which might be useful in ferroelectric and piezoelectric application. The cubic $Pb_2Nb_2O_7$ based glass-ceramics from PGNSAl1 and PGNSAl2 glasses are of interest. This lead germanate phase usually forms with a rhombohedral structure, especially when prepared using conventional ceramic method.[10-11] The cubic $Pb_2Nb_2O_7$ has a similar structure to cubic pyrochlore $Cd_2Nb_2O_7$ which is ferroelectric at low temperature with Curie temperature at about 170 °K. However, Subbarao[12] categorised the $Pb_2Nb_2O_7$ phase as antiferroelectric but mentioned that the antiferroelectricity or the Curie temperature of this phase has not been definitely established. Therefore, it will be interesting to further investigate the dielectric behaviour of these $Pb_2Nb_2O_7$ glass-ceramics especially at low temperature, expecting that the cubic phase may perform differently from the rhombohedral $Pb_2Nb_2O_7$ which was used in the previous study.[13-14] Moreover, all the glass-ceramics from this system have good mechanical strength. Therefore, more samples from this system should be investigated in the future work. Additionally, as the PGNSAl4 glass-ceramics give large amounts of the rhombohedral $PbNb_2O_6$ crystals, it may be interesting to further investigate conversion to the orthorhombic polymorph by either melting at higher temperature and very rapid quenching or by investigating other compositions around this glass.

References

1. Hasegawa, H., Shimada, M. and Koizumi, M. 1982, *Ceramics International*, Volume 8, No. 4, pp.141-149.
2. Anderson R. C. and Friedberg A. L., 1982 *Symposium on Nucleation an Crystallisation in Glasses and Melts*, The American Ceramic Society, INC., pp. 29-34.
3. Ibrahim, M. and Bright, F. H. 1962, *Journal of American Ceramic Society*, Volume 45, Number 5, p. 221.
4. McMillan, P.W. *Glass-Ceramics*, 1979 (Academic Press)
5. Hasegawa, H., Shimada, M. and Koizumi, M. 1973, Journal of Materials Science, Volume 8, p. 1725.
6. Moulson, A. J. and Herbert, J. M. *Electroceramics*, 1990 (Chapman & Hall).
7. Lines, M.E. and Glass, A.M. *Principles and Applications of Ferroelectrics and Related Materials*, 1977 (Clarendon Press, Oxford)
8. Roth, R. S. 1959, *J. Res. Natl. Bur. Stand. (U.S.)*, Volume 62, Number 1, p. 27.
9. Francombe, M. H., 1956, *Acta Crystallogr.*, Volume 9, p. 683.
10. Li C. C., Chiu, C. C. and Desu, S. B. 1991, *Journal of the American Ceramic Society*, Volume 74, Number 1, p. 42.
11. Lu, C. H. and Lo, S. Y. 1997, *Materials Research Bulletin*, Volume 32, Number 3, p. 371.
12. Subbarao, E. C. 1973, *Ferroelectrics*, Volume 5, p. 267.
13. Shirane, G. and Pepinsky, R. 1953, *Physics Review*, Volume 92, p. 504.
14. Hulm, J. K. 1953, *Physics Review*, Volume 92, p. 504.

Chapter 8

Conclusions and future work

Ferroelectric glass-ceramics have been investigated from four glass systems: $BiO_{1.5}$-GeO_2-$BO_{1.5}$, $BiO_{1.5}$-GeO_2-TeO_2, PbO-GeO_2-Nb_2O_5 and $Pb_5Ge_3O_{11}$-$PbNb_2O_6$-SiO_2+15%Al_2O_3. DTA, XRD and SEM techniques were used for crystallographic and microstructural study. Electrical properties, such as permittivity and ferroelectric hysteresis loop of selected specimens were also determined.

The problem of the devitrification of stoichiometric Bi_2GeO_5 from binary Bi_2O_3-GeO_2 suggested the new ternary systems $BiO_{1.5}$-GeO_2-$BO_{1.5}$ and $BiO_{1.5}$-GeO_2-TeO_2. Seven samples around the stoichiometric composition were observed from $BiO_{1.5}$-GeO_2-$BO_{1.5}$ system. The samples with the addition of > 18 mol% $BO_{1.5}$ could form glasses by rapid quenching. However, the stability of these glasses is quite low as confirmed by the small $To - Tg$ values of about 40-70 °C. The starting sample $BiGeB_1$ with added 18.8 mol% $BO_{1.5}$ gave glass-ceramics containing $Bi_4(GeO_4)_3$ and a small amount of the desired Bi_2GeO_5 phase, giving rise to the assumption that Bi^{3+} ions may be lost during heating. Therefore, $BiO_{1.5}$ oxide was added in order to compensate for the vaporising ions. The glass-ceramic from $BiGeB_2$, with about 14% more $BiO_{1.5}$ than $BiGeB_1$, contains more Bi_2GeO_5 with the ratio of volume fractions of $Bi_4(GeO_4)_3$:Bi_2GeO_5 equal to 2:11. However, further addition of $BiO_{1.5}$ resulted in formation of an unidentified phase and bismuth borate phases in glass-ceramics of sample $BiGeB_3$ to $BiGeB_5$. A pure Bi_2GeO_5 based glass-ceramic was achieved from the $BiGeB_6$ sample, having the same $BiO_{1.5}$:GeO_2 ratio as that of $BiGeB_2$ but only 18.8 mol %. $BO_{1.5}$ oxide. However, there are three unidentified peaks at high angle which were not matched by the JCDPS file. These peaks were successfully indexed as

(313), (530) and (622) reflections. The $BiGeB_6$ glass-ceramic, subjected to heat treatment at 475 °C for four hours, gave surface crystallisation of Bi_2GeO_5 with preferred orientation perpendicular to (311) planes. Using dielectric and ferroelectric hysteresis loop measurement, it was found that the Bi_2GeO_5 based glass-ceramic is ferroelectric with a Curie temperature of about 407 °C. This is less than the predicted value (> 527°C) from Bi_2GeO_5 single crystals which may result from the effects of the elastic and the electrostrictive forces exerted by the surrounding glass matrix on the crystallites. However, the Cole-Cole plots of this glass-ceramic shows tails at high frequency, indicating high loss from interfacial polarization either at the electrodes or due to mobile ions from the residual glass. Impedance spectroscopy at different elevated temperatures should be performed in order to solve this problem. The observed P_s of this glass-ceramic was about 14 $\mu C/cm^2$ which is comparable to $BaTiO_3$ ceramics. This value may be improved if the glass-ceramics containing a-axis orientation of Bi_2GeO_5 crystals can be formed. Thus future work on this glass-ceramic would concentrate on obtaining grain-oriented glass-ceramic by recrystallising glasses in a temperature gradient. Various heat treatment schedules for controlling crystallite size in this glass-ceramic were tried but no transparent glass-ceramic with high volume fraction of crystals could be achieved. Therefore, further studies should be performed to investigate using nucleation control in order to obtain transparent glass-ceramic. In this case, a two step heat treatment would be applied, with the first step being at the nucleation temperature which would need to be determined.

The $BiO_{1.5}$-GeO_2-TeO_2 system has a narrow glass-forming region especially near the stoichiometric composition (Bi_2GeO_5). Only one composition ($BiGeTe_2$) gave a good glass, others devitrified on cooling. The glass-ceramics formed from $BiGeTe_2$ glass by various heat treatments gave only a small amount of Bi_2GeO_5 phase

together with other unwanted phases, such as bismuth tellurate. Therefore, this system is not likely to justify further investigation.

The devitrification of $Pb_5Ge_3O_{11}$ in the stoichiometric $5PbO:3GeO_2$ ($Pb_5Ge_3O_{11}$) resulted in broken pieces of partly glassy material. In order to achieve $Pb_5Ge_3O_{11}$+$PbNb_2O_6$ based glass-ceramics, the $Pb_5Ge_3O_{11}$:$PbNb_2O_6$ (PG-PN) system was investigated. Nine compositions around stoichiometric $Pb_5Ge_3O_{11}$ were melted and quenched on the liquid-N_2 cooled stainless steel plates. It was found that the compositions PG:xPN, where x = 0.5, 1, 2 and 3, devitrified on cooling. However, the sample PG:0.5PN was mechanically robust and formed interesting phases such as ferroelectric $Pb_5Ge_3O_{11}$ and $Pb_2Nb_2O_7$. The SEM backscattering image showed that bulk crystallisation of $Pb_2Nb_2O_7$ happened first followed by surface crystallisation of $Pb_5Ge_3O_{11}$. By applying heat treatment at 667 °C for 48 hours to the PG:0.5PN bulk sample, the surface crystallisation of $Pb_5Ge_3O_{11}$ could be grown further into the sample with preferred orientation perpendicular to the (h00) planes. However, the mechanical strength of this heat-treated sample was poorer than that of the untreated sample. A ferroelectric hysteresis loop could be observed from the heat-treated sample with P_s = 1 $\mu C/cm^2$ while the untreated sample showed no sign of a hysteresis loop. The temperature dependence of the dielectric constant indicated a Curie temperature in the heat-treated sample at T_C = 166 °C which is related to the $Pb_5Ge_3O_{11}$ phase transition from ferroelectric to paraelectric phase. Five more samples were investigated by adding more GeO_2 but only two samples, 5%PN (42 mol% GeO_2) and 5%PN2 (47 mol% GeO_2) formed glasses. The rest with mol % GeO_2 less than 40 showed some devitrification on cooling. The glass-ceramics from the two glasses contained $Pb_2Nb_2O_7$ and $PbGeO_3$ and the expected $Pb_5Ge_3O_{11}$ and $PbNb_2O_6$ could not be obtained. Since, this PG-PN system has a narrow glass-forming region, especially near the stoichiometric $Pb_5Ge_3O_{11}$, giving rise to the difficulty in

achieving a good parent glass for precipitating both ferroelectrics $Pb_5Ge_3O_{11}$ and $PbNb_2O_6$, the investigation of the multiple ferroelectric glass-ceramic from this PG-PN system should be discontinued. The exception is the PG-0.5PN sample which showed interesting dielectric and ferroelectric properties but whose surface crystallisation produced a-axis orientation of the $Pb_5Ge_3O_{11}$. It would be interesting to further investigate grain-oriented glass-ceramics of this composition, aiming to form c-axis orientation of $Pb_5Ge_3O_{11}$ phase as this may improve the electrical properties of the glass-ceramic.

The new system $Pb_5Ge_3O_{11}$-$PbNb_2O_6$-SiO_2+15 mol% Al_2O_3 was studied with the aim of producing the multiple ferroelectric glass-ceramics containing $Pb_5Ge_3O_{11}$ and $PbNb_2O_6$ phases. The preliminary study of this system started with six samples along the tie line from 62.5 mol%PbO: 25 mol%GeO_2: 12.5 mol%SiO_2 to 40 mol%$PbNb_2O_6$: 60 mol%SiO_2 (15 mol%Al_2O_3 was also added). Most samples exhibited glass-in glass phase separation, especially the samples near the ends of the tie line. The samples (PGNSAl1 and PGNSAl2) near the $Pb_5Ge_3O_{11}$ rich end were extensively phase separated while the sample (PGNSAl4) near the $PbNb_2O_6$ rich showed only a small region of glass-in glass phase separation. It may be assumed that the ratios of Nb_2O_5/SiO_2 for PGNSAl1 to PGNSAl3 glasses and Al_2O_3 contents in PGSAl and PNSAl glasses are the primary parameters which control glass-in glass phase separation and this should be confirmed by more detailed study. The glass-ceramics formed in this system have good mechanical strength and contain many interesting phases. The orthorhombic $PbNb_2O_6$ phase formed in PNSAl glass should provide a good ferroelectric behaviour. The face-centered cubic $Pb_2Nb_2O_7$ phase is formed in PGNSAl1 and PGNSAl2 glasses and may show interesting dielectric behaviour at low temperature where it has the possibility of being antiferroelectric or even ferroelectric. Again, the study of the microstructure and electrical properties of

these glass-ceramics should be continued. Since the glass-ceramics from this system have good mechanical properties and interesting phases, the most promising compositions should be studied more fully.

The summary of the important glass-ceramics from this study is presented in Table 8.1.

Table 8.1 *The glass-ceramics of interest from this study.*

System	Glass-ceramic	Crystalline phase	Comment
$BiO_{1.5}$-GeO_2-$BO_{1.5}$	$BiGeB_6$ (T_X = 475°C, 12 hrs)	Bi_2GeO_5	Ferroelectrics at room temperature, $T_C \sim 407$ °C, $P_s \sim 14$ μC/cm^2
PbO-GeO_2-Nb_2O_5	PG-0.5PN (T_X = 667°C, 48 hrs)	$Pb_5Ge_3O_{11}$ *$Pb_2Nb_2O_7$	Ferroelectrics at room temperature, $T_C \sim 166$ °C, $P_s \sim 1$ μC/cm^2
$Pb_5Ge_3O_{11}$-$PbNb_2O_6$-SiO_2+15%Al_2O_3	PGS (T_X = 538°C, 4 hrs)	$Pb_5Ge_{3-x}Si_xO_{11}$ (x = 1)	Potentially ferroelectric glass-ceramic
	PNSAl (T_X = 866°C, 4 hrs)	$AlNbO_4$ *$PbNb_2O_6$	Potentially ferroelectric Glass-ceramic
	PGNSAl2 (T_X = 711°C, 4 hrs)	**$Pb_2Nb_2O_7$	Potentially antiferroelectric or ferroelectric at low temperature
	PGNSAl4 (T_X = 935°C, 4 hrs)	$AlNbO_4$ **$PbNb_2O_6$	Large amount of $PbNb_2O_6$ crystals is of interest to convert to ferroelectric phase

Note: *$Pb_2Nb_2O_7$ = Rhombohedral (dielectric phase)
**$Pb_2Nb_2O_7$ = Cubic pyrochlore (may be either ferroelectric or antiferroelectric phase at low temperature)
*$PbNb_2O_6$ = Orthorhombic (ferroelectric phase)
**$PbNb_2O_6$ = Rhombohedral (paraelectric polymorph phase)

The dielectric and ferroelectric properties of the glass-ceramics from $Pb_5Ge_3O_{11}$-$PbNb_2O_6$-SiO_2+15%Al_2O_3 system have not yet been determined.